

Some pages of this thesis may have been removed for copyright restrictions.

If you have discovered material in AURA which is unlawful e.g. breaches copyright, (either yours or that of a third party) or any other law, including but not limited to those relating to patent, trademark, confidentiality, data protection, obscenity, defamation, libel, then please read our [Takedown Policy](#) and [contact the service](#) immediately

Design and development of a Time of Flight Fast Atom Scattering Spectrometer

A quantitative surface analysis technique and a new approach towards the experimental investigation of the surface particle interactions.

ROGER GILES
Doctor of Philosophy

THE UNIVERSITY OF ASTON IN BIRMINGHAM

May 1995

This copy of the thesis has been supplied on condition that anyone who consults it is understood to recognise that its copyright rests with its author and that no quotation from the thesis and no information derived from it may be published without prior acknowledgement.

Design and Development of a Time of Flight Fast Atom Scattering Spectrometry

Roger Giles B.Sc.

A Thesis submitted for the Degree of Doctor of Philosophy, 1995

Summary

A new surface analysis technique has been developed which has a number of benefits compared to conventional Low Energy Ion Scattering Spectrometry (LEISS). A major potential advantage arising from the absence of charge exchange complications is the possibility of quantification. The instrumentation that has been developed also offers the possibility of unique studies concerning the interaction between low energy ions and atoms and solid surfaces. From these studies it may also be possible, in principle, to generate sensitivity factors to quantify LEISS data. The instrumentation, which is referred to as a Time-of-Flight Fast Atom Scattering Spectrometer has been developed to investigate these conjecture in practice. The development, involved a number of modifications to an existing instrument, and allowed samples to be bombarded with a monoenergetic pulsed beam of either atoms or ions, and provided the capability to analyse the spectra of scattered atoms and ions separately. Further to this a system was designed and constructed to allow incident, exit and azimuthal angles of the particle beam to be varied independently. The key development was that of a pulsed, and mass filtered atom source; which was developed by a cyclic process of design, modelling and experimentation. Although it was possible to demonstrate the unique capabilities of the instrument, problems relating to surface contamination prevented the measurement of the neutralisation probabilities. However, these problems appear to be technical rather than scientific in nature, and could be readily resolved given the appropriate resources. Experimental spectra obtained from a number of samples demonstrate some fundamental differences between the scattered ion and neutral spectra. For practical non-ordered surfaces the ToF spectra are more complex than their LEISS counterparts. This is particularly true for helium scattering where it appears, in the absence of detailed computer simulation, that quantitative analysis is limited to ordered surfaces. Despite this limitation the ToFFASS instrument opens the way for quantitative analysis of the 'true' surface region to a wider range of surface materials.

Key Words Time of Flight, ToFFASS, LEISS, Fast Atom Scattering. Surface particle interaction. Charge Exchange.

Acknowledgements

I owe my sincere thanks to Dr.J.L.Sullivan for his continued support throughout the duration of this work. Special thanks are also due to Dr S.O.Saied for carrying out the XPS analysis. I am particularly grateful to A.Abbot for his invaluable technical support and many useful discussions. Thanks are also due to Mr C.G.Pearse for his continuing interest in the work. I also take pleasure in acknowledging the enthusiastic assistance of Z.Bochnicek and R.Mazanek who visited the department from Masaryk University, Brno.

I am deeply in debt to my wife who has displayed inexhaustible patience during the writing up period, and who has been responsible for endless proof reading.

2.4.2 The validity of the Henry's Law approximation in the simulation of adsorption data	17
2.4.3 Experimental measurement of ΔH_{ads}	18
2.4.4 LEIS as a probe of adsorption	19
2.4.5 Resolution of the data from the LEIS measurements	20
2.4.6 LEIS for surface reconstruction	21
2.4.7 The use of LEIS in the study of the adsorption of CO on Pt	22
2.4.8 The use of LEIS in the study of the adsorption of CO on Pt	23
2.4.9 The use of LEIS in the study of the adsorption of CO on Pt	24
2.4.10 The use of LEIS in the study of the adsorption of CO on Pt	25
2.4.11 The use of LEIS in the study of the adsorption of CO on Pt	26
2.4.12 The use of LEIS in the study of the adsorption of CO on Pt	27
2.4.13 The use of LEIS in the study of the adsorption of CO on Pt	28
2.4.14 The use of LEIS in the study of the adsorption of CO on Pt	29
2.4.15 The use of LEIS in the study of the adsorption of CO on Pt	30
2.4.16 The use of LEIS in the study of the adsorption of CO on Pt	31
2.4.17 The use of LEIS in the study of the adsorption of CO on Pt	32
2.4.18 The use of LEIS in the study of the adsorption of CO on Pt	33
2.4.19 The use of LEIS in the study of the adsorption of CO on Pt	34
2.4.20 The use of LEIS in the study of the adsorption of CO on Pt	35
2.4.21 The use of LEIS in the study of the adsorption of CO on Pt	36
2.4.22 The use of LEIS in the study of the adsorption of CO on Pt	37
2.4.23 The use of LEIS in the study of the adsorption of CO on Pt	38
2.4.24 The use of LEIS in the study of the adsorption of CO on Pt	39
2.4.25 The use of LEIS in the study of the adsorption of CO on Pt	40
2.4.26 The use of LEIS in the study of the adsorption of CO on Pt	41
2.4.27 The use of LEIS in the study of the adsorption of CO on Pt	42
2.4.28 The use of LEIS in the study of the adsorption of CO on Pt	43
2.4.29 The use of LEIS in the study of the adsorption of CO on Pt	44
2.4.30 The use of LEIS in the study of the adsorption of CO on Pt	45
2.4.31 The use of LEIS in the study of the adsorption of CO on Pt	46
2.4.32 The use of LEIS in the study of the adsorption of CO on Pt	47
2.4.33 The use of LEIS in the study of the adsorption of CO on Pt	48
2.4.34 The use of LEIS in the study of the adsorption of CO on Pt	49
2.4.35 The use of LEIS in the study of the adsorption of CO on Pt	50
2.4.36 The use of LEIS in the study of the adsorption of CO on Pt	51
2.4.37 The use of LEIS in the study of the adsorption of CO on Pt	52
2.4.38 The use of LEIS in the study of the adsorption of CO on Pt	53
2.4.39 The use of LEIS in the study of the adsorption of CO on Pt	54
2.4.40 The use of LEIS in the study of the adsorption of CO on Pt	55
2.4.41 The use of LEIS in the study of the adsorption of CO on Pt	56
2.4.42 The use of LEIS in the study of the adsorption of CO on Pt	57
2.4.43 The use of LEIS in the study of the adsorption of CO on Pt	58
2.4.44 The use of LEIS in the study of the adsorption of CO on Pt	59
2.4.45 The use of LEIS in the study of the adsorption of CO on Pt	60
2.4.46 The use of LEIS in the study of the adsorption of CO on Pt	61
2.4.47 The use of LEIS in the study of the adsorption of CO on Pt	62
2.4.48 The use of LEIS in the study of the adsorption of CO on Pt	63
2.4.49 The use of LEIS in the study of the adsorption of CO on Pt	64
2.4.50 The use of LEIS in the study of the adsorption of CO on Pt	65
2.4.51 The use of LEIS in the study of the adsorption of CO on Pt	66
2.4.52 The use of LEIS in the study of the adsorption of CO on Pt	67
2.4.53 The use of LEIS in the study of the adsorption of CO on Pt	68
2.4.54 The use of LEIS in the study of the adsorption of CO on Pt	69
2.4.55 The use of LEIS in the study of the adsorption of CO on Pt	70
2.4.56 The use of LEIS in the study of the adsorption of CO on Pt	71
2.4.57 The use of LEIS in the study of the adsorption of CO on Pt	72
2.4.58 The use of LEIS in the study of the adsorption of CO on Pt	73
2.4.59 The use of LEIS in the study of the adsorption of CO on Pt	74
2.4.60 The use of LEIS in the study of the adsorption of CO on Pt	75
2.4.61 The use of LEIS in the study of the adsorption of CO on Pt	76
2.4.62 The use of LEIS in the study of the adsorption of CO on Pt	77
2.4.63 The use of LEIS in the study of the adsorption of CO on Pt	78
2.4.64 The use of LEIS in the study of the adsorption of CO on Pt	79
2.4.65 The use of LEIS in the study of the adsorption of CO on Pt	80
2.4.66 The use of LEIS in the study of the adsorption of CO on Pt	81
2.4.67 The use of LEIS in the study of the adsorption of CO on Pt	82
2.4.68 The use of LEIS in the study of the adsorption of CO on Pt	83
2.4.69 The use of LEIS in the study of the adsorption of CO on Pt	84
2.4.70 The use of LEIS in the study of the adsorption of CO on Pt	85
2.4.71 The use of LEIS in the study of the adsorption of CO on Pt	86
2.4.72 The use of LEIS in the study of the adsorption of CO on Pt	87
2.4.73 The use of LEIS in the study of the adsorption of CO on Pt	88
2.4.74 The use of LEIS in the study of the adsorption of CO on Pt	89
2.4.75 The use of LEIS in the study of the adsorption of CO on Pt	90
2.4.76 The use of LEIS in the study of the adsorption of CO on Pt	91
2.4.77 The use of LEIS in the study of the adsorption of CO on Pt	92
2.4.78 The use of LEIS in the study of the adsorption of CO on Pt	93
2.4.79 The use of LEIS in the study of the adsorption of CO on Pt	94
2.4.80 The use of LEIS in the study of the adsorption of CO on Pt	95
2.4.81 The use of LEIS in the study of the adsorption of CO on Pt	96
2.4.82 The use of LEIS in the study of the adsorption of CO on Pt	97
2.4.83 The use of LEIS in the study of the adsorption of CO on Pt	98
2.4.84 The use of LEIS in the study of the adsorption of CO on Pt	99
2.4.85 The use of LEIS in the study of the adsorption of CO on Pt	100

CONTENTS

page

Summary	3
Acknowledgements	4
Contents	5
List of Figures	12
List of Tables	16
Chapter 1 - Introduction	17
Chapter 2 - Background and Basic principles of ion beam scattering spectroscopy	19
2.1 Common surface analysis techniques	19
2.2 Incident ion techniques.	19
2.2.1 Ion/atom Scattering Techniques	20
2.2.2 Secondary particle Techniques	21
2.3 The surface collision process of ions and atoms in the low energy ion scattering range (0.1 to 10 keV).	23
2.4 Physical basis and principals of Low Energy Ion Scattering Spectroscopy (LEISS)	24
2.4.1 Classical description the Ion/Atom Collision Process	24
2.4.2 The validity the Binary Collision Approximation in the simulation of scattering particle spectra.	25
2.4.3 Experimental arrangement of LEISS	27
2.4.4 LEISS in single collision mode	27
2.4.5 Resolution considerations of LEISS in SBC mode	29
2.4.6 LEISS for surface structure analysis	33
2.4.6.1 Concept of the shadow cone	33
2.4.6.2 Impact Collision Ion Scattering Spectroscopy (ICISS)	33
2.4.6.3 Differences between 180° and near 180° scattering	37
2.4.6.4 Glancing angle techniques	37
2.5 Factors complicating the interpretation of LEISS spectra.	38
2.5.1 Multiple scattering from polycrystalline and single crystals surfaces	38
2.5.2 Thermal vibrations	40
2.6 Applications of LEISS	42
2.6.1 Composition analysis	42

2.6.1.1 Qualitative analysis	42
2.6.1.2 Quantitative analysis	43
2.6.2 Structural information using multiple collision mode	45
2.6.3 LEISS studies of fundamental processes	45
2.7 Limitations of conventional LEISS and corresponding developments	46
2.7.1 Damage and excessive erosion rates	46
2.7.2 Charging effects in insulators and semiconductors	47
2.7.3 Lack of quantification	47
2.7.4 Developments for structural analysis	48
2.8 Scattered neutral spectra and time-of-flight analysis	50
2.8.1 Time-of-flight analyser resolution	50
2.8.2 Time-of-flight spectral broadening	52
2.8.3 Intermediate scattering angles from non-ordered surfaces	55
2.8.4 Scattering data at intermediate angles from ordered surfaces	62
2.8.5 Large angle and co-axial impact ToF data	66
2.8.6 General conclusions	73
2.9 Fast atom scattering data	77
4.3 The parametric pulsed ionization technique	77
Chapter 3 - Charge exchange and inelastic loss processes	80
3.1 Mechanisms for Charge Transfer.	80
3.1.1 Auger neutralisation (AN)	82
3.1.2 - Resonant Neutralisation (RN) and Resonant Ionisation (RI)	82
3.1.3 Quasi Resonant Neutralisation (qRN)	83
3.1.4 Re-ionisation - The Electeron Promotion Mechanism	84
3.1.5 Re-ionisation - Autoionisation	87
3.2 Inelastic Energy Loss	87
3.2.1 General Electron Stopping Models	89
3.3 Development of Parametric Adiabatic Models	90
3.3.1 The Hagstrum Model	91
3.3.2 Godfrey Wodruff Model	92
3.3.3 Verbist Model	94
3.4 Quantum Mechanical Treatments	95
3.5 Verhey's three stage model	98
3.6 Experimental investigation of charge exchange	98
3.6.1 Measurement of charge exchange probabilities	98

3.6.2 Measurement of inelastic energy losses.	106
Chapter 4 - Development of a Pulsed Ion/Atom Source	109
4.1 Introduction	109
4.2 Background and History	109
4.2.1 Construction philosophy	109
4.2.2 Development history	110
4.2.3 The specific requirements of a ion/atom source for ToFFASS	112
4.2.4 Physical description of the prototype pulsed ion/atom	112
4.3 Basic principles of ion source operation	115
4.3.1 The Ion source	115
4.3.2 The extraction optics.	118
4.3.3 Optical quality of the extracted beam	119
4.3.4 Ion optics of the beam transport system	119
4.4 Experimental procedure	126
4.4.1 Measurement of continuous beam current	126
4.4.2 Measurement of beam profiles	128
4.4.3 Measurements of the primary beam spectra	130
4.4.4 Differential pumping of the ion/atom source	130
4.5 The prototype pulsed ion/atom source	133
4.5.1 Initial operation	133
4.5.1.1 Beam current	135
4.5.1.2 Beam profile	141
4.5.1.3 Primary spectra	141
4.5.2 Limitations of the prototype source	148
4.5.3 Analysis of prototype characteristics	148
4.5.3.1 Ion source and extraction optics	148
4.5.3.2 The optics	158
4.5.3.3 The primary beam filter	159
4.5.3.4 General discussion	167
4.6 The modified source - FAB1	168
4.6.1 Re-design	168
4.6.1.1 Beam chopping system	168
4.6.1.2 Ion optics	174
4.6.1.3 General	179
4.6.2 Experiment	180
4.6.3 Experimental characteristics of FAB-1	180
4.6.3.1 Beam profile	181

4.6.3.2	Beam current	184
4.6.3.3	Primary spectra	187
4.6.4	Remaining limitations	192
4.6.5	Analysis of operation	192
4.6.5.1	Ion optics	192
4.6.5.2	Pulsing system	192
4.6.5.3	Pumping of the transport column and CEC	193
4.7	Modified ion source - FAB2	197
4.7.1	Design principles of new elements	197
4.7.1.1	Ion optics	197
4.7.1.2	Wein filter	197
4.7.1.3	The neutral dump unit	202
4.7.1.4	The chopping plates	204
4.7.2	Characterisation of the FAB-2 source	204
4.7.2.1	Beam current	205
4.7.2.2	Beam profile	207
4.7.2.3	Primary spectra	207
4.8	Conclusions	217
4.8.1	Final characteristics	217
4.8.2	Operational problems	218
4.8.3	Future development	218
Chapter 5 - Development of the Spectrometer		220
5.1	Description and limitations of the prototype instrument	220
5.2	Collimation of the scattered particle beam - flight tube stop apertures	223
5.2.1	Evidence of internal scattering	223
5.2.2	Reduction of internal tube scattering	224
5.3	Scattered ion/atom separation	229
5.3.1	Acceleration tube - design and operation	231
5.3.2	Acceleration tube - design criteria and constraints.	232
5.3.3	Acceleration tube - construction	236
5.3.4	Acceleration tube - experimental verification	236
5.4	Miscellaneous aspects of instrument development	238
5.4.1	Primary beam alignment	238
5.4.2	Source gas supplies	238
5.4.3	The sample stage	240
5.4.4	Scattered particle detection	243

5.5 Development of a sample rotation goniometer	246
5.6 Conclusions	250
Chapter 6 - Scattering Results	253
6.1 Experimental results 90° scattering	253
6.1.1 Scattering from a polycrystalline copper	254
6.1.1.1 Helium scattering - ion bombardment	254
6.1.1.2 Helium scattering - neutral bombardment	257
6.1.1.3 Neon Scattering	257
6.1.1.4 Argon scattering - ion bombardment	260
6.1.2 Scattering from amorphous silicon	260
6.1.2.1 Helium scattering	260
6.1.2.2 Neon scattering	264
6.2 Experimental results - 164° scattering - flight/acceleration tube	265
6.2.1 Helium scattering	265
6.2.1.1 from an evaporated gold surface onto single crystal silicon.	265
6.2.1.2 from polycrystalline Gold and Nickel surfaces	269
6.2.2 Neon scattering	272
6.2.3 Argon spectra	275
6.3 164° scattering employing the modified flight/acceleration tube	275
6.3.1 Helium Scattering	277
6.3.2 Neon Scattering	279
6.3.2.1 from polycrystalline gold	279
6.3.2.2 from polycrystalline nickel	282
6.3.3 Argon Scattering	285
Chapter 7 - Discussion of Results	288
7.1 Discussion of the experimental spectra in relation to the surface-particle interaction process and surface composition.	288
7.1.1 Multiple scattering and peak broadening features of the experimental spectra.	288
7.1.2 The absence of a scattered ion peak	293
7.1.3 Recoiling features of the experimental spectra.	297
7.1.4 Surface contamination	300
7.1.5 Neutral bombardment	302
7.2 Limitations of the ToFFASS technique.	303

LIST OF FIGURES

2.1 Possible events when an energetic ion strikes a solid surface.	22
2.2 A typical cascade atom distribution - (TRIM).	22
2.3 Mono-layer formations time as a function of gas pressure calculated from Boltzman's equation.	28
2.4 Schematic of a single-scattering collision.	28
2.5 Solutions of eq 2.7.	30
2.6 Mass resolutions factors as a function of ϑ .	30
2.7 Total Mass resolution in LEISS as a function of ϑ .	34
2.8 Calculated asymptotic scattered trajectories.	34
2.9 Focusing effects at the shadow cone edge.	35
2.10 $I - \theta$ pattern of the backscattered signal, $\vartheta = 165^\circ$, Ne^0 scattered from Pt(111).	35
2.11 Characteristic scattering loops - obtained for fixed angle of incidence.	39
2.12 Single and double collision energies.	41
2.13 Comparison of the resolving power of ESA and ToF analysers.	51
2.14 Scattered particle energy spectra derived from experimental ToF spectra.	56
2.15 He^+ scattered from Ni.	57
2.16 Ne^+ scattered from a Si, after Buck et al.	59
2.17 Round Robin comparison of scattered neutral particle data, 5keV He-Au.	60
2.18 Round Robin comparison of scattered neutral particle data, 5keV Ne-Au.	60
2.19 Round Robin comparison of scattered neutral particle data, 5keV Ar-Au.	61
2.20 Ne^+ scattered from a CsBr, $E_o = 3 \text{ keV}$, $\vartheta = 135^\circ$.	63
2.21 Ar^+ scattered from CsBr. $E_o = 3 \text{ keV}$, $\vartheta = 90^\circ$.	64
2.22 Ne^+ scattered from Cu(100), $E_o = 10 \text{ keV}$, $\vartheta = 30^\circ$.	64
2.23 Ne^+ scattered from Ni(001) $\vartheta = 90^\circ$, $E_o = 2.4 \text{ keV}$.	67
2.24 K^+ ions scattered from clean W(110) (ESA data) $E_o = 250 \text{ eV}$ at $\vartheta = 90^\circ$. $\theta = 45^\circ$.	68
2.25 Ne^+ scattered from $\text{Cu}^3\text{Au}(100)$, $E_o = 5 \text{ keV}$, $\vartheta = 90^\circ$.	69
2.26 NICISS spectra from Pt(111), $E_o = 2 \text{ keV}$, $\vartheta = 165^\circ$.	70
2.27 NICISS spectra, Ne^+ scattered from Pt(111), $\vartheta = 180^\circ$, $E_o = 2 \text{ keV}$.	72
2.28 Ne^+ scattered from Pt(110), 2 keV, $\vartheta = 90^\circ$.	74
2.29 Ar^+ scattered from Ni(100), $E_o = 8 \text{ keV}$, $\vartheta = 166^\circ$.	74
2.30 CAICASS - He^+ from $\text{Si}(111)\sqrt{3}\times\sqrt{3}\text{R}30^\circ$ with deposited Ag. $E_o = 2 \text{ keV}$.	75
2.31 CAICASS - He^+ from InAS(001), $E_o = 2 \text{ keV}$.	75
3.1 The basic physical scenario involving various charge exchange processes.	81
3.2 Oscillating structure in the ion intensity when plotted against the inverse of	81

ion velocity.	
3.3 Schematic showing the ionisation of He ⁰ by the electron promotion mechanism.	85
3.4 A Schematic of the charge exchange model of surface collisions suggested by Verhey et al.	99
3.5 A Schematic of the charge exchange model suggested by Aono and Souda.	99
3.6 Possible sequences of charge exchange during the scattering event.	101
3.7 LEISS spectra. He ⁺ and He ⁰ from TaC(001), E ⁰ = 389 eV, $\theta=120^\circ$.	108
4.1 The basic FAB source construction.	111
4.2 Elements of the prototype FAB source.	113
4.3 Ionisation cross-section data.	117
4.4 Beam emittance diagram.	117
4.5 The application of Gauss' law may to a simple aperture lens calculation.	121
4.6 Basic lens structures.	121
4.7 Basic lens combinations.	124
4.8 Beam current measurement apparatus.	127
4.9 Co-ordinate system used in description of primary beam measurements.	129
4.10 Spectrometer configuration for measurement of primary beam spectra.	129
4.11 Differential pumping geometry.	131
4.12 Experimental values of V_w v V_o - prototype source.	136
4.13 Total beam current as a function of V_w - prototype source.	137
4.14 Total ion and neutral currents, as a function of V_w - prototype source.	138
4.15 Total beam current as a function of V_o , fixed V_w - prototype source.	138
4.16 Typical beam profile - prototype source.	139
4.17 Beam profile data - prototype source.	139
4.18 Beam profile dependence on V_w - prototype source.	140
4.19 Pulsing Circuits - prototype source.	142
4.20 Primary Spectra - showing the effect of biased counting statistics - prototype source	144
4.21 Primary ion spectra - dependency on V_{ext} - prototype source	146
4.22 Primary spectrum resulting from the pulsing the x-y deflection plates - prototype source.	147
4.23 Details of prototype ion source.	149
4.24 Simulated electron trajectories in the ion cell.	151
4.25 Calculated ionisation probability distribution.	152
4.26 Histogram showing the extraction time distribution.	154
4.27 Histogram showing the distribution of extracted ion energies.	154

4.28 Simulated phase space emittance diagram of the extraction ion beam.	156
4.29 Graph showing the form of equation 4.27.	160
4.30 Distribution of the axial positions of the extracted ions.	160
4.31 Geometry of the - prototype Wein filter.	162
4.32 Mass resolution v field strength - prototype Wein filter.	162
4.33 Axial field of the - prototype Wein filter.	164
4.34 Ion trajectories - prototype Wein filter.	165
4.35 Basic beam chopping system.	170
4.36 Beam Chopping Unit (BCU) - FAB-1 source.	170
4.37 Schematic of the chopping plate pulsing circuit.	173
4.38 An oscilloscope trace of the beam chopping waveform.	173
4.39 Illustration of the calculation model - relating to beam chopping.	175
4.40 Calculated deflection curve.	176
4.41 Geometry of the 1st lens - FAB-1 source.	178
4.42 Vertical beam scans - FAB-1 source.	182
4.43 Vertical beam scans - FAB-1 source.	183
4.44 Ion beam current measured as function of pressure.	185
4.45 Neutral beam current measured as function of pressure.	186
4.46 Ion beam current measured as a function of E_0 .	186
4.47 Primary beam spectrum - FAB-1 source.	188
4.48 Primary Spectra - FAB-1 source.	190
4.49 Primary Spectra showing the 'scattered peak' - FAB-1 source.	191
4.50 Re-calculated deflection curves.	194
4.51 Experimental deflection curves.	194
4.52 Optical Characteristic of the 1st lens - FAB-2 source.	198
4.53 Geometry of the Re-Design Wein Filter - FAB-2 source.	200
4.54 Dimensions of the Neutral Dump Unit - FAB-2 source.	200
4.55 Characteristic of the Wien filter for a helium beam - FAB-2 source.	206
4.56 Helium beam profiles - FAB-2 source.	208
4.57 Helium neutral beam profiles - FAB-2 source.	209
4.58 Flight time of ions through the chopping plates - FAB-2 source.	211
4.59 Primary spectra - Argon - ion beam - FAB-2 source.	212
4.60 Primary spectra - Neon - ion beam - FAB-2 source.	213
4.61 Primary spectra - Helium - ion beam - FAB-2 source.	214
4.62 Primary spectra - ion and neutral beam - FAB-2 source.	216
4.63 Primary spectra - 1 keV neon beam - FAB-2 source.	216
5.1 Diagram of the main vacuum chamber.	221
5.2 A figure illustrating the difference with regard to scattering from the internal.	225

walls of the flight tube between the primary and scattered spectra configurations.	
5.3 Geometry of the aperture system for the prevention of scattering within the flight tube.	227
5.4 $\Delta\theta$ v position of aperture within the flight tube.	230
5.5 Diagram showing the importance of matching r_a and r_s .	230
5.6 S v $A - S$ in the domain between 0 and 1 corresponding to E_a/E_j between 0 and ∞ .	233
5.7 Construction of the acceleration tube lens system.	233
5.8 Calculated peak separations.	235
5.9 Flight/acceleration tube geometry.	237
5.10 Shift in the primary ion peak due to the acceleration tube.	239
5.11 Comparison of experimental and calculated separation times.	239
5.12 Schematic of the modified source gas feed arrangement.	241
5.13 Schematic of the sample stage.	242
5.14 Co-ordinate system to describe the motion of the 3-axis sample goniometer.	247
5.15 Stepper motor angles A and B .	249
5.16 Sketch of the 3 axis goniometer.	250
5.17 Instrumental resolution, expressed in terms of $\Delta t/t$.	251
6.1 Experimental spectra - He ⁺ scattered from polycrystalline Cu.	255
6.2 Calculated positions of the QS, QD and QT peaks.	256
6.3 Calculated spectrum showing the expected position of the accelerated ion peak.	256
6.4 He ⁺ and He ⁰ scattered from polycrystalline copper, variation with incident angle.	258
6.5 Experimental spectrum - Ne ⁺ scattered from polycrystalline Cu.	259
6.6 Calculated spectra - Ne ⁺ scattered from polycrystalline Cu.	261
6.7 LEISS spectrum - He ⁺ scattered from polycrystalline Cu.	262
6.8 Experimental spectra - He ⁺ scattered from Si.	262
6.9 Calculated spectra showing the expected position of the accelerated ion peak.	264
6.10 Experimental spectra of He ⁺ scattered from Au evaporated onto a Si(001) wafer.	267
6.11 Spectra of the evaporated Au after heating.	268
6.12 Comparison of He-Si region before (a) and after (b) prolonged heating.	270
6.13 Experimental spectrum - He ⁺ scattered from polycrystalline Au.	271
6.14 Experimental spectrum - He ⁺ scattered from polycrystalline Ni.	271
6.15 Experimental spectrum - Ne ⁺ scattered from polycrystalline Ta.	273

6.16 Experimental spectrum - Ne ⁺ scattered from polycrystalline Au.	273
6.17 Experimental spectrum - Ne ⁺ scattered from contaminated Ni.	274
6.18 Experimental spectrum - Ar ⁺ scattered from contaminated Au.	274
6.19 Experimental spectrum - Ar ⁺ scattered from contaminated Ni.	276
6.20 Experimental spectra - He ⁺ scattered from (a) Au, (b) Pt, (c) Ta, (d) Ni	279
6.21 Experimental spectrum - Ne ⁺ scattered from polycrystalline Au.	280
6.22 Calculated spectra showing expected ion-neutral separation - acceleration/ flight configuration 2.	281
6.23 Experimental spectra - Ar ⁺ scattered from contaminated polycrystalline Au. (V _a - 3.0 k V applied to the acceleration tube)	281
6.24 Experimental spectrum - Ne ⁺ and Ar ²⁺ scattered from polycrystalline Au.	283
6.25 Experimental spectrum - Ne ²⁰⁺ and Ne ²²⁺ scattered from polycrystalline Au.	284
6.26 Experimental spectrum - Ne ⁺ scattered from polycrystalline Ni.	286
6.27 Experimental spectrum - Ar ⁺ scattered from polycrystalline Au.	286
7.1 Experimental LEISS spectra, He ⁺ scattered from Si.	291
7.2 Calculated a shadow cones, (a) for a 2000 eV Ar-Au collision, and (b) for a 2000 eV He-Au collision.	292
7.3. Methods of integration to extract an estimation of the QS signal intensity.	294
7.4 - Schematic of the contamination layer, depicting some of the possible scattering, neutralisation and recoil process.	296
7.5 A collision sequence leading to the recoiling of target atom froms.	298
7.6 - Energy recieved by a hydrogen recoil as a function of the impact parameter.	301

LIST OF TABLES

Table 2.1 - Time of flight scattering data	53
Table 4.1 : SEE data, γ values.	126
Table 4.2 : Conductance data	132
Table 4.3 : Gauge sensitivity factors	132
Table 7.1 : Ion survival probabilities	295
Table 7.2 - Ion peak detection limits (this work) 2.2 keV primaries scattered from a Au surface.	295
Table 7.3 Total collision cross-sections for collisions $> 1^\circ$ deflection by the primary / 10^{-16} cm ²	299
Table 7.4 Maximum deflection angles (degrees)	299
Table 7.5 Energy transferred factors to recoil atoms	299
Table 7.6 - Sample dose and collection times ($\Delta\theta = 0.85^\circ$)	305
Table 7.7 - Sample dose and collection times ($\Delta\theta = 8^\circ$)	305
Table 7.8 Spectral resolution	306

Chapter 1 Introduction

Surface science is an important branch of science as all solids 'communicate' with the outside world through their surfaces. Many areas of modern technology, for example microelectronics, thin-film devices and heterogeneous catalysis are increasingly employing large area-to-volume ratio devices. Processes such as wear, corrosion, and passivation all take place at the surface. There are many surface analysis techniques presently in use, each of which has its own particular strength and weakness. The technique of Low Energy Ion Scattering Spectroscopy (LEISS) is one of the most surface specific of all surface analysis techniques, providing physical and chemical data of solid surfaces at a depth resolution of a single mono-layer. As such it represents a unique tool both in fundamental studies and industrial research. The scattered signal conveys compositional¹⁻⁶ as well as surface structural⁷⁻¹³ information. The capabilities of LEISS are compared with surface analysis techniques in chapter 2. It is also shown in chapter 2, that in addition to its attributes, there are a number of problems associated with LEISS in the conventional form. These problems have restricted the use of the technique.

Typical LEISS instrumentation consists of a d.c. inert gas ion source and a high resolution electrostatic analyser, components already available on many UHV surface analysis instruments. However, in this form three basic problems arise: (i) surface damage and excessive erosion rates (ii) lack of quantification and (iii) surface charging in insulators and semiconductors. The first limitation is largely a direct consequence of the surface particle interaction process, which generally leads to the neutralisation of a large proportion (typically > 95 %) of the scattered particle yield, representing a corresponding loss of the LEISS signal. To combat the loss of signal the primary beam current must be increased by the same factor. The second limitation is attributed to the complex nature of the neutralisation processes, which has prevented the development of a reliable model capable of predicting neutralisation probabilities, which are very sensitive to many different factors. The third limitation is a direct consequence of the charge injected by the primary beam.

A simple solution to (i) and (ii) is to employ an analyser capable of collecting the full scattered yield, and a number of ToF systems have been built and their benefits over conventional LEISS reported¹⁴⁻²⁵. The ToF

method gains signal through the collection of the full yield, and additionally by the multi-channel nature of the analysers. Thus ToF analysers have been shown to give significant reductions in the sample dose necessary to perform the analysis. However, the third limitation concerning the charging of insulating samples is not addressed, and can only be overcome by the employment of a neutral primary beam. This has a dual advantage. Firstly, due to the removal of the charge input, the surface can charge only to a potential equal to that of the secondary electrons. This is a few eV only, which is not sufficient to cause beam steering problems. Thus insulating samples can be analysed. The second advantage relates to a reduction in charge induced physical and chemical degradation.

Having experienced the above difficulties with their conventional LEISS system, the Aston Group commenced a programme to investigate the feasibility of combining ToF analysis with neutral beam bombardment: it was apparent at this stage that an instrument with these capabilities offered the prospect of quantitative analysis, with comparable surface specificity to LEISS, but without the associated damage problems. Such an instrument based on an adapted Kratos Macro-FAB source was constructed and some initial scattering data gathered, which are described in a number of publications²⁶⁻²⁸. As these results indicated some severe instrumental limitations a complete redesign of the instrument was initiated. At the onset of this doctoral work the basic components of the new instrument had been assembled, but no measurements of its capabilities had been made. The initial phase of this work was therefore to examine the capabilities of the existing instrumentation and to undertake the necessary development. It was also apparent that if the neutral and ion fractions of the scattered yield could be measured separately the instrument would provide a unique experimental facility for studying the fundamental aspects of the surface/particle interactions process. It was seen by exploring these ideas further, that more fundamental information concerning these processes could be gained if the sample could be rotated around three independent axes, and this capability formed a further aspect of instrument development.

Chapter II

Background

Principles of ion and neutral beam scattering spectroscopies

2.1 Common surface analysis techniques.

ToFFASS involves probing the surface with an ion/atom beam and the extraction of information from the scattered ion/atom signal. The underlying principle is that of elastic scattering. Other techniques based on other physical principles gain surface information conveyed by scattering of emitted photons and electrons, ions and neutrals. Most techniques currently in use have evolved since the early 1960's, and are generally based on one of the following interaction processes: elastic or inelastic scattering, diffraction, ionisation, bond breaking and charge exchange. Distinct from most techniques are those which employ a solid tip or electric field to probe the surface. Examples of these are the scanning tunnelling microscope and field electron microscope. This wide diversity of techniques is necessary to study a broad range of surfaces, with respect to their composition, structure, and chemical state. Additionally, greater confidence may be associated with the data where more than one technique is employed. Further considerations relate to the resolution of the data, in terms of the lateral and depth dimensions, and mass/energy of the scattered/emitted particles. For these reasons modern analysis chambers usually employ a range of analytical techniques with differing capabilities. The techniques which have shown themselves to be of most use in the solution of practical problems in surface science and surface engineering are Auger Electron Spectroscopy (AES), Low Energy Electron Diffraction (LEED), X ray Photoelectron Spectroscopy (XPS), Secondary Ion Mass Spectroscopy (SIMS) and Low Energy Ion Scattering Spectroscopy (LEISS).

2.2 Incident ion techniques.

There are a variety of incident ion/atom beam techniques in use which provide a wide range of information. These techniques may be grouped into the following categories.

1] Elastic scattering: Primary particles having undergone collision with

surface atoms are analysed in terms of their energy and angular distributions.

2] Secondary ion/atom: Secondary ions or atoms sputtered from the surface as a result of the primary particle impact are mass analysed.

3] Secondary electron: Secondary electrons emitted as a result of the primary particle impact are energy analysed; the analysis of auger electrons emitted as a result of valence band transitions forms the basis of the technique of Ion Neutralisation Spectroscopy (INS).

This work mainly concerns the first group, although features relating to the generation of secondary particles were observed in the ToF spectra.

2.2.1 Ion/atom Scattering Techniques

Further distinction is necessary relating to the incident particle energy, which depending on the particular technique may range from 1eV to a $\sim 10^3$ keV:

<1 eV - Thermal energy atoms are used to gain structural information of ordered surfaces in Thermal Energy Atom Scattering (TEAS). As in LEED information is obtained in reciprocal space from the scattered particle diffraction pattern.

1eV to 50 eV - The use of atom scattering in the hyperthermal region has recently attracted much theoretical interest but is yet to be exploited experimentally due to the problems of producing the primary beam.

50 eV to 5 keV - This region relates to this work and is occupied by Low Energy Ion Scattering Spectroscopy (LEISS) and associated techniques. The relevant processes are discussed further in the following sections.

10-150 keV - This region is occupied by the technique of Medium Energy Ion Scattering (MEISS). The scattering cross-section is decreased compared to LEISS resulting in a greater signal from sub-surface layers, the technique is therefore correspondingly less surface sensitive than LEISS.

>150 keV Rutherford Backscattering (RBS). In this technique energies up to 1 MeV are commonly used, giving rise to further reduction in the scattering cross-section. At these energies neutralisation does not play a role, and information is gained from the sub-surface region, up to ~ 15 atomic layers.

As screening of the nuclear charge by the atomic electrons at this energy has much decreased influence, shadowing effects can be calculated with high accuracy. As a result bulk and top layer lattice locations are found more accurately than by LEISS, however it should be noted that the capital cost of RBS and MEISS is much greater than LEISS.

2.2.2 Secondary Particle Techniques

A brief summary of secondary particle techniques is given as the sputtering and recoil processes are inherent in all incident ion/atom techniques, and can also contribute features to the scattered particle spectra.

Of all the secondary particle techniques SIMS is the most commonly used. Here the surface is bombarded with an ion beam of energy comparable to LEISS, and data is derived from the mass spectrum of positive or negative secondary ions. The technique finds very different applications to LEISS: the main strength is the capability to provide analysis with very high sensitivity to absorbate atoms, within the top ~ 3-4 atomic layers. By the very nature of the technique, the surface to a small extent is 'consumed', and this inherent erosion can lead to problems in static 'studies'. In 'dynamic' SIMS surface layers are intentionally etched away in order to give a profile of composition in the surface region. Typically, dynamic SIMS removal rates are ~10 $\mu\text{m/hr}$ compared to those of LEISS or 'static' SIMS of ~1 \AA/hr . In theory structural information is also available from the secondary ion signal if angle resolved measurements were to be made³⁸, although in practice structural information is more readily obtained from the scattered particle signal. A significant advantage of SIMS is the possibility to employ a sharply focused primary beam, leading to good spatial resolution, or a highly magnified secondary particle image of the surface. Some recent developments in instrumentation have broadened the application base of SIMS: SNMS instruments employ 'post ionisation' of the secondary neutral emission and provide a significant advantage in terms of surface damage. Whereas ToFSIMS instruments use ToF rather than quadrupole analysers to gain the mass spectrum, giving rise to higher mass resolution and/or mass range. Both SNMS and ToFSIMS allow damage to be reduced below that of conventional SIMS.

Direct Recoil Spectroscopy, DRS represents another technique based on the analysis of secondary particles. In this technique direct recoil

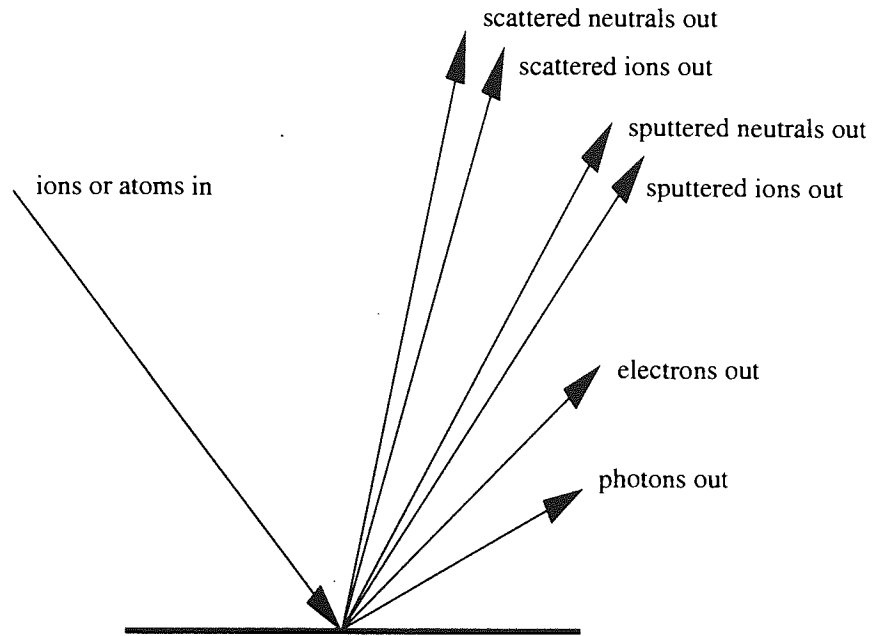


Figure 2.1 - Figure showing possible events resulting when an energetic ion strikes a solid surface

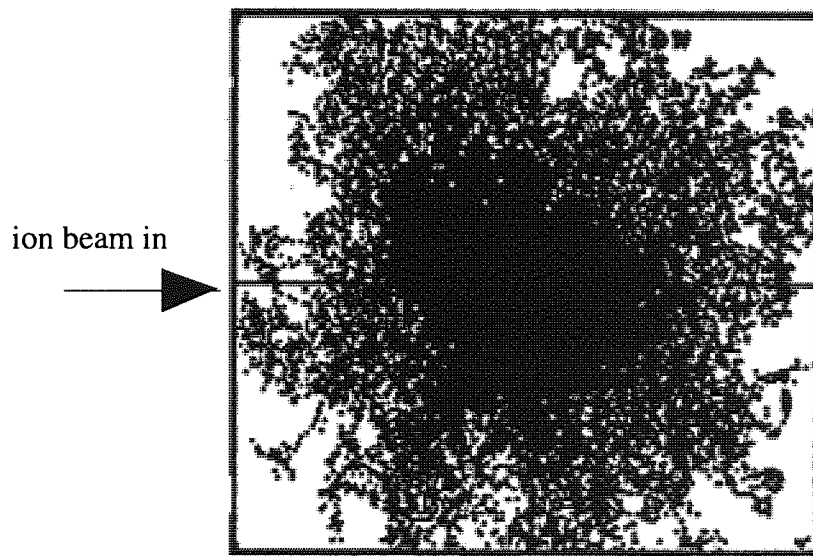


Figure 2.2 - An ion cascade calculated by TRIM, 5 keV Ar⁺ bombardment of a silicon surface, normal incidence, showing the final positions of the cascade atoms (region 20 x 20 nm)

ions are energy analysed. The fundamental difference between sputtered and recoil particles is that the latter gain their energy from single impact collisions, and consequently can process significantly greater energy.

2.3 The surface collision process

Complete description of the physical interaction between energetic ions or atoms is very complex; the impact can result in many physical phenomena, and associated information is conveyed to the outside world via the processes depicted in figure 2.1. In this section a review of the effects of the ion impact upon the surface is given. The discussion relates to primary energies in the LEISS regime only. These aspects are of relevance in that they can directly or indirectly influence the scattered particle spectrum, and the information presented here is used in later chapters. Aspects relating to scattered particles are covered in later sections of this chapter.

Primary ions impart an energy to target atoms, that is atoms of the uppermost surface layer, which is typically hundreds of times greater than lattice bond energies. This results in the displacement of target atoms, giving rise to the ejection of direct recoils and the formation of a cascade within the surface region. A cascade results from a large number of knock collisions, causing the displacement of a large number of atoms from their original lattice position. Sputtered particles arise when the trajectory of a cascade recoil intersects the surface with sufficient momentum to overcome the surface binding energy. Particles emitted in this way originate mainly from the top 3 to 4 mono-layers, with a mean energy of a few electron volts, and may be positive or negative ions, atoms, or neutral or charge molecules. A number of Monte Carlo computer simulation codes have been developed to study the phenomenon. A distribution calculated by the TRIM code^{29,30}, is shown in figure 2.2, in which case the sputtered yield, S , that is the number of atoms ejected per incident ion is 0.22. As a result of this process 'mixing' of atoms within the surface region occurs. For example, a crystalline surface exposed to a high fluence ion beam completely loses its structure and effectively becomes amorphous. The sputtering process forms the basis of many ion beam processes, including unwanted damage in LEISS and static SIMS. In general the removal rate of surface material is difficult to quantify accurately: S is sensitive to energy and mass, angle of incidence, electron configuration and charge state of the primary, as well as the binding energy, crystal structure and orientation of the surface. One of the most important factors is the energy

transfer factor; light primaries incident on heavy target atoms lead to a low yield, whilst that for heavy particles incident on light target atoms is much greater. In terms of the primary energy, S increases first exponentially and then linearly before reaching a maximum value, above a given threshold energy. Typical values for S were given by Sigmund³¹ for the He⁺ Ne⁺ and Ar⁺ primaries incident on pure polycrystalline metal surfaces. Sigmund's multiple collision theory gives an expression S as a function of the depth of the sputtered particle³². Sputtering yields are modified by incident angle, initially as $1/\cos\theta$, although at glancing angles sputtering yields become very low, due to decreased penetration and energy transfer. However, Sigmund's theory applies to elemental surfaces only. For surfaces composed of two or more species the sputtering rate of the two components may differ, leading to preferential removal of one species, and thus a change in the composition of the surface region.

As depicted in figure 2.1 secondary electrons may also result from the ion/atom impact process, which may originate from the surface valence band and atomic levels. These electrons which maybe ejected via a variety of processes have a mean energy of a few eV and give rise to a secondary electron coefficient, γ . γ is generally less than unity for most conditions encountered in LEISS, but is strongly dependent on the target surface, the primary species, energy and incident angle. Values of γ have been measured for a number of specific ion surface combinations, but no widely applicable data is available. Clearly the emission of secondary electrons indicates an inelastic loss on the part of the incident ion/atom. These processes are discussed in detail in chapter 3.

2.4 Principles of Low Energy Ion Scattering Spectroscopy (LEISS)

2.4.1 The validity of the classical description

The kinematics of individual particle-particle collisions in LEISS experiments are treated on a classical basis. The basic physics corresponds closely to gas ion/atom collisions, which is well developed, and covered by Bransden³³. In the general case the collisions must be treated by the quantum partial wave theory of potential scattering, involving the construction of appropriate quantum wave functions for the colliding particles. However, for collision energy involved in LEISS, the quantum and classical treatments converge. The classical limit is defined by the following criteria:

1] The De Broglie wavelength associated with the motion of the two particles must be smaller than the interaction region, that is

$$\lambda = 2\pi/\mu v_o \quad -(2.1)$$

where v_o is the initial velocity, μ the reduced mass, and λ the De Broglie wavelength.

2] Heisenberg's principle defines a minimum critical angle ϑ_c . Collisions below ϑ_c lead to a violation of the uncertainty principle. This can be expressed as:

$$\vartheta \gg 1/p\Delta b \gg 1/pb \quad -(2.2)$$

where ϑ is the scattering angle, p is the momentum and b is the impact parameter of the collision. Thus the critical angle is given by:

$$\vartheta_c = 1/(b\mu v_o) \quad -(2.3)$$

Evaluation of equations 2.1 and 2.3 shows classical mechanics to be well founded in all particle collisions encountered in LEISS.

2.4.2 The Validity of the Binary Collision Approximation in the description of LEISS experiments

Smith [1967]³⁴ was first to use a low energy ion beam to analyse solid surfaces. His experiments demonstrated that the energy lost by the scattered ions could be predicted by a simple 'billiard ball' model. Justification of Smith's experimental results can be given in terms of the following considerations:

1] Diffraction effects, encountered in TEAS can be discounted in LEISS, as the associated wavelength is very short relative to lattice dimensions.

2] Lattice dimensions are larger than the effective range of the interatomic potential, therefore forces acting between any two individually colliding particles are solely between those particles and not appreciably influenced by the presence of surrounding lattice atoms.

3] Lattice binding effects on the target atoms do not influence the collision process. Justification for this assumption originates from comparison of the collision interaction time and the period of a single lattice vibration, which is two orders of magnitude shorter. As a consequence, the scattering particle has moved far away from the collision site before the target atom can move appreciably.

These three basic approximations together form the basis of the Binary Collision Approximation, BCA. This implies that the individual collisions between the primary particle and individual atoms of the surface lattice may be treated as gas phase collisions. Further to this Smith's original work showed for the first time that most backscattered ions result from Single Binary Collisions, SBC, and the position of the resulting peaks in the LEISS spectra are well predicted by the Single Binary Collision Energy, SBCE. The accuracy and 'point' of breakdown has been the subject of much investigation, and remains the subject of some dispute. The main area of dispute relates to the second of the three assumptions given above. Hart and Cooper found the SBCE to be valid for primary energies as low as 25eV³⁵. However, in this case the BCA is employed to predict a relatively straight forward collision mechanism. A more stringent test of the BCA, is where its use is extended to description of more complex collision phenomena. For example the BCA forms the basis of Monte Carlo simulation codes, such as Marlowe³⁶ and TRIM^{29,30}, which are used to study multiple collisions of primaries as well as the secondary particle phenomena of sputtering and implantation. Investigations of the validity of the BCA in such applications, have been made by comparison with Molecular Dynamics (MD) based simulation codes³⁷⁻³⁹. MD codes assume energetic particles to interact via a sum of additive 'pairwise' potentials. In this case all particles of the simulation, including the incident ion interact simultaneously. In such a comparison Rosato³⁷ concluded that the BCA provides valid description of the interaction kinetics above energies of ~100 eV. However, this contrasts sharply with the conclusions of Garrison et al³⁸: They simulated He⁺, Ne⁺ and Ar⁺ ions scattering from Ni(110) and concluded that BCA based simulations are only valid in the prediction of very simple collision mechanisms. Walker⁴⁰ investigated the importance of the interatomic interaction potential in BCA based simulations. This work also called into question the validity of the BCA in the prediction of complex scattering mechanisms. It is generally agreed that MD simulations are inherently more suited to modelling 3D collision dynamics, because the

BCA is avoided, however MD codes are extremely computation intensive, and hence not suitable for routine simulation of scattered particle spectra. For this reason BCA based codes are most widely used in the identification of features of scattered particle spectra⁴¹. However, the major difficulty relating to the simulating of real LEISS spectra concerns the charge exchange processes.

2.4.3 Experimental Arrangement of LEISS

The basic components of a LEISS system were defined in the introduction. Generally, inert gas ion sources are used which must be capable of producing low divergence, monoenergetic (energy spread < 1%) and pure ion beam. Analysers are usually the electrostatic hemispherical sector type, although cylindrical mirror analysers are sometimes used and have specific advantages. Recently an angular resolved electrostatic analyser has been reported⁴². As a general rule, an instrumental energy resolution of 1% with an acceptance angle of, $\Delta\theta$ of < 5° is sufficient to ensure that the mass resolution is not instrument limited. A further requirement of LEISS is a very clean UHV system, capable of reaching residual gas pressures of < 10⁻¹⁰mbar. This latter requirement is a consequence of the very surface specific nature of the technique. With this respect the residual gas pressure of the chamber must be sufficiently low to ensure that the number of foreign gas atoms absorbed on the surface during analysis is insignificantly small. The mono-layer formation times may be calculated from Boltzman's equation which is plotted as a function of pressure in figure 2.3. Additionally, surfaces that are introduced into the vacuum system from the atmosphere, must be processed in order to remove the absorbed layers of carbonaceous material and water vapour. This is typically achieved by heating the sample or by exposure to an ion beam.

2.4.4 LEISS in Single Collision Mode

Given that conventional LEISS spectra largely consist of peaks originating from SBCs their positions can be predicted by the SBCE. An expression for the SBCE can be obtained directly by applying the principles of conservation of momentum and energy to the collision pair. Applying these two principles in the laboratory frame of reference yields:

$$1/2 m_1 v_o^2 = 1/2 m_1 v_1^2 + 1/2 m_2 v_2^2 \quad \text{-(2.4)}$$

$$m_1 v_o = m_1 v_1 \cos\theta + m_2 v_2 \cos\alpha \quad \text{-(2.5)}$$

$$0 = m_1 v_1 \sin\theta + m_2 v_2 \sin\alpha \quad \text{-(2.6)}$$

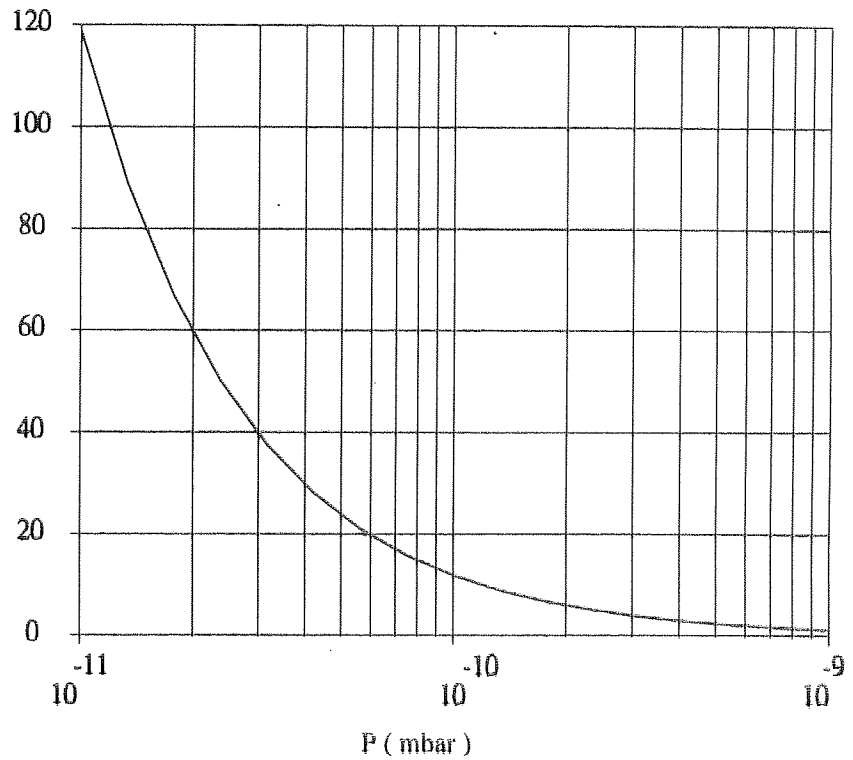


Figure 2.3 - The mono-layer formations time as a function of gas pressure. Molecular oxygen on a copper surface, (Constant sticking coefficient with coverage)

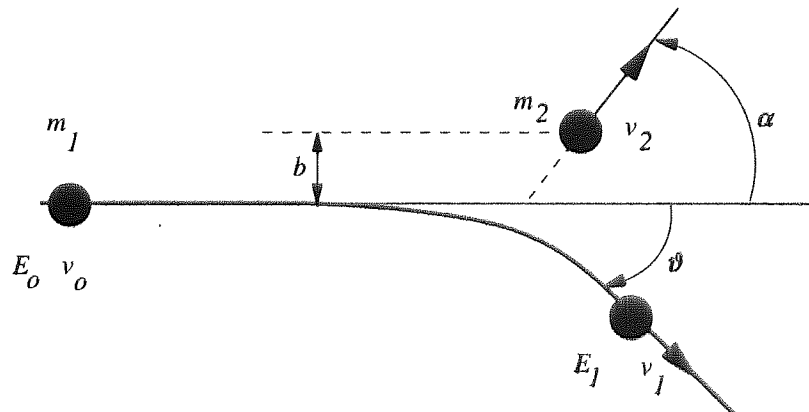


Figure 2.4 - A schematic of a single-scattering collision represented in the laboratory frame of reference. The projectile has the initial energy, E_0 and velocity v_0 . The projectile is scattering through an angle ϑ , and has a final energy E_1 and velocity v_1 . The target atom is initially at rest with mass m_2 , and recoils with velocity v_2 at an angle α . b is the impact parameter of the collision.

where the collision parameters are shown in figure 2.4. Eliminating α and v_2 leads to an expression for the fractional energy loss:

$$k = \{[\cos\vartheta \pm \sqrt{(A^2 - \sin^2\vartheta)}]/(1+A)\}^2 \quad -(2.7)$$

which will subsequently be referred to as the kinematic factor or 'k value'. Eq 2.7 demonstrates the simplicity of the LEISS technique as the k -value is dependent upon the primary target mass ratio ($A=m_2/m_1$) and the primary particle scattering angle ϑ only. The peaks of LEISS give k -values directly which in turn lead to direct identification of surface species. Only the positive route of eq 2.7 is physically applicable when the target atom is heavier than the primary, otherwise both solutions have physical meaning. However, it is clear that when the target atom is lighter than the primary, ($A<1$), scattering is then limited to forward angles, given by $\vartheta < \sin^{-1} A$. The range of solutions of eq 2.7 is shown in figure 2.5. It is useful to note that the expression for k simplifies for scattering angles of 90° and 180° :

$$k_{90} = (m_2 - m_1)/(m_2 + m_1) \quad -(2.8)$$

$$k_{180} = [(m_2 - m_1)/(m_2 + m_1)]^2 = k_{90}^2 \quad -(2.9)$$

In general the measured LEISS peaks are within ~1 to 2 % of their predicted position, however there are a number of possible factors which may contribute to peak shifts from their predicted position, as discussed in section 2.5.

2.4.5 Resolution Considerations of LEISS in SBC mode

An important consideration in LEISS is the mass resolving power, $m/\Delta m$, which can be expressed in terms of the first differential of k wrt to m_2 and the energy resolving power, $E_1/\Delta E_1$.

$$\begin{aligned} m_2/\Delta m_2 &= (E_1/\Delta E_1) (m_2 k) dk/dm_2 \\ &= (E_1/\Delta E_1) f_{mr}(\vartheta, A) \end{aligned} \quad -(2.10)$$

where

$$\begin{aligned} f_{mr}(\vartheta, A) &= \{ 2A/(A+1) \} \cdot \{ A + \sin^2\vartheta - \cos\vartheta(A^2 - \sin^2\vartheta)^{1/2} \\ &\times 1/(A^2 - \sin^2\vartheta + \cos\vartheta(A^2 - \sin^2\vartheta)^{1/2}) \} \end{aligned} \quad -(2.11)$$

Thus $m/\Delta m$ is given by $E_1/\Delta E_1$ modified by the factor f_{mr} . It can be seen that f_{mr} is a monotonically increasing function of ϑ . Hence, for a given resolving

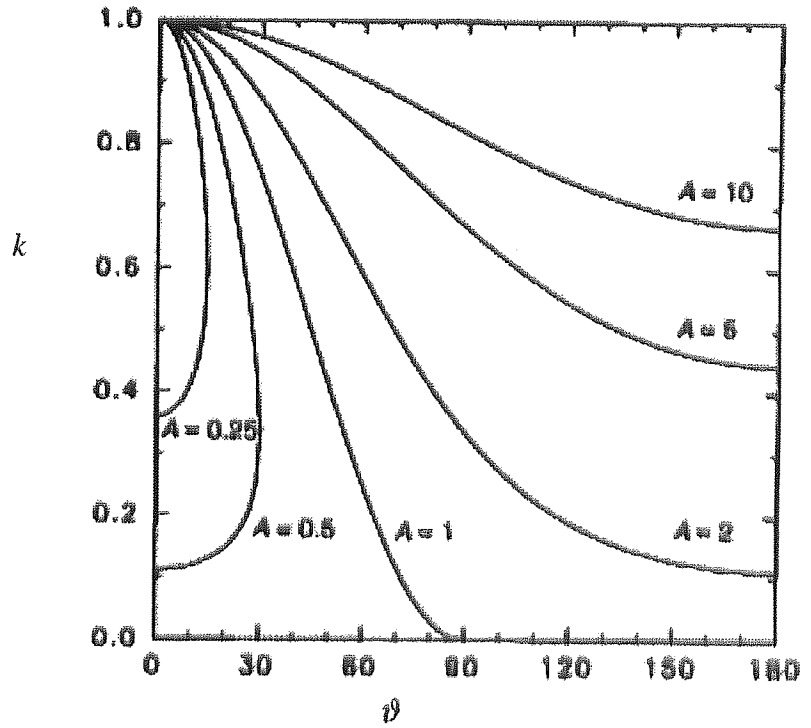


Figure 2.5 - Solutions of eq 2.7.

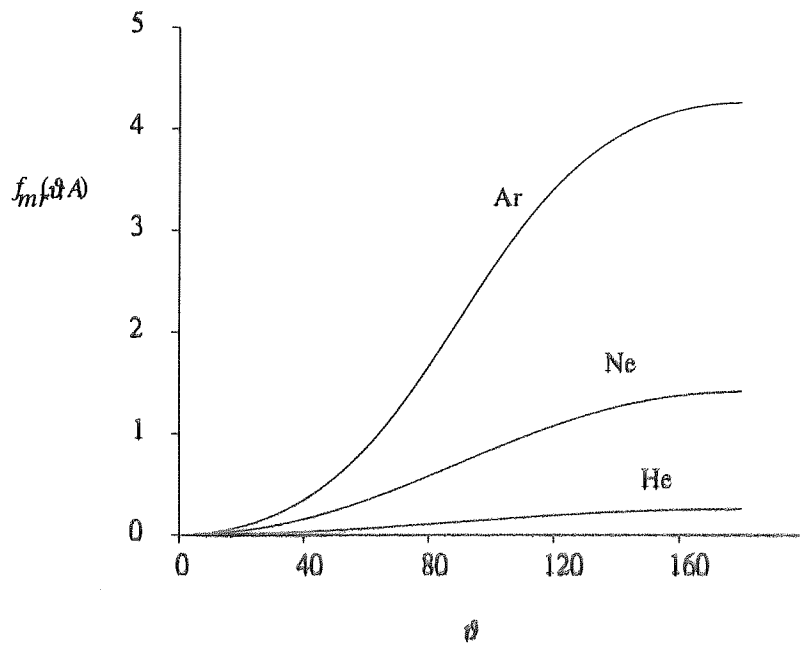


Figure 2-6 - $f_{mr}(\vartheta, A)$ plotted for He, Ne and Ar scattered from gold.

power, $E_j/\Delta E_j$, the maximum mass resolving power is obtained for conditions of maximum energy transfer, that is large ϑ , and $A \sim 1$. As an example the f_{mr} is plotted as a function of ϑ in figure 2.6, for the cases of He, Ne and Ar scattered from a gold surface. The figure shows that very poor resolution is obtained in the case of helium regardless of scattering angle. In the case of argon mass resolution ~ 4 times the energy resolution can be obtained at large scattering angles. However, it is misleading to consider $E_j/\Delta E_j$ as constant. In what follows ΔE_j represents the FWHM of the scattered ion peaks, which may have both instrumental and inherent origins. Contributions to instrumental broadening arise from the energy resolution of the analyser ΔE_{esa} (given by a constant fraction multiplied by kE_o), the energy spread of primary particles ΔE_o , and the angular spread, $\Delta\vartheta$. An expression for the total instrumental broadening ΔE_{inst} is given by the partial derivative of E_j with respect to variables E_o and ϑ , leading to the following expression:

$$\Delta E_{inst} = \sqrt{[k\Delta E_o]^2 + [\Delta E_{esa}]^2 + [f_{er}(A, \vartheta)]^2} \quad (2.12)$$

where $f_{er}(A, \vartheta)$ is given by

$$\begin{aligned} f_{er}(A, \vartheta) &= E_o \Delta\vartheta \left(\frac{\partial k}{\partial \vartheta} \right) \\ &= E_o \Delta\vartheta 2k(-\sin\vartheta - \sin\vartheta \cos\vartheta [A^2 - \sin^2\vartheta]^{-1/2}) \times \\ &1/(\cos\vartheta + [A^2 - \sin^2\vartheta]^{1/2}) \end{aligned} \quad (2.13)$$

In eq. 2.12 the contributions arising from ΔE_o and ΔE_{esa} are proportional to k and so are independent of ϑ . Whereas broadening from $\Delta\vartheta$ is proportional to $dk/d\vartheta$. There are two major contributions to inherent broadening, the first, due to the isotopic spread of the surface atoms and primary particles, and secondly, as a result of the thermal vibrations of the surface atoms. A crude expression for the latter can be developed on the basis of the single collision model, after Hulpke⁴³:

$$\Delta E_{Hulpke} = 8(A-1)\sqrt{(AE_o E_{phonon})}/(A+1)^2 \quad (2.14)$$

Where E_{phonon} is the surface phonon energy. Comparison of experiment with calculation indicates $\Delta E_{ih} \sim 3/4 \Delta E_{Hulpke}$, corresponding to $E_{phonon} = 30$ meV. To obtain the total broadening ΔE_{ih} and ΔE_{inst} must be combined in quadrature:

$$\Delta E_j = \sqrt{(\Delta E_{ih})^2 + [k\Delta E_o]^2 + [\alpha kE_o]^2 + f_{er}(A, \vartheta)]^2 \Delta E_{inst}^2} \quad (2.15)$$

Thermal broadening is distinct from other sources of peak broadening in that it is independent of ϑ , and has the most significant influence at large scattering angles. Examination of eq 2.15 shows that when A is small, ie close to unity, ΔE_{th} is the main contribution to overall broadening. For example, for $A = 1.75$, $\vartheta = 180^\circ$ the overall energy resolution $\Delta E_I/E_I$ is reduced by a factor of 0.16 due to thermal broadening, compared to ~ 0.8 at $A = 15.75$, $\vartheta = 180^\circ$. Generally, when LEISS is used in composition analysis the mass resolving power $m_2/\Delta m_2$ is the most important consideration. Substitution of eq 2.15 into 2.10 gives:

$$m_2/\Delta m_2 = \frac{1}{\sqrt{[k\Delta E_o]^2 + [k\Delta E_{esa}]^2 + f_{er}(A, \vartheta, \Delta \vartheta)^2 + \Delta E_{th}(A, E_o, E_{phonon})^2}} f_{mr}(\vartheta, A) \quad (2.16)$$

It can be seen from eq 2.16 that $\Delta m_2/m_2$ is a complex function of; $A, k, E_{phonon}, \vartheta, E_o, \Delta E_o, \Delta E_{esa}, \Delta \vartheta$. It is therefore not possible to fully examine the properties here. However, it is clear that $\Delta E_o, \Delta E_{esa}, \Delta \vartheta$ should always be minimised to gain maximum mass resolution, whilst the parameters $A, k, E_{phonon}, \vartheta$ are determined by experimental conditions. Calculated values of $m_2/\Delta m_2$ are plotted as a function of ϑ for a range of A values in figure 2.7. An important aspect of this result is the behaviour of $m_2/\Delta m_2$ at small values of A . In this region, maximum $m_2/\Delta m_2$ is not obtained at $\vartheta = 180^\circ$. For example, at $\vartheta = 180^\circ$, the scattering of 1 keV argon from copper at 300°C gives rise to a resolution of 60. Whereas the maximum attainable resolution is ~ 85 , which is achieved for $\vartheta = 109^\circ$. This result has important implications as it shows that the experimental scattering angle must be adjusted in order to maximise resolving power for given experiment conditions. This is a consequence of the thermal broadening, so in theory the problem may be overcome by cooling the surface. A second advantage of an adjustable ϑ is that the energy broadening of two peaks relating to different surface masses may be made equal, making spectra analysis more straightforward. However, in most LEISS systems it is not possible to change ϑ without unbolting components. In choosing the scattering angle of a fixed angle instrument one must also bear in mind the intensity of the scattered signal. As the angle is increased the scattering cross-section falls off rapidly. Consequently, systems with ability to vary ϑ using internal rotatable energy analysers like that of O'Conner⁴⁴ are considerably more flexible.

2.4.6 LEISS for Surface Structure Analysis

When LEISS is used to obtain structural information, the angular distribution of the scattered ion signal must be measured. To interpret such data the scattering kinetics must be considered in greater detail: further explanation requires the introduction of the shadow cone concept.

2.4.6.1 Concept of the Shadow Cone

The repulsive potential acting between an incident ion and target atom leads to a region behind the target into which the ion cannot enter. Thus effectively a shadow is cast behind the target particle. Given an appropriate interaction potential the collision cross-section and shadow cone parameters may be calculated. The differential cross section, $d\sigma(\vartheta)/d\Omega$ defines the following relationship between the scattered particle projectile flux and the uniform incident particle flux:

$$2\pi b db = -2 [d\sigma(\vartheta)/d\Omega] b \sin\vartheta \quad -(2.17)$$

where the negative sign indicates a decreasing cross-section with increasing scattering angle. The asymptotic scattered trajectories resulting from a uniform incident flux are plotted in figure 2.8. The intersection of adjacent scattered trajectories defines the shadow cone edge, where there is a significant concentration/focusing of particle trajectories, see figure 2.9.

2.4.6.2 Impact Collision Ion Scattering Spectroscopy (ICISS)

Experimental information is gained by measurement of the mass specific backscattered signal, ($\vartheta \sim 180^\circ$) as a function of the incidence angle, θ . Variation of θ leads to characteristic intensity versus angle curves, for example see figure 2.10, after Niehus[1986]. As θ is increased the shadow cone is swept over the neighbouring atoms in the first atomic layer and a sharp increase in the scattered flux arises when the shadow cone edge passes over a neighbouring atom. From glancing angles of incidence to $\sim 30^\circ$ the $I-\theta$ curve contains information of the top layer only, at higher angles, the shadow edge is focused onto second and third row atoms. In this arrangement the critical angles, θ_c can be related to the shadow cone parameters by following the simple geometrical relations:

$$r = d \sin\theta_c \quad -(2.17)$$

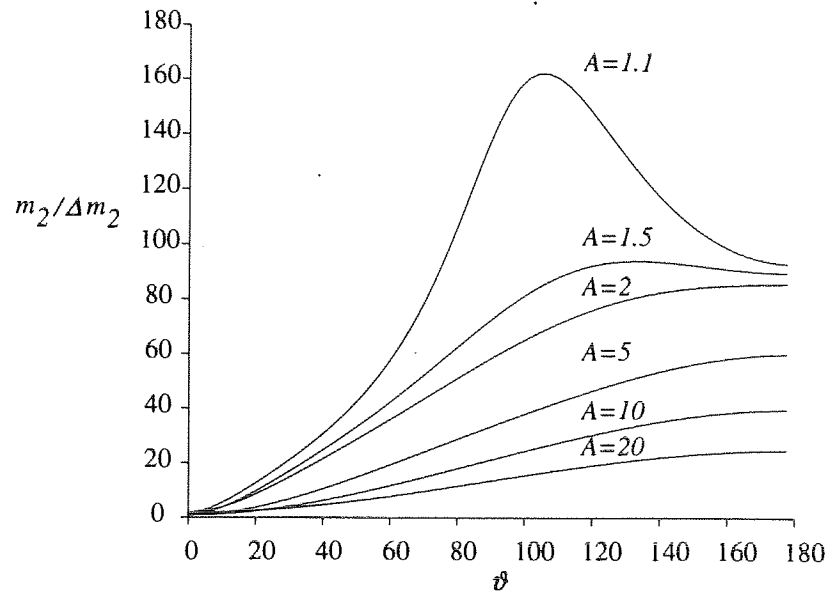


Figure 2.7 - Mass resolution $m/\Delta m$, of LEISS as a function of ϑ .

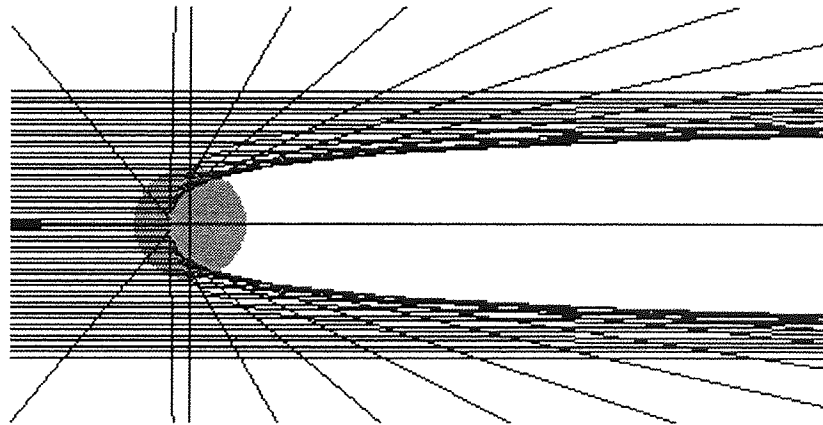


Figure 2.8 - Calculated asymptotic scattered trajectories resulting from a uniform incident flux.

Conditions $E_0 = 1$ keV, $m_1 = 4$, $m_2 = 197$

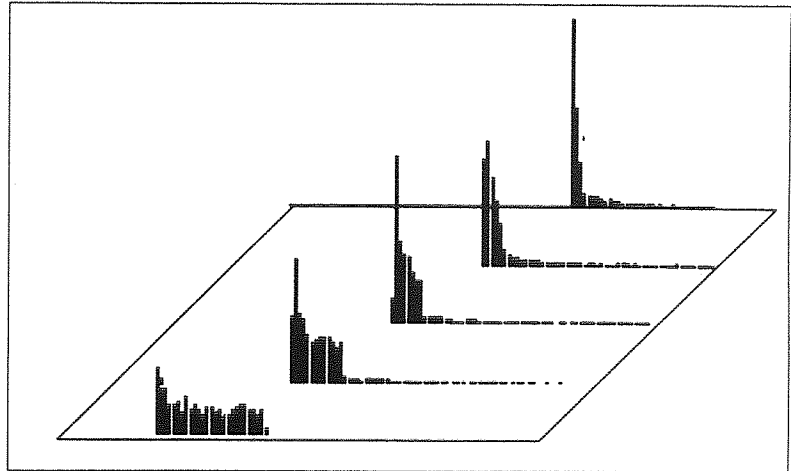


Figure 2.9 - Focusing effects of the scattered particle flux intensity at the edge of the shadow cone. The flux profile is shown at the impact site, and at 1 Angstrom intervals behind the impact site. Conditions:- $E_o = 1 \text{ keV}$, $m_1 = 4$, $m_2 = 197$.

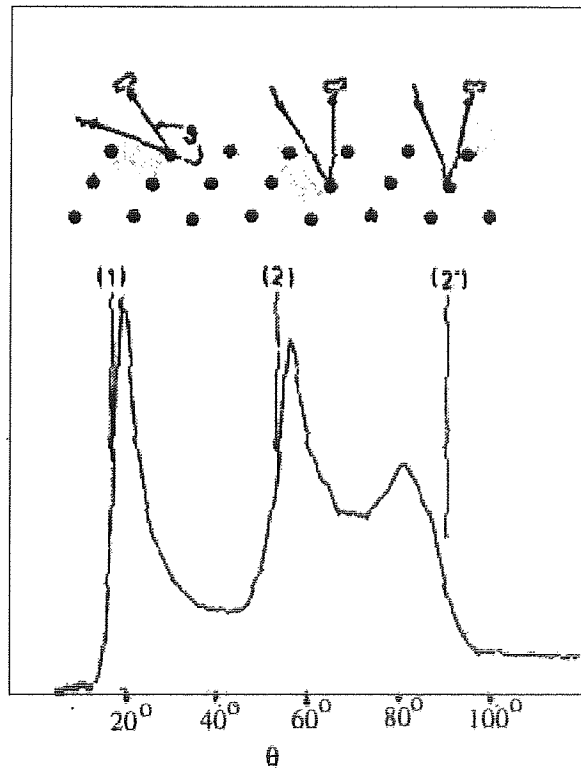


Figure 2.10 - θ - I pattern of the backscattered signal, $\vartheta = 165^\circ$, Ne^0 scattered from $\text{Pt}(111)$ after Niehus et al⁴⁵.

$$l = d \cos \theta_c \quad (2.18)$$

where r is the radius of the shadow cone at a distance l from the apex, and d is the interatomic spacing.

In principle structural surface information is available at any scattering angle, however significant advantages are gained at large impact angles and co-axial impact angles. This was illustrated by the rapid increase in the use of ICISS following its initial introduction by Aono et al[1981]⁴⁶⁻⁴⁸. The simple development of increasing the scattering angle therefore represented a big step forward for direct structure determination. A comprehensive review of the principles of the interpretation of ICISS spectra was given by Fauster⁴⁹.

The advantage of the ICISS arrangements compared to lower angles can be attributed to two factors, firstly, at small scattering angles, ions must approach or leave the surface at low incidence. As will be discussed in section 2.5.1, the collision process is not accurately described by a SBC. Secondly at low ϑ the signal from multiple collision sequences is greater leading to more complex spectra. These problems were symptomatic of the studies of Hieland and Taglauer⁵⁰⁻⁵² and Brongersma^{53,54}, which were heavily dependent on simulation codes for their interpretation. A compounding problem is that simulations rely on the accuracy of the employed interatomic potential. Even straightforward calculation of the shadow cone parameters is sensitive to the interatomic potential, as was shown by Oen⁵⁵ and Jackson⁵⁶. At larger impact angles the SBC is valid and the impact parameter of the collision becomes virtually zero. In this case lattice parameters may be determined directly from the critical angle (θ_c) and the shadow cone radii using simple geometry⁴⁹. In the absence of accurate inter-atomic potential models the shadow cone radii may be calibrated experimentally using standard surfaces⁵⁵. These factors improve accuracy and remove uncertainties making data interpretation more straightforward and less reliant on simulation codes. The shadow cone principle allows atom positions to be determined with an accuracy of $\sim 0.1 \text{ \AA}$.

2.4.6.3 Differences between 180° and near 180° scattering

For practical reasons ϑ in many experimental ICISS instruments is limited to $\vartheta \sim 165^\circ$, however, some basic differences exist between this

arrangement and $\vartheta=180^\circ$ systems. The most important of these is the enhanced focusing effect that occurs in the 180° arrangement; the entrance and exit trajectories are identical, whereas in $\vartheta < 180^\circ$ arrangement the two paths in and out of the target are geometrically quite different. This has a significant effect on the form of the $I-\theta$ characteristics: double focusing (shadowing and blocking) occurs when a particle is scattered from a second row atom⁵⁷. In the $\vartheta < 180^\circ$ case, as the two trajectories are different, only one of the focusing effects may occur. Double focusing effects are particularly apparent for collisions of large energy transfer, as the projectile travels considerably more slowly on the outward trajectory, and the shadow cone is considerably larger. This is found to further enhance the features of the angle resolved signal.

2.4.6.4 Glancing angle techniques

Glancing angle scattering has also emerged as a useful tool for surface structure determination in certain types of studies. Here experiments are conducted at a constant grazing scattering angle of $\sim 5^\circ$ at a constant incidence angle. For such low ϑ the scattering process is most accurately described by a continuous planar or axial potential, and the scattered particle momentum is conserved in the direction perpendicular to the surface plane. Scattering particles are either channelled or blocked by the surface structure, depending on the orientation of the ion beam to the crystal lattice. Channelling is also thought to occur between the 1st and 2nd atomic layers. Surface information is extracted from the scattered ion intensity by its measurement as a function of azimuthal angle. This gives rise to deep intensity minima, at channelling directions, providing a method for 'mapping out' the various surface channels. This represents an alternative approach to ICISS for structure determination, and is particularly useful for the in-situ alignment of single crystals as well as the determination of surface imperfections.

2.5 Factors Complicating the interpretation of LEISS spectra

One of the major advantages of LEISS is the simple dependency of spectral peak positions on the mass of the surface species. This primarily relies on the use of the SBCE to predict peak positions. However, a number of phenomena can complicate LEISS, and these must be considered for certain experimental conditions and modes of scattering.

2.5.1 Multiple Scattering

Multiple scattering is a term broadly used to describe collision sequences other than single collisions, such collisions can have a number of influences on scattered particle spectra. Strictly all collisions must be considered as multiple collisions. This can be demonstrated by considering the trajectory of an ion scattering from a linear one-dimensional atom chain. In this case the incoming ion undergoes a sequence of small angle collisions. As the ion approaches the surface the impact parameter diminishes until a high impact collision with a single surface atom is encountered, at which point the ion is scattered through a large angle. A similar sequence of small angle collisions takes place on the outgoing trajectory. This model offers insight into 'in-plane' scattering mechanisms and is often referred to as the 'string' or 'chain' model.

String calculations are performed by calculating the final energy of all possible scattered particle trajectories by variation of the initial impact parameter. This operation, performed as a function of the final scattering angle, gives rise to 'characteristic scattering loops' as shown in figure 2.11. Experimentally produced scattering loops have also been reported in the literature⁵⁸. The lower portion of the loop represents Quasi Single, (QS) scattering. Strictly the QS energy should be used for predicting LEISS peak positions, however in the backscattering mode, that is the conditions of this work, the SBCE provides a sufficient approximation. Departure between the QS and SBCE increases for conditions of low particle velocity, small lattice spacing, and low scattering angle. At glancing incidence angles of less than a few degrees the chain model no longer provides a valid description as all the surface atoms lie within the shadow of their neighbours, and the incident particle 'skims' off the repulsive potential of several atoms. The upper part of the loop corresponds to particles that have undergone a number of smaller equally sized in plane collisions, that is Quasi Double and Quasi Triple, (QT)

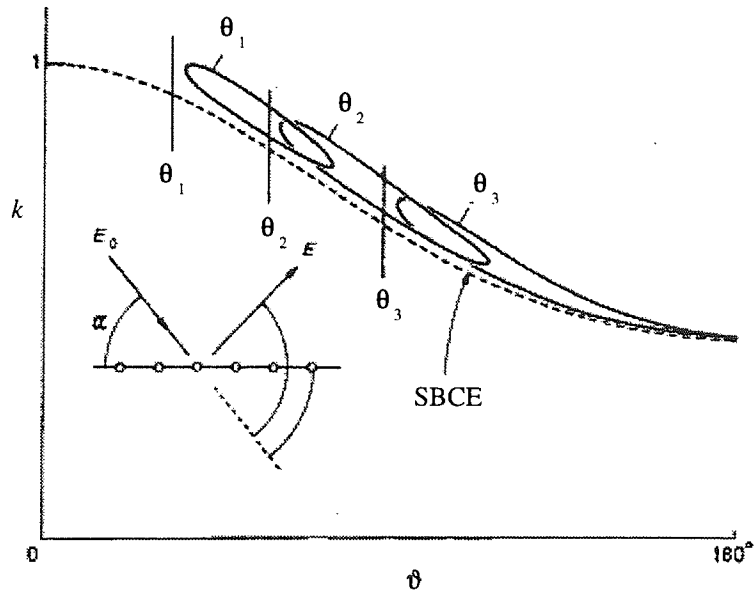


Figure 2.11 - Characteristic scattering loops - obtained for fixed angle of incidence.

mechanisms. At large ϑ the QD mechanisms may be approximated to two in plane SBC collisions each of ($\vartheta/2$). The departure of the QS and QT peaks is strongly dependent on the value of A and ϑ , as shown in figure 2.12. In the case of ordered surfaces separated peaks can be observed relating to the QD and QT energies, at specific orientations. Whereas from polycrystalline or amorphous surfaces these mechanisms do not lead to well defined peaks.

These simple chain model calculations do not provide information concerning the relative probabilities of the various mechanisms. For this, one must look to more detailed simulation models: a study by Garrison⁵⁹ using an MD based simulation code predicted a peak in the scattered intensity, corresponding to the maximum of the ϑ - E scattering loops. This so called 'rainbow scattering' in the ϑ - I angular intensity distribution, was confirmed by the experimental measurements of Nielsen et al⁶⁰ and Hulpke et al⁶¹, and relates to stationary values in the deflection function.

Three dimensional simulation also predicts mechanisms leading to the scattering of particles with widely distributed energies below the QS peak. These include various 'zig zag' collisions, relating to non-planar scattering from the surface chains⁶² and random collision sequences relating to the penetration of the top surface layer. This latter mechanism is particularly significant in the case of non-ordered surfaces, where the QS scattering mechanism is shown to be the simplest of a large number of possible collision mechanisms with only a minor overall probability⁶³⁻⁶⁶. Sub surface multiple scattering becomes more significant at larger primary energies.

2.5.2 Thermal Vibrations

The thermal motion of the surface atoms can influence the scattered particle spectra in a number of respects, and these have been comprehensively reviewed by Poelsema^{67,68}. Collision interaction times are $\sim 10^{-15}$ seconds compared to the period of a lattice vibration $\sim 10^{-13}$ seconds, and thus the target atom does not change position appreciably during the interaction period. Thus in terms of the collision dynamics the target atom can be considered to be static. However, as was shown by Hulpke⁴³ spectral features under certain conditions may be appreciably broadened as a result of the thermal energy. A second consequence is that the atoms are displaced from their equilibrium lattice position. The effect of this can be clearly illustrated by

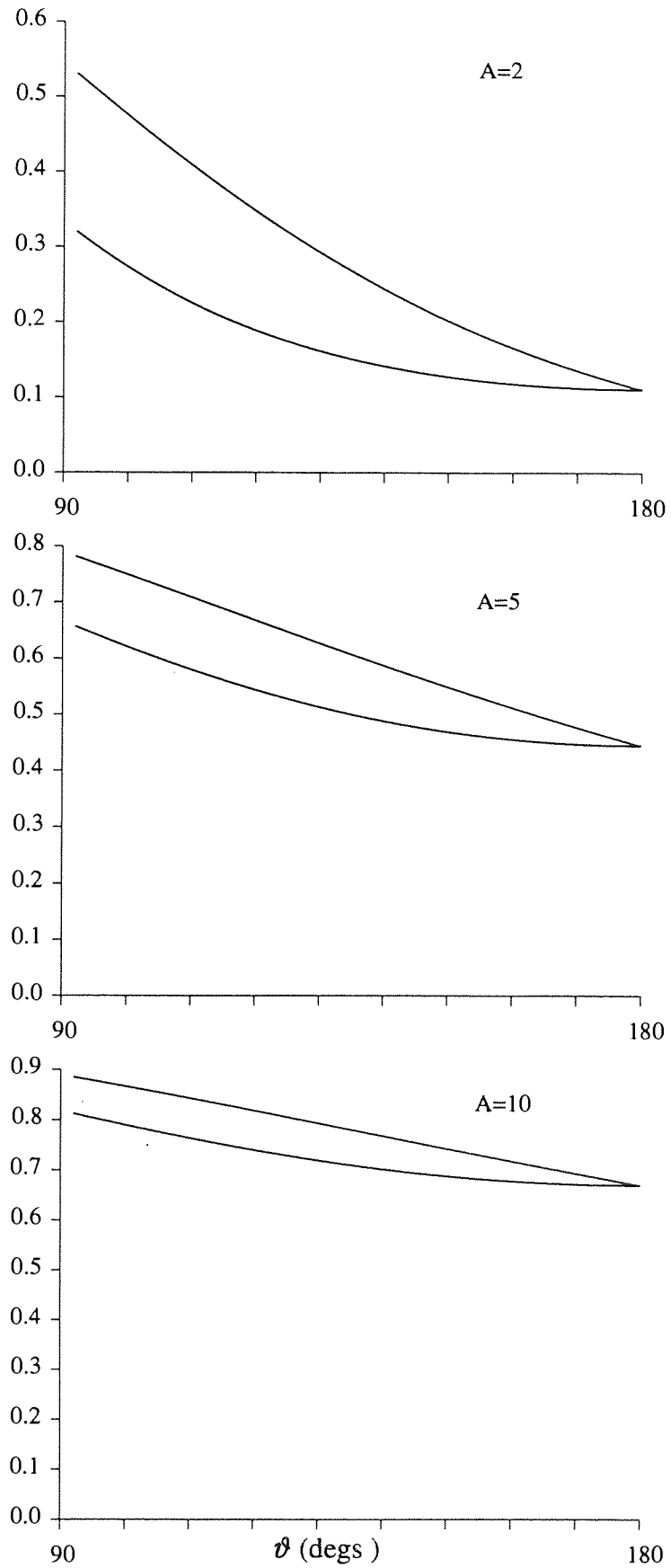


Figure 2.12 - Single and double collision energies

the introduction of random displacements into the 1D chain simulations. A significant widening of the characteristic scattering loop takes place as a direct result of the displacements. This leads to further complications in the interpretation of the scattering data for the purpose of surface investigation. In basic terms the 'shadowed' atom can move in and out of the shadow cone, resulting in blurring and shifting of the $I-\theta$ curve features. For these reasons it has been necessary to incorporate thermal vibration into simulation codes. To a first approximation the amplitude of the static displacement can be assumed to be independent, although correlated vibration models have also been used, and these are considered to be more realistic^{10,40}. In either case the surface displacements are determined by the Debye model in the high temperature limit⁶⁹. An important parameter of this model is the surface Debye temperature, or the surface phonon energy. Data here is not widely known in the case of most materials, however experimental values have been obtained from scattering data by various groups^{8,40,70-73}. Generally the surface temperature was found to be lower than that of the bulk by a factor of 2 to 3.

2.6 Applications of LEISS

Also included in the following discussion are a number of associated and descendant techniques, that have been developed in an attempt to overcome the limitations of the conventional format. The applications discussed fall into the two basic categories of composition analysis and structure analysis.

2.6.1 Composition Analysis

Despite severe limitation of LEISS, to be discussed in section 2.6, LEISS has been used in many successful studies of surface phenomena, and has made a valuable contribution to the understanding of many practical surface problems.

2.6.1.1 Qualitative

In many studies it is sufficient to identify an unknown species without the need for quantified composition concentrations. A large number of studies following Smith's initial results were reviewed by Taglauer[1977]⁷⁴. An example was the investigation of CO absorption on binary alloys, where

information conveyed by the scattered ion beam revealed sites of preferential absorption. A second example studied was the desorption of absorbed layers under the influence of ion impact, leading to conclusions that were in agreement with corresponding surface models. It was concluded by Taglauer that LEISS represented a unique analysis tool, that could be applied to a wide range of applications. This was despite the more recently published problems of erosion, charging and quantification. In a more recent review, Taglauer[1988]⁷⁵, one of the major applications to have emerged was in the composition analysis of realistic, non-ideal, surfaces in the field of heterogeneous catalysis. Here the mono-layer surface sensitivity of LEISS is ideal, as the catalytic activity is confined to the uppermost mono-layer, with lower lying layers taking no part in the catalytic action. LEISS can be used to study the kinetics and spreading behaviour of the supported species, and monolayer preparation techniques. Typically, support materials are wafers of titanium or silicon oxides in granular form, and the active catalytic components are typically molybdate, vanadate or tungstate. As such samples are insulating, a charge compensating electron 'flood' gun was required to neutralise the charge input of the ion bombardment.

2.6.1.2 Quantitative

The principle of quantitative analysis is straightforward: the surface area density of species, N_i is related to the scattered particle flux, I_i , by:

$$I_i = I_o T(\Omega, \theta, E) \{ (d\sigma/d\Omega)_i (1-P_n) G N_i \} \quad -(2.20)$$

where I_o is the incident particle flux and $T(\Omega, \theta, E)$ is an instrumentation factor. Of the remaining terms $(d\sigma/d\Omega)_i$ is the differential scattering cross-section, P_n is the neutralisation probability and G is a geometrical factor. The shielding term implies that the signal from species i is reduced by a factor α due to shadowing from species j .

All terms other than G and P can be readily evaluated, which are generally unknown and strongly matrix dependent, as well as being sensitive to the trajectory and energy of the scattered ion. Direct quantitative elemental analysis therefore is not straightforward and only possible in a few isolated cases. Niehus[1975]⁷⁶, in studying these considerations concluded that there were few prospects for the employment of LEISS as a tool for direct quantitative composition analysis, where he pointed to P as the main obstacle.

This study was based on the absorption of oxygen on a tungsten surface, where it was found that both the substrate and oxygen signals were non-linear functions of coverage. It was shown that the experimental results could only be explained if P were supposed to be coverage dependent. A recent investigation of matrix dependent neutralisation effects was conducted by Van Den Oetelaar et al[1994]⁷⁷. This study, which compared the scattered He⁺ signal from graphite carbon and carbidic carbon, related the differences to an interaction with the so² band.

In contrast to the general conclusions that the LEISS signal cannot be quantified, some specific cases have been reported where quantitative relative measurements have been made. In these cases a linear relation between the QS signal and coverage was assumed, and standard samples were used to calibrate the LEISS signal, with a sample of known surface density. The application of this approach to two element systems was examined by Niehus⁷⁶. In this scheme the concentrations of N_a and N_b ions/cm² relate to species A and B respectively, and the signals I_a^o and I_b^o represent the signals obtained from the respective elemental surfaces. These are related to the surface standard concentrations, N_a^o and N_b^o by:

$$I_a^o = I_o A T (d\sigma/d\Omega)_a (1 - P_a) G_a N_a^o \quad - (2.21)$$

$$I_b^o = I_o A T (d\sigma/d\Omega)_b (1 - P_b) G_b N_b^o \quad - (2.22)$$

The surface concentration of the composite system N_a and N_b can then be found from the ion yields I_a and I_b measured from the composite surface by:

$$N_a = (I_a / I_b^o) N_a^o \quad - (2.23)$$

$$N_b = (I_b / I_a^o) N_b^o \quad - (2.24)$$

A further approximation of this scheme is the geometrical screening factor, G_i which is assumed to be the same in the standard and sample surfaces. Clearly from the above discussion this is not always the case. This approach is also complicated by the presence of atomic oxygen and hydrogen. For example, neither of these species can be detected in the case of backscattered neon, but still have a screening effect on other surface species. In this case the total surface density is not simply given by $N_a + N_b$, and eq 2.18 and 2.19 must be replaced by:

$$N_a/N_o = s I_a / (s I_a + I_b) \quad - (2.25)$$

$$N_b/N_o = s I_b / (s I_b + I_a) \quad - (2.26)$$

where s is the screening factor. The standard sample approach was employed by Baraz et al⁷⁸ in a study of Ga and As implanted in substrates of Si, SiO₂, SiN₄, Ta, Ta₂O₅. Baraz found, in general, that the neutralisation probability depends on the chemical environment of the target atom, but some systems were found where the standard samples method could be applied. G and P were found to be independent of coverage for low concentrations in all cases, and P was found to be independent of the chemical matrix for many of the III-V compounds, for example GaP, GaAs, GaSb, InP, InAs, InSb. This result has been exploited in a number of studies of III-V compounds, and binary alloys.

79-82

2.6.2 Structural information using multiple collision mode

The atomic structure of a solid surface results as a consequence of the bulk structure termination, the break of periodicity causes binding electrons to establish a new energetic minimum, usually resulting in a repositioning of the surface atoms - relaxation effects. In pure metals for example a contraction of the inter-planar distance of the top few atomic crystal planes usually occurs. In certain cases the new energy minimum results in a reconstruction of the crystal structure or the formation of a complex 'superstructure'. It is a matter of fundamental interest to determine the ground state surface structure of pure compounds, but these processes are also influenced by the presence of absorbed species. Conventional ICISS is a unique tool for the analysis of these surfaces, and is capable of providing unique real space information. As the signal is mass specific the respective surface species may also be identified. ICISS was first used by Aono to determine the reconstructed surfaces of annealed pure Si(001) ((2x1) and (4x2))⁴⁶ and Si(111) ((7x7))⁴⁷, where scattering data was interpreted directly without comparison to simulation. At the time of Aono's result the Si(111)7x7 surface had been a long standing problem in surface science, although the structure was also independently predicted using X-ray diffraction techniques within a short period. Structural investigations are often made using ICISS in combination with other techniques, for example with LEED and STM. In

studies of absorbed surface structure the angular dependence of the scattered adsorbate/substrate signal ratio allows the position of adsorbed atoms to be determined. A further area of application is in assessing surface quality of mono-crystals by the observation of steps and defects. In summary, a wide range of clean reconstructed surfaces of pure element materials, adsorption induced reconstructions, and adsorbate overlayers have now been determined by the variants of LEISS. A comprehensive review was recently given by Niehus et al[1993]⁸³.

2.7 Discussion of the Limitations of conventional LEISS and corresponding developments.

2.7.1 Surface damage and excessive erosion rates

The signal collected in the conventional LEISS format represents a very small fraction of the total scattered ion distribution, which is dependent on the parameters of eq 2.7. Further losses of signal originate from the single channel nature of the ESA: As the electrode potential is scanned, only a small fraction of the scattered ion signal is detected at any one time. Typically a fraction of $\sim 10^{-7}$ to 10^{-9} of the incident signal is detected. This indicates a total sample dose of $\sim 10^{12}$ to 10^{14} incident particles to obtain a spectrum comprising 10^5 counts. As discussed previously, each incident particle produces surface damage: this surface damage is an inevitable feature of the scattering technique, however, due to the nature of conventional LEISS the damage level is much greater than is necessary.

ToF systems reduce the sample dose to a minimum and therefore reduce surface damage as far as possible. A second approach is to employ a neutral beam, which can reduce both the sputtering yield and damage induced in the case of non-metal surfaces^{84,85}. Brown et al[1984]⁸⁴ compared ion and neutral beam bombardment of polymer, polystyrene, and oxide semiconductor surfaces. They concluded that in the case of poorly conducting materials atom bombardment causes significantly less damage, and identified possible charge related mechanisms to explain this phenomenon. The above dose levels also impose substantial 'atomic mixing', ion induced segregation and preferential sputtering, resulting in significant changes in surface morphology. These phenomena represent the most severe limitation in studies which involve the collection of a number of spectra, for example in the determination of surface structure or studies of dynamic surface processes⁸⁶

Clearly the sample dose may be reduced by de-focusing the beam in order to analyse a bigger area, at the expense of spatial resolution, or by increasing $\Delta\theta$ at the expense of energy resolution. Another approach is to employ a CMA rather than a hemispherical analyser. This is achieved by collecting the full scattered cone of ions at a given scattering angle. However, the potential for dose reduction does not approach that possible with the ToF analyser, and the azimuthal variation of the scattered signal is lost, removing the possibility for structural information. Thus the ToF analyser offers the greatest potential for reducing the surface erosion problems suffered by LEISS. For comparable conditions of resolution the dose level can be reduced by a factor of 10^4 - 10^5 .

2.7.2 Charging effects in insulators and semiconductors

The second major problem associated with LEISS is that for samples of low conductivity, the flux of incident ions results in the accumulation of excess positive charge on the sample surface. As well as enhancing the sputtered rate the charge build up produces an electric field which deflects the ion beam so as to decrease the effective scattering angle and decrease the primary collision energy, displacing the LEISS peaks from their predicted positions⁸⁷. Thus, if the excess charge build up is not compensated by a beam of thermal electrons from an electron flood gun interpreting spectra becomes impossible. Where the surface is not homogeneous regions of differing potentials may build up making charge compensation impossible, in which case spectra cannot be generated. The use of fast atoms rather than lower energy ions avoids these problems as well as reducing physical and chemical damage. Studies showing the fundamental differences between fast atom and ion bombardment are reviewed in section 2.9. No instrument has been reported which allows ToF analysis to be combined with fast atom bombardment.

2.7.3 Lack of Quantification

The neutralisation process is largely responsible for the simplicity of the conventional LEISS technique, as the neutralisation probability of MS ions is very high. Thus the MS signal is conveniently eliminated from the LEISS spectrum, leaving only the QS signal to convey the surface composition. However, the QS signal also suffers substantial neutralisation.

Owing to the complexities of charge transfer processes, in the absence of a reliable model, it is difficult to derive sensitivity factors akin to other spectroscopes. Furthermore, as discussed previously, neutralisation probabilities may also be trajectory, matrix and coverage dependent. The extent to which these effects influence the final charge fraction is not clear, with much contradiction apparent in the literature.

The complexities of charge transfer may be circumvented by either using alkali ion scattering, S-ESA, or ToF detectors. In the case of alkali ions neutralisation does not strongly affect the scattered ion yield. In the case of S-ESA, scattered neutrals are post ionised in an electron stripping cell⁸⁸. However this method is experimentally quite difficult as the efficiency of the cell must be known for the different energies of the scattered particles, the stripping cell efficiency is typically ~ 0.1 %. Thus the ToF technique is the only method by which neutralisation can be completely avoided, and is compatible with the requirements of the previous sections. Thus the ToF approach potentially allows direct quantitative analysis, however, MS particles now contribute to the scattered particle spectrum. As a result spectra may be more complex than those observed in conventional LEISS. So although ToF analysers can avoid the uncertainties in quantitative analysis due to neutralisation, other factors must be considered. These effects are considered in the following section by comparing a wide range of ToF data from the literature.

2.7.4 Developments for structural analysis techniques

There remain a number of problems associated with ICISS in the form initially introduced by Aono⁴⁶. One important problem is the low intensity of the backscattered signal. Factors contributing to this are the same as those of standard LEISS systems, with the addition of decreased differential scattering cross-section due to the high impact angle. This leads to the same problems relating to surface damage, and this becomes particularly acute when a number of spectra are generated, for the production of the $I-\theta$ curves. A second problem was illustrated by Aono's initial results: the structure in the $I-\theta$ arises from the previously described shadowing and blocking effects. These effects correspond to double collisions, which have a higher associated neutralisation probability than the single collisions. As a result structure is lost from the $I-\theta$ curve. Again this problem may be overcome by the use of a ToF analyser to collect the scattered neutral signal. A similar advantage may be

gained by the use of alkali ions rather than noble gas ions. This gives rise to Alkali Impact Collision Ion Scattering Spectroscopy (ALICISS)⁸⁹. However, the use of ToF analysers to overcome this problem is more widely reported, and this is referred to as Neutral Impact Collision Ion Scattering Spectroscopy (NICISS). The NICISS data of Niehus⁴⁵ clearly demonstrated the distinct advantages over ICISS: the corresponding $I-\theta$ is of much greater intensity and exhibits much sharper structure. An additional advantage was that the structure of the first 2-3 layers can be determined by NICISS, thus extending possibilities of studying reconstruction and relaxation. In recent years NICISS has been used to determine a variety of relaxed and reconstructed surfaces, both of pure elements and adsorbate systems. The summary of specific surfaces studied was given by Niehus et al⁸³.

2.8 Scattered neutral Spectra and Time of Flight Analysis.

In principle the limitations of LEISS, relating to erosion and quantification can be overcome by ToF analysers. However, although uncertainties in relation to neutralisation are clearly removed, new complications arise due to the MS signal. The extent to which this signal obscures the 'information carrying' QS signal is examined in the following subsections, where the existing body of scattering data obtained using ToF systems is reviewed.

2.8.1 ToF analyser - Instrumental Resolution

In order to compare broadening of spectra collected on instruments of different laboratories, it is necessary to consider instrument resolution. To calculate this it is necessary to know the following parameters:

ΔE_o - energy spread of primary beam

$\Delta\vartheta$ - combined angular width of the incident and detected beams

Δt - ion pulse duration

l - length of flight path

The equivalent parameter to the ΔE_{esa} , which was just a constant fraction to the scattered particle energy is ΔE_{tof} . This is expressed by:

$$\Delta E_{tof} = [\Delta t/l] [(2v_o E_o k^{3/2})] \quad \text{-(2.27)}$$

where the component $[\Delta t/l]$ is purely instrumental, and the component $[2v_o E_o k^{3/2}]$ is dependent on the experimental conditions. Thus maximum resolution is achieved for low velocity scattered particles. Comparison shows that the ToF analyser resolving power exceeds ESA analysers for certain conditions, see figure 2.13. In calculation of these curves typical instrumental parameters were assumed, and the inherent broadening contributions were omitted. It can be seen that the ESA resolving power is maximum for $\vartheta = 0^\circ$ and 180° and decreases significantly at intermediate angles. The ToF analyser follows a similar trend, however R_e also increases to greater values as ϑ approaches 180° . Thus the maximum resolution of the ToF analysers exceeds that of the ESA. In both cases, the resolution is independent of scattering angle for large values of A . The expected widths of the QS peaks in the ToF spectra are given by:

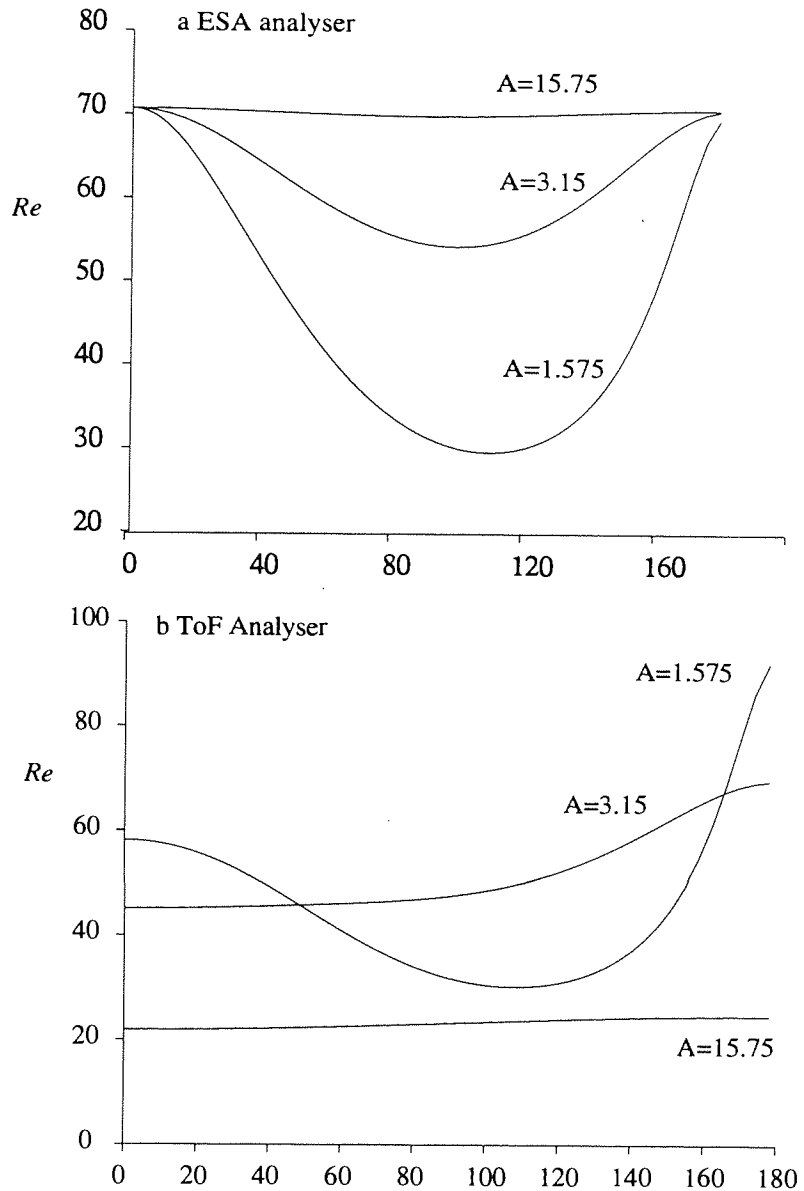


Figure 2.13 - Comparison of the resolving power of (a) ESA ($\Delta E_{anal} = 0.5\%$) and (b) ToF ($\Delta t = 50$ ns, $l = 2000$ mm), $\Delta \vartheta = 1^\circ$, $\Delta E_o = 1\%$.

The curves shown are for 1 keV He, Ne and Ar particles scattered from a Cu surface.

$$\Delta t = [t/E_1] \sqrt{(\Delta E_{th})^2 + [k\Delta E_o]^2 + [\Delta E_{tot}]^2 + f_{er}(A, \vartheta)^2 \Delta E_{inst}^2} \quad - (2.28)$$

which corresponds to an energy resolution, R_e , given by:

$$R_e = \Delta E_1/E_1 = \Delta t/2t \quad - (2.29)$$

2.8.2 ToF Spectral Broadening due to Multiple Scattering

This section considers the complications of the additional contribution of multiply scattered (MS) particles in ToF spectra. For the purpose of most studies it is an advantage to chose experimental conditions for which the MS signal is a minimum or separated from the QS peak. In an attempt to identify conditions leading to minimisation of the MS signal a review of existing ToF data in the literature is given. A summary of the surfaces and conditions included are summarised in table 2.1. The data can be divided into three distinct groups: spectra from non-ordered surfaces at intermediate scattering angles, spectra from ordered surfaces at intermediate scattering angles and spectra from ordered surfaces in the impact collision mode. Experimental peak widths are compared with expected values given by eq 2.28.

Table 2.1 - Time of flight scattering data

E_0	ϕ	θ	primary	target	orien	preparation	year	ref
kev	deg	deg	species	species	tation	technique + notes		
5	90	45	Ne ⁺	Ni(001)	[100]	Mechanical polishing with syton	1979	100
5	90	35	Ne ⁺	Ni(001)	[110]	Rinsed in HNO ₃ /glacial acetic acid,		
5	90	45	Ne ⁺	Ni(001)	[100]	acetone , de-ionised water.		
5	90	35	Ne ⁺	Ni(001)	[110]	Cleaned in UHV chamber with Ne ⁺		
						bombardment at 600-700°C, then		
						annealed at 400°C		
2.4	90	45	Ne ⁺	Ni(001)	[110]			
2.4	90	35	Ne ⁺	Ni(001)	[110]			
2.4	90	45	Ne ⁺	Ni(001)	[100]			
2.4	90	35	Ne ⁺	Ni(001)	[100]			
10	30	15	Ne ⁺	Cu(100)	[100]	separated QS & QD	1979	17
10	30	15	Ne ⁺	Cu(100)	[110]			
10	30	15	Ne ⁺	Cu(100)	[210]			
10	30	15	Ne ⁺	Cu(100)	[310]			
5	90	45	Ne ⁺	Cu ₃ Au	[100]	-500 eV Ar ⁺ bombardment at 700° C,	1977	20
5	90	45	Ne ⁺	Cu ₃ Au	[100]	- followed by annealing at 300°C		
				(100)		-Sharp LEED pattern		
5	90		Ne ⁺	Au	-	NK	1978	19
5	90	NK	Ne ⁺	Si(111)	-	Chamber also equipped		
						with a rotateable ESA analyser.		
1.5 to 15	135	90	He ⁺	Ni	-	NK	1978	90
5	90	NK	H ⁺	Au	-	Round Robin comparison	1982	91
5	90	NK	He ⁺	Au		ToF x 2, simulation x 2, S-ESA x2		
5	90	NK	Ne ⁺	Au		Various grain sizes, preparation		
5	90	NK	Ar ⁺	Au				
2	180	0 to 180	Ne ⁺	Pt(111)	[112]	NK	1990	57
3	135	NK	Ne ⁺	CsBr	-	Evaporated films of CsBr	1983	92
3	90	NK	Ar ⁺	CsBr		on stainless steel		

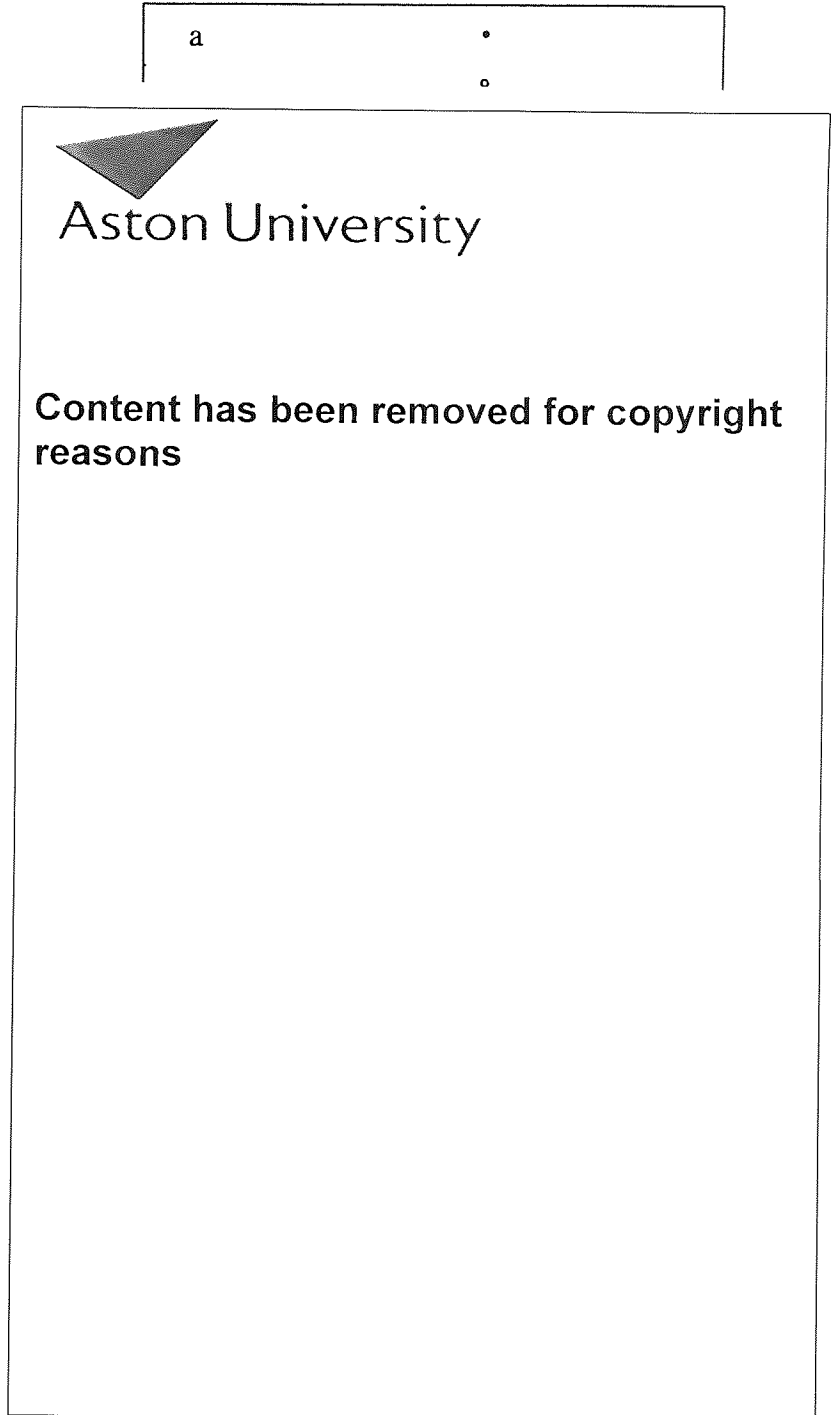
chapter II, Background

8	90		Ar ⁺	Au		Trichloroethylene & acetone	1975	14
24	90		Ar ⁺	Au		+ electro-etched in NaCl/HCl solution		
8	90		He ⁺	Au		+ rinsed in de-ionised water		
16	90		He ⁺	Au		+ annealed to yield a grain size of		
32	90		He ⁺	Au	1	~ 0.1 mm		
2	165	10 to 120	Ar ⁺	Pt(111)	<112>	annealed	1986	18
2	165	0 to 120	Ne ⁺	Pt(111)	<112>		1986	18
2	149	10	Ne ⁺	Pt(110)	<112>	Mechanical polishing - alumin -20 $\mu\text{A}/\text{cm}^2$ Ar ⁺ fluence annealed to 1300°C, O ₂ treatment to remove impurities diffused from bulk.	1991	93
2	180	45	He ⁺	InAs(001)	[110]	InAs wafer dipped in (NH ₄) ₂ S ₃ solution	1991	94
2	180	45	He ⁺	InAs(001)	[111]	to remove the native oxide, Heated to 650 K.		
8	166	18	Ne ⁺	Ni(100)	[100]	Mechanical polishing - diamond paste cyclic heating to ~500° C and 2 keV Ar ⁺ bombardment. Annealed at ~ 600°C	1991	41
2	180	90	He ⁺	Au/Si (111)	NA	Au layer grown on Si surface with MBE	1991	95

2.8.3 Intermediate scattering angles from non-ordered surfaces

The advantage of energy analysis of scattered neutrals was first reported by Buck¹⁴. This instrument, built at Bell Labs, New Jersey had a 93 cm flight path, and a 50 ns pulsed width (subsequently referred to as the *NJ* instrument.) This instrument demonstrated for the first time the high neutralisation probability of noble gas ions scattered from metal surfaces. An energy spectra derived from the experimental ToF spectrum is shown in figure 2.14a; the QS_{Ar-Au} peak at $E_f/E_o = 0.666$ is prominent. A pronounced shoulder can be seen to the high energy side of the QS_{Ar-Au} peak which was attributed to multiple 'in-plane' scattering mechanisms. The QD energy, the energy resulting from two a double 'in-plane' collision consisting of two 45° deflections, in this case is $\sim 0.787E_o$. The intensity falls to zero at approximately the QT energy, which is $0.849E_o$ (corresponding to three in plane collisions each of 30°). Close inspection of the spectra at energies higher than the QT energy reveals an 'anomalous hump' at $E > E_o$ which cannot be attributed to argon scattering. The hump was identified by Chen et al⁹⁶, using a combined ToF-ESA technique, to result from direct recoils of light atoms such as H and C. The experimental resolution of the QS_{Ar-Au} peak, $R_e(exp)$ is ~ 16 compared to $R_e(calc)$ of 37. A much greater MS contribution was observed in the case of 8 keV helium employed as the primary species, figure 2.14b. The QS_{He-Au} peak, expected at a $0.977E_o$ is completely 'swallowed' by a broad MS feature. Again the extension of the peak above $E_f/E_o > 1$ was attributed to hydrogen recoils.

Similar experimental data were reported from a ToF instrument built at the Max-Planck Institut für Plasma Physik, by Eckstien et al⁹⁰ (subsequently referred to as the *IPP* group). Spectra from the *IPP* instrument of 1.5 to 15 keV He⁺ scattered from a polycrystalline nickel surface at $\vartheta = 135^\circ$ are shown in figure 2.15. This instrument was equipped with an ESA analyser and allowed direct comparison between ESA and ToF spectra. From figure 2.15a it can be seen that the onset of the low energy tail in the ESA spectra began at ~ 3 keV, and increased monotonically with increasing energy. In contrast the ToF spectra exhibited a very significant tail at all energies, and above ~ 5 keV the QS_{He-Ni} peak (at $0.793 E_o$) was not visible due to the domination of the MS signal. It can also be seen that the ToF peaks extend to higher energies than their ESA counterparts. For example the half width at half maximum height of the 1.5 keV ToF peak is ~ 70 eV, compared to ~ 40 eV for the corresponding ESA peak. Therefore even at the relatively large



E/E_0

Figure 2.14 - Scattered particle energy spectra, derived from experimental ToF spectra . After T.M.Buck (1975)¹⁴
a) 8 keV Ar⁺ scattered from a polycrystalline Ag surface. $\vartheta=90^\circ$, black circles ion+neutrals, white circles neutrals only
b) 8 keV He⁺ scattered from a polycrystalline Ag surface. $\vartheta=90^\circ$

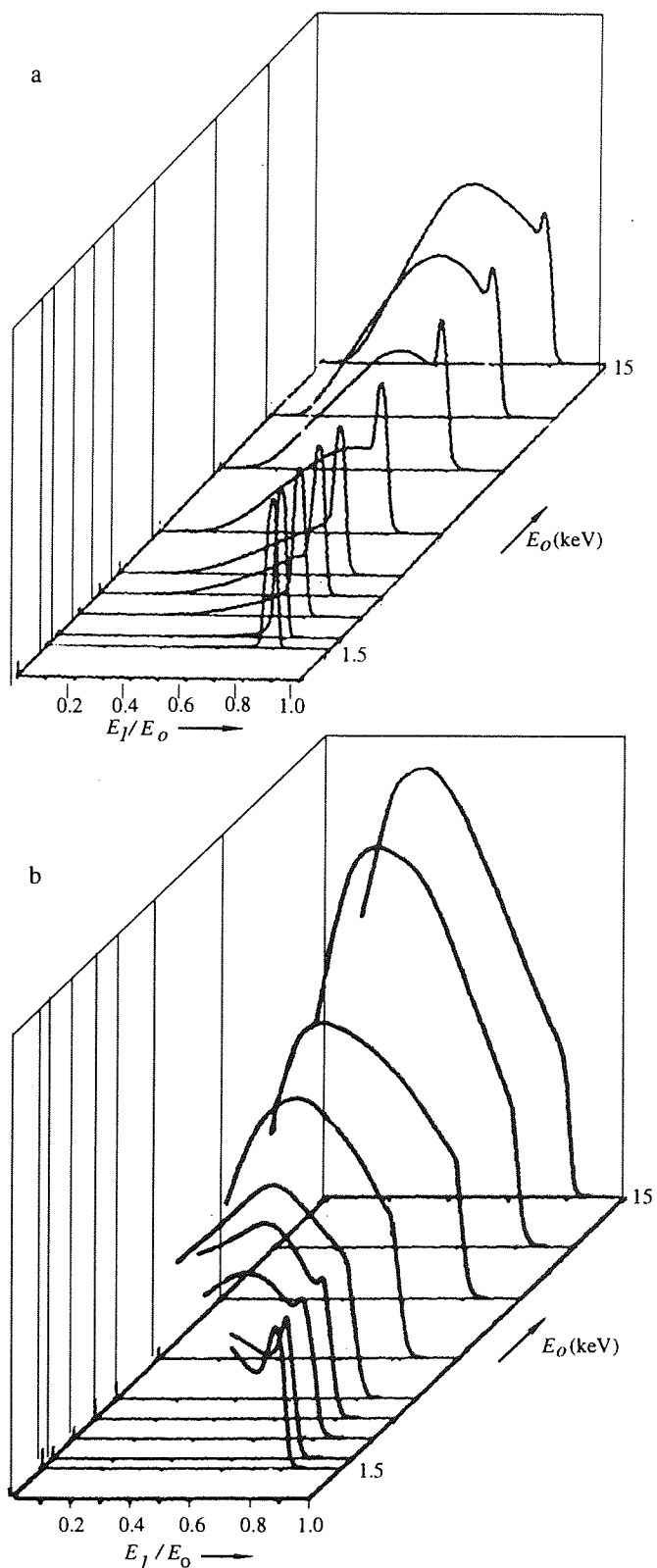


Figure 2.15 - Helium scattered from a polycrystalline nickel surface, after Eckstien et al ⁹⁰
Conditions: - $\vartheta = 135^\circ$, $\theta = 90^\circ$
(a) obtained with ESA analyser, (b) obtained with ToF analyser, neutrals+ions

scattering angle of 135° the MS signal was strongly dominant even at low primary energies.

Broad MS peaks were also observed in the ToF spectra of 5 keV Ne ions scattered from an amorphous Si surface¹⁹, as shown in figure 2.16. The Si(111) surface, had been subjected to a high current argon ion beam without subsequent annealing, and therefore can be assumed to be amorphous. In the ToF spectra shown in figure 2.16a the most prominent peak at $7.4 \mu\text{s}$ is attributed to double scattering, which corresponds to the $QD_{\text{Ne-Si}}$ energy, $\sim 0.36 E_0$. The cusp at $10.6 \mu\text{s}$ corresponds to the $QS_{\text{Ne-Si}}$ energy $0.17E_0$. Again the QS peak is very severely broadened and dominated by MS. For these conditions, $R_e(\text{calc}) \sim 20$, corresponding to a peak width of 250 ns. As the primary and target atoms are close in mass, ($A=1.4$), double scattering collisions result in scattering at energies significantly higher than the QS energy. The corresponding ESA spectrum, shown in figure 2.16b, also exhibits double and triple in-plane scattering, but with significantly less intensity at lower energies, and a much sharper QS peak. In this case $R_e(\text{calc})$ is in good agreement with the calculated value, $R_e(\text{exp})$.

Data from the *NJ*-ToF instrument and ToF data generated by an instrument constructed by A.L.Boers et al, at the University of Groningen⁹⁷, (subsequently referred to as the *UG* group) were published in a 'round robin' comparison of ToF, (S-ESA)⁹⁷, and computer generated data⁹¹. Data from the participating groups were produced independently for 5keV He, Ne and Ar ions scattered from polycrystalline gold. The resulting total particle spectra are shown in figures 2.17, 2.18 and to 2.19. It can be seen from figure 2.17, in the case of helium, that the scattered particle spectra were dominated by MS. All three data sets exhibited a large low energy tail extending towards zero energy. Significant intensity was also observed above the $k=1$ threshold. In the case of the *UG* data, subtraction of the neutral fraction from the total spectra displayed a very sharp peak due to scattered ions, giving $R_e(\text{exp}) \sim 140$. Whereas the *UG*-ToF instrumental parameters of $\Delta E_0 = 0.005E_0$, $\Delta t = 20$ ns, $l = 111.6$ cm and $\Delta\theta = 0.32^\circ$ predicts $R_e(\text{calc}) \sim 42$. In the case of neon scattering, all data sets exhibited a significant reduction in the MS signal. In this case a pronounced 'high energy shoulder' extending beyond the QD peak energy of $\sim 0.888E_0$ was observed. This QD intensity can be seen to be significantly lower than that of the Ne-Si of figure 2.16. Furthermore, the $QS_{\text{Ne-Au}}$ peak was significantly less broadened by multiple scattering; that of the *UG*-ToF data was the sharpest, and exhibited a resolving power of ~ 90 , which is comparable to $R_e(\text{calc})$, and equal to that of the derived ion peak. In

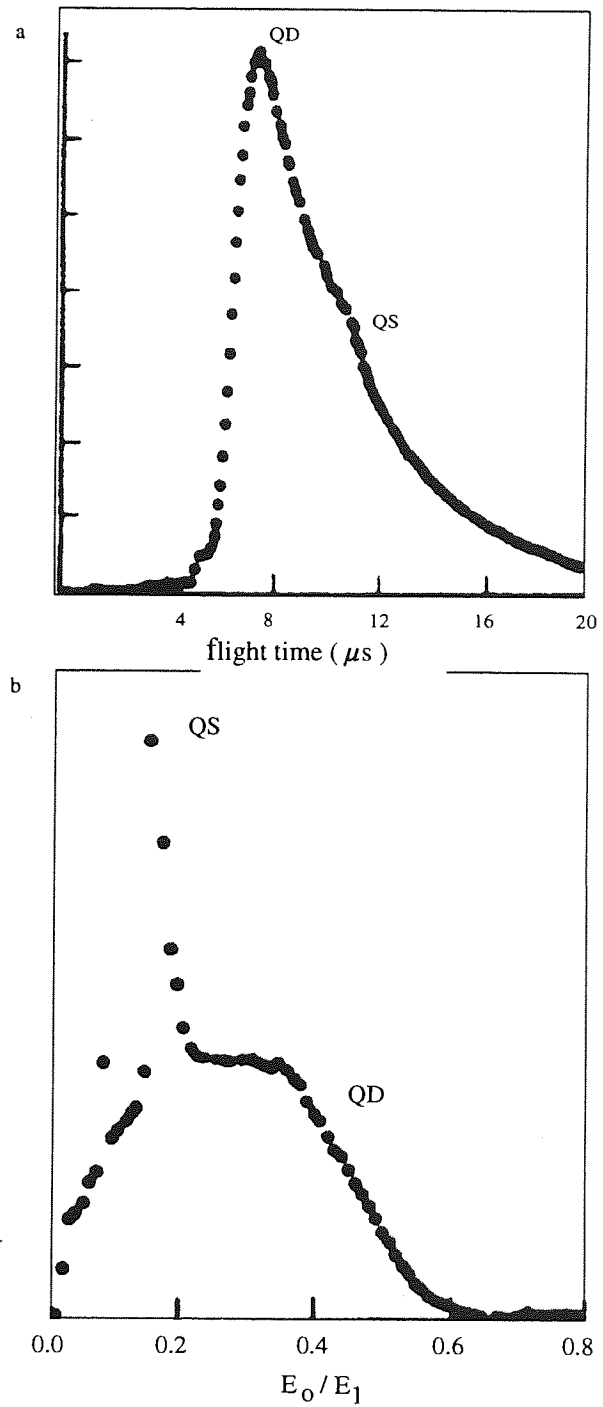


Figure 2.16 - Ne⁺ scattered from a Si, after Buck et al¹⁹.

Conditions: - 5 keV, $\vartheta=90^\circ$

a) ToF spectrum

b) LEISS spectrum (ESA analyser)

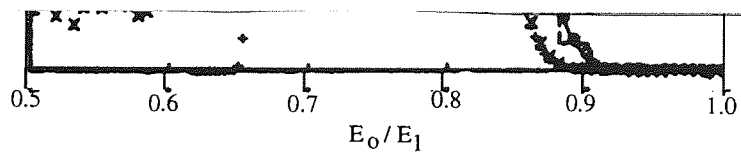
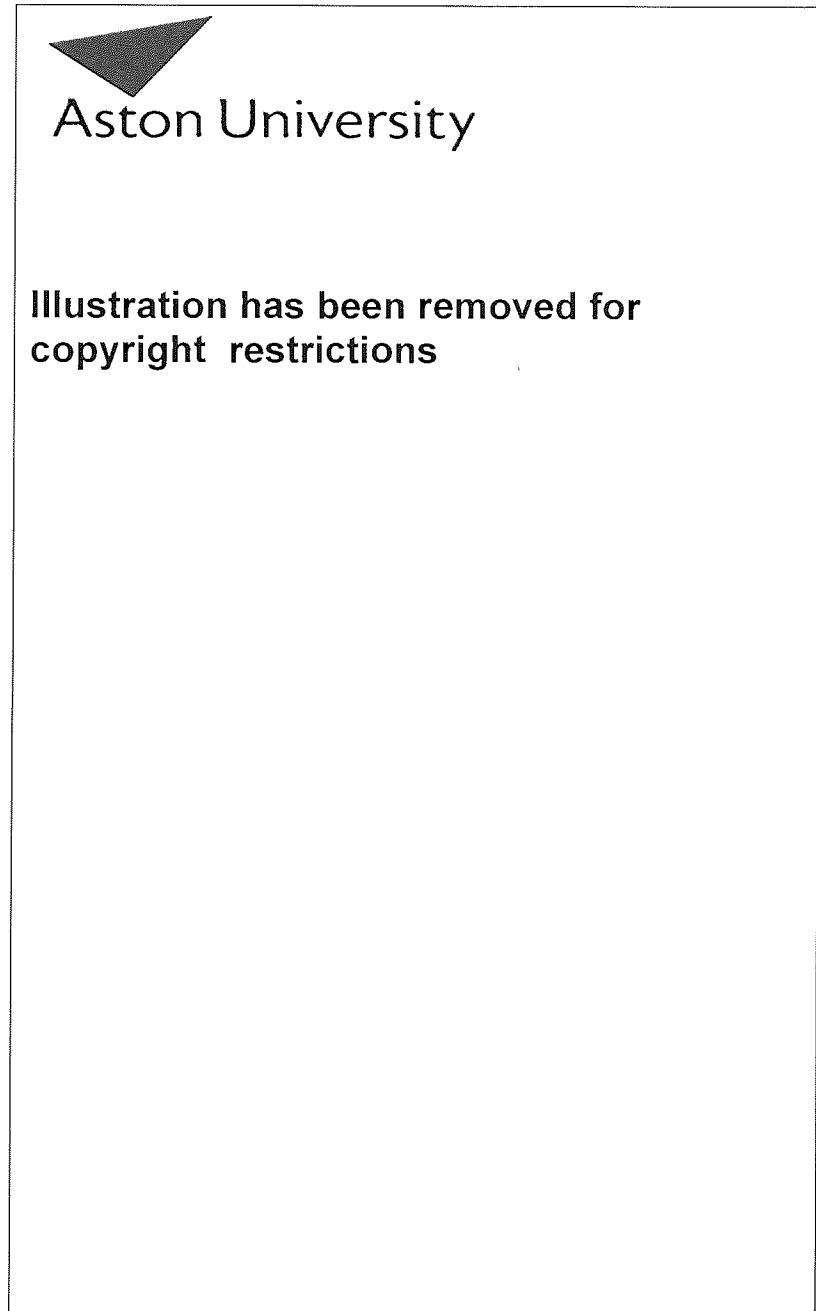
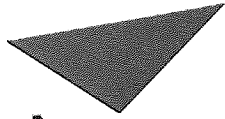


Figure 2.18 Round Robin Comparison from reference 91, (ion+neutrals spectra), neon from gold - polycrystalline. Conditions: - $E_0 = 5\text{keV}$, $\vartheta = 90^\circ$.



Aston University

Content has been removed for copyright reasons

E_1/E_0

Figure 2.19 - Round Robin Comparison from reference 91,
(ion+neutrals spectra), argon from polycrystalline gold.
Conditions: - $E_0 = 5\text{keV}$, $\vartheta = 90^\circ$.

contrast to this the *NJ*-ToF data exhibited no peak in the derived ion spectrum. Similar trends can be seen for argon spectra in figure 2.19, with the QS_{Ar-Au} peak further increased relative to the MS signal. As with helium and neon, the extreme high energy edge corresponds to the QT energy of $0.849E_o$. The variation of peak QS width across the data sets is also repeated, $R_e(exp) \sim 30$ for the *NJ*-ToF data compared to ~ 100 for the *UG*-ToF data, where both values are in agreement with prediction. The authors of the comparison concluded that, in general, the ToF total particle spectra showed reasonable qualitative agreement when differences in the instrument resolving power were considered. However, larger differences were seen when the derived ion spectra and positive ion fractions were compared: the most striking of which was the absence of a QS ion signal in the *NJ*-ToF data compared to a very sharp peak in the *UG*-ToF data. The chief cause of the discrepancies was attributed to variations in surface crystallinity and surface preparation procedures.

ToF spectra from a non-crystalline binary alloy surface were produced from an instrument built by Rabalais et al⁹² at the University of Houston. Figures 2.20 & 2.21 show the ToF spectra of 3 keV neon and argon ions scattered from an evaporated film of CsBr at $\vartheta=135^\circ$. Again the spectra feature broad surface peaks. In this case the QS peak width cannot be accounted for by the instrument resolving power, which in this case is low: $l=56.5$ cm, $\Delta t=300$ ns, leading to $R_e(calc) \sim 21$ and 23 for the QS_{Ne-Cs} and QS_{Ne-Br} peaks respectively, which is a factor of four greater than experiment. The calculated energy resolving power corresponds to mass resolving powers, $m_2/\Delta m_2$ of ~ 11 and 21 . Given the two corresponding masses of 133 and 80 amu they would normally be well separated in a LEISS spectra. However in figure 2.20 the QS_{Ne-Br} peak is positioned within the low energy tail of the higher energy QS_{Ne-Cs} peak. In figure 2.21, the QS_{Ar-Cs} and QS_{Ar-Br} peaks are more widely separated, as predicted: $(m_2/\Delta m_2)$ is ~ 16 and 27 respectively. In this case recoiling impurity atoms were thought to be the cause of the continuous intensity to short flight times. No information on the crystal structure of the CsBr film was given in reference 92, however, the surface was subjected to prolonged sputtering with an argon beam, without subsequent annealing, and therefore can be assumed to be disordered.

2.8.4 Scattering data at intermediate angles from ordered surfaces

The ToF spectra of single crystal surfaces contrast sharply with

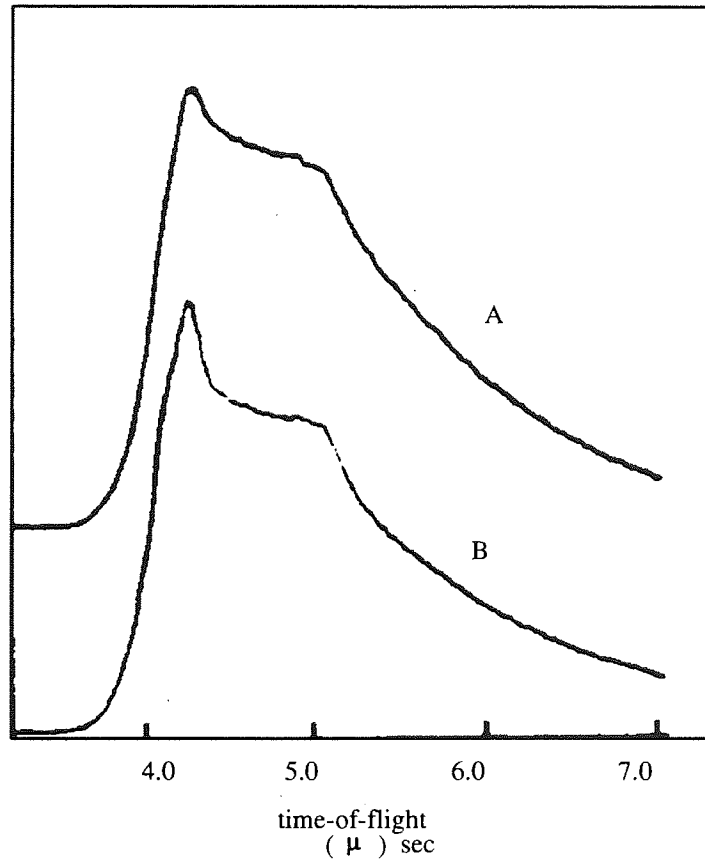
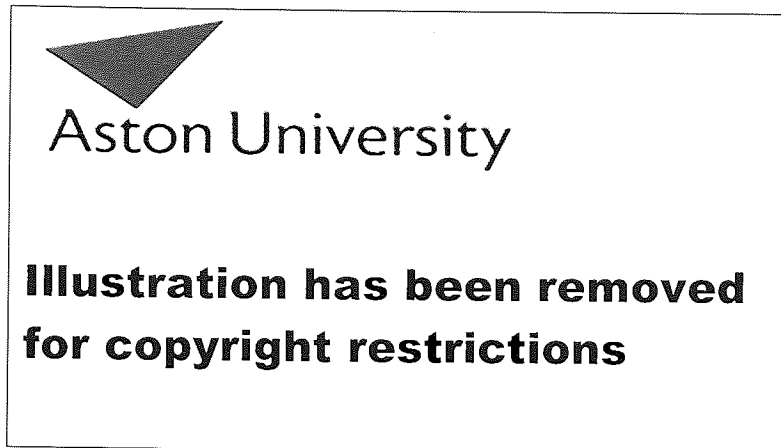


Figure 2.20 - Ne^+ scattered from a CsBr, After Rabalais et al⁹².

Conditions: - $E_o = 3 \text{ keV}$, $\vartheta = 135^\circ$.

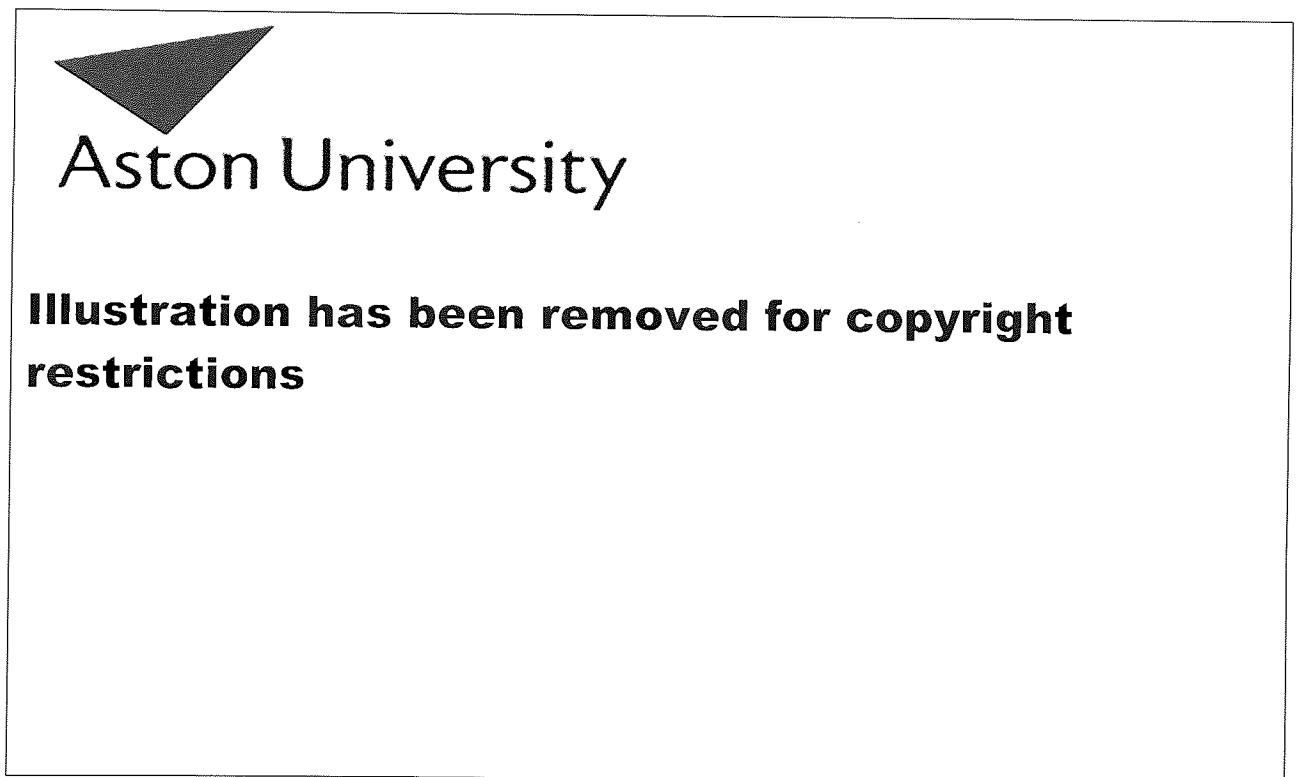
(A) After sputter cleaning with a dose of $1.5 \times 10^{14} \text{ Ne}^+ \text{ ions/cm}^2$.

(B) After bombardment with a total dose of $8.3 \times 10^{14} \text{ Ne}^+ \text{ ions/cm}^2$.



(μ) seĉ

Figure 2.21 - Ar⁺ scattered from CsBr. After Rabalais et al⁹².
Conditions: - $E_o=3$ keV at $\vartheta=90^\circ$.



0.90

0.93

0.96

E_o/E_1

Figure 2-22 - Ne⁺ scattered from Cu(100). After Luitjens et al ¹⁷, showing the experimental ToF spectra of ion+neutrals, neutrals only, ion fraction, and the experimental ESA spectrum.

Conditions: - $E_o = 10$ keV, $\vartheta=30^\circ$, $\theta=15^\circ$, orientation $\langle 100 \rangle$.

those of the previous subsection.

The first such data, was reported by the UG group¹⁷, involving Ne⁺ scattered from Cu(100), see figure 2.22. Although the primary energy is large, $E_o=10$ keV, and the scattering angle low at 30° , there is a notable reduction in the MS contribution compared to the previous spectra from non-ordered surfaces. Furthermore the QS peak is sharp: $R_e(exp) \sim 70$ in good agreement with the predicted value of 68. Instead of the double scattering shoulder seen previously, there is a distinct peak corresponding to the QD peak energy of $0.96E_o$.

The absence of MS low energy tails was also seen in the NJ-ToF spectra of 2.4 keV Ne⁺ scattered from Ni(001) at $\vartheta=90^\circ$ ¹⁰⁰. These results demonstrate the influence of azimuth and incident polar angles on the scattered neutral energy distribution. The spectra shown in figure 2.23 were collected at the [100]45°, [100]35°, [110]45°, [110]35° orientations. An orientation dependency of the MS contribution can clearly be expected from shadowing considerations: for example at the [100]45° orientation the incident beam aligns along <110> 'channelling axis' and ions are guided or channelled between atomic planes. In the case of the [100]45° orientation, only top layer atoms are exposed to the incident beam, as a consequence the MS signal is virtually absent. The QS_{Ne-Ni} peak at $0.493E_o$, is slightly greater than the SBCE of $0.487E_o$, in agreement with the discussion of section 2.5.1. In this case the instrumental resolving power, $R_e(exp) \sim 40$, slightly exceeds $R_e(calc) \sim 27$, as calculated from the published instrumental parameters. It can be seen in figure 2.23b that if θ is decreased by 10° , so as to misalign the incident ions with the <110> channelling axis a small increase of the MS contribution can be observed. Whereas in the [110]35° orientation the incident beam is aligned with the <111> channelling axis, however second layer atoms are in this case exposed to the incident beam. As a result the QS peak width is noticeably increased, $R_e(exp) \sim 24$. Further enhancement of MS trajectories results from a 10° misalignment of the incident beam, as seen in figure 2.23c.

The experimental contribution of MS scattering trajectories in scattered particle spectra can also be seen in alkali ion spectra obtained with an ESA. Owing to the low neutralisation of these the ion spectra in this case provide a reasonable indication of the total yield spectra. The spectra of 250 eV K⁺ scattered from W(110) are shown in figure 2.24, after Von Dem Hagen et al⁹³. Here again it can be seen that the MS contribution is strongly influenced by the azimuth angle of the primary beam: the position and shape of both the QD peak and QS peaks vary as a function of azimuthal angle, ψ .

Simulation of the experiment by the authors showed the shift in the double scattering peak to be caused by the differing contributions to 'out of plane' scattering, whilst the lower energy peaks could be attributed to top row 'zig zag' collisions.

The final data considered in this section is that from a single crystal alloy $\text{Cu}_3\text{Au}(100)$ surface. A ToF spectrum of 5 keV Ne^+ with the incident beam orientated along the $\langle 110 \rangle$ channelling axis is shown in figure 2.5a²⁰. The broad low level features are attributed to top layer zig zag collisions and second and third layer MS mechanisms. It can be seen however that these mechanisms do not lead to significant broadening of the $\text{QS}_{\text{Ne-Cu}}$ and $\text{QS}_{\text{Ne-Au}}$ peaks. A larger MS signal resulted when the incident beam was moved to the $\langle 111 \rangle$ orientation due to scattering from deeper layers, see figure 2.25b.

2.8.5 Large angle and co-axial impact ToF data

ToF scattering data reported in the previous two subsections stimulated the construction of a number of large scattering angle ToF instruments, where ϑ is made equal or close to 180° . These instruments are primarily intended for and applied to the investigation of surface structure, as described previously.

The first near 180° scattering data was produced by Niehus et al of the Institut für Grenzflächenforschung und Vakuumphysik der Kerforschungsanlage, Jülich (subsequently referred to as the GVK group). This NICISS, employed a scattering angle 165° , and a pulsed primary ion beam of $\Delta t \sim 40$ ns. The flight path, l , was 100cm. An 'acceleration tube' was also employed in the flight leg for separation of scattered ion and neutrals peaks. Spectra of Ne^+ and Ar^+ scattered from the Pt(111) surface^{18,45,89}, are shown in figures 2.26 in which θ is varied from 1 to 120° . The intensity of the small $\text{QS}_{\text{Ne-Pt}}$ ion peak appearing at shorter flight times as a result of the acceleration tube, is only weakly influenced by θ . In comparison the scattered neutral intensity is a strongly dependent on θ , which demonstrates the advantage of NICISS for structure analysis. The $\text{QS}_{\text{Ne-Pt}}$ atom peak is the dominant feature of the scattered neutral intensity, for which $R_e(\text{exp})$ and $R_e(\text{calc})$ are in good agreement ~ 40 . The first two maxima in intensity curve at 20° and 55° result from focusing by first layer atoms onto first and second layer atoms respectively. Whereas the third peak at 80° followed by the rapid fall at $\sim 92^\circ$ results from focusing of the outgoing particles by the first-layer



Aston University

Illustration has been removed for
copyright restrictions

Figure 2.23 - Ne⁺ scattered from Ni(001). After Buck et al⁸⁹.

Conditions: - $\vartheta=90^\circ$, $E_o=2.4$ keV.

Incident beam orientation: (a) [100]45°, (b) [100]35°, (c) [110]45°, (d) [110]35°.

The corresponding QS peak heights are (a) 3400, (b) 3900, (c) 7000, (d) 1800 counts.

QS	OD
----	----



Aston University

Illustration has been removed for copyright restrictions

0.2 0.4 0.6 0.8 1.0
 E_o / E_I

Figure 2.24 - K^+ ions scattered from clean W(110) (ESA data). After Von Dem Hagen et al ⁶²

Conditions: - $E_o = 250$ eV at $\vartheta = 90^\circ$, $\theta = 45^\circ$.

Instrument parameters: - $\Delta E_{ESA}/E = 1.5\%$, $\Delta\vartheta = 5^\circ$

Incident beam orientation (a) [223], (b) [113], (c) [110], (d) [001], (e) [111].

(The vertical lines indicate the SBCE and QD energy)

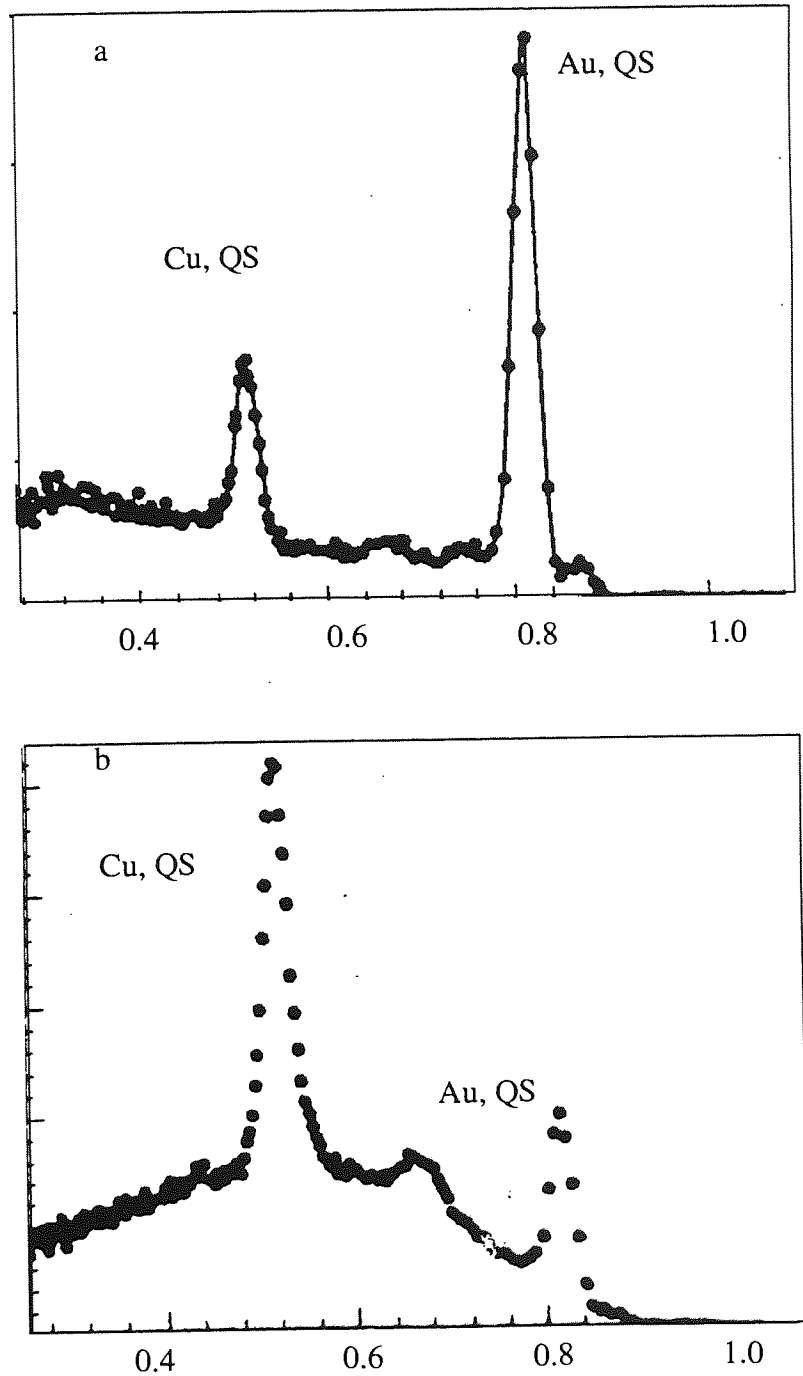


Figure 2.25 Ne⁺ scattered from Cu₃Au(100), after Buck et al²⁰, (energy spectrum derived from ToF data)
Conditions:- 5 keV , $\vartheta = 90^\circ$, orientation (a) [100]45, (b) [110]35.

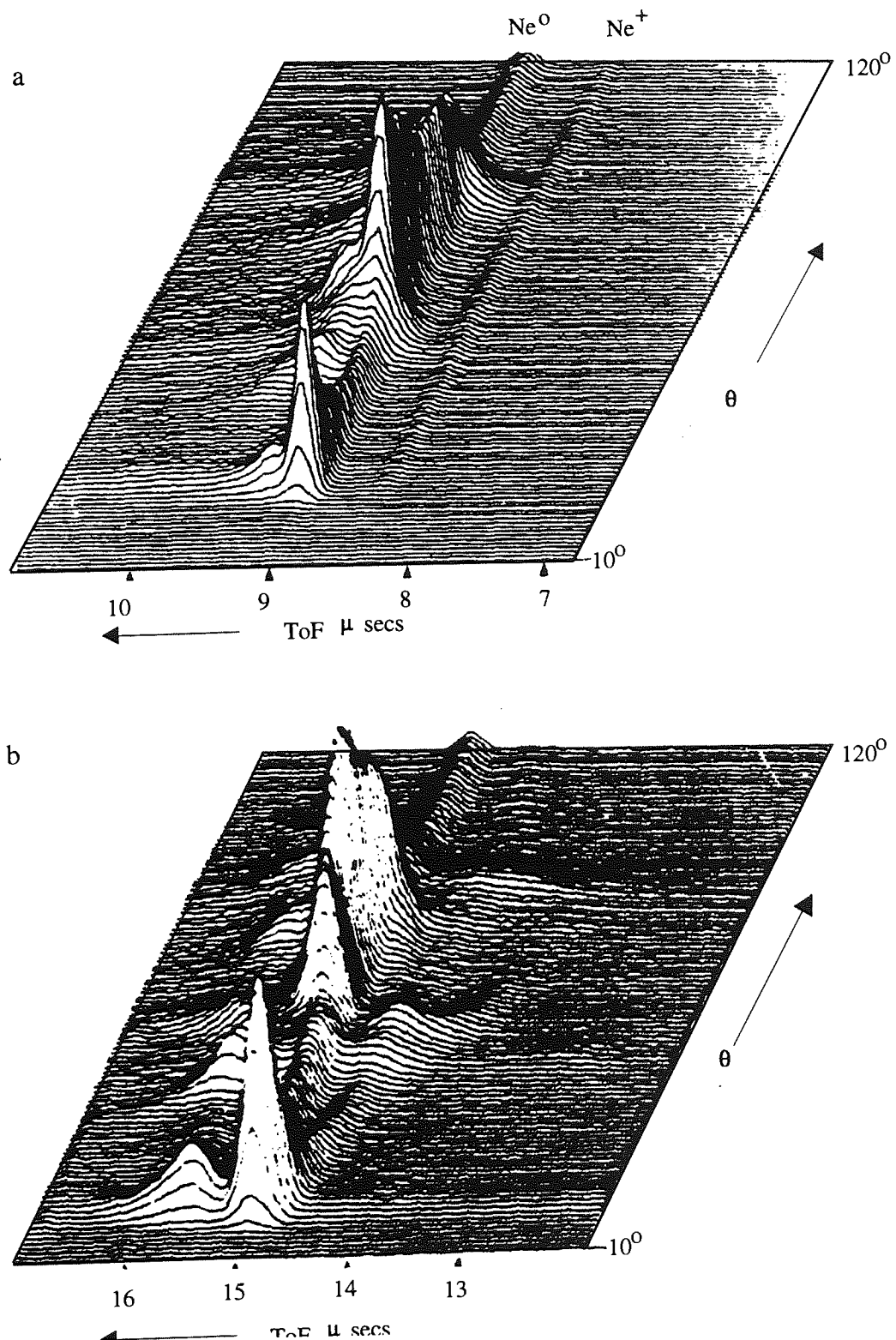


Figure 2.26 - NeCISS spectra from Pt(111) in the [112] plane. After Niehus and Comsa^{18,89}, and shown as a function of the incidence angle.

Conditions: - $E_0 = 2$ keV, $\vartheta = 165^\circ$.

Instrumental parameters: - $\Delta t \sim 40$ ns, $l = 100$ cm.

(a) Ne⁺ beam, acceleration voltage = -500 V.

(b) Ar⁺ beam acceleration voltage = -500 V.

atoms towards the analyser. The QS_{Ne-Pt} peak suffers little MS broadening effects despite misalignment with channelling directions as θ is varied. the QS_{Ne-Pt} peak appearing distinct from MS features irrespective of the incident angle: Only at $\theta \sim 50^\circ$ does the MS tail have a greater intensity than the QS_{Ne-Pt} peak, and only at $\theta \sim 55^\circ$, and $\theta \sim 90^\circ$ is there significant broadening at the high energy side of the QS peak due to double scattering.

Similar observations apply for argon scattering data from the same surface and experimental conditions, figure 2.26b. The main difference is the appearance of a distinct double scattering peak at incidence angles between $\sim 30^\circ$ and 60° , and a significant but well separated low energy MS tail at various angles.

Modification of the GVK instrument allowed true 180° scattering, achieved using an electrostatic condenser lens to deflect the incident beam⁵⁷. This arrangement is more suitable for obtaining structural information for the reasons discussed in section 2.3.6.3, and this can be seen in figure 2.27, ie the $I-\theta$ curve is richer in the number of peaks of increased intensity. An important point to note is that the QS_{Ne-Pt} peak width is twice that predicted by $R_e(calc)$ which is 40 and there appears to be no broadening to higher energies due to double scattering. This can be explained by the exact super-imposition of the QS and QD peaks. That is the SBCE, of $0.663E_o$, is exactly equal to the energy of two symmetric 90° in-plane collisions, leading to symmetrical peak broadening as seen in the experiment spectra.

A large impact angle ToF spectrometer was also constructed by the Houston group²⁴. This instrument consisted of a semicircular vacuum chamber of ~ 100 cm diameter and contained an internal rotatable MCP detector, allowing ϑ to be continuously varied from 0° and 165° . This experimental arrangement is referred to as ToF-Scattering and Recoiling Spectrometry (ToF-SARS), and has been used to study the Pt(110)(1x2) reconstructed surface⁹³. A ToF spectrum, of 2 keV Ne^+ is shown in figure 2.28, which was obtained following the collection of a sharp LEED pattern. The experimental resolving power $R_e(exp)$ of the main peak, which was attributed to QS scattering is only ~ 5 . This compares to the predicted value $R_e(cal)$, of 67 (assuming $\Delta E_o/E_o = 0.01$) The spectrum is therefore uncharacteristically broad compared to the others from ordered surfaces. Further spectra of 8 keV Ar^+ from Ni(100) also exhibited a large MS signal, which appears to contribute to the broadening of the QS peak, figure 2.29. Here again the surface exhibited a distinctive LEED pattern, although the various MS mechanisms merge giving rise to a single broad peak. However,

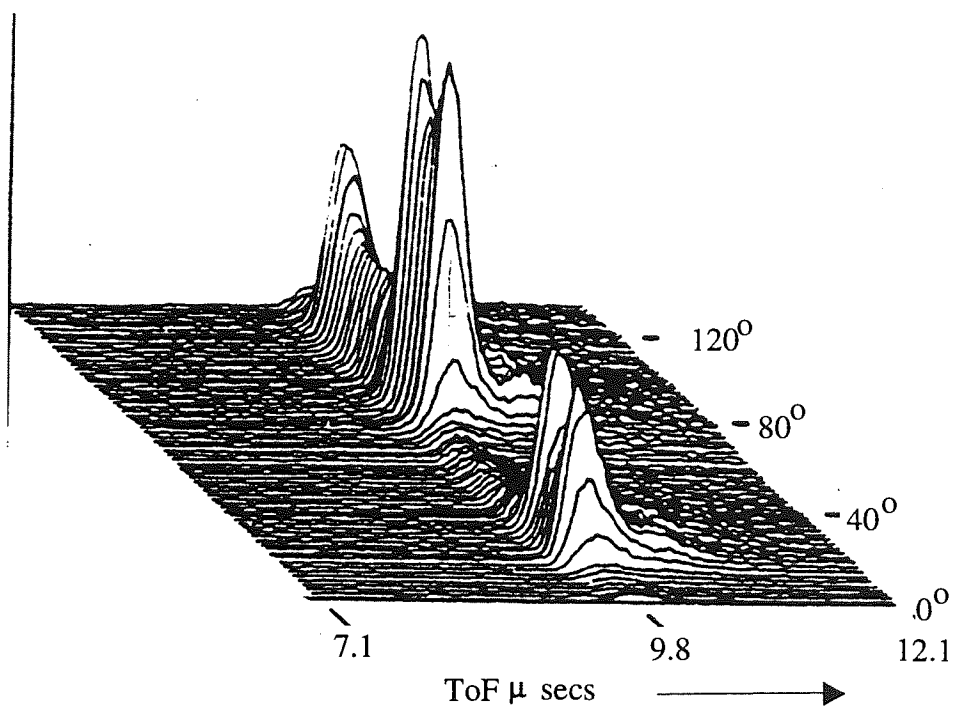


Figure 2.27 NICISS spectra, Ne⁺ scattered from Pt(111), shown as a function of the incidence angle, θ . After Spitzl, Niehus and Comsa⁵⁷.
Conditions: - $\vartheta=180^\circ$, $E_o=2$ keV, [112] orientation, acceleration tube voltage =0V.

the ion peak derived from the ToF spectrum is also broad, $R_e(exp) \sim 10$, therefore suggesting that the broadening cannot be fully attributed to MS scattering.

Finally, a number of large angle ToF spectra have been produced by the *RIKEN* group, using an instrument they call CAICISS, that is CoAxial Impact Collision ISS^{98,99}. The instrument employs a flight path of only 58 cm, but has a pulse duration, Δt of 5 ns. An 'acceleration tube' was also available for ion/neutral separation. Normal incidence helium spectra of a Si(111) $\sqrt{3}\sqrt{3}$ surface supporting epitaxially grown Ag crystallites⁹⁵ are shown in figure 2.30. For such experimental conditions $R_e(calc)$ is 150 and 90 for the QS_{He-Ag} and QS_{He-Si} peaks respectively. As in the *GVK* instrument the experimental peaks are broader than the predicted values: $R_e(exp) \sim 20$ for both the ion and neutral QS_{He-Ag} and QS_{He-Si} peaks. Additionally the QS_{He-Si} neutral peak is super-imposed on a broad MS background intensity. This intensity was reported to increase following depositing of further silver onto the surface. It may also be seen that the neutral QS_{He-Ag} peak was broadened by MS when further layers of silver were added to the surface, this corresponded to a reduction in $R_e(exp)$ from 20 to ~ 7 . Although the surface was reported to be annealed, no information on the quality of the crystal surface was available.

Further CAICISS spectra are shown of 2 keV He⁺ scattered from InAs(001)⁹⁴ in figure 2.31. The spectra correspond to the [010]45° 'channel aligned' incidence orientation, where the QS_{He-In} and QS_{He-As} peaks are clearly separated, but are superimposed on a large MS background and are significantly ($\times 3$) broader than predicted. For this surface a large MS presence may be expected as the surface was not fully ordered, as indicated by a 'diffuse' LEED pattern. In accordance with earlier data a significantly greater MS contribution was observed for the non-channelling [010]35° orientation.

2.8.6 General Conclusions

From the preceding review of ToF data it is possible to draw a number of general conclusions: the spectra of polycrystalline samples in all cases exhibit a signal intensity broadly dispersed in energy, far in excess of that expected by the purely single collision treatment of eq 2.24. In some cases a sharp QS peak is superimposed upon the MS intensity, but is not appreciably broadened by it, in which case an MS signal does not hinder analysis. In other cases, notably when helium is employed, the QS peak may be completely obscured with MS signal. The backscattered intensity

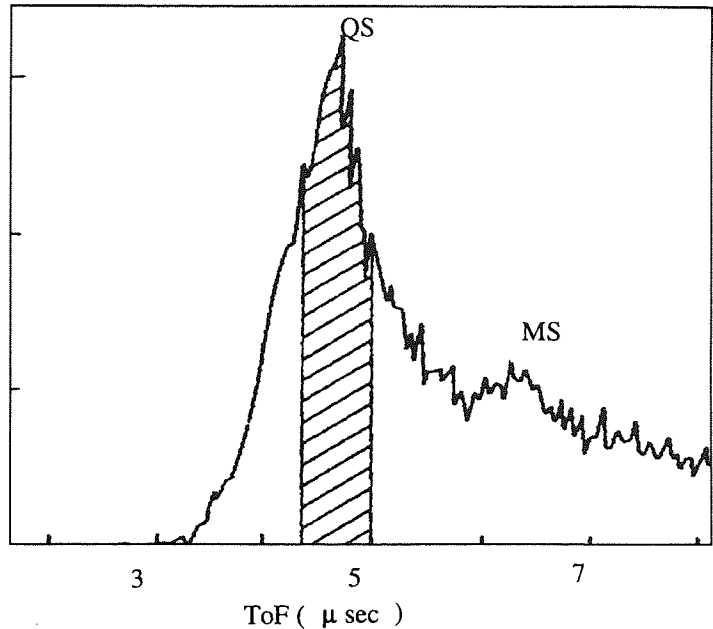


Figure 2.28 - Ne^+ scattered from Pt(110). After Masson and Rabalais ⁹³
 Conditions: - 2 keV, $\vartheta = 90^\circ$, orientation $[112]10^\circ$
 Instrumental parameters: - $l=53\text{cm}$, $\Delta t=50\text{ ns}$.

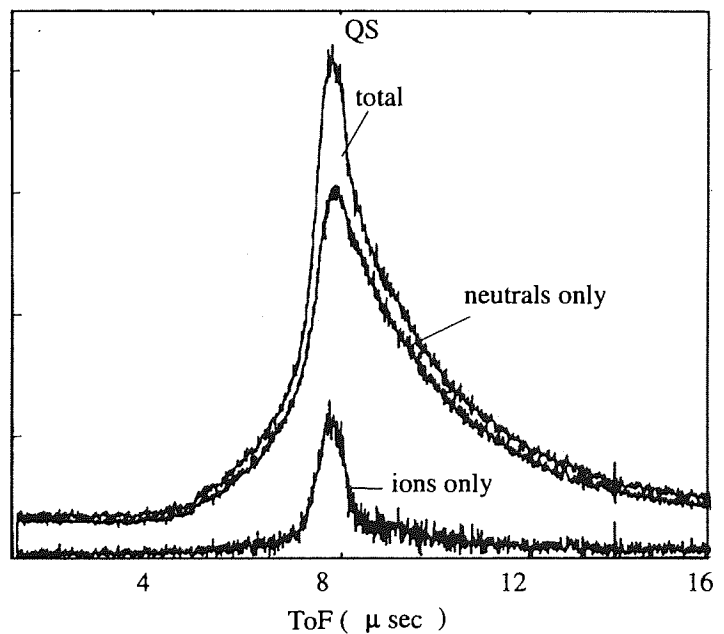


Figure 2-29 - Ar^+ scattered from Ni(100), showing neutrals +ions , neutrals only and ions only, after Masson and Rabalais ⁴¹.
 Conditions: - $E_0 = 8\text{ keV}$, $\vartheta = 166^\circ$, orientation $[100]18^\circ$.
 Instrumental parameters: - $l=100\text{cm}$, $\Delta t=30\text{ ns}$.

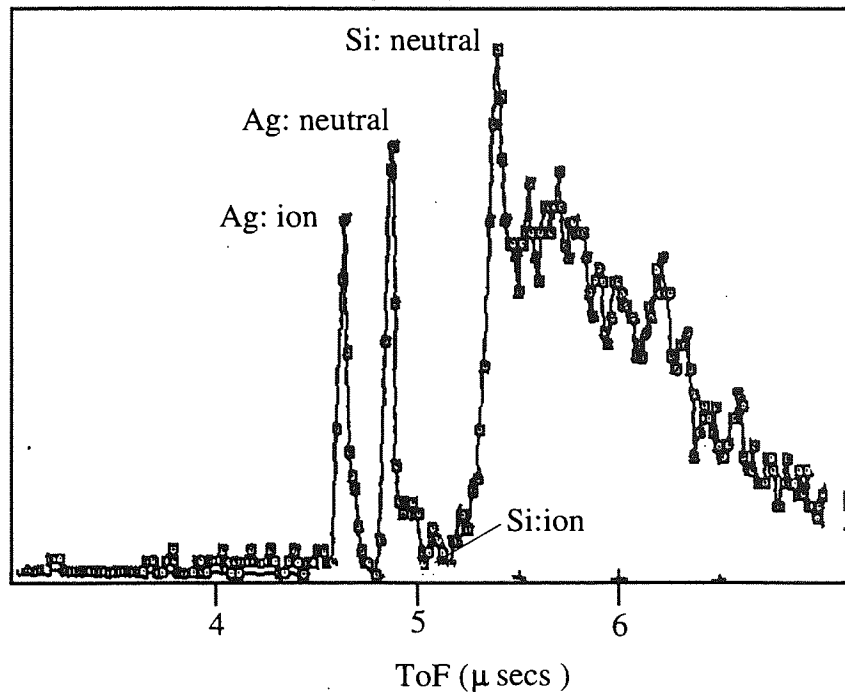


Figure 2-30 - CAICASS - He_+ from $\text{Si}(111)\sqrt{3}\times\sqrt{3}R30^\circ$ with deposited Ag, after Aono et al⁹⁵
 Conditions: - $E_o = 2 \text{ keV}$, $\vartheta=180^\circ$, acceleration voltage = -1.5 kV .
 Instrument parameters: - $\Delta t= 5 \text{ ns}$, and $l= 58 \text{ cm}$.

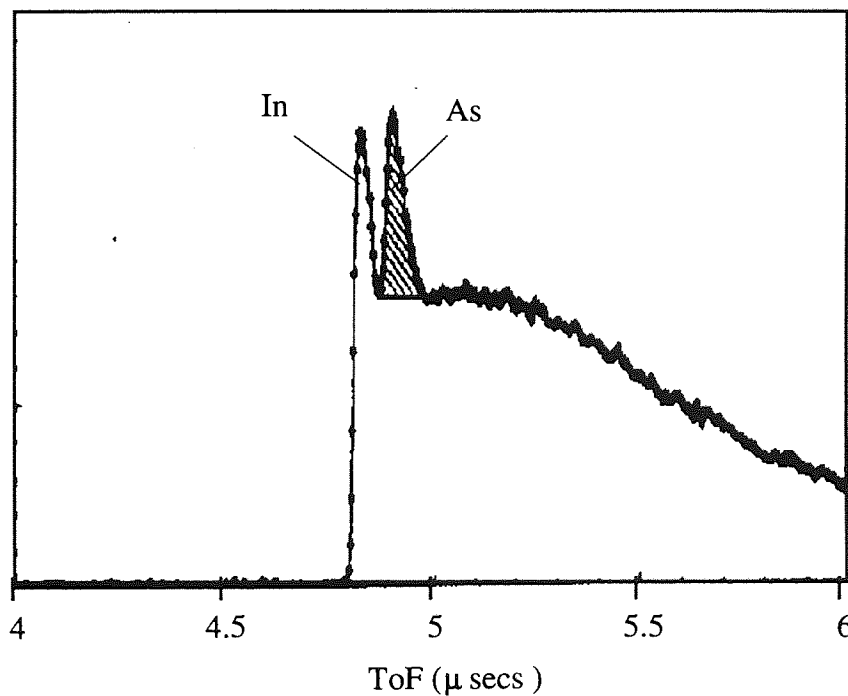


Figure 2.31 - ToF / CAICASS - He^+ from $\text{InAS}(001)$, After Aono et al⁹⁸
 Conditions: - $E_o=2 \text{ keV}$, orientation $[010]45^\circ$ (parallel to the $\langle 011 \rangle$ axis)

constituting the low energy tail is conventionally attributed to multiple scattering trajectories from sub-surface layers. This contribution is generally seen to decrease with increasing scattering cross-section as penetration into the surface is reduced.

A second influential factor in determining the MS signal contribution is surface structure. If the incident beam is aligned with a 'channelling direction' of the crystal lattice MS features are virtually eliminated. Increasing the scattering angle also reduces the MS contribution, although this appears to be a second order effect compared to surface structure. One notable exception was the spectra of Masson et al⁹³, where the QS peaks are much broader than other comparable data. It can also be seen that increasing the scattering angle to 180° increased the QS peak width due to QS-QD peak superimposition.

In summary the data shows that, although free of uncertainties from charge transfer processes, scattered neutral particle ToF can be complicated greatly by MS contributions. In some cases this can completely obscure QS peaks. The problem is most acute for high energy helium scattering from non-ordered surfaces. In semi-ordered multi-component surfaces the QS peaks may appear above a broad non-ordered background intensity.

2.9 Fast Atom Scattering Data

Despite the experimental evidence demonstrating the potential advantages of FAB bombardment, discussed earlier, the employment of FAB has been restricted mainly to studies of a fundamental nature, and is not widely employed as a substitute for ion bombardment in surface analysis. One of the reasons for this is, perhaps, that there have been few satisfactory commercially available atom sources. However, a neutral beam of noble gas atoms may be produced by passing a primary ion beam through a high pressure gas cell. In ion scattering experiments there are practical difficulties in combining the use of FAB with ToF analysers which has been the focused area of development of a number of groups engaged in researching low energy particle scattering technique, and was the main challenge of this work.

There are four basic physical differences between the two types of scattering, two of which are marginal in respect to composition analysis:

- I] Atoms unlike ions may not be neutralised during the incoming phase of their scattering trajectory
- II] Ions and atoms experience different electron stopping power.
- III] Atoms do not experience the attractive force due to the image potential close to the metal surface
- IV] The shielding of the nuclear charge is modified by the presence of the additional electron, although this is widely ignored in the literature.

In this section existing fundamental studies that have investigated these differences are summarised. This existing experimental FAB data has been obtained through detection of the ion fraction only.

The first investigation of FAB was carried out by Verhey et al^{ref} who studied the differences in the QS ion peak position resulting from the incident charge state, for helium scattered from crystalline copper. This energy difference was measured as a function of primary energy, E_o (4 to 10 keV) and incidence angle. The resulting data revealed that the QS ion peak due to the incident neutrals could actually lie lower in energy, by ~20 eV. This indicated that the neutrals lost more energy in the surface collision than the corresponding ions. Similar measurements were carried out with neon and argon by Luitjens et al^{15,16}, of energies between 5 and 10 keV, also scattered from polycrystalline copper. In the case of neon, the QS peak resulting from neutral bombardment was again seen to occur at lower energies, by up to 24eV. No differences however were observed in the experiments with argon. These observed differences are thought to result from ionisation of the

incident neutrals during the violent collision, with further differential losses caused by differences in the electron stopping power of the ions and atoms during the incoming phase (with a greater power for the ion state).

A more thorough comparison of rare gas ions and atoms scattering was made by R.Souda et al^{101,102}, in which 0.2 to 2 keV Helium particles were scattered from 29 different target species, at $\theta=120^\circ$. Again only the scattered ion spectra were measured. The study showed, by high resolution spectral analysis, the peaks of conventional LEISS to consist of two resolvable components. The higher energy peak was attributed to ions that survived neutralisation during the surface collision. Whereas the lower energy peak was attributed to ions experiencing neutralisation on the incoming trajectory followed by subsequent re-ionisation in the collision step. Souda observed that the position in energy of the lower lying peak coincided precisely with the single peak observed when FAB was employed, which confirmed these conclusions. Measurements were made of the peak separation and also the threshold energy for the onset of the re-ionisation process. The study reveals an interesting relation between the threshold energy and position in the periodic table. The same threshold energies were calculated theoretically by Tsuneyuki et al¹⁰². A more detailed discussion of these results is given in chapter 3.

It was also shown by Souda et al¹⁰³ that LEISS executed with fast atom bombardment, referred to as Neutral Beam Ion Scattering Spectroscopy (NBISS) can also hold certain advantages in structure analysis. This can be appreciated by considering that ions which take part in shadowing and blocking, are the richest in structural information, but these ions also have the highest neutralisation probability. Conversely, ions which are not neutralised convey minimal structural information. NBISS avoids this problem as the possibility for neutralisation during the incoming stage is removed. Therefore, ions which are collected in NBISS have an angular dependence which is more sensitive to the structure of the surface. Differences between ion and fast atom scattering were also studied by Sullivan et al²⁶. In this case however the differences were observed in the neutral particle spectrum. In this case fast atoms scattering without suffering ionisation losses may also be detected. However, the interpretation of the results was additionally complicated as a polycrystalline sample was employed thus the spectra exhibited a large MS intensity. Without accounting for these effects the results indicated a greater loss in energy on the part of the incident ions. This was also considered to originate from the same electron stopping origins as

observed by Verhey¹⁰⁴.

Chapter III

Charge exchange and inelastic loss processes

In addition to offering the possibility of overcoming the limitations of conventional LEISS, it is also evident that ToFFASS is capable of unique investigation of the surface particle interaction process. This aspect of the instrument's capability is explored further in this chapter. Initially, to provide the necessary background for the proceeding discussion, a review of current knowledge of inelastic and charge exchange processes is presented.

3.1 Mechanisms for Charge Transfer.

Electrons may be transferred between the scattering primary particle and surface through a number of possible processes. The interaction is characterised by the electronic properties of the surface, such as the work function, and the ionisation energy and excitation levels of the incident particle. Figure 3.1 shows a metallic surface with the conduction band filled to the fermi level and the localised potential well of the approaching particle. Within this framework there are a number of possible electron transition processes. The most important processes being Auger neutralisation and resonant exchange. Quasi resonant exchange between a core level of the surface and an aligned vacant level of the projectile and other ionisation processes are also possible. Radiative neutralisation has a very small probability and so will be excluded from further discussion. The final charge state is determined by the product of probabilities of the combining processes. The whole spectrum of processes may be possible for certain conditions, which is true for example of He^{2+} interacting with a Pb surface¹⁰⁵. It should be noted that the preceding discussion is solely concerned with the interaction of particles of sub-fermi velocities, as greater velocity requires a fundamentally different treatment of the inelastic interaction¹⁰⁶. Discussion is also restricted to quasi singularly scattered particles, as the neutralisation constants of multiply scattered ions are dependent on the precise trajectory of the scattering particle, and therefore would involve a detailed calculation of the ion trajectory. Secondly, since the multiply scattered particles are neutralised with very high efficiency, these trajectories yield little or no information about the neutralisation process.

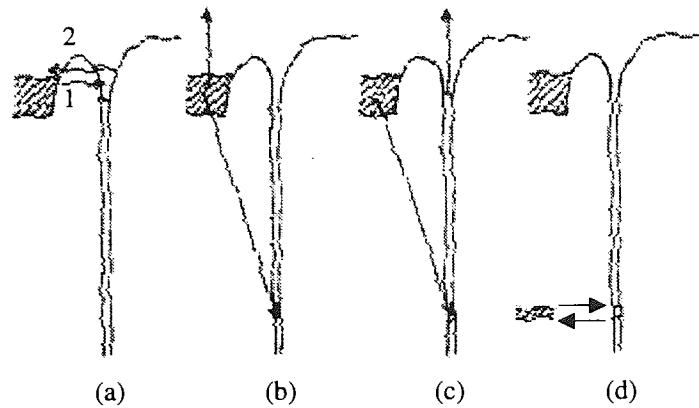


Figure 3.1 - Schematic showing the various possible processes by which an electron may be transferred between a metallic surface and the localized potential well of a scattering ion. (a) resonant charge transfer, (b) Auger neutralisation, (c) Auger de-excitation, (d) quasi-resonant charge transfer.

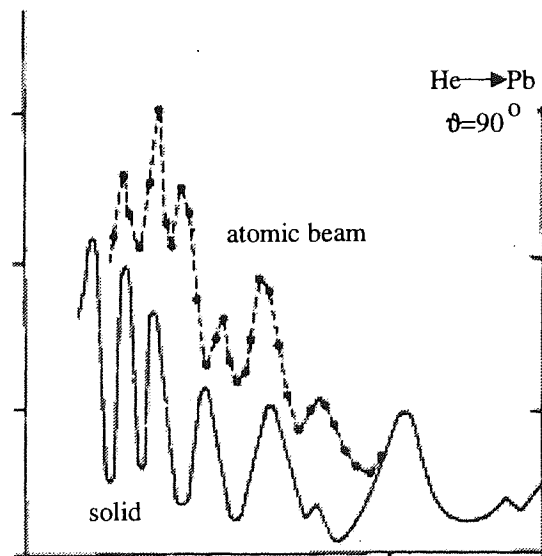


Figure 3.2 - Oscillating ion yields exhibited by He^+ scattering from Pb, arising from qRN between the Pb 5d and He 1s states. Solid line - (a Pb surface), Dashed line (atomic beam). After Zartner et al¹¹⁴

3.1.1 Auger Neutralisation (AN)

Auger neutralisation is a two electron process, possible when the ionisation energy E_i of the projectile is more than twice the work function, ϕ , of the surface, and AN dominates other neutralisation processes for many projectile-target combinations. The process proceeds by a valence electron neutralizing the projectile ion by tunnelling through the potential barrier, from the surface into the potential well of the projectile. This electron subsequently falls down to a deeper lying vacant state. A second valence electron must take up the excess energy of the first in order to conserve momentum. This electron is emitted from the surface as a secondary electron, and carries information of the band structure and density of states of the surface region, giving rise to the INS technique. The range of the Auger transition process is determined by overlap of the wave functions, which is given approximately by the sum of the radii of the electron orbitals of the projectile and the valence orbital of the surface atom, $\sim 2 \text{ \AA}$.

3.1.2 - Resonant Neutralisation (RN) and Resonant Ionisation (RI)

Resonant charge transfer refers to the process of electron tunnelling between the potential well of the surface valence band and a hole state of the scattering particle. The transfer probability is determined by quantum mechanical tunnelling probability. RN, the transfer of an electron from the surface to a projectile ion, is possible whenever a vacant energy level of the scattering particle is straddled by or lies close to the valence band. If the ionisation potential coincides with the Fermi level, the reverse process of RI is also possible. However, if the vacant level lies lower than the Fermi level tunnelling is limited to the neutralising transition only, and the process is essentially one way. Both transitions involve no loss or gain of energy on the part of the scattering ion, however an electron retained by the scattering particle will reside in an excited state on leaving the collision site, ultimately decaying to the ground state; in doing so, emitting the characteristic emission line of the atom^{107,108}. Both the RN and RI process can take place within a region ~ 5 to 10 \AA of the surface.

Atomic energy levels of the surface atoms and incident particle tend to shift and broaden throughout the duration of the collision, which can be viewed as the formation of a temporary 'surface molecule' over this period. These changes result directly from valence electron interaction and

Hiesenberg's uncertainty principle. It is a simple matter to calculate energy broadening due to the uncertainty principle, which is ~ 1 eV for a 1 keV He ion, assuming an interaction time of $\sim 10^{-15}$ s. A full quantitative theoretical solution however is very challenging: the perturbation of levels resulting from electron overlap requires a many body and time dependent treatment. However such calculations are important for the fundamental understanding of the interaction process as energy level shifts and broadening can dramatically increase electron exchange transition probabilities.

Favourable conditions for resonant exchange are found in the scattering of alkali ions and hydrogen ions from most metal surfaces. Here the vacant ground state of the ion coincides with the fermi level and RN and RI processes dominate, leading to a neutralisation probability which is much lower than that of noble gas ions. In such cases other processes may be neglected. Experimental measurement of ion survival probabilities were made by Algra¹⁰⁹ for lithium, sodium and potassium ions scattered from a Cu(100) surface, which has a work function, ϕ of 4.6 eV. The ionisation potentials are 5.39 eV, 5.14 eV and 4.34 eV respectively, corresponding to the measured probabilities of 60%, 75% and 99% respectively. These values were found to be relatively insensitive to the ion trajectory. Thus the ion fractions are much greater and less uncertain than those of noble gas ions, and as previously stated, alkali ion scattering is sometimes used as an alternative to ToF analysis. However, as shown by Overbosch¹¹⁰ and Kimmel¹¹¹, this approach is limited to surfaces with a spatially homogeneous work function.

A theoretical treatment of resonant processes was given by Nørskov¹¹², who developed the following expression for neutralisation probability:

$$P(E) \propto \exp [-pC_1(E_i - e\phi + C_2)/C_3v_{\perp}] \quad -(3.1)$$

The constants C_1 , C_2 and C_3 are dependent upon the position and width of the localized alkali ion energy levels in the collision vicinity, and E_i is the ionisation potential of the scattering particle.

3.1.3 Quasi Resonant Neutralisation - qRN

Quasi Resonant Neutralisation is found to be important in a number of specific ion-target combinations, for example helium scattering

from Ga, Ge, As, In, Sn, Sb, Tl, Pb and Bi. Unlike other mechanisms qRN is a nonadiabatic two way resonant process, and is an ion-atom interaction rather than an ion-surface interaction, as shown by experiments employing a Pb atom beam as the target species¹¹³. The process is possible when a core level of a surface atom aligns with a vacant core level of the projectile ion. If the two interacting particles had sufficient time to establish equilibrium, the incident particle would always be left in the neutral state. However, in the brief time interval of the collision the electron oscillates between the two resonant states of the collision complex, and the projectile may leave the surface in either state. qRN may be identified by the strongly oscillating structure in the ion intensity when plotted against the inverse of the projectile ion velocity, see figure 3.2, which is shown after Zatner et al¹¹⁴. The process can be described theoretically by Landau-Zener type charge exchange effects^{105,115,116} and the periodicity of the oscillations can be predicted by eq 3.2¹¹⁷, where $\Delta V(r)$ is the potential energy difference between the He^+-Pb^0 interaction and the He^0-Pb^+ interaction.

$$P_{osc} = \sin^2[(1/hv_{\perp})\Delta V(r)dr] \quad -(3.2)$$

P_{osc} is seen to be an oscillating function of the time the ion spends in the vicinity of the surface, which is proportional to v^{-1} . A classification of target elements was made by Rusch and Erikson¹¹⁸ based on such yield-velocity curves for He, Ne and Ar primaries. Elements exhibiting an oscillating ion yield were classified in group II. The oscillating yields of these elements further hinder the quantitative composition analysis in LEISS, however, they can also be exploited for the considerable electronic information they contain, which can be used as a 'finger print' for the particular atomic species. Thus the qRN process provides an additional method of element identification.

3.1.4 Re-ionisation - The Electron Promotion Mechanism

Souda and Aono^{101,102} have demonstrated experimental evidence of re-ionisation as well as neutralisation in surface collisions, and they attributed this to an electron promotion mechanism¹¹⁹. This mechanism can be understood in terms of the total energy curves of the two interacting particles as a function of their inter-nuclear separation distance, as shown schematically in figure 3.3. The two plots result firstly from He^0 and B^0 , and secondly from

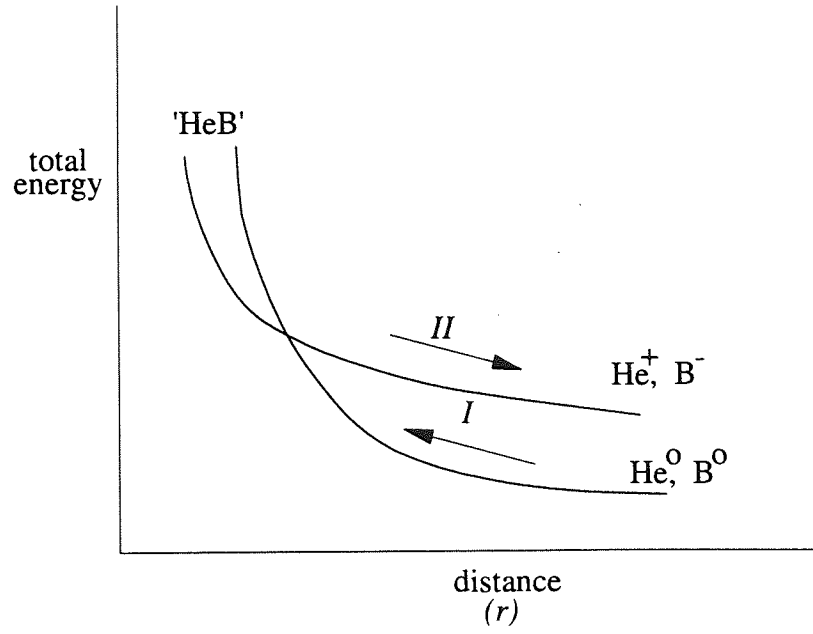


Figure 3.3 - Schematic figure showing the ionisation of He^0 by the electron promotion mechanism.

He⁺ and B⁻, where B is the surface target atom. As shown in the figure the two curves cross at a certain inter-nuclear separation. A helium neutral of sufficient energy approaching along curve I may exit along either curve. Exiting along the upper curve leads to ionisation through the following reaction:



where 'HeB' is a temporary 'quasimolecule'. Evidence of the reverse process has also been seen if a neutral enters along the top curve^{101,102}. The crossing of the two curves defines the boundary of the 'crossing region', which has a radius of $\sim 0.5 \text{ \AA}$. Inside the crossing region the molecular orbits evolve as a function of the internuclear separation. This evolution is determined by attractive binding between the nuclear charge and atomic electrons, short range repulsion between atomic electrons, and constraints imposed by selection rules and the Pauli exclusion principle. A method for calculating theoretical threshold energies and crossing radii, based on *ab initio* Hartree-Fock self-consistent calculations was developed by Tsuneyuki, Shima and Tsukada¹⁰². On the basis of these calculated results a number of factors were found to be influential for the occurrence of re-ionisation of helium: [1] the energy of the lowest unoccupied orbital of the target atom, [2] the occupation of the valence orbitals which strongly interact with the He 1s level [3] The strength of the He 1s and target core level antibonding interaction. The calculations which are based on an adiabatic assumption give unreliable results for heavier target atoms, although the authors concluded that a more realistic calculation is necessary for full understanding of the mechanism.

Experimental threshold energies for ionisation were measured by Aono et al¹⁰¹ for a range of elements, and a number of general observations resulted: [1] Experimental threshold energies were found to be very low for target elements in groups I and II of the periodic table and increase with the increasing number of electrons across the periods. This is thought to result from decreasing crossing radius of the quasimolecular energy level across each period. [2] Above the threshold energy the intensity of the re-ionised peak increases with increasing collision energy. [3] Threshold energies are greater for neon primaries than helium and greater still for argon. [4] Experimental threshold energies are generally in good agreement with the calculations of Tsuneyuki, Shima and Tsukada¹⁰². The study also concluded that crossing of the quasimolecular orbital energy levels is a prerequisite for ionisation, however other workers have reported evidence of ionisation below the

crossing threshold^{120,121}

Re-ionisation was not observed for helium scattered from Cu below 2000 eV, and at ~ 300 eV for helium scattered from silicon.

3.1.5 Re-ionisation - Autoionisation

Autoionisation provides a further mechanism, similar to that of electron promotion, for the re-ionisation of particles that are initially neutralised in the incident trajectory. The process was suggested by Grizzi et al¹²² in order to account for experimental data which could not be explained within the framework of the electron promotion mechanism; Grizzi reported anomalously large experimental ion fractions, values of up to ~ 70%, for the scattering of Ne⁺ from light target elements: Al, Mg and Si. Evidence of autoionisation transitions has also been demonstrated recently by Lacombe et al¹²³ in the case of He⁺ and Ne⁺ scattered from a Mg surface, and by Zeijlmans¹²⁴ for grazing incidence scattering of He²⁺ from a Cu(110) surface. Lacombe's experimental results indicate that Ne and Mg atoms form a $4f\sigma$ molecular orbit below a critical internuclear distance, which in turn results in the formation of a doubly excited neon atom (Ne^{**}(2p⁴3s²)). This excited state later decays in the vacuum to the ground state (Ne⁺ (2p⁵)). For the mechanism to be observable, the excited state must have a long enough lifetime so as to allow the neon atom sufficient time to travel away from the surface before decay. If this is not the case then re-neutralization on the outward trajectory would be possible. Autoionisation is currently under detailed experimental investigation through electron spectroscopy and ToF measurements by Lacombe et al. (Université Paris Sud)¹²⁵

3.2 Inelastic Energy Loss

Inelastic, or electronic energy losses of low energy ions travelling within a solid may originate from the wide variety of possible mechanisms:

- 1] Core level excitation and ionisation of either the target and projectile particles
- 2] Excitation of band and conduction-electrons
- 3] Direct kinetic energy transfer to target electrons.

Collectively these processes give rise to 'electronic stopping'. Above the ion

velocity threshold of $\sim 3 \times 10^6 \text{ m s}^{-1}$ ionisation cross-sections are much greater than neutralisation cross-sections, and so projectiles in this energy region become highly charged and lose a large fraction of their energy inelastically. However, at higher velocities still, within the Bethe-Block regime elastic losses decrease again. In this work consideration is confined to particles of sub-fermi velocities at which the collision velocity is much less than the thermal electron velocity of the target. Here valence electron interactions are dominant. Such losses contribute a small proportion of the overall loss, but cause a number of secondary processes, eg auger electron and photon emission. In most LEISS systems peak shifts due to electronic energy losses are comparable or smaller than the peak widths themselves and can generally be neglected. Typical values are 1-2% of the primary energy: a loss of $\sim 2\%$ of primary energy was measured for He^+ singularly scattered from $\text{Ni}^{126,127}$, and $\text{Si}(111)^{128}$ surfaces, and $\sim 1\%$ Ar scattered from a W surface⁴⁴. Losses due to excitation in the target atoms have been found to be target species dependent in a number of studies^{129,130}; the energy loss is proportional to the number of occupied valence states. For example losses of $\sim 8 \text{ eV}$ were observed for He scattered from Zr, which has only two valence electrons ($4d^2$) compared to no observed loss for He scattered from Zn, which has a full valence level. Ionisation by contrast can result in the largest inelastic loss, and where this takes place via the electron promotion mechanism the primary loses an energy given by the difference between its ionisation energy and the electron affinity of the surface, $\sim 20 \text{ eV}$.

A further loss mechanism may result from the image potential between an ion and a conducting surface: a charged particle travelling close to a conducting surface, irrespective of energy regime, experiences an interaction due to the image potential, which is a dominant force at large distances. If the charge of a particle is changed within the effective range of the image potential, either by ionisation or neutralisation, energy equal to the potential $V_{image}(r)$ will be lost or gained by the projectile. Calculations show however, that this effect can only introduce losses of a fraction of an eV, and therefore can be neglected in most circumstances.

3.2.1 Electron Stopping Models

A complete quantum mechanical description of electron stopping is not possible, and existing theoretical treatments fall into two categories; those in which the energy loss is calculated for each collision; for example Firsov¹³¹

and Oen and Robinson¹³², and those where the ion loses energy continuously as it proceeds through the solid, for example Lindard and Scharff¹³³, and Echenique¹³⁴.

The Firsov treatment is based on a Thomas-Fermi description of the atom, and thus assumes excitation of atomic electrons to be distributed throughout the atom. The energy lost in a single collision, Q_n is expressed in terms of Z_1 and Z_2 , v_o . The total energy lost by the scattered particle is obtained by summation over the total number of collisions, and is proportional to \sqrt{E} . A semi-empirical model, also including an impact parameter dependence, was developed by Oen and Robinson¹³², where Q_n , the energy lost in each collision is given by;

$$Q_n = (0.045kE^{1/2}/\pi a_f^2) \exp[-0.3R_o(b, E_o)/a_f] \quad -(3.3)$$

this expression is found to be more satisfactory for the description of light ions¹⁰⁴. Incorporation of eq. 3.3 into a MC simulation code¹³⁵ was also found to give better agreement with experimental data than the Firsov model¹³⁶. Other more sophisticated single atom models have also been developed such as those which are based on the Hartree model of the atom.

All models lead to an expression for the electron stopping cross-section, S_e , given by

$$S_e = K(E)(1-\alpha) \quad -(3.4)$$

where α is dependent on the density of the target and is typically 0.1¹⁰⁴. These studies also suggest that K is dependent on the charge state of the primary particle, which may change as the scattering particle proceeds along its trajectory. Although experimentally there is agreement with the prediction that the stopping cross-section is proportional to \sqrt{E} there are two residual problems with this. Firstly, a straight line plot of energy loss v \sqrt{E} does not intersect the origin as expected. Secondly there are a small number of target species which do not follow the \sqrt{E} dependence, for example Si and Ge¹³⁷.

Modes which assume the solid to be a continuous loss media also predict a \sqrt{E} dependence. The model of Lindard and Scharff, which describes the solid as a uniform electron gas. The same dependence is also found by more recent theoretical treatments, based on advanced solid state models¹³⁸⁻¹⁴¹. In this case the solid is treated as a continuous dielectric, in which the electronic collisions are treated as electron hole pair excitations. The

excitations losses are calculated in terms of the plasma frequency, ω_o and charge density, ρ , and Q is expressed as

$$Q = \gamma \nu L \quad \text{-(3.5)}$$

where γ is a 'friction' coefficient and L is the total trajectory length, defined rather arbitrarily as the trajectory length within a distance d_s above the topmost ion cores of the surface, where $d_s \sim$ half an interlayer spacing. The model also distinguishes between charged and neutral particles, where the charged particle friction coefficient γ^+ is greater than that of the neutrals, γ^0 .

This model has been primarily used to predict energy losses of particles scattering through small scattering angles and incident to the surface at low angles, $\theta < 5^\circ$, where good agreement has been found¹⁴². In such experiments, L is much longer than the mean distance for neutralisation, so the projectile for most of its trajectory is a neutral. At these low scattering angles processes such as electron promotion and auto-ionisation are not probable.

Acceptance of any continuum model leads to an expression for the total energy loss, $\Delta E_{\text{inelastic}}$ of the scattered ion, which is proportional to the length of the particle's trajectory in the vicinity of the surface. So for an ion incident to the surface at an angle θ , and scattered through an angle ϑ , $\Delta E_{\text{inelastic}}$ is given by:

$$\Delta E_{\text{inelastic}} = k(E) [1/\sin\theta + 1/\sin(\vartheta - \theta)] \quad \text{-(3.6)}$$

this is found to be in reasonable agreement with experimental results¹⁰⁴. However objections to the continuum model have been raised, as the notion of a definite trajectory length is rather undefined for particles scattered from single top layer locations. Additionally, the notion that energy lost in each collision can be 'averaged out' is rather questionable for ions that are scattered from the surface by a SBC.

3.3 Development of Parametric Adiabatic Models

The neutralisation models described in the following sections are based on the pioneering work of Hagstrum, who developed a description of the neutralisation processes through the observation of the energy distribution of ejected electrons, as a function of incident ion energy. The description assumes

the process to be adiabatic, which is only strictly valid at lower particle velocities. The adiabatic model assumes that a charge equilibrium is reached between the surface and the projectile, which is not possible in practice because the collision time is too short. However, the adiabatic model does have validity in the description of Auger and resonance processes^{116,143} in the sense that these processes do not involve energy exchange between electronic and nuclear motion. A further feature of Hagstrum's model is that transitions are assumed to take place with a homogeneous conduction band. These assumptions lead to an expression for the neutralisation rate which is proportional to the overlap integral of the wavefunctions of the interacting particle and the surface. To a good approximation this leads to a neutralisation rate which is proportional to the exponential of the inter-nuclear separation:

$$R_n = Ae^{-as} \quad -(3.7)$$

where A and a are the neutralisation constants for a specific incident ion and metal surface and s the distance from the surface. Eq 3.7 gives no consideration to the ionization and quasi resonant exchange processes, although some attempts have been made to introduce such processes into the model on an 'ad hoc' basis these have little theoretical foundation. In general therefore adiabatic models provide an approximate description of the surface charge exchange process. In addition to the adiabatic assumption, further approximations must also be made to obtain an analytical expression for the neutralisation probability. However, adiabatic models remain prominent in the literature for the description of neutralisation in LEISS experiments, as they present the best possibility for comparing calculated and experimental data, and as a basis for the incorporation of charge exchange effects into simulation programmes. The models discussed below share the additional common feature that they parameterise the neutralisation probability into a functional form containing a number of adjustable parameters, which are found empirically by fitting to experiment data.

3.3.1 The Hagstrum's Model

The most simple evaluation of eq 3.7, as shown by Hagstrum is by integration over asymptotic entrance and exit trajectories:

$$r(t) = r_o + v_{in}t, (t < 0), r(t) = r_o + v_{out}t, (t > 0) \quad -(3.8)$$

where r_o is the intersection of the asymptotes. This leads to:

$$P = \exp(-v_o/v_{\perp}) \quad -(3.9)$$

where P is the neutralisation probability, v_o is the characteristic velocity of the order of 10^7 cm s⁻¹ and dependent on the ion species and target, and v_{\perp} is the velocity component of the ion perpendicular to the surface. This simple evaluation only has relevance in the case of pure metal surfaces. For such conditions eq 3.9 gives reasonable qualitative agreement between experiment and simulation^{11,143-145}. If integration is performed along the real trajectories the exponential of eq 3.9 must be multiplied by a linear polynomial¹⁴⁴.

3.3.2 Godfrey Wodruff Model

A modification to Hagstrum's model, to describe the charge transfer of projectiles scattered from surfaces not exhibiting a continuous electron distribution, was made by Woodruff and Godfrey^{146,147}. The basic assumptions of the Hagstrum model are retained, but the interaction was assumed to take place within a sphere surrounding the target atom. Accordingly the neutralisation rate is expressed in terms of the inter-nuclear separation distance rather than the distance from the surface. In this case the neutralisation rate is given by:

$$R_{at}(t) = A_a \exp -(a_{at} | r(t) - r_{at} |) \quad -(3.10)$$

where r_{at} denotes the position vector of the target atom, $r(t)$ is the position of the projectile, and A_a and a_{at} are the empirically determined neutralisation constants. The subscript "at" indicates that neutralisation takes place at an individual atom site. This modification results in some important differences. Firstly the latter is able to account for experimentally observed anisotropies in the neutralisation probability, and secondly it is possible to apply the model to composite surfaces. For example, experimentally determined data of He⁺ scattering from Ni and Cu surfaces, was used to obtain a parameterised expression for the neutralisation probability. From this separate neutralisation constants were obtained for the metallic and absorbed oxygen atoms^{146,147}.

Similar to Hagstrum's expression, the ion survival probability P is given by integration of the neutralisation rate over the collision trajectory.

$$P = \int \exp[R_{at}(r(t))dt] \quad -(3.11)$$

An exact analytical solution of equation 3.11 is possible only where the projectile ion is assumed to pass the target atom with a straight line trajectory, given by $r(t) = s + v_{in}t$, without deflection or change of velocity. This approximation yields the following expression for the neutralisation probability:

$$P_{at} = \exp [2v_{at}/v \text{ as} K_1(as)] \quad -(3.12)$$

where K_1 is a modified Bessel function of the second kind. This is a crude simplification of the projectile's trajectory. A more accurate approximation can be made by the integration over the asymptotic trajectories, however this cannot be performed exactly. If appropriate approximations are made the ion survival probability is expressed as:

$$P_{at} = \exp (-v_{at}/v_{in} - v_{at}/v_{out}) \quad -(3.13)$$

where $v_{at} = A_d/a_{ar}$. Note that equation 3.13 is of the same form as equation 3.9, with v replaced with its perpendicular component.

Equation 3.13 can be replaced by a more exact expression by integration of eq 3.11 over the true trajectory. A method was demonstrated by Richard and Eschebacher¹⁴⁸, using a projectile trajectory calculated assuming a Thomas-Fermi-Moliere (TFM) inter-atomic model potential. Again by introducing appropriate approximations to perform the integration a more exact expression for P can be obtained, from which it can be seen that the trajectory strongly influences the calculated ion fraction, through both the distance of closest approach and the radial velocity. A number of further models have been suggested in the literature¹⁴⁹⁻¹⁵¹, which are based on the solution of equation 3.11. All these models rely on an empirical determination of the neutralisation constants.

One of the shortcomings of the adiabatic rate equation is the over prediction of the neutralisation rate at small ion-atom distances, as pointed out by Engelmann et al¹⁵². In an attempt to correct this problem Engelmann suggested the introduction of a constant value of $R_{at}(r)$ below a minimum internuclear separation. This empirically based modification yields a new

neutralisation constant, s_{at} .

3.3.3 Verbist Model

A more generalized adiabatic treatment was proposed by Verbist et al¹⁴⁸. In this model the Hagstrum and Woodruff expressions represent the extreme limiting cases, with validity restricted to specific conditions. In this new treatment the projectile ion is considered to interact with a number of scattering centres simultaneously. The neutralisation rate of the individual interactions is given by eq. 3.11. Based on this description, an expression is obtained for the total neutralisation rate due to each species, j contained within the unit cell. Significantly, the expression is dependent on all three spatial co-ordinates of the projectile, within the immediate surface region. As before it is possible to arrive at an analytical expression for the ion survival probability when the asymptotic trajectory approximation is made, which can be expressed in the following form;

$$P^+ = \exp -\sum_{j=1 \text{ to } N} (f_j) \quad \text{-(3.14)}$$

where f_j is the contribution from the j th atom, summed over all lattice positions. The above expression also contains a number of neutralisation constants which must be determined empirically. Eq. 3.14 can be expressed in such a way so that the neutralisation constants have useful physical meaning.

For example, the constant ρ_{at} gives the radius of a sphere centered on each lattice atom inside which neutralisation may occur. In the limit $\rho_{at} \gg a$, as is typically the case for metal surfaces, the spheres will overlap and the neutralising surface will appear homogeneous to the projectile ion. In this case it can be shown that eq. 3.14 becomes equivalent to eq. 3.9 the continuum model of Hagstrum. For the opposite case, $\rho_{at} \ll a$, the spheres appear well separated, and eq. 3.14 tends to the Woodruff Godfrey expression. Models such as Verbist's therefore extend the validity of the simple adiabatic model to a wider range of surfaces, particularly those consisting of a regular lattice, where the surface electron density is not homogeneous due to chemically different atoms in the unit cell. It has been shown that eq. 3.14 can be fitted to experimental data to determine the constants A_a , a_{at} for the individual atoms composing the surface^{153,154}.

Verbist et al also suggested an analytical expression for P , which attempts to account for electron promotion by the addition of a term in the

collision integral¹⁵⁵.

3.4 Quantum Mechanical Treatments

Theoretical calculations of the ion fractions provide an alternative to the empirical models described above, and have received significant attention in the literature. The complete theoretical description, however, is extremely complex and an 'a priori' solution of surface neutralisation is not currently possible. A comprehensive discussion of such theoretical calculations therefore is not relevant to this work, and only a basic revue of present theories will be given.

The most widely accepted description of the ion solid system is by means of a time-dependent Anderson-Newns model Hamiltonian. In this case the two interacting particles are treated as two 'hydrogen like' particles, that is a projectile ion, A^+ , and target atom B, comprising an ionic core, B^+ , and a valence electron. Within this simple framework four collision events are possible:

1] Elastic scattering, which involves no exchange of electron or energy



2] Excitation of the target atom, which does not involve the exchange of an electron but energy is lost inelastically by the primary ion.



3] Ionisation of the target atom, which also involves inelastic energy loss by the primary ion.



4] Neutralisation, involving the transfer of an electron from the target atom to the primary ion. There are a number of mechanisms by which this reaction may proceed, and the energy lost by the primary is mechanism dependent.



All four of these reactions are coupled, and therefore quantum theory treatments of single channel cross-sections is not strictly valid. From a quantum mechanical view, all these reactions depend upon the relative spatial positions of the electronic wavefunctions of the two particles. The system is described mathematically by the time-dependent, non-relativistic Schrödinger equation:

$$H\Psi = E\Psi \quad (3.19)$$

where H denotes the Hamiltonian operator, given by the sum of the kinetic and potential energy operators:

$$H = T + V \quad (3.20)$$

and E represents the total energy.

As already stated, the surface scattering process may involve a number of different mechanisms. Theoretical consideration also shows that many states of the atom may be involved simultaneously in the coupling. This being so, a 'many channel' description must be adopted, for which the 'hydrogen like' atom approach is inappropriate. In this case the full theoretical treatment becomes a many channel and many body problem. Direct solution of such a model Hamiltonian is not possible, without the introduction of many crude simplifying approximations.

Several theoretical descriptions of ion surface neutralisation based on the Anderson model Hamiltonian have been developed, and these have been extensively reviewed by Newns et al¹⁵⁶. A typical time dependent Hamiltonian for a three particle system is given in eq 3.21. This is a 'quasi-ab-initio' model, in which electron spin is neglected. The three terms in this case relate to the primary atom, the substrate and their interaction, respectively.

$$H(t) = \epsilon_a(t)n_a(t) + \sum_k \epsilon_k n_k(t) + \sum_k [V_{ak}c_a^\dagger c_k + \text{H.c.}] \quad (3.21)$$

The energy of the vacant level, $\epsilon_a(t)$, has a time dependency which is related to the substrate separation, $z(t)$. $n_a(t)$ and $n_k(t)$ are density operators for the primary and substrate, given by the creation and annihilation operators $c_a^\dagger c_a$ and $c_k^\dagger c_k$. Examples of such operators for a linear chain substrate is given by Newns¹⁵⁷. The particular 'channel' represented and therefore the interaction

mechanism is determined by the interaction matrix, V_{ak} , which must be first calculated using the Self Consistent Field (SCF) method. Once the Hamiltonian for a given system has been constructed solutions may be generated by the methods described by Bloss-Hone¹⁵⁸ and Brako-Newns¹⁵⁹, using time dependent Hartree-Fock theory. Under this framework nonadiabatic as well as adiabatic processes may be treated.

Muda-Newns type calculations require a number of apparently crude approximations (tight binding surface model, linear ion-surface interaction etc). However, agreement has been found with experiments scattering results; He⁺ from Si¹⁶⁰ and Cu¹⁶¹. Although a many electron approach has been proposed by Sulston et al¹⁶², the significant restriction that only single mechanisms can be treated remains.

There have been few reports where more than one mechanism is considered on an equal footing, one such a study was made by Snowdon et al¹⁶³ in the adiabatic limit, in which both the Auger and resonant mechanisms were treated together, in the scattering of H, He, and Li from a Al surface. The calculation demonstrated that when both resonant and Auger coupling are energetically possible, electron band and atomic wavefunction distortion must be modelled accurately if realistic results are to be expected. Thus for such conditions all possible coupling mechanisms must be considered simultaneously.

A less computer intensive approach for calculating transfer probabilities than solving the Hamiltonian was suggested by Tsuneyuki and Tsukuda¹⁰². This approach is based on the Landau-Zener¹⁶⁴ formula to calculate the probability of electron promotion. The transition is treated as a one-way nonadiabatic process, where the ionisation probability, P_i is given by:

$$P_i = 2Fp(1-p), \quad -(3.22)$$

and $p = \exp(-v_l/v)$, v_l is a constant and v is the relative velocity of the projectile given by $(2(E-E_{th})/m)^{1/2}$, where E_{th} is the crossing point threshold energy. The above formula was used to calculate the energy dependence of P_i . Similar calculations were made by Muda and Newns, who found the same dependency, but with a smaller maximum value for the ionisation probability. The Landau-Zener approach is sufficiently simple to be used in simulation calculations, as shown by Pierson et al¹⁶⁵ in the simulation of He→Cu,Au,W. The inclusion resulted in better comparison with experiment data in terms of

background, peak width and position, although the validity of the Landau-Zener approach could not be fully assessed.

3.5 Verheys three stage model

Considering the model of charge exchange collisions suggested by Verhey et al^{104,120,135}, in which the scattering particle trajectory is divided into three distinctly localised phases, the final charge state of a scattered particle is determined by charge transfer probabilities associated with the incoming path, the 'violent' collision step and the outgoing trajectory. This is illustrated in figure 3.4, where Auger and resonant mechanisms may act in phases I and III, and the associated probabilities can be calculated from either eq 3.9, 3.13 or 3.14. If the collision energy is greater than the threshold energy then ionisation may take place during the violent collision step. The boundary between the two regions is determined by the crossing point radius. Within the framework of the model neutralising transitions are also permitted within phase II.

Clearly Verhey's model simplifies the collision for the purposes of a mathematical description. The notion of spatial localisation is taken a stage further in the model proposed by Aono and Souda¹⁶⁶, in this case the trajectory is considered in five distinct phases. AN, valance level RN, RI and ionisation by electron promotion are all assumed to be possible. The spatial regions in which these processes are deemed to occur are shown in figure 3.5. Region A, inside which RI ($\text{He}^* \rightarrow \text{He}^+$) and the reverse process, RN ($\text{He}^+ \rightarrow \text{He}^*$) are deemed possible extends to a distance of $\sim 5\text{-}10\text{\AA}$ from the topmost ion cores of the surface. AN is considered possible within radii $\sim 2\text{\AA}$ from the top layer atom centres, region B. As shown in the figure the boundary between A and B may contain significant corrugations. Region C, as in the Verhey model is defined by the minimum distance for the formation of molecular orbits, $R_c \sim 0.5\text{\AA}$, thus the three stages of Verhey's model are extended to five.

3.6 Experimental Investigation of Charge Exchange

3.6.1 Measurement of charge exchange probabilities

A recurrent problem in the investigation of charge exchange processes taking place during particle-surface collisions is the difficulty in making direct comparisons between experimental and theoretical results. The difficulty arises due to the large number of possible processes which may

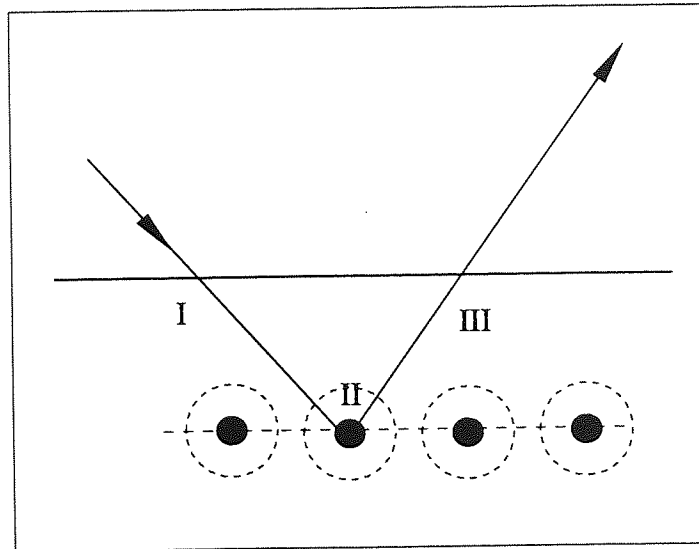


Figure 3.4 - A Schematic of the charge exchange model of surface collisions suggested by Verhey et al ^{104,120,135}

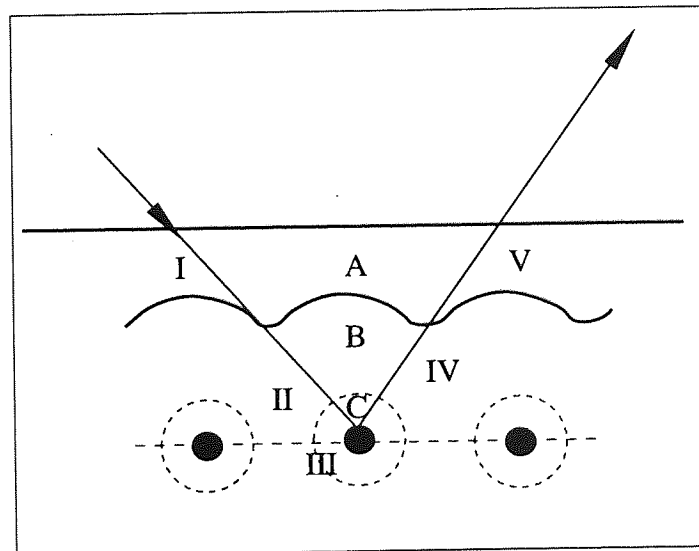


Figure 3.5 - A Schematic of the charge exchange model suggested by Aono and Souda¹⁶⁶

occur in various sequences. A more detailed discussion of this problem can proceed in terms of the Verhey model, which is generally thought to be valid, with some exceptions. The four processes are assigned the following probabilities:

- f_1 - neutralisation probability in stage I
- p_n - neutralisation probability in stage II
- p_i - ionisation probability in stage II
- f_2 - neutralisation probability in stage III.

and in this framework the final charge state of the scattered particle may be gained through one of a number of possible sequences of the four processes. This is shown schematically in figure 3.6, where it can be seen that a incident neutral may proceed along two paths in which it leaves the surface in the neutral state and one as an ion. A greater number of paths are available to an incident ion; a scattered ion may result from two paths, whilst a neutral may result from four.

Early experiments by Verhey et al, employed an instrument capable of Neutral Scattering Spectroscopy (NSS) with a 3 to 10 keV helium beam scattered from Cu(100) at a fixed scattering angle of 30° ¹⁰⁴. Although primary bombardment was due to either neutrals or ions, only the scattered ion spectrum could be detected. In terms of the above probabilities, the scattered ion yield due to fast atom bombardment is given by:

$$P_i^o = p_i (1-f_2) \quad \text{-(3.23)}$$

as can readily be seen from figure 3.6. The superscript 'o' indicates that the primary beam is neutral and the subscript 'i' indicates measurement of scattered ions. Verhey's experiment did not allow P_i^o to be measured. Due to the limitations of the instrument only the absolute ion intensity, I_i^o was assessable, which is given by:

$$I_i^o = [I_o A T(\Omega, \theta, E) \Delta\Omega (d\sigma/d\Omega)_i G N_i] p_i (1-f_2) \quad \text{-(3.24)}$$

Verhey was able to extract the probability f_2 by making differential measurements of I_i^o with respect to the incident polar angle, θ . This was possible within the specular reflection region as all terms within square brackets can be considered independent of θ , and the ionisation probability p_i

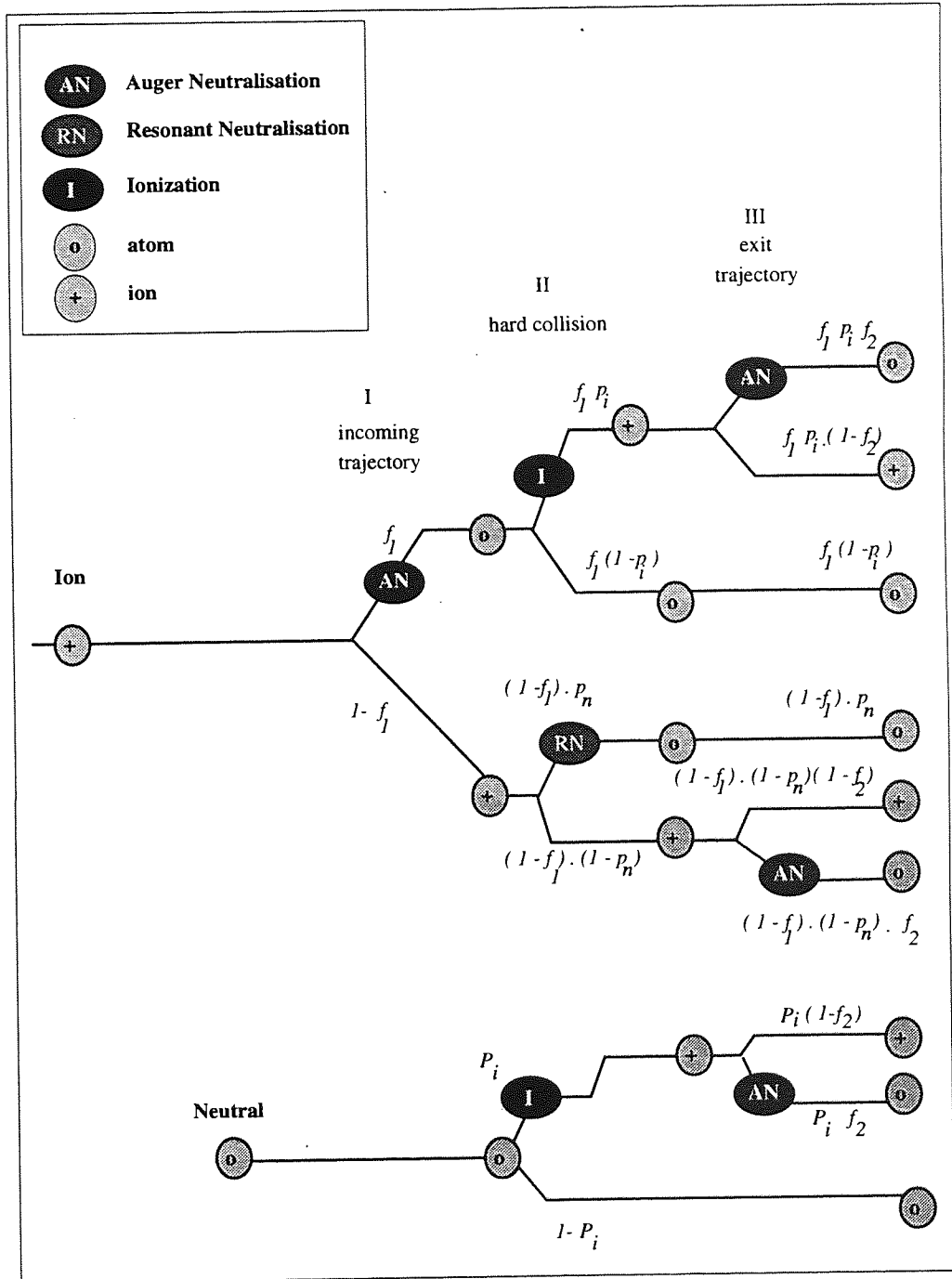


Figure 3.6 - Possible sequences of charge exchange during the scattering event. Four processes are assumed: (1) neutralisation - phase I, (2) ionisation - phase II, (3) resonant neutralisation - phase II, (4) neutralisation - phase III. The individual probabilities for these processes are f_j , p_n , p_i , f_2 respectively.

of the close collision was considered to be independent of θ . This implies the relationship:

$$I_i(\alpha-\delta)=I_i(\alpha+\delta) \quad -(3.25)$$

where $\alpha = \vartheta/2$ and $\delta=|\alpha-\theta|$. The following expression can be derived from eq 3.25 and Hagstrum's relation, (eq 3.9).

$$\ln[I_i^o(\alpha-\delta)/I_i(\alpha+\delta)] = v_c/v_o \cdot 2\cos\alpha \cdot \sin\delta/(\sin^2\alpha-\sin^2\delta) \quad -(3.26)$$

Thus by measuring I_i as a function of θ with both the incident and detected beams fixed in the plane normal to the sample surface, v_c/v_o and f_2 may be determined experimentally by NSS. The ionisation probability, p_i , may only be determined experimentally if the differential elastic scattering cross-section and instrumental terms are known. This method of determining p_i however is not very reliable as the instrumental terms usually carry a large uncertainty. In the above experiments v_c was determined to be $\sim 2 \times 10^{-5}$ ms⁻¹ and found to be a slowly increasing function of primary energy, (increasing by 15 % from 4 to 10 keV). p_i was found to vary from ~ 2 % at 2 keV to ~ 30 % at 10 keV. It was not, however, possible to determine the probabilities f_2 and p_n , and so the validity of the three stage model could be experimentally verified by NSS arrangement of Verhey.

Luitjens et al^{15,16} also employed a ToF analyser, in an attempt to verify Verhey's model. Here, the scattered neutral intensity, I_n , could be measured, although only a charged primary beam could be employed. Experiments were conducted for neon and argon ions (5 to 10 keV) scattered from Cu(100) at $\vartheta=90^\circ$. The instrument also provided a primary neutral beam, however, in this case the ToF analyser could not be used, and only I_i^o could be measured by a ESA analyser. With a charged primary beam Luitjens was able to measure both I_i^+ and I_n^+ and thus determine the ion fraction, P_i^+ , which is given by:

$$P_i^+ = I_i^+ / (I_i^+ + I_n^+) \quad -(3.27)$$

In terms of Verhey's model P_i^+ is given by:

$$P_i^+ = (1-f_1)(1-f_2)(1-p_n)+f_1(1-f_2) \cdot p_i \quad -(3.28)$$

and the neutral fraction, P_n^+ , is given by:

$$P_n^+ = 1 - P_i^+ \quad -(3.29)$$

However, Luitjens was not able to measure the probabilities P_n^o and P_i^o . It was possible only to measure I_i^o which is given by:

$$I_i^o = CP_i^o = C(1 - f_2)p_i \quad -(3.30)$$

where C is a constant of the experimental conditions, which must be known if P_n^o is to be determined. Thus Luitjens was not able to evaluate the individual probabilities, f_1 , f_2 , p_n , p_i and again Verhey's model could not be rigorously verified.

A further investigation of Verhey's model was conducted by MacDonald et al¹⁶⁷, in which the neutralisation probability of stage III, f_2 , was measured. This was achieved using a three-dimensional angular resolved energy spectrometer in an otherwise standard LEISS instrument. The three-dimensional analyser consisted of a standard ESA analyser which could be rotated around the target sample within the vacuum chamber. By exploiting this feature, the scattered intensity I_i^+ could be measured as a function of the take off angle, ϕ , with the angles θ and ϑ maintained constant. The experiment was conducted by rotating the ESA in the plane perpendicular to the primary beam. Thus the measured singularly scattered intensity is given by:

$$I_i^+ = [I_0 A T(\Omega, \theta, E) (d\sigma/d\Omega)_i N_i G]. P_i^+ \quad -(3.31)$$

The terms inside the square brackets can be assumed to be independent of ϕ for a non crystalline surface, as shadowing and blocking effects cancel, so in the absence of charge exchange effects, the scattered intensity can be assumed isotropic. Verhey's model predicts:

$$P_i^+ = (1-f_1)(1-f_2)(1-p_n) + f_1(1-f_2) \cdot p_i \quad -(3.32)$$

As ϑ and θ remained constant in MacDonald's experiment the probabilities p_n and p_i , consequently also remained constant, and P_i^+ is given by:

$$P^+_i = a_1(1-f_2) \quad \text{-(3.33)}$$

where a_1 is a constant dependent on the experimental conditions; E_o , ϑ and θ . In the case of a pure metallic surface the dependence of I^+_i on ϕ is given by Hagstrum:

$$I^+_i(\phi) = a_1(1 - \exp(-v_c/v_2 \cos\phi)) \quad \text{-(3.34)}$$

Thus f_2 and v_c can be found by making differential measurements of $I^+_i(\phi)$ with respect to ϕ . Macdonald et al made such measurements for Ne and He ions scattered from polycrystalline nickel. v_c was found exhibit fine structure when observed as a unction of E_o , giving evidence of RCT rather than Auger transfer. This work also showed f_2 to have little dependence on surface parameters such as surface work function, conduction band width, or fermi energy, for the above system however, due to limitations of the instrument no decisive conclusions concerning the validity of Verhey's model could be offered.

In what follows, the features of an instrument required for comprehensive verification of Verhey's model are described. Firstly it must be possible to measure both P^+_n and P^o_n . This must also be coupled with the ability to vary the incident and take off angles independently. It is shown below that these capabilities make all four individual probabilities of the Verhey model experimentally assessable. As previously shown P^+_n and P^o_i can be expressed in terms of the individual probabilities summed for all possible pathways of figure 3.6. In the case of neutral bombardment, the ion fraction is given by:

$$P^o_i = p_i f_2 p_i \quad \text{-(3.35)}$$

which is the total ionisation probability of the surface collision. The neutral fraction is given by:

$$P^o_n = (1 - P^o_i) = (1 - p_i) + f_2 \cdot p_i \quad \text{-(3.36)}$$

and can be seen that equations 3.35 and to 3.36 are equivalent. In the same manner an expression for the neutral fraction, P^+_n , in the case of ion

bombardment, is given by:

$$P_n^+ = p_n + f_1(1-p_i) + f_2(1-p_n) + f_1 f_2 (p_i + p_n - 1) \quad -(3.37)$$

which is the total neutralisation probability of the surface collision. The ion fraction is given by:

$$P_i^+ = (1-f_1)(1-f_2)(1-p_n) + f_1(1-f_2) \cdot p_i \quad -(3.38)$$

The sum of eqs 3.37 and 3.38 is unity, and thus again the two equations are equivalent. Thus the problem is reduced to two equations containing four unknown probabilities: f_1 , f_2 , p_i and p_n . It is, therefore, not possible to solve these equations for f_1 , f_2 , p_i and p_n directly. However, if angle resolved measurements were to be made, f_1 and f_2 could be determined independently, so reducing the problem to two simultaneous equations with two of unknowns, and therefore yielding solutions for p_i and p_n .

Using the approach of Verhey, f_2 can be determined by employing a primary neutral beam and making differential measurements of I_i^o wrt θ , with the incident and detected beams fixed in the plane normal to the sample surface. This approach requires 1 axis sample rotation only, however, f_1 may not be determined by this method. Whereas using an approach of the manner of Macdonald's would also allow f_1 to be determined. However, this would require rotation of ToF detection system around the sample. Alternatively, independent θ and ϕ variation could be achieved by appropriate orientation of the sample to the incoming and outgoing beams. In either case, differential measurements of I_n or I_i wrt θ and ϕ would provide data for the determination of both f_1 and f_2 . For metallic surfaces, the most simple empirical expressions are given by:

$$I_n^+ = A + B \exp\{-v_{c1}/(v_o \cos\theta)\} \quad -(3.39)$$

$$I_n^o = C + D \exp\{-v_{c2}/(v_o \cos\phi)\} \quad -(3.40)$$

after Hagstrum, where A, B, C and D are constants. Fitting of measured values of I_n^+ and I_n^o as a function of ϕ and θ to eqs 3.37 and 3.38 respectively allows v_{c1} and v_{c2} and hence f_1 and f_2 to be obtained.

In conclusion, a method has been identified which would allow the four individual components of the three stage model to be determined without

prior knowledge of differential scattering cross-sections and instrumental factors. This would allow the dominant processes in influencing the final charge state of scattered particles to be ascertained and their trajectory and energy dependencies to be studied. The data would also provide a rigorous test as to the validity of Verhey's model. The approach would also promise a more rigorous assessment of the validity of the empirical models such as those of Hagstrum, Woodruff and Verbist et al for neutralisation in stages I and III of the collision process. Comparison with the theoretical models described in section 3.4 describing the individual processes and relating to probabilities f_1 , p_i , p_n and f_2 would also be possible. Ultimately a semi-empirical formula for charge exchange processes with more predictive power than is currently available may be possible.

3.6.2 Measurement of inelastic energy losses.

Charge transfer process may also be studied by investigating the associated inelastic energy losses which accompany some mechanisms. This may be done by the measurement of small changes in the position of the QS peaks due to the primary charge state, as well as the charge state of the scattered particles. The basic concept of such measurements is simple, and can be expected to deliver more complete understanding of scattering processes than the probability measurements alone. However, such measurements are restricted to conditions which give a low MS intensity, which implies a clean crystalline surface. Measurements are also limited to conditions which give high energy resolution, thus restricting the primary to target mass ratio at which such experiments can be conducted. Bearing in mind these restrictions the unique measurements that are made possible by the ToFFASS instrument are described in what follows.

The ToF instrument of Luitjens et al^{15,16} was able to measure charge dependent inelastic energy losses. Two different measurements were possible with that instrument. Following the notation of these workersac: ΔE_I - the difference in QS peak position in the ion spectrum due to primary particle charge state. Adopting the notation introduced above this is given by:

$$\Delta E_I = E_{I^+} - E_{I^0} \quad -(3.41)$$

The QS^0_i peak must be composed of atoms which have undergone ionization during stage II of the collision. Whereas the QS^+_i peak may be composed

either of ions which have retained their charge, or of ions which have been neutralised and subsequently re-ionised. The energy difference, ΔE_1 , may result from the different transfer process, and/or differences in the electron stopping powers of the two particles. The second energy loss measurement in Luitjens' experiments was ΔE_2 - which was the measured difference between the total QS peak (ions + neutrals) and ions only with ions incident. If the neutralisation probability P_n^+ is assumed to be high ΔE_2 can be expressed as:

$$\Delta E_2 = E_{I^+} - E_{I^+} \quad \text{-(3.42)}$$

Here again ΔE_2 may originate from different transfer mechanisms, or charge dependent electron stopping. In

As Luitjens' instrument was not able to record the energy spectrum of scattered neutrals when a primary neutral beam was employed, the energy $E_{I^0_n}$ relating to the QS^0_n peak could not be determined. However, the capabilities of the ToFFASS instrument allow measurement of $E_{I^0_n}$. This extra capability allows a number of additional energy difference measurements to be made. These additional energy differences that become observable are expected to be useful in two respects. Firstly, as the electronic energy differences are related to the mechanisms by which charge transfer takes place, they may offer additional evidence for mechanism identification: a primary suffering ionization via the electron promotion mechanisms will lose energy equal to the difference between its ionization energy and the electron affinity of the surface. Whereas resonant and Auger processes involve no loss of energy by the primary. Secondly charge sensitive electron stopping losses, could be distinguished from losses related to charge transfer. Under conditions of high energy resolution and for certain combinations of primary and target species, as shown in figure 3.7, a splitting of the QS peak may be expected according to the particular 'pathway' of charge exchange. Such splitting of the QS peak was observed in the experiments of Souda et al^{101,167}. Thus an important feature of an instrument intended to conduct these experiments is that of high spectral resolution.

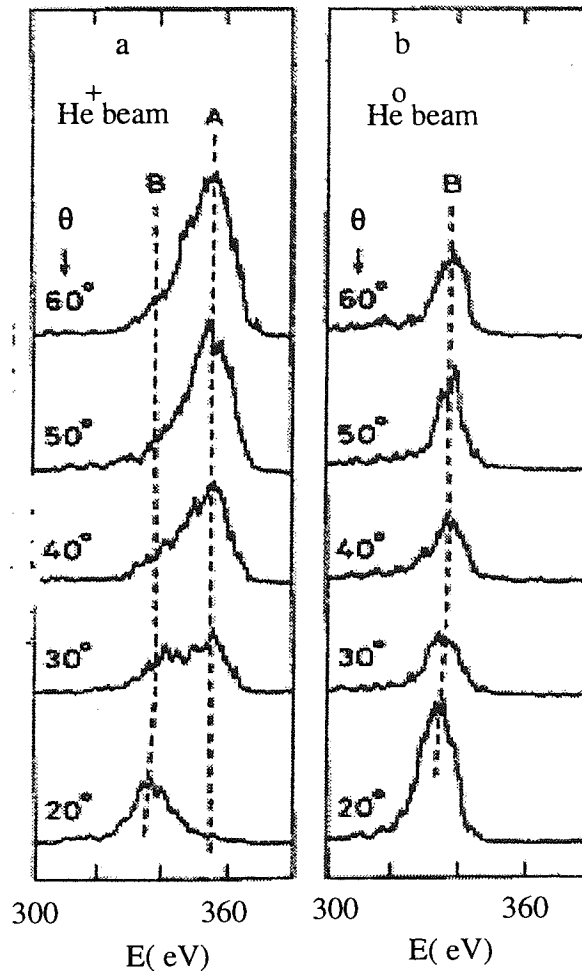


Figure 3.7 - LEISS spectra. Showing the Ta peak of a TaC(001) surface. Conditions: $-E_0 = 389$ eV, $\vartheta = 120^\circ$.

(a) due to He^+ beam

(B from ions neutralised in Phase I, and ionisation in Phase II
A from ions avoiding neutralisation at all phases of the collision)

(b) due to He^0 beam

(B from atoms ionised in Phase II)

CHAPTER IV

Development of a pulsed Ion/Atom Source

4.1 Introduction

A pulsed ion/atom source of the right specification was a crucial aspect of the spectrometer development, and constituted a major part of the work of this Phd programme. Prior to the work of this thesis, some fast atom and ion scattering experiments were conducted with a Kratos minibeam FAB source²⁶, but the scope of this work was limited by problems associated with the primary particle source. These included an excessively low neutral current and unacceptable levels of contaminant species in the beam, and poor attainable resolving power. As there was no suitable alternative available commercially a FAB source development programme was initiated by the Aston University Surface Science group. This programme commenced in 1988, with the intention of producing a source with specification suitable for ToFFASS. It was also initially intended for the source to be useful for other applications: conventional LEISS, SIMS, sample cleaning, ion milling, thus adding commercial appeal to the project. However, the modifications described here, to an initial prototype source, are intended specifically for the ToFFASS application.

There have been a number of pulsed low energy ion sources reported in the literature which have been constructed by various groups for use in specific ion scattering and secondary ion mass spectrometer applications^{169,96,170-172}, some of these also include a primary beam mass filter. A smaller number of instruments have been constructed which are capable of producing primary beams of fast atoms^{173,15,16,101,168}. However, there has been no instrument constructed which is capable of producing a pulsed neutral beam.

4.2 Background and history

4.2.1 Construction Philosophy

In all cases reported above the necessary 'beam manipulation' functions (ie filtering, focusing, chopping, neutralisation) are provided by discrete units bolted together to form a long beam line. The philosophy of the

Aston FAB source differs from this in that all beam manipulations are provided within a single unit, which can be bolted straight onto the analysis chamber, with all necessary components mounted on a single ion optic column. A modular approach is maintained in the design so that individual units of the column may be re-designed and substituted. A schematic of the basic construction is given in figure 4.1, which shows three steel column mounting studs running the length of the column. These studs are sleeved by ceramic tubes, (3mm OD). The individual electrode assemblies are separated, located and electrically insulated by further ceramic tubes of a larger diameter (3mm ID, 6 mm OD) which fit precisely over the inner tubes. The whole assembly is secured onto the mounting studs by three end nuts. Electrical connections to individual electrodes are routed through a concentric annular ring of ceramic tubes (3mm OD) of diameter 28 mm. An additional advantage is that contaminated components can be replaced rather than disposing of the whole column. This basic mechanical design was made in partnership with an industrial manufacturer of vacuum equipment.

4.2.2 Development history

At the start of the programme a prototype source had already been produced, and this provided the starting point for development described here. The elements of the prototype source are shown in figure 4.2. Initial measurements showed further developments to be necessary, and so modifications were tackled in a number of distinct stages. This enabled the consequences of the physical changes to be monitored. Throughout, the basic modular construction has been maintained. The development is described here as it proceeded, by sequence of experimental measurement, computer simulation, and re-design. As a result of this cyclic process, three main versions were studied, the first being the prototype, the shortcomings of which prevented the initialisation of scattering studies prior to further development. Problem areas were then analysed in detail, aided by the development of numerical computer simulation models. Following re-design and re-positioning of key components, further experimental measurements were made. This version will subsequently be referred to as FAB-1. Measurements on FAB-1 showed some significant improvements, and although some preliminary scattering studies were initiated at this stage, in order to assess other aspects of the instrument, the source characteristics were still not satisfactory. Based on

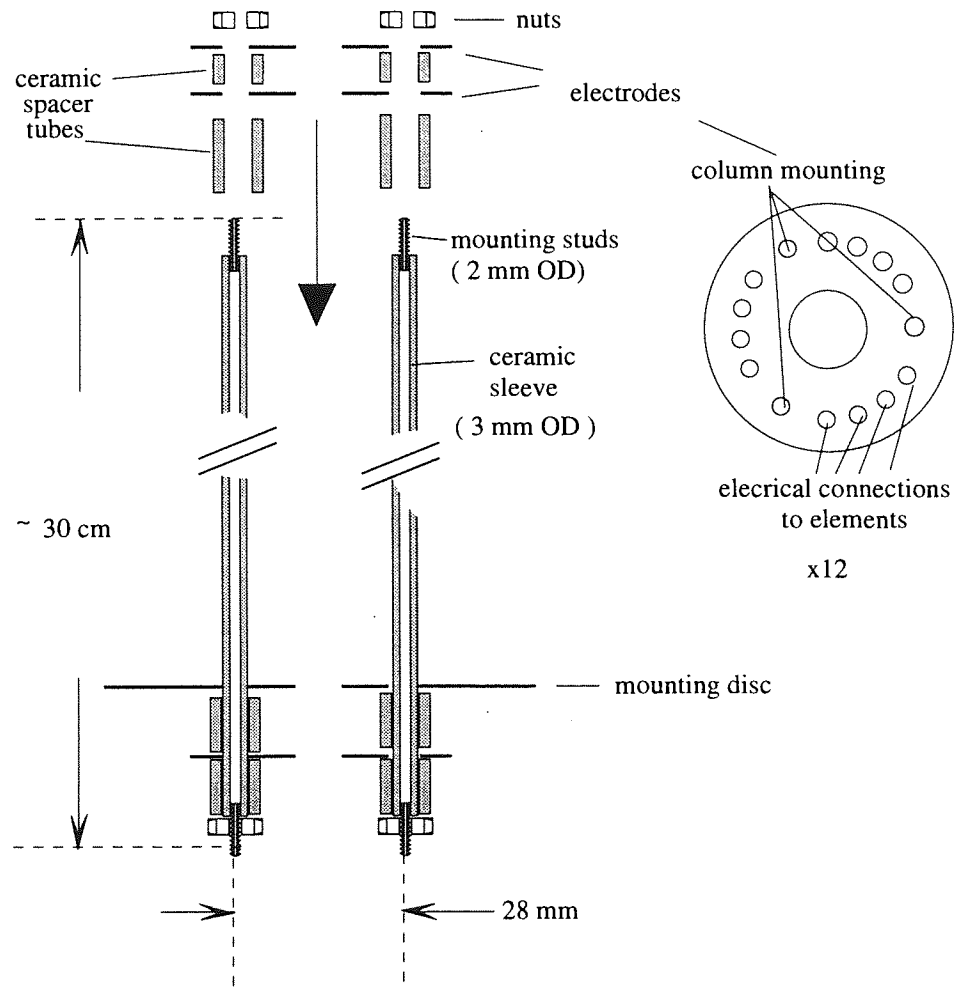


Figure 4.1 - A schematic of the FAB source construction

the experimental data and further simulation some more design changes were implemented. This second version will be subsequently referred to as FAB-2. Characterisation of this source showed the required specification to be met in most aspects.

4.2.3 The specific requirements of an ion/atom source for ToFFASS

The experiments outlined in the previous chapter demand very specific capabilities of the primary particle source. It was therefore important to establish these characteristics and other key parameters at an early stage. This requires very different design criteria compared to a particle source for more general application. A second consideration was the restriction of available resources and time: even though certain physical modifications were clearly shown to be beneficial through theoretical analysis, they were not implemented unless the improvement in performance was crucial to the objectives of the experimental programme.

The important characteristics, established in chapter 2 were: low energy spread, ($\Delta E_0/E_0 < 0.01$), high beam purity, and a method of chopping the beam into pulses of short duration ($\Delta t/t \sim 0.005$). For the experiments described in chapter 3, it must also be possible to provide pure ion or pure neutral beams. Properties which are often important elsewhere such as a sharply focused beam, and maximum current output were considered to be of secondary importance. As shown in chapter 2, it is counter productive to make the analysis area very small for a technique claiming to have mono-layer resolution, as the erosion rate increases in inverse proportion to spot size. A beam diameter of 1 to 2 mm is sufficient. The only influence of the beam current is on the collection time, and although it is clearly desirable to collect the data in as short a time period as possible, low beam current does not impose a fundamental restriction.

Finally, a stable beam is important in quantitative analysis experiments which demand accurate dosimetry of the sample current.

4.2.4 Physical description of the prototype pulsed ion/atom

The following description refers to figure 4.2. Unless stated otherwise all electrodes were made from tantalum. Describing the elements from top to bottom, the first component is the ion source consisting of a

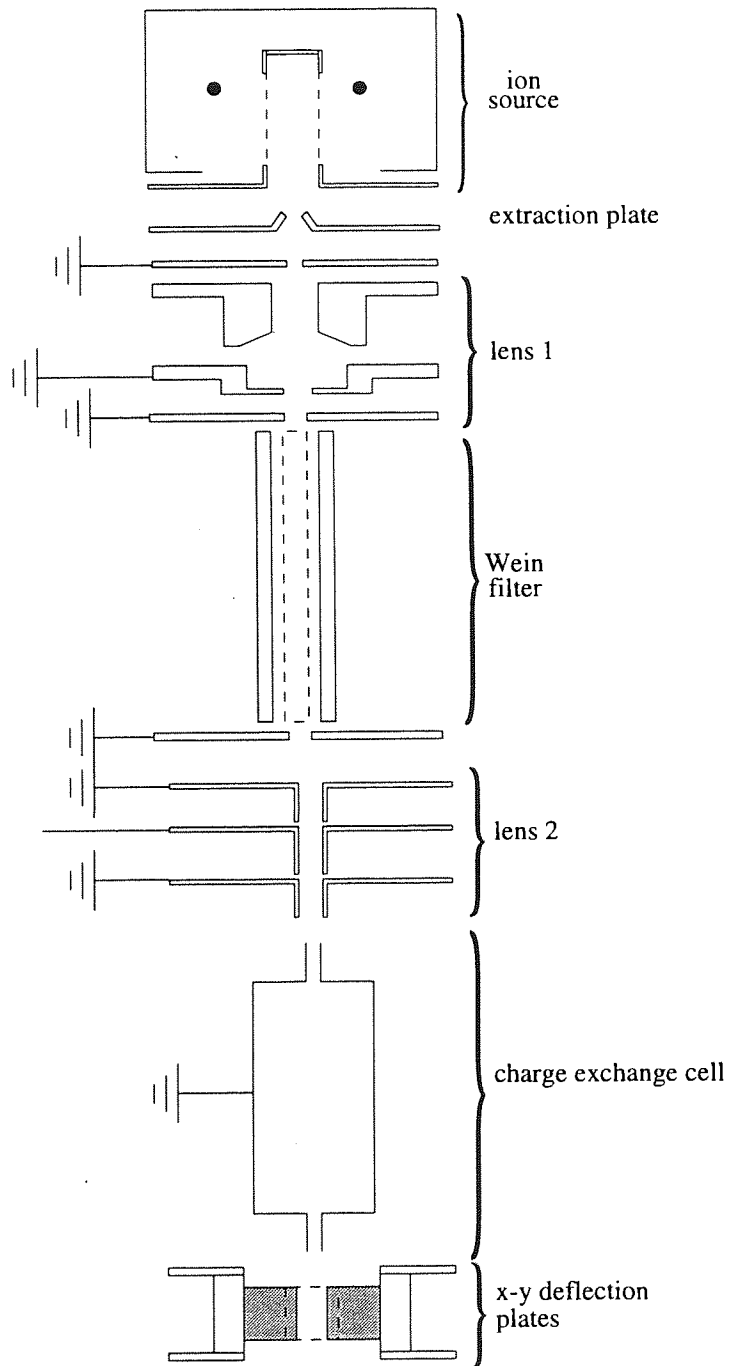


Figure 4.2 - Elements of the prototype FAB source

cylindrical grid anode and a circular filament, contained within the outer housing. The source gas was supplied to the ionisation cell at a constant flow rate via a controllable leak valve. The design was intended to provide insulation up to a 5 keV. To operate the source a potential, V_o , was applied to the grid electrode, and the filament was made negative with respect to V_o , by the emission voltage, V_e . A circular filament of total length ~ 15 mm can be accommodated within the ion cell. Proceeding the grid is an extraction plate electrode at an intermediate potential of V_{ext} which consisted of a single disc containing a 2 mm diameter central aperture. The extraction plate was separated from the grid electrode by ceramic tubes of 1.5 mm length. The prototype was designed to operate with V_{ext} set to $0.75 V_o$. The next element is a tri-electrode lens operated in enizel mode, which was intended to form a parallel beam as required by the proceeding Wein filter. The Wein filter consisted of orthogonal electric and magnetic fields, and the pole pieces consisted of four separate ceramic bar magnets, giving a mean field strength of ~ 0.26 T. The magnetic poles and the electric field plates were housed in an electrically earthed ferromagnetic steel tube, of 20mm internal diameter, with entrance/exit apertures of 5 mm diameter. Proceeding the filter is a second enizel lens whose function was to form a focused image at the sample. The distance between the principle plane of this lens and the first was 100 mm. Following the lens is the charge exchange cell, hereafter CEC. This was intended to present the beam with a region of high pressure gas, and achieve a neutral beam by the process of resonant charge exchange. The required pressure differential between the CEC and the rest of the transport column relied on the low conductance of its entrance and exit tubes. The final unit is the X-Y deflection electrodes, which constituted two orthogonal pairs of electrodes, of 5mm in length, and 7 mm separation.

There were no specific components to provide the necessary beam chopping function. It was the intention of the original design to achieve this by application of a pulse between the cathode and anode of the ion source. This was an experimental approach, specifically introduced in an attempt to reduce contamination problems due to sputtered material. This has historically been a problem in ion sources leading to reduced lifetime. Thus electron impact pulsing offered a method to significantly lengthen source lifetime.

4.3 Basic principles of ion source operation

Ion beam production by the electron bombardment technique dates from the beginning of the century. The basic physics of the components essential to all sources of this type: the ion source, extraction optics and lens system, are reviewed in this section. The theory associated with the additional component units required for the production of a chopped beam ion/atom source, that is mass separation, beam chopping, and charge exchange, are discussed in later sections.

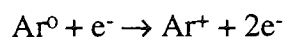
4.3.1 The ion source

Where ion production is due to electron bombardment, the ion source is a primary consideration as the design directly determines many properties of the beam. In such sources ions are created by electrons accelerated from a hot filament, and the rate of ion production is determined by several factors: electron current, gas pressure, electrode geometry, and ionisation cross-section. Many different variants have been developed based on this basic method, to meet the requirements of a range of specific applications. For gas pressures employed in most electron impact sources the mean free path of the impacting electrons is much larger than the physical dimensions of the source. Hence only a very small fraction of the electrons produced at the filament contribute to ion production, thus the ionisation efficiency is low. One way to improve this efficiency is by the application of an external magnetic field, which causes the electrons to spiral tightly, resulting in a large increase in the mean electron trajectory length.

A number of collision processes take place within the ion cell. Irrespective of collision process, the mean free path, λ , between consecutive collisions is given by:

$$\lambda = 1/\sigma n \quad \text{-(4.1)}$$

where n is the number density and σ is cross-section associated with the collision process. To calculate the cross-section for an electron-atom collision:



resulting in ionisation of the atom, one must look to inelastic scattering processes.

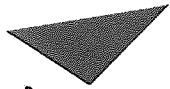
Empirical data for various gases as a function of electron energy is well known¹⁷⁴ and is shown in figure 4.3. The most efficient electron energy is ~4 times the ionisation potential of the gas atom, although the process is complicated by the production of excited state and doubly charged ions, and by ionisation due to secondary electrons. Thus the macroscopic behaviour of the ion source is determined by the statistical average of many collisional events involving all these phenomena.

Both the gas pressure and the ionisation rate are crucial parameters to the operation of the ion source. If the electron, ion and neutral densities between cathode and anode of the source exceed a certain threshold level, a discharge plasma will form. Above this threshold the ionisation efficiency increases sharply. Thus ion sources which are designed to sustain a stable plasma discharge offer greatest brightness. If the particle densities or electrode geometry are not appropriate for plasma formation, ions must be extracted from a more extensive region of the ion cell. This results in a reduction of beam quality compared to plasma sources where ions are extracted from the plasma boundary. In the former case the energies of extracted ions are determined by the potential at their point of origin, and the dominant influence on energy spread is usually the cathode-anode potential. This energy spread may be minimised by shielding the region from which ions are extracted from the cathode-anode field. The use of such sources is restricted to applications which require low energy spread but not a high beam current, such as an analytical probe beam. In the absence of a plasma, the forces acting upon the ions and electrons are due to the macroscopic electric field within the source. By neglecting the free charge in the ion cell space, the calculation of the electric potential is straightforward. Given the electrode geometry and potentials, the electrical potential within the ion cell space is determined by solution of Laplace's equation:

$$\nabla^2\phi=0 \quad \text{-(4.2)}$$

which can be solved by either finite element or finite difference methods.

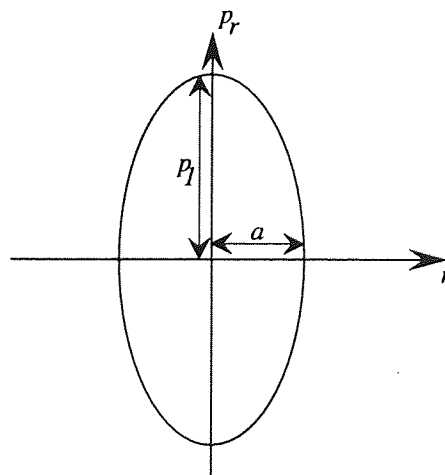
Where the space charge does significantly influence the potential in the ion cell Poisson's equation must be used:



Aston University

Content has been removed for copyright reasons

Figure 4.3 - Ionisation cross-sections of noble gases, from Chapman¹⁷⁴
 $\pi a_0^2 = 8.82 \times 10^{-17} \text{ cm}^2$.



$Pr - r$ Phase space

Figure 4.4 - Beam emittance. The area enclosed by the phase space ellipse represents the emittance.

$$\nabla^2\phi=\rho_f/\epsilon\epsilon_o \quad \text{-(4.3)}$$

Solution of eq. 4.3 is significantly more difficult, as free charge density distribution is unknown.

4.3.2 The extraction optics.

The transport of ions into the beam transfer systems is provided by the extraction optics which is an integral part of the ion source. Primarily the design of electrodes composing the extraction system is dependent on the ion source and the applications to which the final beam is to be employed. Commonly, the most important properties of the final beam are current, I_b , energy, E_o , and energy spread, ΔE_o , purity, focused beam diameter, r_f^{min} , and current stability. All these properties are influenced by the extraction optics, although parameters may subsequently be improved by elements of the transport system, with the exception of beam current, and such improvements can only be achieved at the expense of beam current. Additionally the ion source and extraction optics are often closely coupled with the design of subsequent elements of the transport system.

The transport system will usually contain beam limiting apertures in order to remove ions of high transverse thermal velocities, therefore utilising only the high quality centre of the beam at the expense of the total beam current. However, it is not ideal to allow a substantial proportion of the beam to be restricted by apertures, as the resulting contamination from sputtered material shortens the source's operating lifetime. In principle energy spread may be improved by employment of an energy filter, again at the expense of total beam current. The beam purity is influenced by the source design, as the beam will contain as many different ion species as there are atom species in the discharge. In this case however, contaminant ions are a small fraction of the total current and their removal by appropriate filtering does not produce a significant reduction in beam current.

An extensively investigated electrode geometry for plasma forming sources is the two-tube immersion lens, for which much tabulated data has been produced ¹⁷⁵. Data for sources which do not form a plasma is scarce.

4.3.3 Optical quality of the extracted beam.

The optical quality of an ion source is measured in terms of the source brightness, β_s , which is defined as the current density per unit solid angle of the extracted beam (μ amps m^{-2} str^{-1}). β is a useful quantity as it determines how the beam may be controlled and transported from the ion source to the target. In an 'aperture free' transported system, β is conserved, provided the axial momentum remains constant, and therefore may be used to calculate the minimum focused beam radius, r_t^{min} , for a given collimation angle, α_r . In the calculation of β_s a symmetrical beam is assumed. In which case β_s is given by:

$$\beta_s = I_b / (\pi \cdot r_s \cdot \alpha_s)^2 \quad -(4.4)$$

where r_s and α_s are the radius, and total divergence angle of the extracted beam. So a high brightness beam is one that originates from a localized source, and is transmitted into a narrow emittance cone. In sources where ions are emitted from a very small region, such as liquid metal ion sources, the quasi point brightness is used instead, which is the emitted current per unit solid angle. Where accelerating lenses are present in the transport system the reduced beam brightness, β_r must be used, which is simply the brightness divided by the beam energy:

$$\beta_r = \beta / V_o \quad -(4.5)$$

Thus if the reduced brightness of the sources is known, the minimum spot size of an aberration free transport system can be calculated, and is given by:

$$r_t^{min} = I_b^{1/2} / (\pi \cdot \beta^{1/2} \alpha_r) \quad -(4.6)$$

r_t^{min} represents a limiting value which can only be attained in the case of 'no' beam current and chromatic and spherical aberration free lenses.

4.3.4 Ion optics of the beam transport system

Lenses within the transport system are employed to form an image of the ion source at the target, and the optical design of the elements is strongly

dependent on the properties of the extracted beam. A useful quantity for this purpose is the emittance, which should be matched with the acceptance of the individual elements of the column. The emittance can be understood as follows. Assuming cylindrical symmetry, with the beam direction orientated along the z axis, the individual ions are fully defined by the two position co-ordinates, z and r , and the two momentum co-ordinates, P_z and P_r . A plot of radial velocity, (dr/dt) against r , for all ions in the beam yields phase space information of the beam. The resulting plots are generally elliptical in shape, similar to figure 4.4. The area enclosed by the ellipse gives the emittance of the beam. An idealized beam with no intersecting ion trajectories, emerging from a virtual focal point with P_r proportional to r would be represented by a single line in the phase space diagram. The emittance is preserved along the beam transport system in the absence of accelerating/de-accelerating lenses. Clearly the radii and divergence angles of individual ions will change as they propagate but the emittance of the beam will remain constant. For this reason emittance is particularly useful when the emphasis is on maximising the beam transport properties. This is achieved by comparison of the emittance with the phase space acceptance of each element 'upstream' from the ion source. As a general rule the beam can be transmitted by an element if the acceptance area of the elements is greater than the emittance, but an appropriate ion-optical lens may be required in order to make the beam 'fit into' that element. If accelerating/de-accelerating lenses are present in the column the momentum normalized emittance should be used.

A number of basic lens shapes/types are employed in ion/electron optical systems. The most simple electrode shape is the single 'aperture lens'. As its name implies, this lens consists of a single circular aperture in a solid electrode, separating regions of different field strength. This simple geometry has the advantage that the focal properties can be found analytically. Consider the cylindrical region in the field space of the aperture as shown in figure 4.5. If the ends of the cylinder are chosen to be sufficiently far from the aperture then the field is unperturbed by the aperture's presence, and the electric field 'flowing' from the ends of the region will have no radial component. Then according to Gauss's law an integration $E \cdot ds$ over the surface of the cylinder must be zero. This then yields the approximate expression for the focal length of the aperture:

$$f = 4E_0 / (E_2 - E_1) \quad \text{-(4.7)}$$

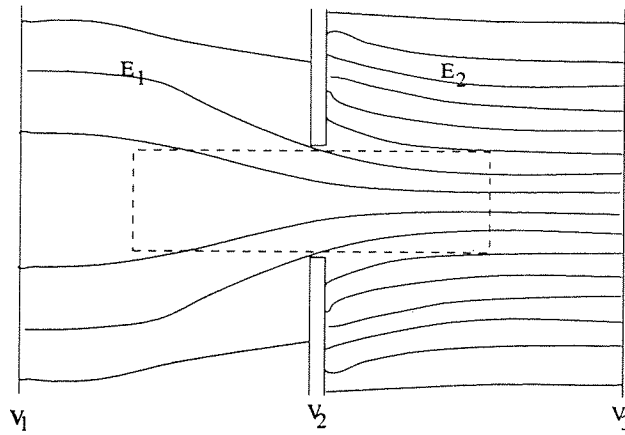


Figure 4.5 -The figure shows a single aperture in a solid electrode, separating regions of different field strength. The dashed line shows a cylindrical region to which Gauss's law may be applied; the integration of $E \cdot ds$ over the cylinder surface is equal to zero.

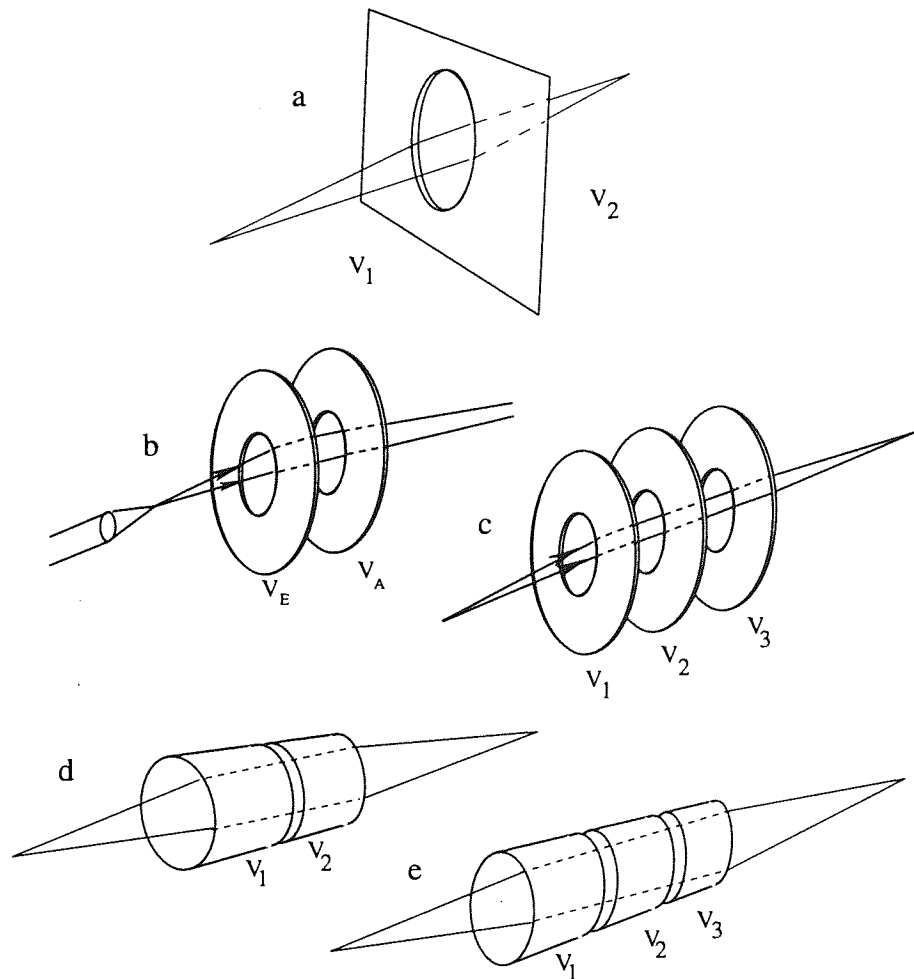


Figure 4.6 - Basic lens structures.
 (a) single aperture lens, (b) double aperture lens, (c) triple aperture lens, (d) double cylinder lens, (e) triple cylinder lens

Thus the focal length is four times the ratio of ion energy to the difference in field strengths of the two regions. Therefore for the geometry and voltage conditions of figure 4.5, the focal length can be expressed in terms of the potentials V_1 , V_2 , V_3 by:

$$f=4 \cdot E_o \cdot a /((V_3-V_2)-(V_2-V_1)) \quad -(4.8)$$

where a is the electrode separation. In practice the aperture lens finds limited application, although this calculation provides a first approximation of focal lengths accessible to electrostatic lenses, given the ion energy, electrode potentials and lens radius. That is the focal length for given electrode voltages, and radial dimensions are only weakly dependent on geometry. For accurate calculation of the optical properties of more complex geometry, it is necessary to calculate the potential more precisely. As there is no general analytical solution to Lapace's equation, numerical solutions of the potential must be generated.

A more commonly employed group of lenses are cylinder lenses. A two electrode cylinder lens is employed when the image and object are required to be in regions of differing potentials. The three electrode cylinder lens can form an image of the object at the same potential, einzel mode, or else function as a zoom lens. Commonly employed electrostatic lenses comprise a combination of thin aperture plates and cylinders, often in a geometry displaying longitudinal symmetry. An einzel lens can be used in either retarding or accelerating mode. In the former the central electrode retards ions as they enter the lens system and accelerates them as they leave, with the opposite for the accelerating mode. The retarding mode is found to give a lower spherical aberration coefficient for a given working distance. Some standard lenses are shown in figure 4.6.

Where a high quality image or fine probe is required the aberrations of the lens system become important and must be considered. In this case the precise lens geometry is an important factor. For such changes of geometry the difference in focal properties lies for the most part in the aberration coefficients.

Various methods have been developed for calculating the fields optical properties, and aberration coefficients of electrostatic lenses^{176,177}. All quantitative results reported in this thesis have been calculated using the MUNRO electron lens programmes package¹⁷⁶, which can be applied to any

rotationally symmetrical geometry containing up to four electrodes. The field is calculated using the finite difference method, with the field assumed to vary linearly within each elemental volume. The mesh sizes are user defined. It is the convention generally (and in this software package also) to define electrode potentials relative to the potential of the electrode on which the ions have zero kinetic energy. The programme uses the axial potential distribution to find paraxial ray equation using a fourth-order Runge-Kutta formula. Aberration coefficients are also evaluated using Simpson's rule to calculate the aberration integral. An alternative approach is described by Mulvey and Wallington¹⁷⁸. The optical properties and aberrations of some basic lens configurations are also tabulated by Harting and Read¹⁷⁹, calculated using the space charge density method¹⁸⁰

Spherical aberrations are introduced by the lens as the image plane for off-axis ions is different from that of paraxial ions. The resulting axial displacement in the image plane is denoted r_i and is expressed in terms of the spherical aberration co-efficient C_s by:

$$r_i = C_s \alpha_i^3 \quad \text{-(4.9)}$$

Whereas chromatic aberrations arise if the beam is not mono-energetic, in this case an axial displacement, dz_i of the image plane arises due to the voltage difference ΔV , which is given by:

$$dz_i = C_c V/\Delta V \quad \text{-(4.10)}$$

These displacements become important in situations where the image is very small, either due to strong demagnification or a very sharply defined initial object, and the minimisation of the aberration coefficient is an important consideration in the optical design. This can be achieved by optimisation of C_s and C_c with respect to the working distance, W , or by using the figure of merit method outlined by Harting and Read¹⁷⁹

The magnification, M_o , of a single lens is given by the image height, h_i at the image plane, relative to the height, h_o , of an object positioned on the object plane, z_o . However this definition is only strictly true for an aberration free system.

Individual lens elements of a beam transport system can be combined in a variety of configurations. The most simple configuration being a

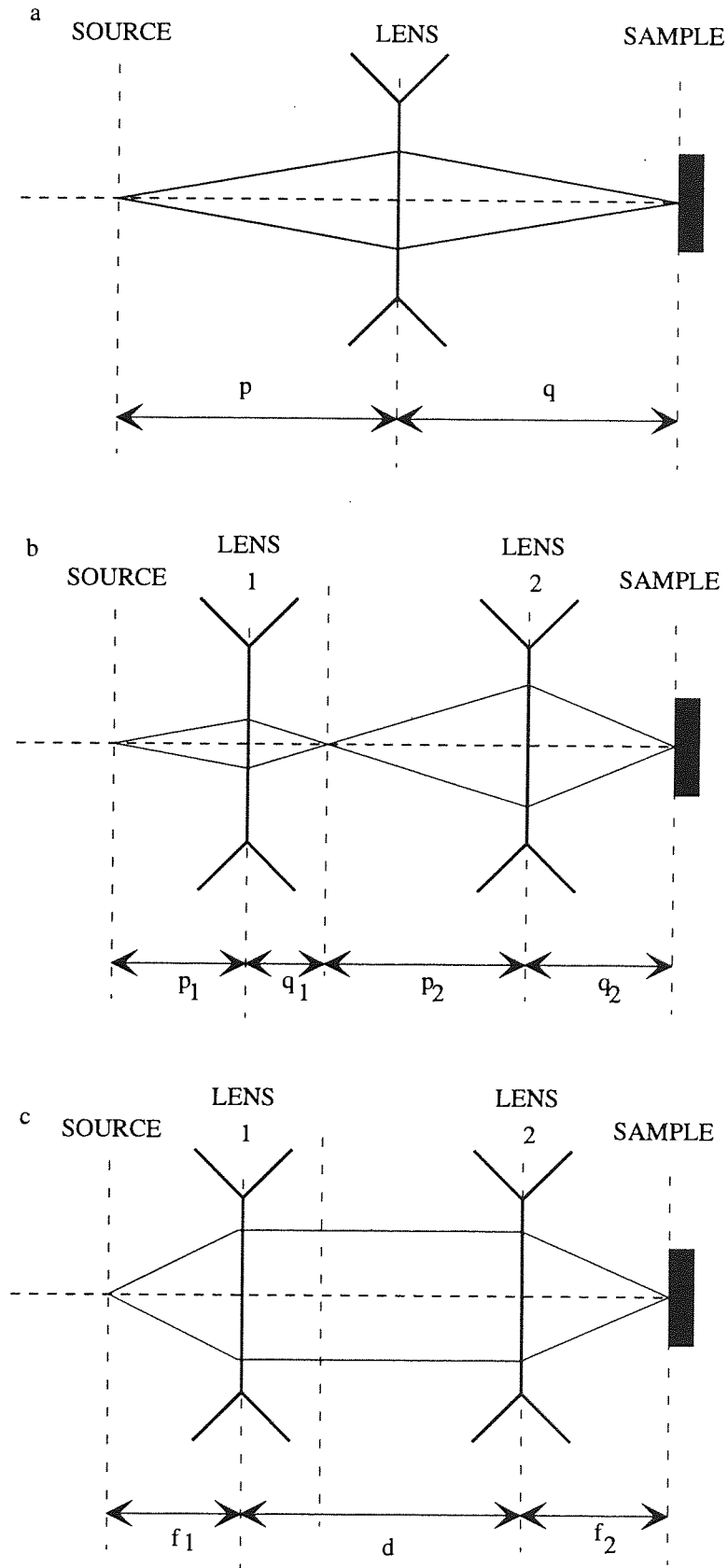


Figure 4.7 - Basic lens combinations

single lens, figure 4.7a, in which case the magnification of the column is just that of the single lens:

$$M = q/p = r_p/r_s \quad -(4.11)$$

and the focused beam diameter is fixed by the mechanical construction. If a small spot size, r_p , is required the necessary de-magnification can only be achieved by making q much shorter than p . Thus, the lens must be positioned very close to the sample, or p must be made very long. Both these solutions may be impractical or prohibitive. For electron impact sources r_s is typically 0.5 mm, and so to obtain, for example, a spot of 100 microns, requires a de-magnification of 10. That is p must be ten times q . For this reason practical systems usually employ at least two lens elements. In the arrangement shown in figure 4.7b, the second lens images an intermediate image formed by the first lens. This intermediate image may be real or virtual. In either case the overall magnification is given by:

$$M = (q_1/p_1).(q_2/p_2) \quad -(4.12)$$

In this case the magnification may be varied for the fixed object and image distances by changing the ratio of q_1/p_2 . Thus de-magnification is achieved by making f_1 , the focal length of the first lens, short. The spot size at the target may be further reduced by placing a beam limiting aperture between the two lenses, thus removing the low quality divergent part of the beam. Clearly the minimum beam diameter is ultimately limited by beam current to brightness ratio as described in the previous section .

If the beam is required to be 'parallel' between the two lenses, the magnification conditions for the 1st and 2nd lens elements should be made infinite and zero respectively. In this case the expression for the overall magnification of eq. 4.13 reduces to:

$$M = q_2/p_1 = f_2/f_1 \quad -(4.13)$$

in which case $p_1=f_1$ and $q_2 = f_2$, thus the magnification is given by the ratio of the focal length of the two lenses. Again the magnification is restricted by the physical positions of the lenses, source and target. It should be noted that a truly parallel beam can only be achieved in the case of a 'point source emitter'.

4.4 Experimental procedure

4.4.1 Measurement of continuous beam current

Total beam currents were collected on a solid nickel plate, the construction of which is shown in figure 4.8. The plate was negatively biased to ensure that secondary electrons were not re-collected and to prevent the collection of residual free electrons in the vacuum chamber. In this case the secondary electron emission (SEE) current contributes to a positive current. A potential of -9 volts was found to be sufficient to suppress secondary electrons^{181,182}. An electrometer with pico amp resolution was employed for the current measurements. The measured current is denoted I_m . The SEE coefficient is denoted γ , which is primarily dependent upon the primary species, its energy, and the surface material. However, the SEE process is also sensitive to the angle of incidence, surface crystallography and surface overlayer contamination.

In this work it is assumed that the SEE coefficient for ions, denoted γ^+ , and the SEE coefficient for neutrals, denoted γ^0 , are the same. This is known to be valid for energies > 1 keV¹⁷³. Initially SEE data was obtained from Chapman¹⁷⁴, where empirically determined data is listed for various ion-surface combinations. The following values of γ have been assumed in the measurements of the ion and neutral beam currents in this work.

Table 4.1 : SEE data, γ values.

	He	Ne	Ar
E_o (eV)			
500	0.30	0.20	0.10
1000	0.35	0.24	0.13
1500	0.40	0.28	0.15
2000	0.45	0.31	0.18
2500	0.50	0.35	0.20

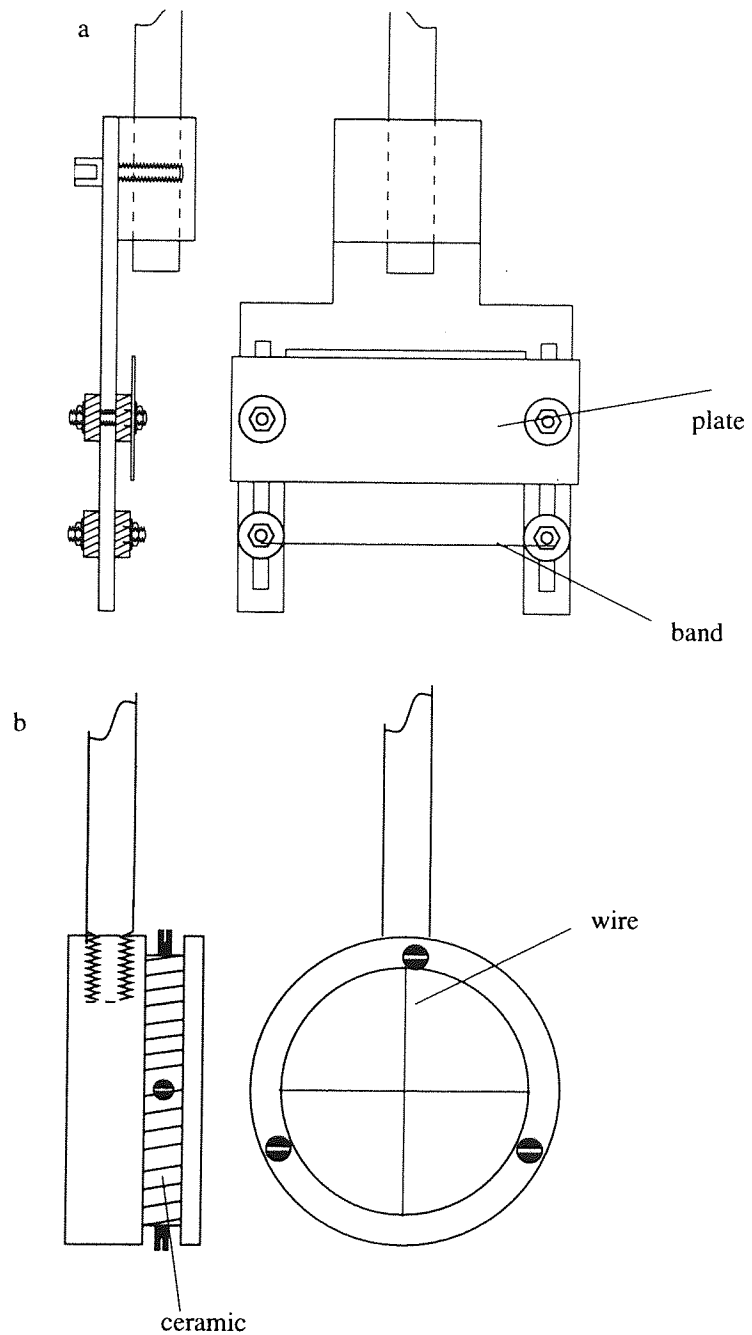


Figure 4.8 - Beam current measurement apparatus.
(a) - Dual plate and band assembly (0.4 mm)
(b) - Cross wire (0.05 mm diameter)

The experimental setup allowed measurement of the total beam, or by application of a voltage to the x-y deflection plates, either neutrals or ions. The ion and atom currents must be corrected according to eq. 4.14 and 4.15 respectively.

$$I_i = I_{mi} / (1 + \gamma) \quad -(4.14)$$

$$I_n = I_{mn} / \gamma \quad -(4.15)$$

Where I_{mi} and I_{mn} are the currents measured by the electrometer with the ion and atom beam incident on the plate.

The use of the nickel plate provided a simple method for measuring ion and neutral components of the beam, and the method was found to be sufficiently accurate for the purpose of source characterisation. However, it is noted that for more accurate ion beam measurements it is necessary to employ a Faraday cup in order to prevent residual electron currents influencing the measurements. In the latter stages of this work a system was constructed for measurement of the SEE coefficients directly by measurements of the secondary electron current, these measured values were in reasonable agreement with the above values. The instrumentation employed for these measurements is discussed in chapter V.

4.4.2 Measurement of beam profile.

Beam profiles were measured by manually scanning the nickel band across the stationary beam in the x direction. Initial measurements were made with a 0.4 mm band, using the apparatus shown in figure 4.8a and later using a 0.05 mm cross wire shown in figure 4.8b. In the latter case the beam could be scanned in both x and y directions. The co-ordinate system used to describe the motion of the xyz sample stage is shown in figure 4.9. The profiles, $J_{mn}(x)$, $J_{mn}(z)$, $J_{mi}(x)$, $J_{mi}(z)$ were obtained by recording the electrometer current at regular intervals of the wire position. The profiles $J_a(x)$, $J_a(z)$, $J_i(x)$, $J_i(z)$ were obtained following the procedure described above. This measured profile can be converted to the radial current distribution $J(r)$ using the Abbel integral as shown by Wronski¹⁸³. It can be seen that if $J(x)$ is gaussian in form then $J(r)$ is also gaussian. Experimentally it is possible to measure the total beam (ions + neutrals), $I_t(x)$, or the ion or atom beams

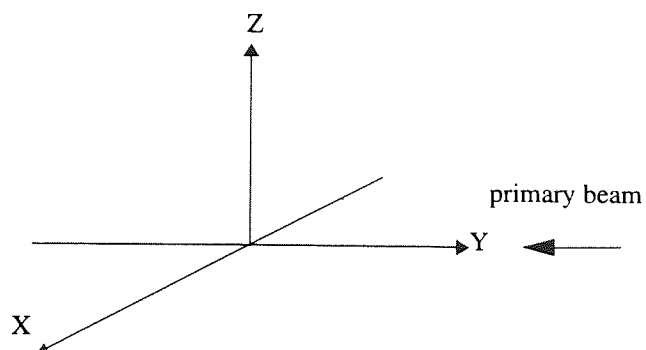


Figure 4.9 - Co-ordinate system used in description of primary beam measurements.

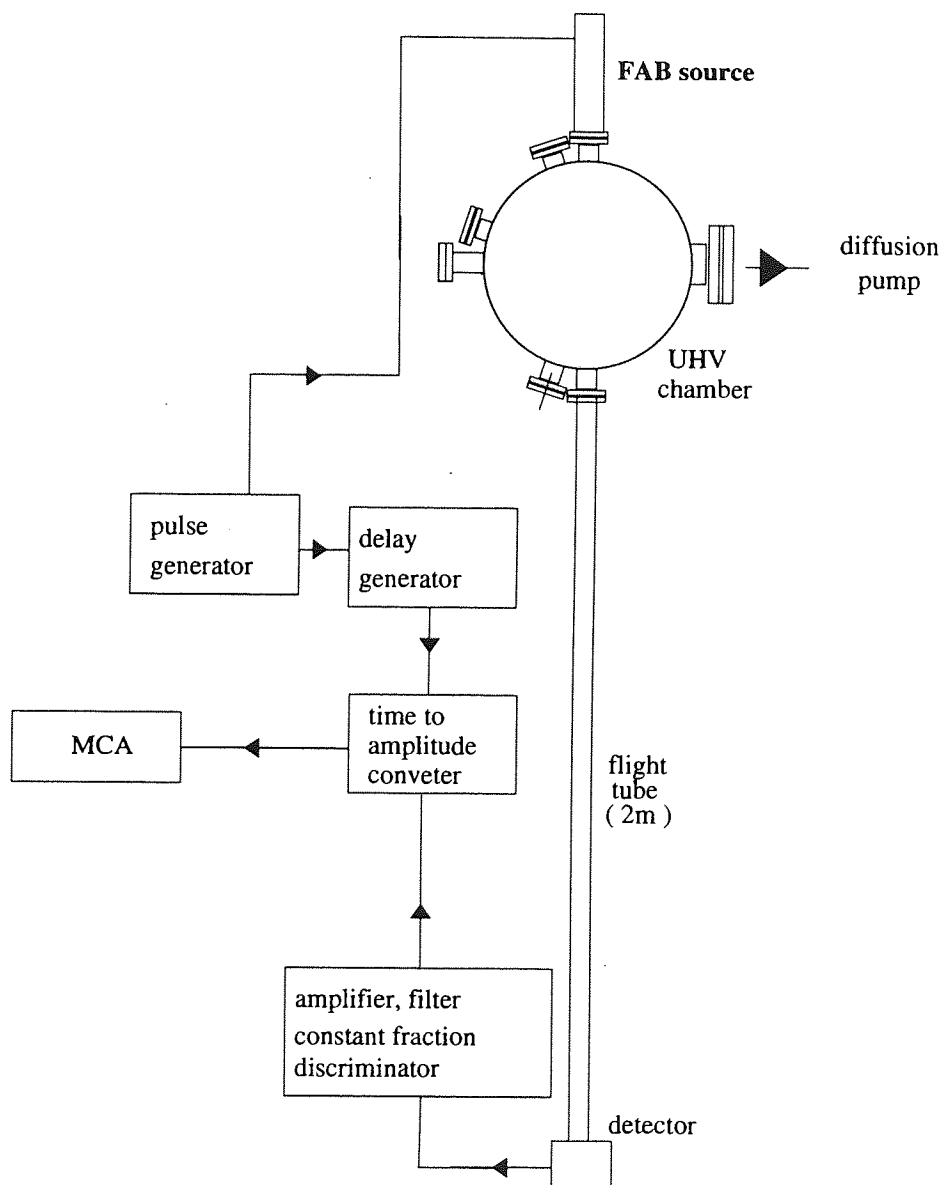


Figure - 4.10 Spectrometer configuration for measurement of primary beam spectra.

individually, $J_i(x)$, and $J_n(x)$.

4.4.3 Measurements of primary beam spectra

To measure the primary spectra of the ion and neutral beams directly from the source, the spectrometer was used in the configuration shown in figure 4.10. That is the source and the flight tube were mounted at directly opposing ports of the main vacuum chamber. The components comprising the spectrometer are described fully in chapter 5. The time range of the MCA can be adjusted to suit experimental conditions by the delay generator and the TAC. The flight tube was of 32 mm internal bore, and initially contained no apertures. The initial flight path length, ie the distance between the ion source and the detector was 2500 ± 50 mm. The beam chopping method was specific to the various versions of the ion source. Initially the electron impact pulsing method was used. That is the emission voltage, V_e was pulsed giving rise to a pulsed emission current, I_e . This method had previously been applied to a Kratos Macro-FAB WG-458 by Xu¹⁸⁴.

4.4.4 Differential Pumping of the ion/atom source

Differential pumping of the source was achieved through the CF70 flange shown in figure 4.11. This flange was connected to a 55 l/s turbomolecular pump via flexible bellow tubing, 32 mm internal diameter and 1150 mm in length. An ionisation gauge was positioned 380 mm from the pump end of the tube. The gauge pressure, hereafter denoted P_B , was therefore significantly lower than that of the source, specifically the ionisation and charge exchange cells, P_{IC} , and P_{CEC} respectively.

The pressure difference between points in the differential pumping line, is determined by the gas throughput, Q , and the conductance of the tube:

$$P_1 - P_2 = Q/C_{tube} \quad -(4.16)$$

Knudsen's formulation for a tube, length l , and radius r is given by:

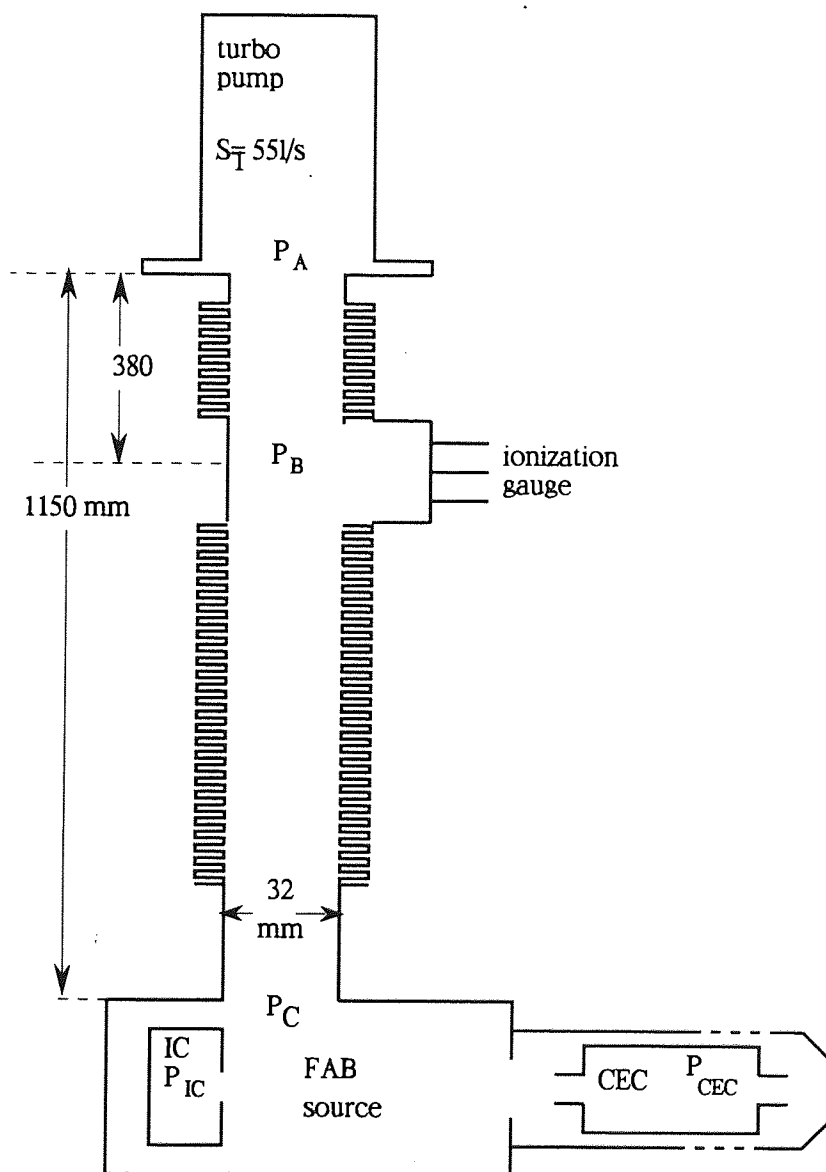


Figure 4.11 - Differential pumping geometry

$$C_{\text{tube}} = [1 + 6l/16r]^{-1} C_r \quad \text{-(4.17)}$$

where C_r is the conductance of an aperture the same radius as the tube, and is given by:

$$C_r = \frac{1}{4} \langle v \rangle \pi r^2 \quad \text{-(4.18)}$$

$\frac{1}{4} \langle v \rangle$ at $T=300$ K for the relevant gases is listed in table 4.2

Table 4.2 : Conductance data.

	$\frac{1}{4} \langle v \rangle$
	($\text{ls}^{-1}\text{cm}^{-1}$)
He	31.4
Ne	14.0
Ar	9.9

As the throughput at all points in the system must be constant, giving:

$$S_A P_A = S_B P_B = S_C P_C \quad \text{-(4.19)}$$

The pumping speed at the gauge head is therefore given by:

$$S_B = (1/S_A - 1/C_{BA})^{-1} \quad \text{-(4.20)}$$

where C_{BA} is the conductance of the tube section between the pump and the gauge head, and is given by eq. 4.17 to be 8 l/s, and S_B is 7 l/s, (argon). The conductance of the tubing between the gauge and the source is 4 l/s, thus the pumping speed at the ion source is reduced to 2.5 l/s.

The sensitivity of penning and ionization gauges varies according to gas type, and the measured pressures must be multiplied by the following factors.

Table 4.3 : Gauge sensitivity factors

	Ionization	Penning
argon	0.9	0.44
neon	3.3	2.2
helium	7.7	3.3

It should be emphasised that at best Knudsen's formulae give approximate results only, even when the system geometry is well represented, and an error of at least 10% must be expected. As the geometry in the above calculations is not fully represented a significantly greater error must be expected.

4.5 The Prototype pulsed ion/atom source

The design and development of the prototype source prior to the initial measurements described here, is described in more detail elsewhere by Xu¹⁸⁵.

4.5.1 Initial operation

Initially it was intended to undertake a thorough characterisation of the prototype source employing the experimental methods described in the previous section. It was intended to measure the dependence of the ion and neutral beam currents (I_i and I_n) and respective focused beam profile on the operating parameters: P_{IC} , P_{CEC} , E_o and lens voltages V_1 and V_2 . However, at the onset it was found immediately that the prototype did not meet the required specification outlined in section 4.2.3. Furthermore the repeatability of measured results was very poor. Characterisation data with large tolerances could not be subsequently used for quantitative ToFFASS analysis, where both ion and neutral components of the primary beam must be known accurately. A full parametric characterisation of the beam current would therefore have been inappropriate. Instead only a limited analysis of source characteristics was made in order to gain sufficient data to carry out a comprehensive analysis of the performance. A further limitation resulted from electrical breakdown of the source and power supply when operated above 3 keV. Therefore measurements were only made below this voltage. Measurements were also confined to argon. The sleeve was not fitted over the column, although the entire length of the column resided in a 36 mm diameter tube. The results reported below highlight the limitations of the source.

The pressure within the source could not be measured directly, instead an estimation was made following the basic principles introduced in section 4.4.4. As the internal source geometry was very complex from a point

of view of evaluating the conductance the calculation only offered a rough approximation. The pumping speed of the IC was dominated by the conductance of the 1mm radius extraction plate aperture which from eq. 4.18 is ~ 0.3 l/s, (argon). Recently a Monte Carlo approach to evaluating conductances of complex vacuum geometry has been developed by Sawemin et al¹⁸⁶, which

$$P_{IC} = P_B \left[\frac{\frac{1}{S_A} + \frac{1}{C_{AC}} + \frac{1}{C_{ext}}}{\frac{1}{S_A} + \frac{1}{C_{ab}}} \right] \quad - (4.21)$$

allows complex geometry to be modelled with greater accuracy. Work with this software has only recently been initiated and so the results will not be reported here.

From the principles outlined in 4.4.4, P_{IC} can be expressed in terms of the various component conductances of the system:

Where

- S_A - pumping speed of the turbo pump = 55 l/s
- C_{AC} - conductance of the full length of the pumping line
= 0.036 ($1/4 \langle v \rangle$)
- C_{ext} - conductance of the extraction plate aperture
= 0.03 ($1/4 \langle v \rangle$)
- C_{AB} - conductance of the pumping line - section between the pump and gauge head = 0.1 ($1/4 \langle v \rangle$)

In the derivation of eq. 4.21 any pumping effect of the main chamber was neglected. For example, a pressure of 5×10^{-5} mbar measured at B, indicates a throughput of 3.2×10^{-4} mbar l/s, and a source pressure, P_{IC} , of 3×10^{-4} mbar, (argon). In the case of helium Q is $\sim 1.2 \times 10^{-3}$ mbar l/s and P_{IC} is 3×10^{-3} mbar.

It can be seen from this analysis that the pressure differential between the IC and the transport column could have been significantly improved by mounting the pump directly onto the flange of the source. For the above parameters the pressure differential would be increased from a factor of 8 to 150. However, there were also a number of practical considerations: firstly

the turbo pump was not bakeable and needed to be placed outside the baking shroud. Secondly, the bellowed tubing conveniently allowed the turbomolecular pump to be mounted in fixed position whilst allowing the ion/atom source to be freely moved to any port on the chamber.

4.5.1.1 Beam current

Initial measurements of the beam current with the nickel plate, showed repeatability to be very poor: the beam current was found to drift significantly over time scales of hours, and typically varied by a factor of 2 to 3 from day to day. The pressure, P_B for maximum beam current was 3 to 5 x 10⁻⁵ mbar. All the measurements were made initially with V_{ext}/V_o set to 0.7 and V_f/V_o set to 0.9, in accordance with the prototype design calculations. In this mode of operation the maximum ion beam current, I_i , measured was ~ 60 namps. although I_i was typically less than this, 10 to 20 n amps.

In order to achieve a maximum beam current for a given beam energy, the filter voltage, V_w , must be set to its tuned value. Figure 4.12 shows experimentally determined tuned values of V_w . The solid line is the best fit to all the data points shown, and is given by

$$V_w^2 = 10.7 V_o - 400 \quad \text{-(4.22)}$$

The dependence of the total beam current, ($I_i + I_n$), on V_w for a fixed V_o is shown in figure 4.13. For both the energies shown, 990 and 2000 eV, the current reaches a maximum value at the tuned voltage, as given by eq. 4.22, however it can be seen that substantial current passes through the filter when V_w is a long way from the tuned voltage. A second peak is also clearly apparent at higher voltages, occurring at a value $\sqrt{2}$ times the main peak. Figure 4.14 shows variation of the ion and neutral current components as a functions V_w . The data was collected at low pressures, $P_B \sim 1 \times 10^{-5}$ with gas admitted to the IC only. It can be seen that the neutral current was not strongly influenced by the Wein filter, and that when the filter is de-tuned the beam was composed almost entirely of neutrals.

Another surprising result can be seen in figure 4.15, where the total beam current was measured, as the beam energy was varied for constant V_w . It

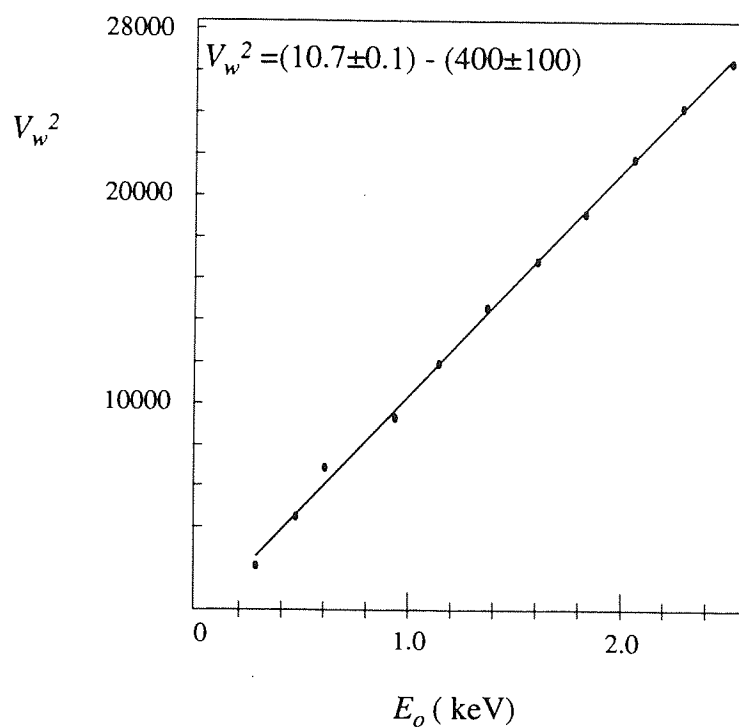


Figure 4.12 - V_w v V_o , (experimental data).

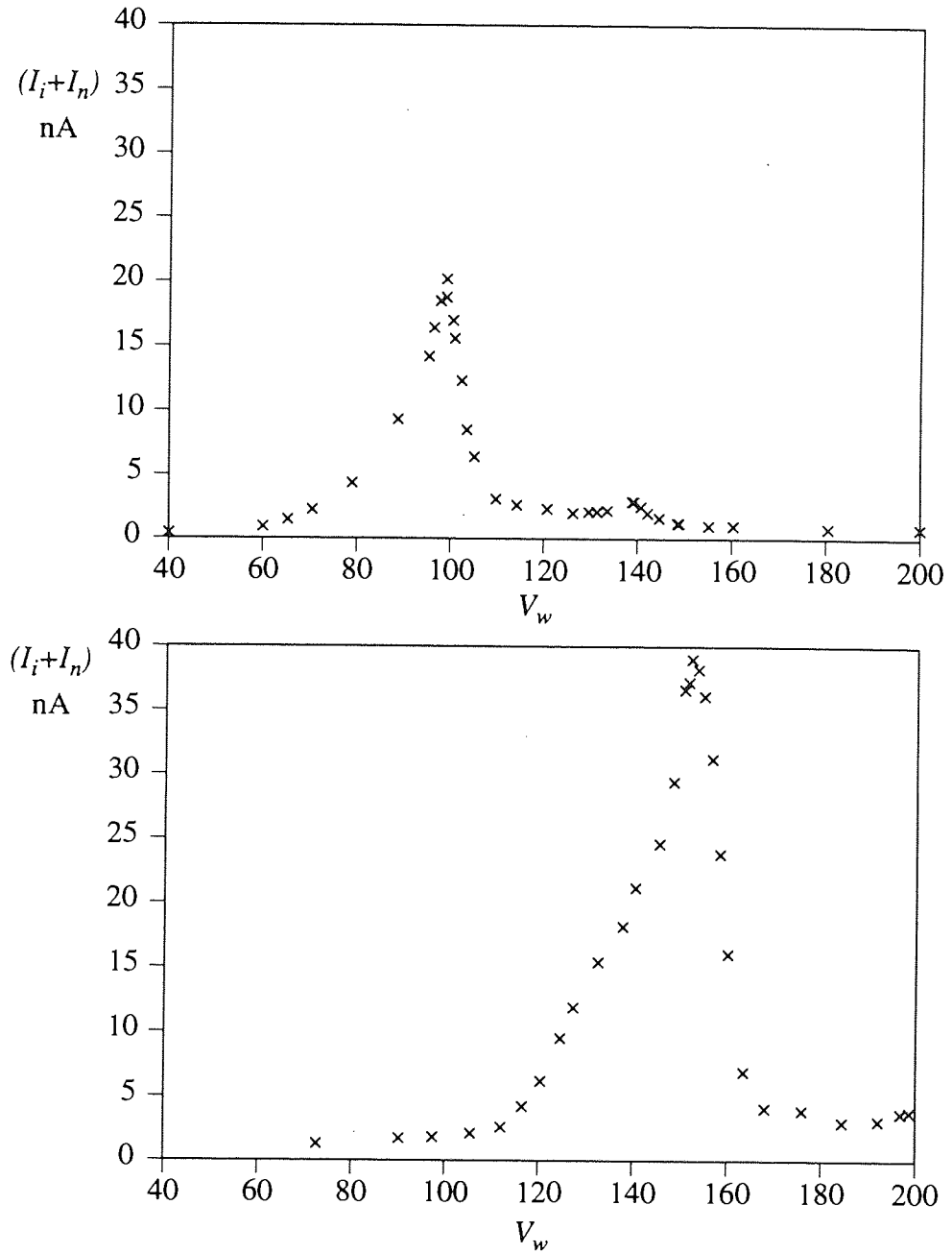


Figure 4.13 - Total beam current measured as a function of V_w
 a) $E_o = 990$ eV and b) $E_o = 2000$ eV.

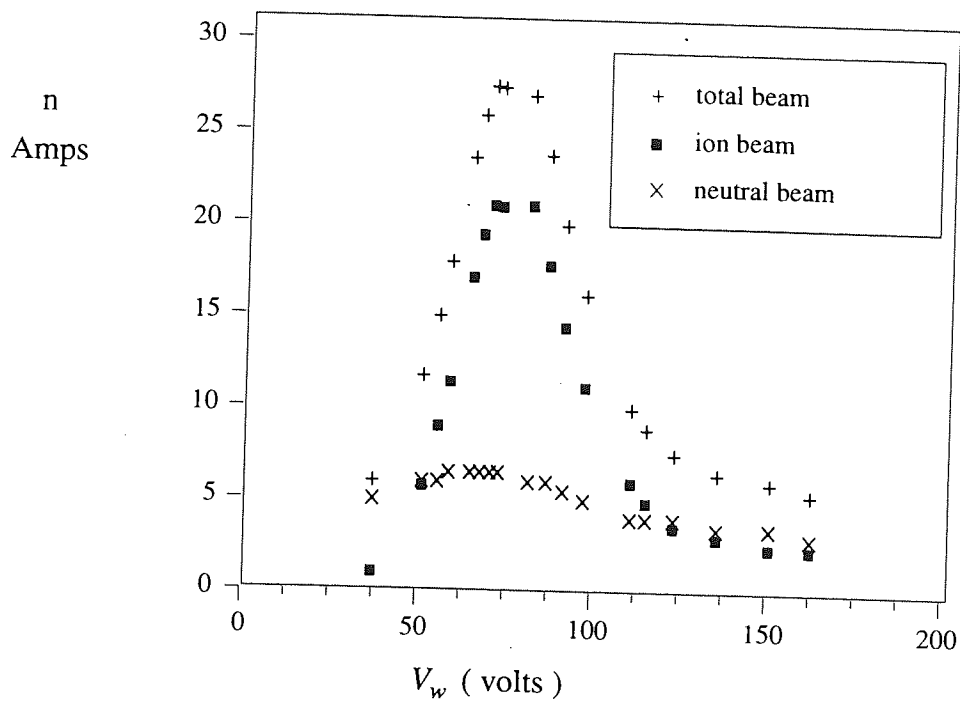


Figure 4.14 - Total, ion and neutral currents, as a function of V_w .
 Conditions: - $E_o = 560$ eV, Ar supplied to IC only, $P_B = 1 \times 10^{-5}$ mbar.

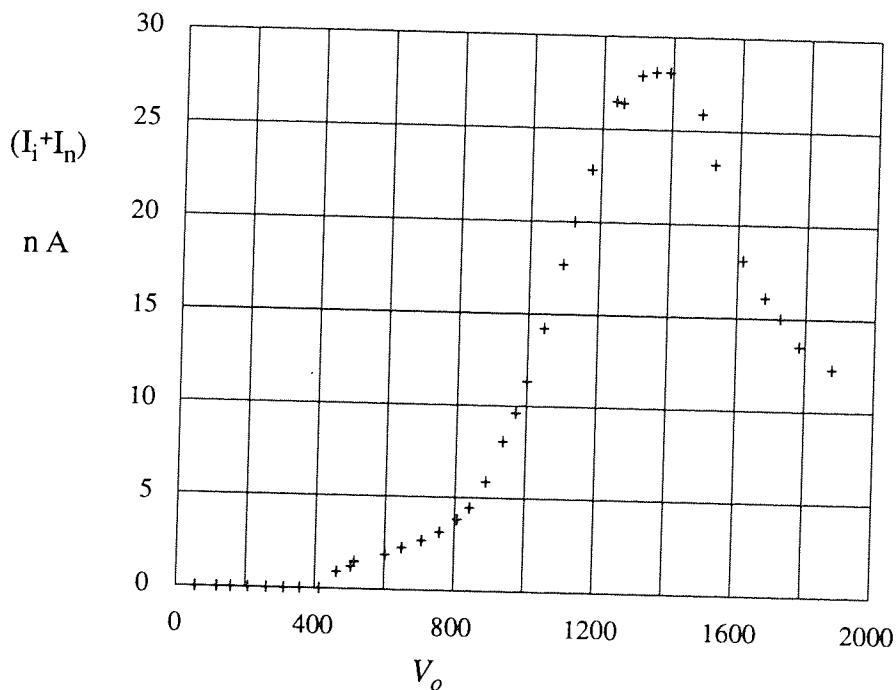


Figure 4.15 - Total beam current as a function of V_o for a fixed V_w of 96 V, (the tuned voltage for $E_o = 900$ eV), $P_B = 2 \times 10^{-5}$ mbar.

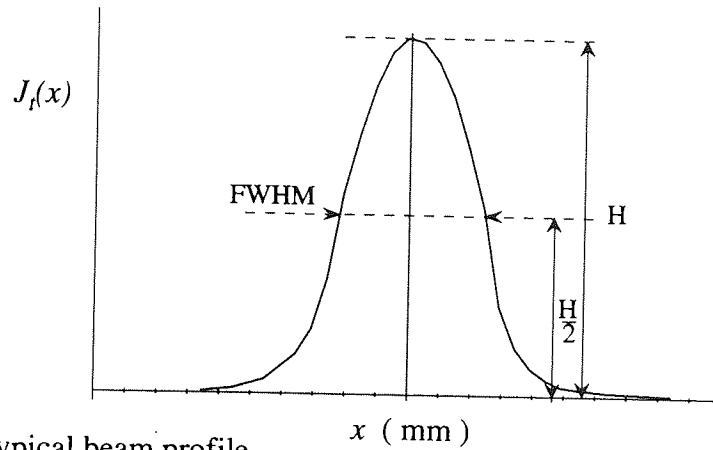


Figure 4.16 - Typical beam profile

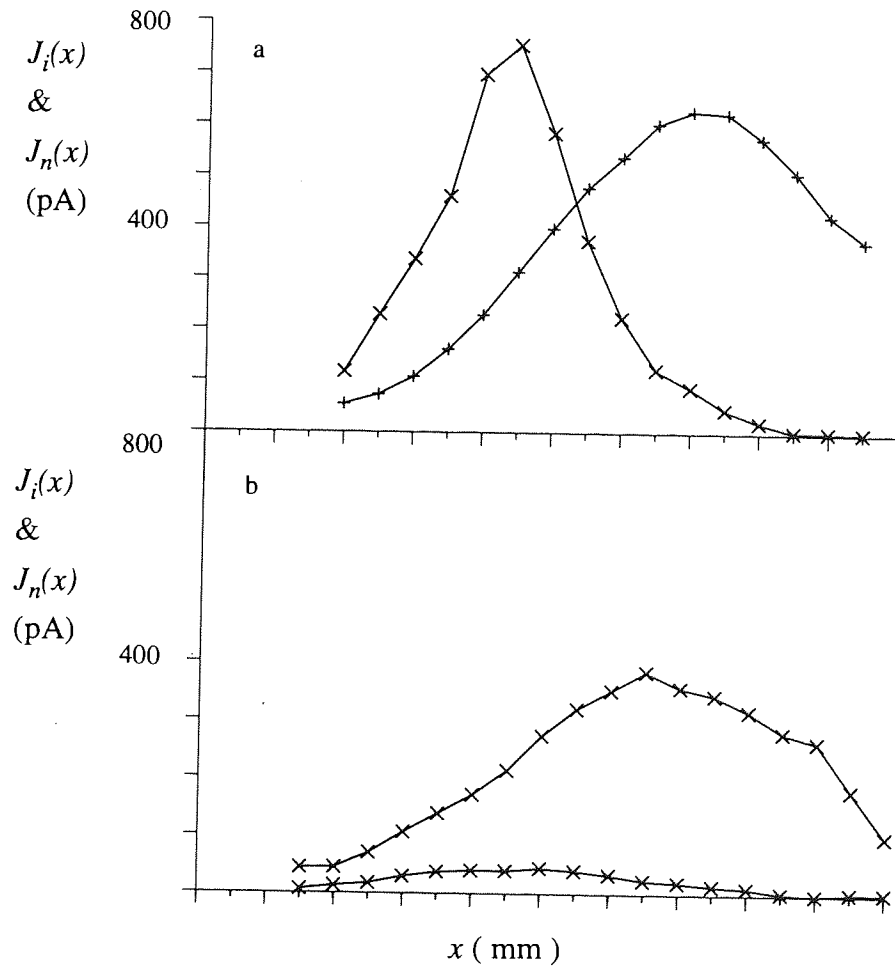


Figure 4.17 - Beam profile data, $E_o = 2000$ eV, Wein filter tuned at $V_w = 145$ V, $P_B = 9 \times 10^{-5}$ mbar, (x ion beam, + atom beam).

(a) Ar supplied to IC only.

(b) Ar supplied to CEC only.

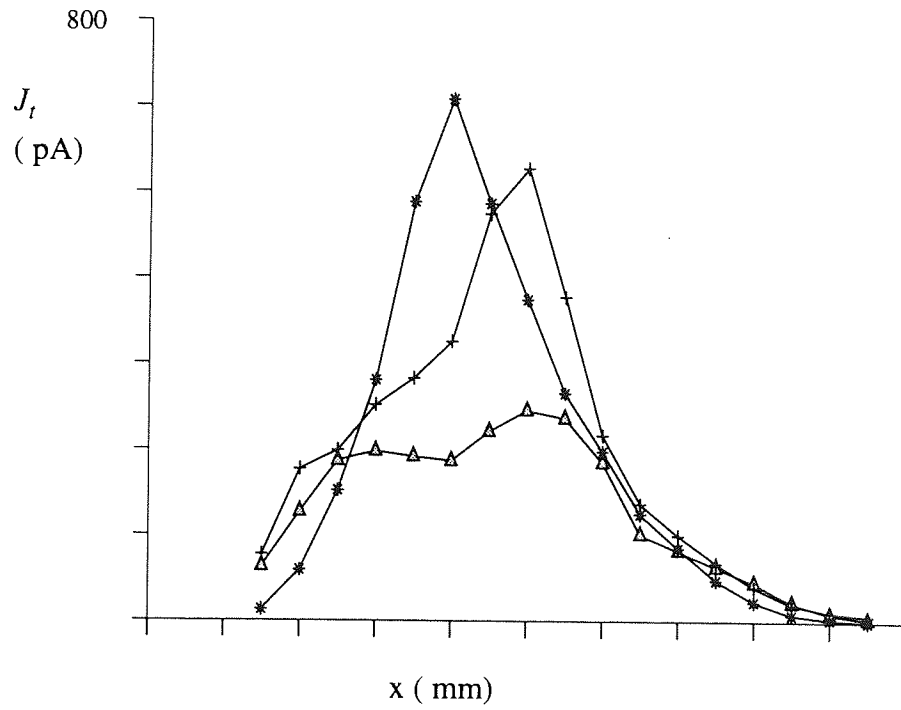


Figure 4.18 - Beam profile dependence on V_w .
 Conditions: $E_o = 1980$ eV, $P_B = 9 \times 10^{-6}$ mbar.

- * - $V_w = 140$ V
- + - $V_w = 150$ V
- triangles - $V_w = 180$ V

was expected that the current would peak at beam energy of 900 volts (the energy at which the filter becomes tuned). However it can be seen that the current continues to rise to $V_o = 1300$ eV.

Finally, the beam current was measured with V_{ext}/V_o and V_f/V_o set to zero. In this mode of operation the first lens is effectively switched off, however it was found that greater values of I_n and I_i could be achieved in this mode.

4.5.1.2 Beam profile

A total beam profile measured with the apparatus of figure 4.8, is shown in figure 4.16, at a working distance of 150 mm. It can be seen that the profile width is broad, ~ 5 mm. In this instance the beam profile is symmetrical, however, the shape of the profile was subject to significant drift, and could only be accurately reproduced over short time scales.

The ion and neutral beam component profiles, $J_i(x)$ and $J_n(x)$ are shown separately in figure 4.17. (a) shows the profiles resulting when gas was admitted to the IC only, with the pressure, $P_B = 9 \times 10^{-5}$ mbar, which was found to be the optimum pressure for production of the largest neutral current. In this case the two components are approximately equal in intensity, that is $\sim 50\%$ of the beam was neutralised. $J_n(x)$ is significantly broader than $J_i(x)$, 5.5 mm, compared to 2.5. Figure (b) shows the profiles when gas was admitted to both gas cells, with the pressure P_B unchanged, and the analysis chamber pressure, $P_{chamber}$ increased. In this case $J_n(x)$ was much greater than $J_i(x)$, and the width of $J_i(x)$ increased to 4 mm. Neutralisation of the ion beam in this case approached $\sim 100\%$. In both cases the centres of the ion and neutral beams were displaced by ~ 3 mm. This displacement did not originate from a voltage on the x-y plates. Possible origins are discussed in later sections.

The profile shape was also found to be strongly dependent on V_w , as can be seen from figure 4.18. In this case the gas was admitted to the IC only, with the pressure conditions favourable for ion beam production, (P_B was 9×10^{-6} mbar). $J_{mi}(x)$ was recorded for a wide range of V_2 . The beam width was found to be virtually independent of V_2 . As the full width of the beam, ~ 6 mm, was greater than the width of the final aperture of the source the beam was clearly divergent.

4.5.1.3 Primary spectra

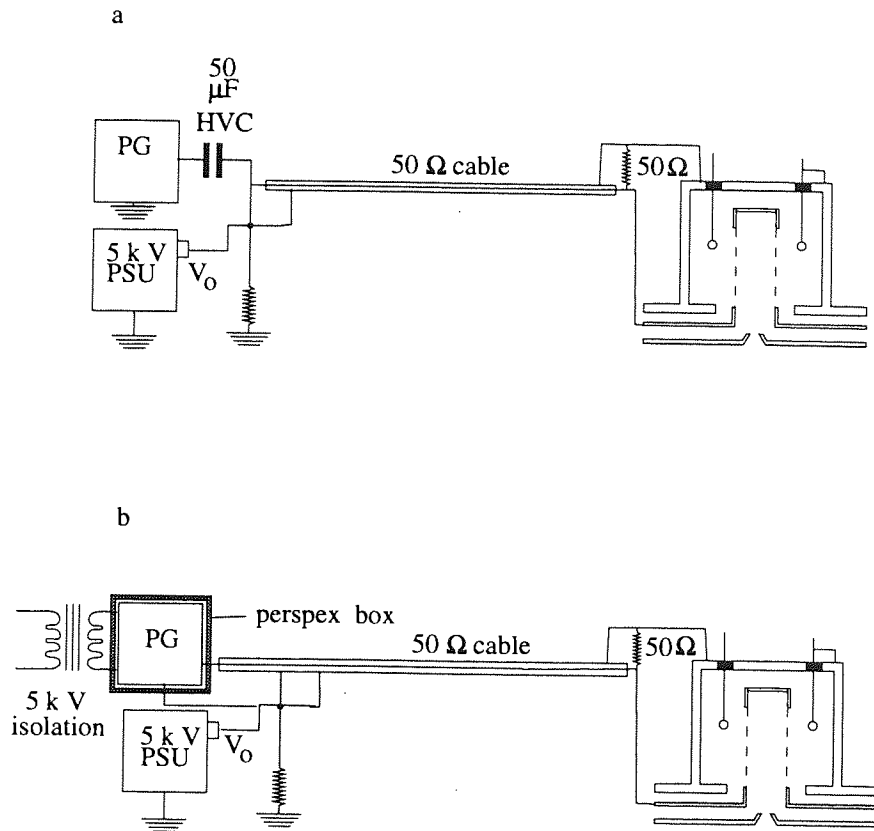


Figure 4.19 - Pulsing Circuits employed to pulse the prototype FAB source
(a) capacitive coupling
(b) direct coupling

Spectra were initially collected with the pulse generator coupled to the ion cell via a 50 μF high voltage capacitor, as shown in figure 4.19a. This was later changed to the directly coupled arrangement, shown in figure 4.19b, in which the pulse generator was floated at the filament potential, and the start pulse for timing circuitry brought to ground potential through an opto-isolator. For this it was necessary to enclose the PG in a perspex box. However, no noticeable difference could be seen in the primary spectrum as a result of this change in pulsing method. Regardless of the coupling method, the resulting spectra consisted of very broad peaks with complicated fine structure. All spectra shown were collected using a HP, model 214A pulse generator as the primary pulse source, which has a minimum pulse width of ~ 100 ns. Attempts to generate spectra using a pulse generator producing a fixed duration pulse of ~ 2 nano seconds were unsuccessful. In this case the pulse duration was too short to accelerate the electrons to their full energy.

For these measurements it was important to operate the source at much lower pressures than those employed for the DC measurements: this consideration along with other details of the spectrometer are discussed in chapter V. However, it is important to note here that only one event is registered following a START pulse. Therefore, if the mean number of ions striking the detector per pulse approaches or exceeds unity, the counting statistics of the spectra will become biased towards short flight times. Thus to ensure unbiased counting statistics, the number of counts striking the detector should be less than $1/f$, where f is the chopping frequency. For f of 20 kHz, this is equivalent to a current of 3 femto amps. A further experimental complication concerns the alignment of the flight tube and the optical column. As it was not possible to control the focus of the primary beam, particles could not be prevented from scattering from the walls of the flight tube.

The effect of biased counting statistics is illustrated in figure 4.20, the two spectra, (a) and (b), were collected with identical settings, other than the beam current, which was significantly lower for (b). It can be seen that the biased counting statistics make the peak appear significantly narrower than it is in practice. Thus all subsequent spectra were acquired with the collection rate of (b) and therefore have unbiased counting statistics.

There are a number of further important points that must be made concerning figure 4.20b. The time of flight of 1keV argon over the flight path of 2500 mm, is 33.8 μs , whereas, experimentally, the leading edge is observed at 36.1 μs . This discrepancy cannot be attributed to the uncertainties in the

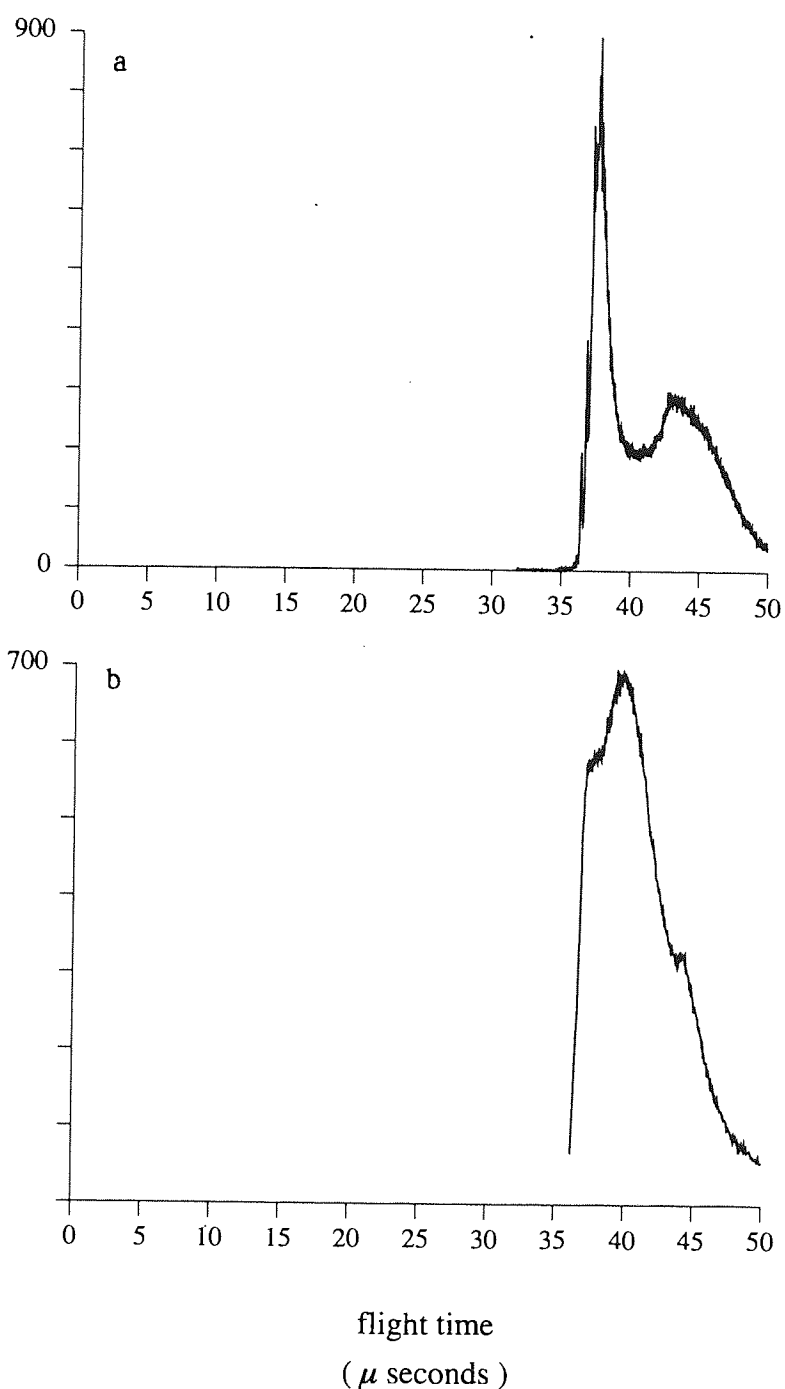


Figure 4.20 - Primary Spectra, - (prototype source), showing the effect of bias counting statistics.

(a) detector current > 1 particle/pulse

(b) detector current < 1 particle/pulse

$E_0 = 1000$ eV

primary energy and flight path. The origin is discussed in the following sections. The peak width is $6.5 \mu\text{s}$, giving rise to very poor instrumental resolution, ($\Delta t/t = 0.16$). It can also be seen that the spectrum is composed of at least two, and possibly three peak. The peaks appearing at $\sim 43 \mu\text{s}$, which is resolved in (a) is attributed to particles that have scattered from internal components of the source or spectrometer.

The relative size of the scattered peak was found to be sensitive to the source orientation and small changes in the x-y deflection voltages, therefore indicating that the scattered peak, at least in part, originated from scattering in the flight tube. The scattered peak in figure 4.20b exhibits a double structure, indicating that scattering is taking place at least at two positions along the flight path. The scattered peak was also found to be sensitive to the voltage setting of the Wein filter: It was seen that de-tuning, the resulting filter caused the spectrum to be composed mainly of neutrals. As the source pressure was very low, it is unlikely that this neutral beam resulted from gas phase charge exchange collisions.

The voltage setting of the extraction plate was also found to have a significant influence on primary spectra. It was seen that reducing V_{ext} and V_J to zero, resulted in a significantly sharper initial peak, although the broad scattered peak remained. This initial peak was also followed by a large number of equally spaced subsidiary peaks. The spectra in figure 4.21 were collected with identical settings with the exception of V_{ext} and V_J , (a) $V_{ext} = V_J = 0$, (b) $V_{ext} = 0.7V_o$, $V_J = 0.9V_o$. The width of the initial peak in (a) is 170 ns, compared to $\sim 1.5 \mu\text{s}$ in (b). The origin of the fine structure was attributed to ringing in the pulsing circuit.

To identify the origin of the broad spectral peaks a different method of beam chopping was tested. The new method was achieved by application of a pulsed waveform to the x-y deflection plates, in order to deflect the beam away from the flight tube port. The port therefore acted as a beam chopping aperture for the purpose of this trial. (36 mm at distance of 300 mm from the x-y plates). The flight distance, L was effectively shortened to ~ 2250 mm.

A spectrum resulting from this trial arrangement is shown in figure 4.22. It can be seen that the spectra consist of much sharper peaks occurring very close to their expected flight time. Here the duration of the chopping pulse was in this case $\sim 1 \mu\text{s}$. The large continuous background count rate results from the formation of neutrals prior to x-y plates, and the two smaller peaks to shorter flight times are in the right positions for O_2 and CO species.

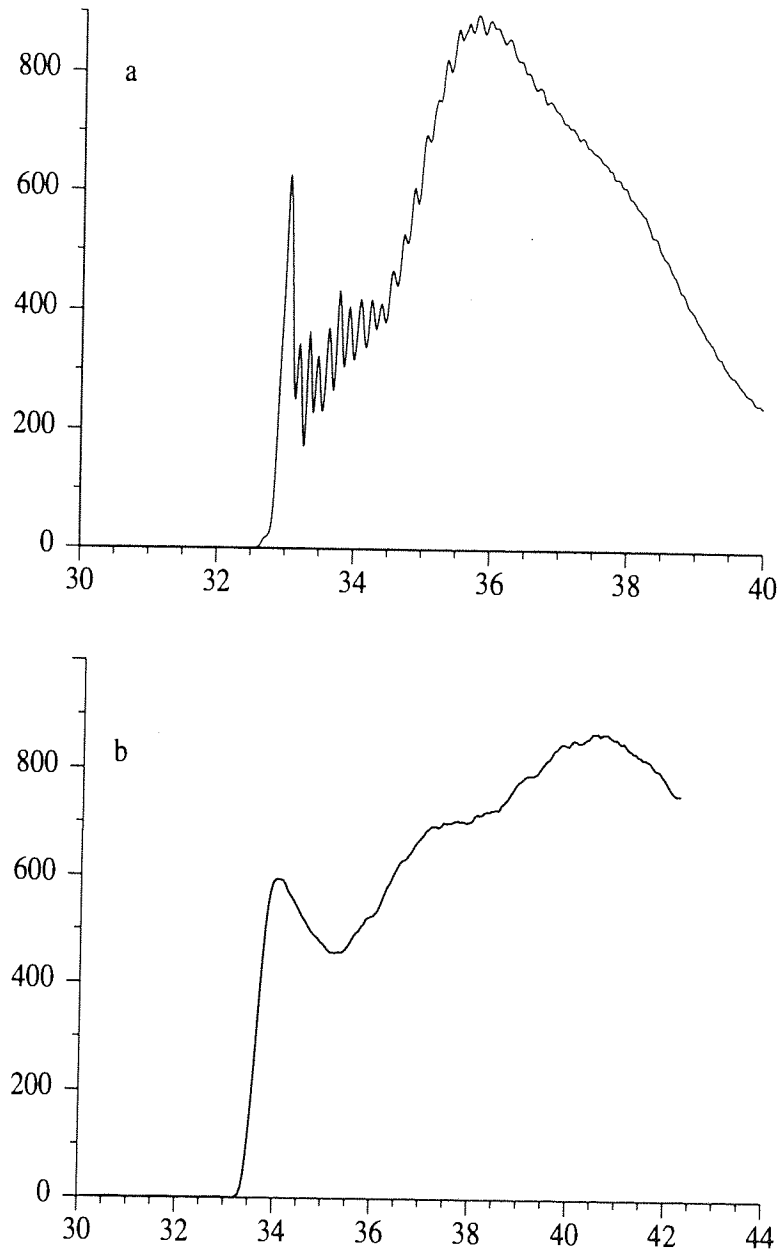


Figure 4.21 - Primary ion spectra, - (prototype source) - dependency on V_{ext} , (calculated flight time = $32.7 \mu s$).

$E_o = 1140 \text{ V}$.

(a) $V_{ext} = 0, V_I = 0$

(b) $V_{ext} = 0.7 V_o, V_I = 0$

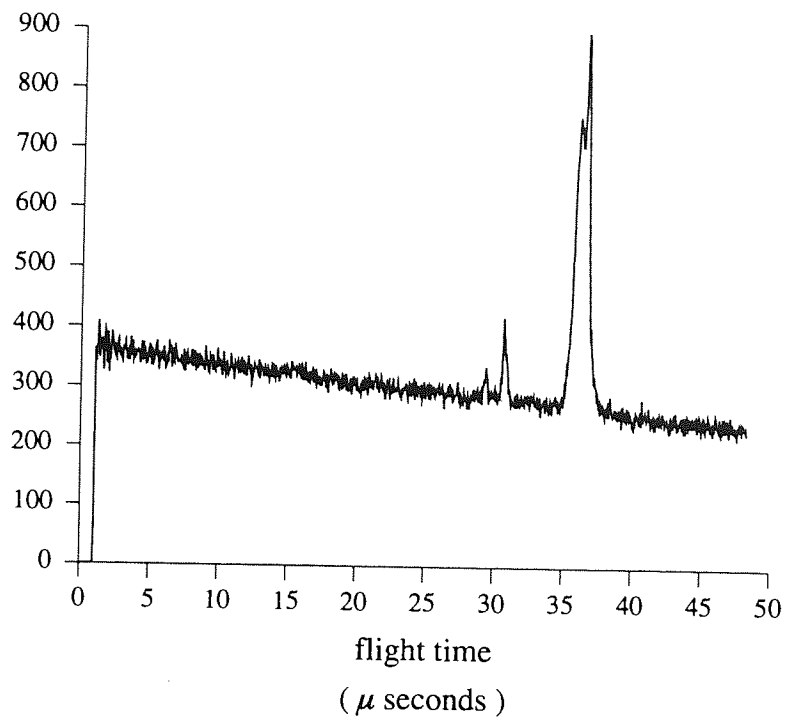


Figure 4.22 - Primary spectrum resulting from the pulsing the x - y deflection plates, - (prototype source), $E_o = 720$ eV.

4.5.2 Limitations of the prototype source

The experimental data reported above revealed a number of severe limitations of the prototype source: the beam profile was too broad, there was no control of width or position of focus, and the spectral peak width was too large. The latter was the most prohibitive limitation, making the source completely unusable for scattering applications. Additionally the Wein filter had poor mass separating power, and appeared to be the origin of an additional spectral peak. Also the maximum current output was low, typically only a few tens of nano amps, much lower than that achieved with other electron impact sources of similar construction. It was therefore necessary to address these problems before the programme could proceed further. In the following sections the measured characteristics are analysed in detail, and the origin of the unsatisfactory performance discussed.

4.5.3 Analysis of Prototype Characteristics.

4.5.3.1 Ion Source and extraction optics

The ion source of the prototype is similar in principle to those employed in a number of commercial sources used for low current analytical applications, but has not been reported in the literature. Thus to gain a better physical understanding a computer simulation model was constructed¹⁸⁷, the basic physical scenario of this model is described below.

As the ionisation region from which ions are extracted is shielded from the anode-cathode field by the anode grid no plasma is formed. For the purpose of the simulation and calculating the electrical potential the ion source was divided into the two regions, A and B as shown in figure 4.23, corresponding to the regions inside and outside the grid. Broadly speaking, the field within A determines the trajectories of ions, whilst the field in B determines the trajectories of the impacting electrons. The electrical potential in both regions is most conveniently described by cylindrical polar co-ordinates, r and z . Due to the cylindrical symmetry, the θ component is redundant. Approximate calculations demonstrated that the free charge density could be neglected, allowing the E field to be found by Laplace's equation¹⁸⁸.

The ionisation probability distribution within region A is dependent upon the energy and spatial distribution of electrons accelerated from the

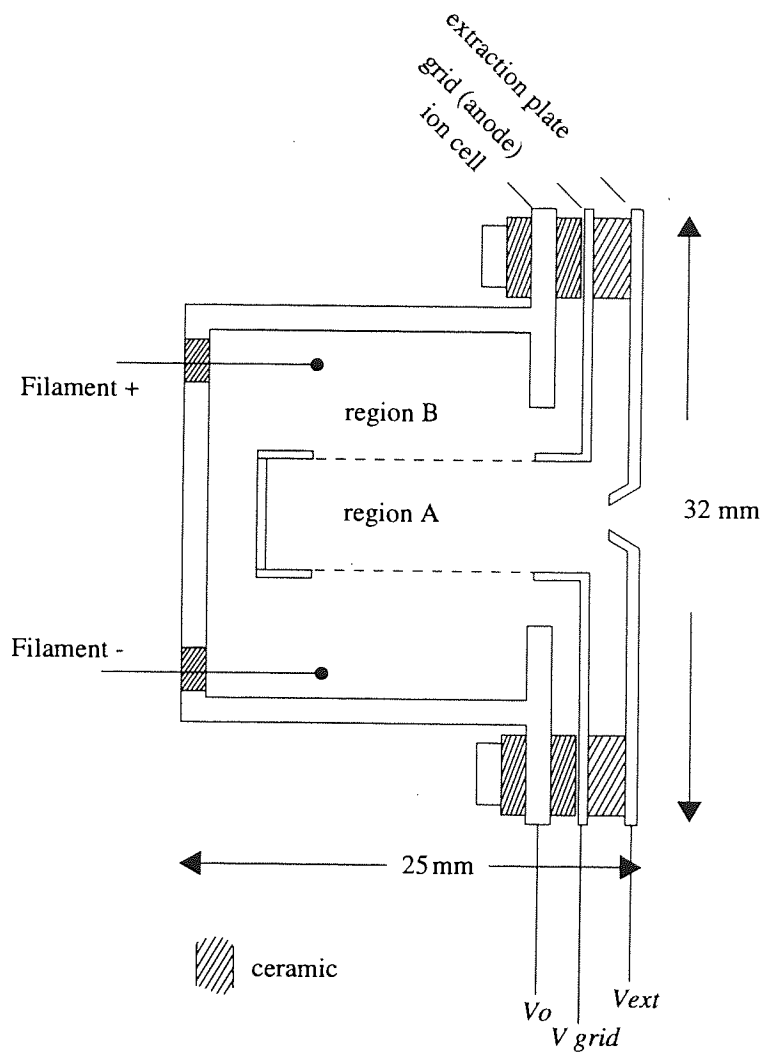


Figure 4.23 - Detail of prototype ion source

filament, which is determined by $E_B(r,z)$. For full details of electron trajectory simulation the reader is referred to the work of Lanyi and Pearce¹⁸⁸, where $V_B(r,z)$ was solved by finite difference methods involving special treatment of the field in the region of the filament. The macroscopic collision cross-section for ionisation, $\Sigma_i(E)$, is given by the product of the microscopic cross-section for ionisation, $\sigma_i(E)$, and the density of gas atoms:

$$\Sigma_i(E) = n\sigma_i(E) \quad -(4.23)$$

The mean free path length between collisions is given by:

$$\lambda = 1/\Sigma_i(E) \quad -(4.24)$$

and the ionisation probability is the product of the electron flux, $\phi(r,z,E)$, and $\Sigma_i(E)$:

$$P_i(r,z,E) = \int \Sigma_i(E) \phi(r,z,E) dE \quad -(4.25)$$

From the simulation it was seen that the majority of the electron momentum is contained in the radial component, and so electrons produced at the filament perform a simple harmonic type motion in a radial plane, before colliding with an electrode after ~ 4 oscillations; see figure 4.24, which shows the electron trajectories for $P_{IC} = 5 \times 10^{-3}$ mbar, and 100 volts between the filament and grid. The mean free path for an ionising collision, λ_i in this case was ~ 200 mm, which gave rise to an ionisation efficiency of only 0.5 to 1 %.

$P_i(r,z)$ was calculated by a three dimensional (r,θ,z) Monte Carlo simulation of electron trajectories, and $\phi(r,z)$ was found to have a complex spatial distribution. The example shown in figure 4.25 was calculated for the prototype source geometry, and shows the regions of highest ionisation probability. It can be seen that $P_i(r,z)$ is not well defined axially, and that ions may be formed over a region of ~ 10 mm, with the region of maximum probability occurring in a disc, at a distance of 10 mm from the back of the grid.

A two dimensional, (r,z) , Monte Carlo simulation of the ion trajectories was made to assess the properties of the extracted beam. The potential, $V_A(r,z)$, was generated using finite element methods. The following

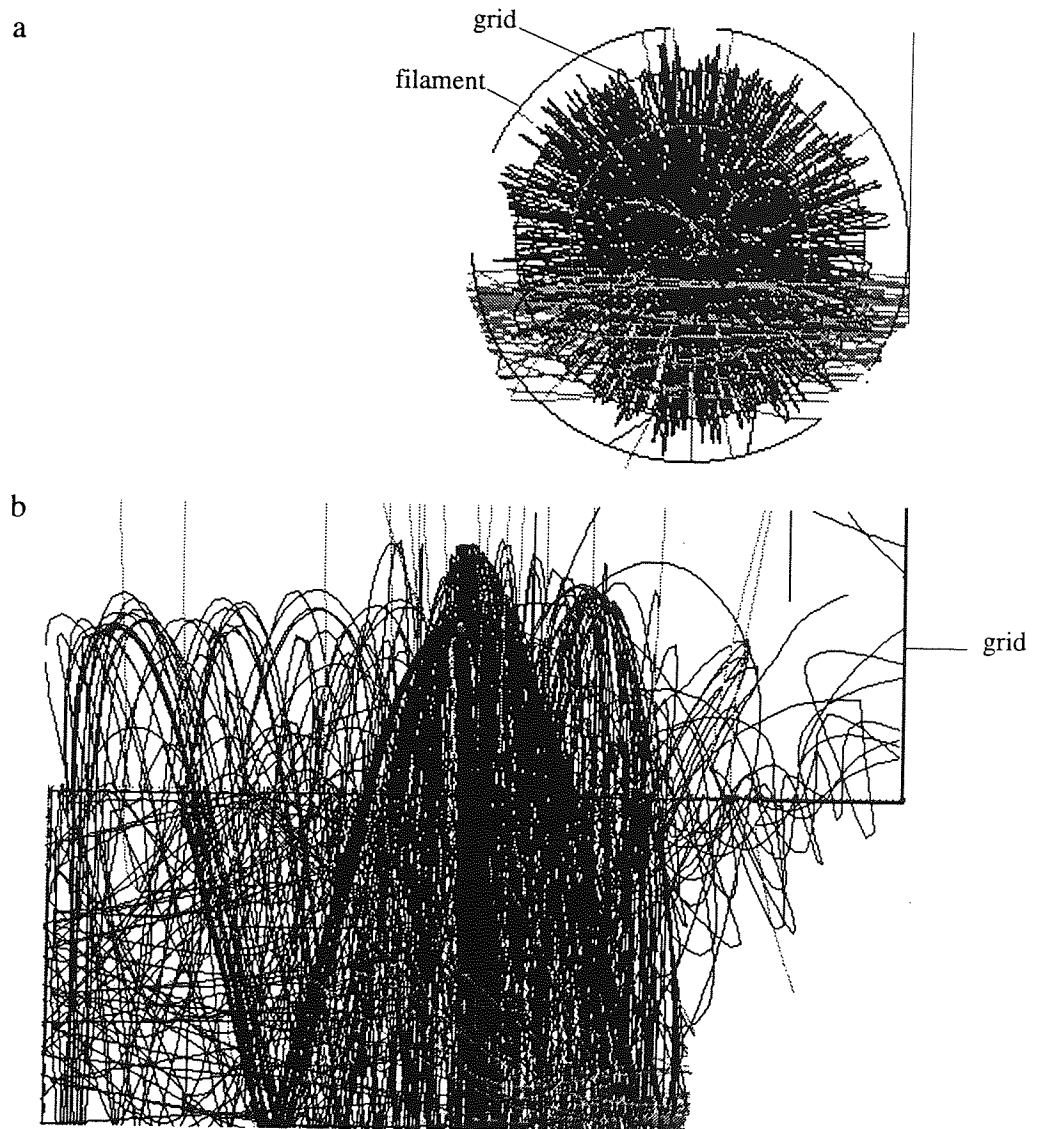


Figure 4.24 - Simulated electron trajectories in the ion cell
(a) shown in the $r-\theta$ plane.
(b) shown in the $r-z$ plane. (only half the cell shown)

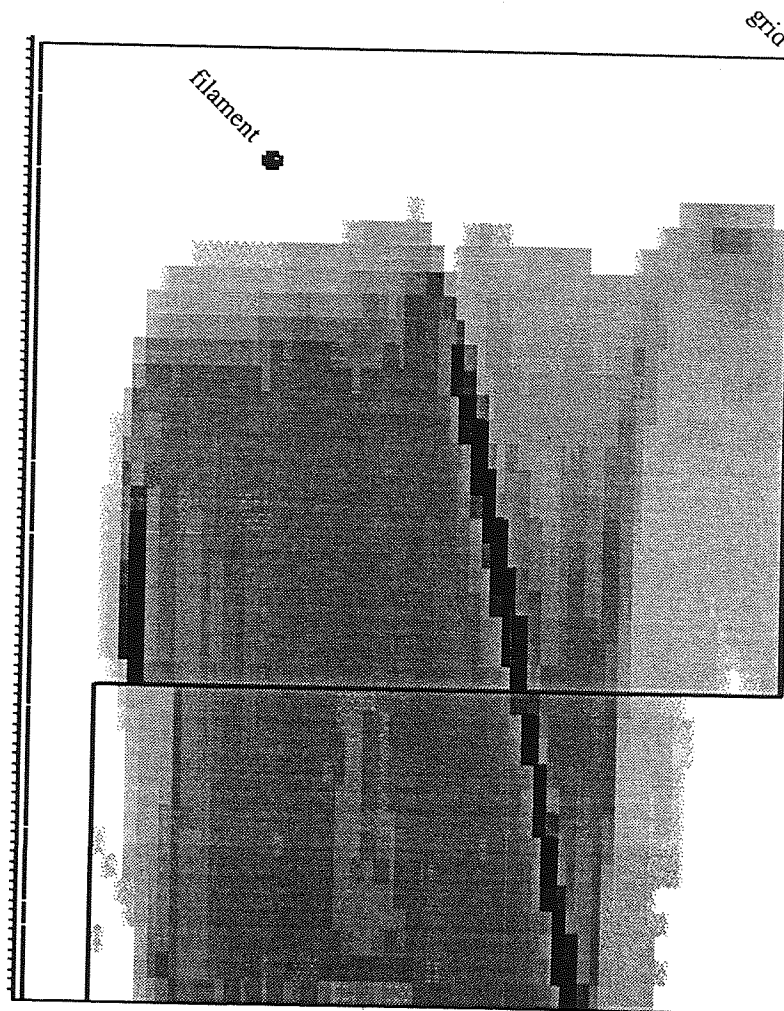


Figure 4.25 - Ionisation probability $P_i(r,z)$, calculated by Monte Carlo simulation of electron trajectories. The darkly shaded regions correspond to regions of greatest ionisation probability. (Only half the cell is shown.)

initial conditions for the ion trajectories were employed in the simulation.

- a] positional co-ordinates - given by $P_A(r,z)$
- b] energy - Maxwellian velocity distribution
($T=1000$ k)
- c] direction - given by $2\pi\text{RND}(1)$

where $\text{RND}(1)$ is a random floating point number between 0 and 1, and $P_A(r,z)$ was approximated by two gaussian functions, one axially and one radial. Inter-particle collisions were not considered. The results of this simulation model are discussed below:

Extraction times.

The broad experimental spectra indicated either large energy or large times spreads, or possibly a contribution from both. However, it was not possible to separate these contributions using the ToF spectrometer and the origin of the broad peaks could not be identified from the experimental data alone. The above simulation model was employed to resolve this problem.

Once ions are created in the IC they are accelerated towards the extraction plate, and the acceleration time contributes to the total flight time. The above simulation was employed to calculate the spread in extraction times, and the results are shown by the histogram of figure 4.26, where the conditions were $V_o = 1$ kV and $V_{ext} = 0.7 V_o$. The spread in times results from variations in initial position and velocity, the latter being dominant for ions originating towards the back of the cell. It can be seen that the calculated spread in acceleration times corresponds well with the peak widths of the ToF spectra, and the minimum calculated extractions time corresponds to the observed time discrepancy between experimental peak positions and the expected flight times. From this result it was concluded that the main contribution to the ToF peak widths is a large dispersion in flight times originating from this larger variation in acceleration times from the ion source. Good agreement was also achieved when the simulation was repeated for $V_{ext} = 0$.

The simulation program was also used to estimate the energy spread of extracted ions. As the final energy of an individual ion is largely determined by its initial position within $V_A(r,z)$ the calculated energy spread is strongly influenced by the assumed distribution of initial positions, $P_A(r,z)$. For

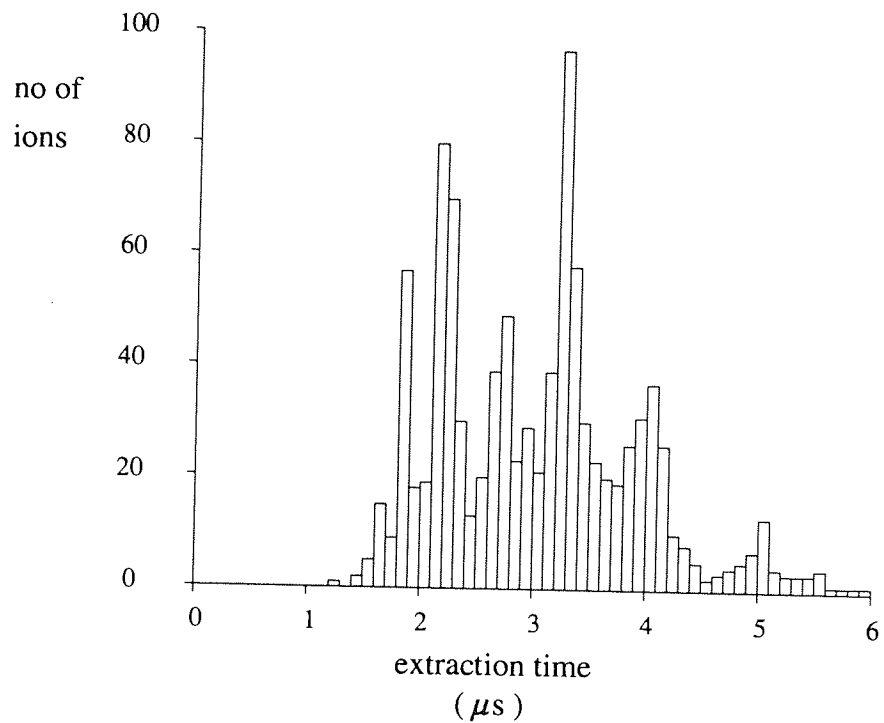


Figure 4.26 - Histogram showing the extraction time distribution. for conditions $V_o = 1$ kV and $V_{ext} = 0.7 V_o$. Calculated for 1000 ions.

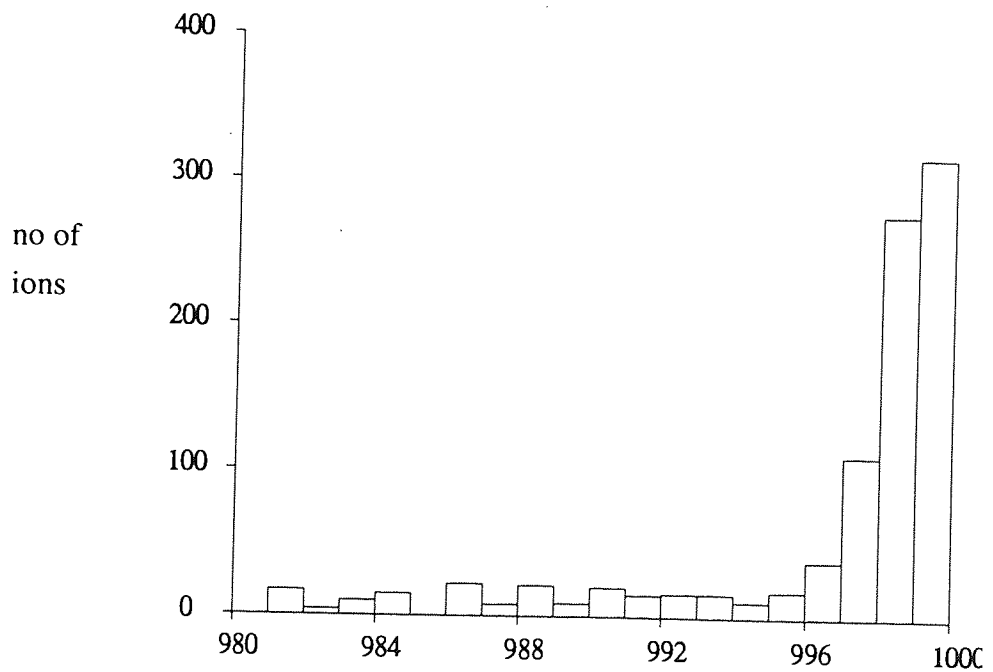


Figure 4.27 - Histogram showing the energy distribution of extracted ions. Conditions $V_o = 1$ kV and $V_{ext} = 0.7 V_o$. Calculated for 1000 ions.

the result shown in figure 4.27, the initial conditions were $z=8$, $\sigma_z = 2$ mm, $r=0$ and $\sigma_r = 1$ mm. It can be seen from the figure that the spread in ion energies was low, ~ 2 eV, for $V_o = 1$ kV, $V_{ext} = 0.7V_o$ giving rise to $\Delta E/E_o$ of 0.2%.

In conclusion, the analysis showed that the broad primary peaks originated from the spread in the acceleration times, and therefore were a feature of the chopping method. It was therefore clear that the chopping method was unsatisfactory. A similar chopping approach was investigated by Van De Gift¹⁷², where similar conclusions were drawn.

Emittance of the extracted ion beam

Ion trajectory calculations were performed in order to find the shape of the emission cone, which is most conveniently expressed by a phase emittance diagram. Simulated diagrams of this kind are shown in figure 4.28. For the case shown, the conditions were: $V_o = 1$ kV, $V_{ext} = 0.7 V_o$. It can be seen that the beam is well distributed in phase space, with the beam width occupying the full diameter of the extraction plate aperture. For these standard conditions $\sim 60\%$ of the beam is contained within a radius, r_s of 0.3 mm, and divergence angle, $\alpha_s \sim 6^\circ$. Again initial ion positions and velocities are influential on the result.

Discussion of the source brightness.

The measured beam current was very low in comparison to other electron impact sources of a similar design, where continuous beam currents of $\sim 10 \mu$ amps, are obtained. However, the simulation model cannot be used to calculate brightness, as the calculated ion probability density distribution represents relative probabilities only, and neutralisation and scattering losses are not considered by the model. Re-neutralisation may arise from resonant charge transfer (RCT). The net flow of electrons from the cathode to anode is given by the emission current, I_e , which was typically 20 mA. Clearly if every electron initiated an ionisation event, and the extraction efficiency were 100%, the extracted ion beam current would also be 20 mA. The ion cell simulation predicted the probability of ionisation for individual electrons to be 0.5 to 1 %, and the extraction efficiency to be 86%. This corresponds well to direct measurements of the extracted beam current. However, the extracted ion current was found to have a strong dependence on the extraction voltage, which

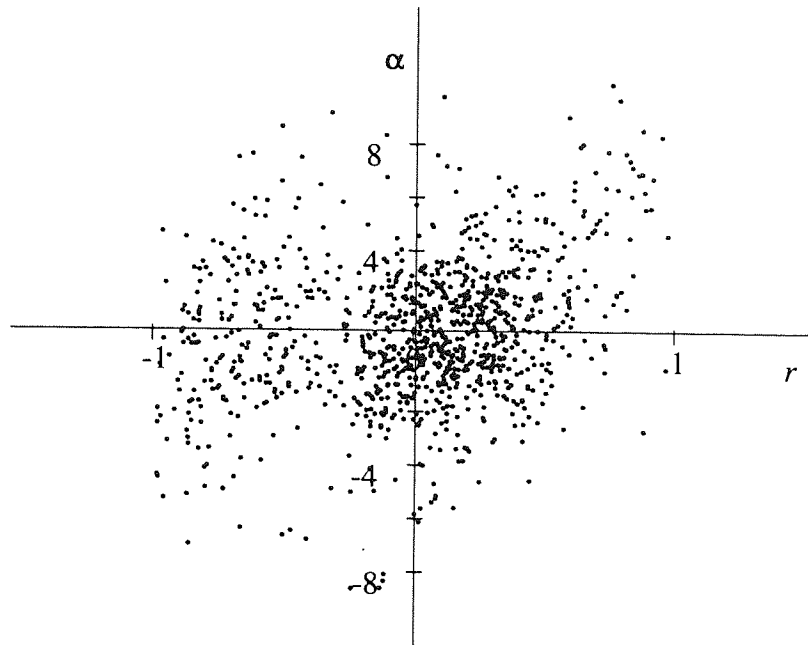


Figure 4.28 - Simulated phase space emittance diagram of the extraction ion beam. - Calculated for 1000 ions - each point in the diagram represents a single ion.

Conditions:- $V_o = 1$ kV and $V_{ext} = 0.7 V_o$

could not be explained in terms of the extraction efficiencies predicted by the simulation. This indicates that the neutralisation of ions before extraction must play an important role in determining the source brightness, but cannot account for the low output current which was in the nano amp range, and this must be attributed to losses in the transport column.

The pressure P_c in the transport column was estimated, in section 4.4.4, to be $\sim 0.1 P_{IC}$, which gives a mean free path between RCT collisions of 220 mm. At this pressure elastic scattering is not significant. Given that the full length of the transport column is 300mm, and there is little or no pressure differential along its length then the probability of neutralisation of an ion travelling the full length of the column is ~ 0.75 . Thus assuming the pressure calculations to be correct, neutralisation significantly reduces the brightness of the extracted beam. Clearly, a proportion of those ions neutralised will contribute to a neutral beam. The gas phase RCT process and associated cross-section is discussed in greater detail in section 4.5.3.4. The remaining losses must be attributed to the optics of the transport column and these are discussed in the following section.

From the above considerations one would expect the brightness to reach a maximum value at a given pressure due to competition between the ionisation and subsequent re-neutralisation of the pre and post extracted beam. This behaviour was observed experimentally in this work and also by Xu et al¹⁸⁵ and Eccles¹⁷³. A similar theory was put forward by Carlston and Magnuson¹⁸⁹ who observed a shift with pressure giving maximum I_b to lower source pressures as the differential pumping speed was increased.

4.5.3.2 The optics

Analysis of the ion optical system of the prototype was made in order to interpret the beam profile measurements, and low observed output current.

The source parameters α_s and r_s impose a fundamental limit of the final beam diameter, which can be calculated from eq. 4.6. As the brightness is unknown, it is most convenient to work in terms of (B/I_b) which is also unchanged as the beam propagates through the transport system, (in the absence of apertures). Equating (B/I_b) at the source and target gives:

$$r_{t \min} = (\alpha_s \cdot r_s) / \alpha_t \quad -(4.26)$$

Thus, for $W=200$ mm and a 2nd lens diameter of 5 mm, the minimum beam radius at the target, achievable with no transmission losses is 2.9 mm. This is the minimum achievable radius in the case of an ideal lens system. It is purely co-incidental that this result is in agreement with the experimentally observed beam diameter: consideration of the source geometry shows that the beam radius at $W=200$ is limited to ~ 3 mm by the final aperture of the source.

In order to calculate the beam diameter that would be expected, in the case of the prototype optics, in the absence of limiting apertures, the optical properties of the two lenses were evaluated individually using the Munro lens simulation program package. In the case of the primary lens, $V_1/V_o = 0.9$ gives $f_1 \sim 9$ mm, the distance between the extraction plate aperture and the principle plane. The second lens provides a focal length of 200 mm at $V_2/V_o = 0.45$. Thus these voltage conditions operate the 1st and 2nd lens in infinite and zero magnification modes respectively, giving a magnification for the combined lens system of f_2/f_1 . From the above values this gives $M = 21$. Thus for $r_s = 0.3$ mm an image radius, r_t of $0.3 \times 21 = 6.3$ mm must be expected, in the absence of limiting apertures.

If the focal lengths f_1 and f_2 are varied by changing the respective lens voltages, the magnification is given by eq. 4.12, and the image position, q_2 , can be estimated by Newton's formula for thin lenses:

$$q_2 = \left(\frac{1}{f_2} - \frac{1}{\left[d - \frac{1}{\frac{1}{f_1} - \frac{1}{p_1}} \right]} \right)^{-1} \quad - (4.27)$$

Where d is the distance separating the object planes of the two lenses. Eq. 4.27 is shown graphically in figure 4.29 for parameters; $f_1=9$, $f_2 = 200$, and $d=200$ mm. It can be seen that the object plane is extremely sensitive to the image position, particularly in the region of $q_1 = f_1$. This provides an alternative approach to predicting beam size at the target for given source and lens conditions. If the source is considered to consist of a series of point sources distributed on the axis in the region of the extraction plate, the corresponding distribution of image positions may be calculated from eq. 4.27. Such an object position distribution could be readily calculated from the simulation model, and a corresponding histogram is shown in figure 4.30. For ion trajectories that do not cross the axis, the position is located by extrapolation. Distributions were found to be equally broad for all conditions of normal operation. From this it can be seen that only a small fraction of the extracted beam is brought to a focus at a working distance of 200mm, indeed only a small fraction of the distribution at $z=0$ mm would be transported from the column. This highlights an origin of substantial beam current loss. This analysis also provides a possible explanation for large drift in beam current: as the characteristic of the combined lens system shown in figure 4.39 effectively contains a singularity, a very small change in the object position is required to produce a very large change in the image position.

This analysis reveals a fundamental problem in the prototype optics, which had to be resolved before the work of the programme could proceed.

4.5.3.3 The primary beam filter

The experimental data described in section 4.4.2 demonstrated that the Wein filter provided a degree of velocity discrimination, although some substantial limitations were also revealed with the design in its initial form.

A Wein filter consists of a region containing orthogonal electrical and magnetic fields. This ExB region provides mass separation by the

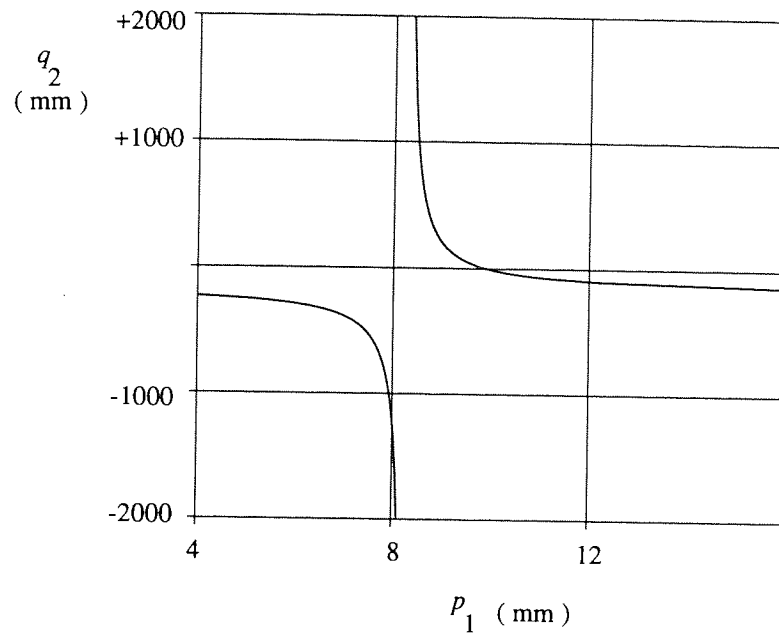


Figure 4.29 - Graph showing the form of equation 4.27, evaluated for $f_1=9$ mm and $f_2 = 200$ mm.

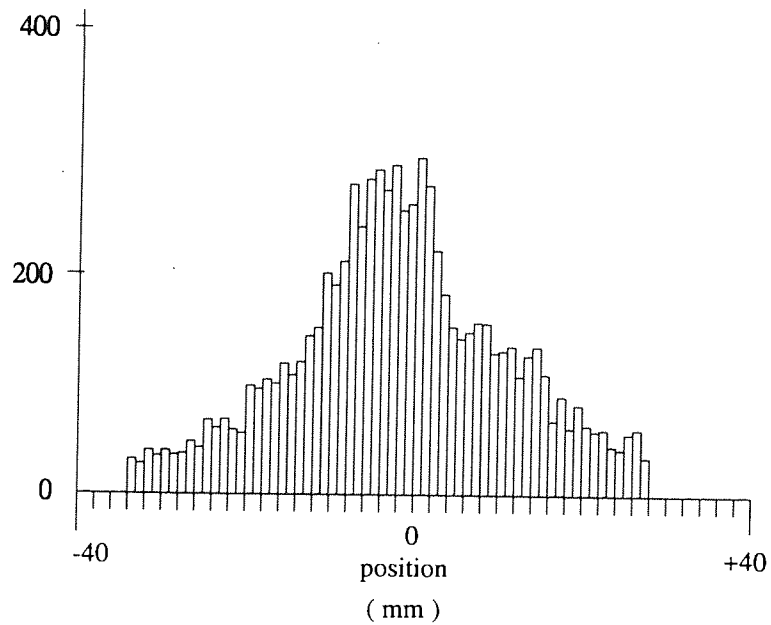


Figure 4.30 - Distribution of the axial positions of the extracted ions. (that is the value of z when $r=0$). The extraction plate position corresponds to $z=0$.

introduction of an angular velocity dispersion. The cross-sectional geometry of the prototype filter is shown in figure 4.31. Within this region ions experience a force given by:

$$\mathbf{F} = q\mathbf{E} + q\mathbf{v} \wedge \mathbf{B} \quad -(4.28)$$

Thus the ExB separator field discriminates between ions of differing velocity, and a mono-energetic beam is a prerequisite if mass separation is to be achieved. As the magnetic field is provided by permanent magnets, the particular ion velocity to which the filter is tuned must be controlled by the electric field strength. The voltage, V_w , required to pass an ion with velocity v_o without any deviation is given by:

$$V_w = d_e B / 2 \sqrt{(2E_o / 2m_o)} = d_e B v_o / 2 \quad -(4.29)$$

where d_e is the deflection plate separation. The form of eq. 4.29 agrees with experimental data shown in figure 4.12. The theoretical gradient is given by $\{(d_e B)^2 (e/m_o)\}$, which for argon is calculated to be 9.1 V^{-1} , compared to the experimental value of 10.7 V^{-1} .

Ions with a velocity greater or smaller than v_o are dispersed with cycloidal trajectories in the plane of the electrical field. The radii of which are dependent on the field separating strength, given by:

$$\theta_L = L / \sqrt{2} r_o \quad -(4.30)$$

where r_o is the cyclotron radius:

$$r_o = m_o v_o / eB = \sqrt{(2E_o m_o) / eB} \quad -(4.31)$$

Thus the angular dispersion of the ions is dependent upon both the field strength and the length of the field region, L . The lateral dispersion in the exit plane of the filter can be expressed as:

$$\Delta y(v) = (v - v_o) B e L^2 / 2E_o \quad -(4.32)$$

Given this expression the maximum and minimum velocities passed by the ExB field can be calculated. When the filter is tuned to particles of velocity v_o ,

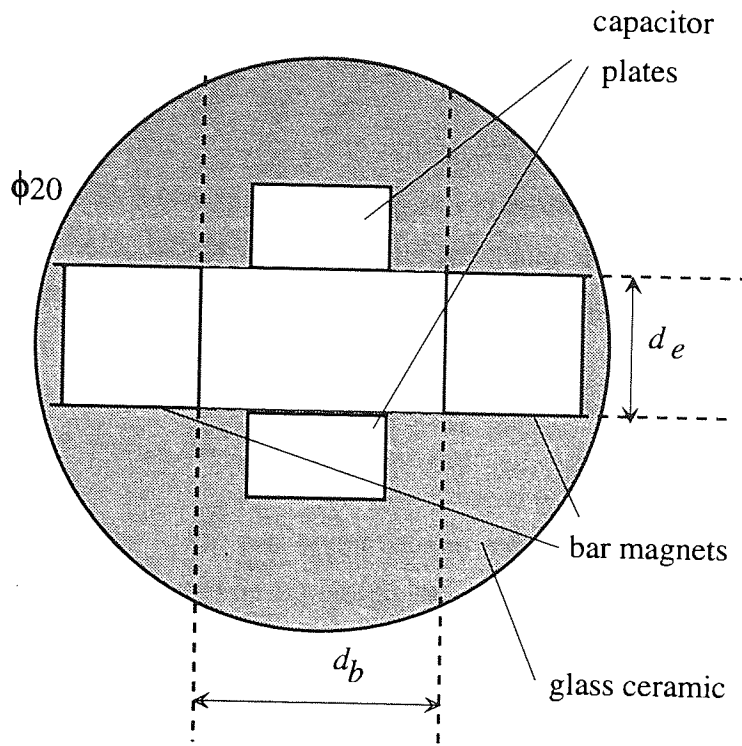


Figure 4.31 - Geometry of the prototype Wien filter

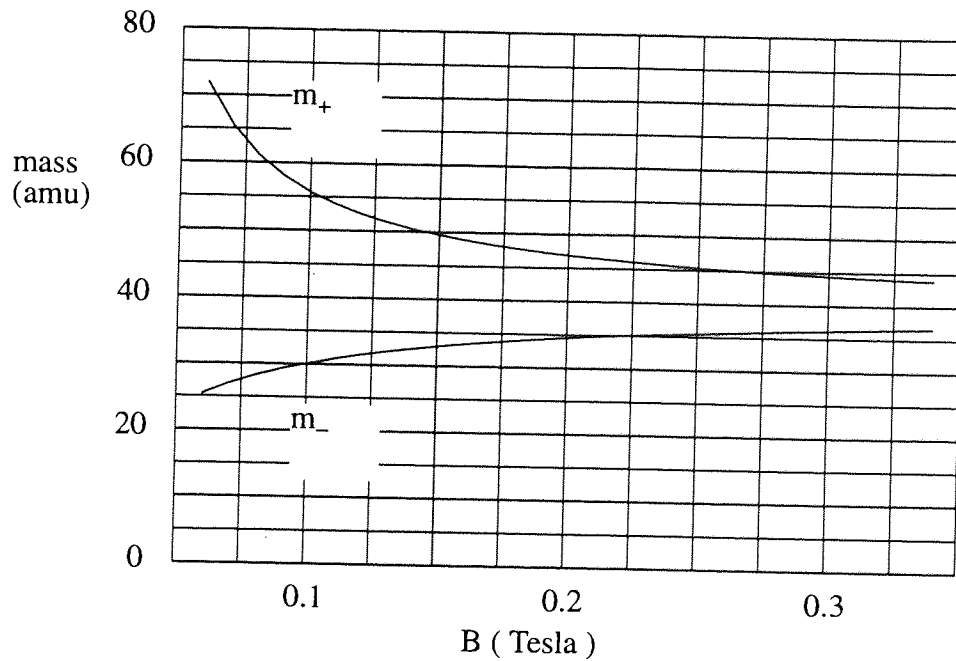


Figure 4.32 - Mass resolution v field strength (1keV Ar)

the maximum and minimum velocities are:

$$v_{\mp} = v_o \pm 4wE_o / BL^2 \quad -(4.33)$$

In the derivation of eq. 4.33 it is assumed that the exit aperture is located in the exit plane of the ExB field, which represents the geometry of the prototype filter. Assuming a mono energetic beam this can be expressed in terms of atomic mass:

$$m_{\mp} = 2E_o (v_o \pm 4wE_o / BL^2)^{-2} \quad -(4.34)$$

Thus m_+ and m_- represent the lower and upper atomic masses that are passed, and so the mass resolving power can be expressed by:

$$m_o / \Delta m = m_o / (m_- - m_+) \quad -(4.35)$$

The two solutions of eq. 4.34 are shown for a 1 keV argon beam as a function of B, in figure 4.32. For B= 0.26 T the figure predicts a mass resolution of 8 amu. Thus masses 28 and 32 should be removed from the argon beam. However, these masses were visible in the primary spectrum of figure 4.22.

In addition to velocity discrimination the ExB field also has asymmetric focusing properties, thus even in the absence of a velocity spread in the primary beam, focusing will take place in the plane of the E field. Such focusing properties were considered in detail by Seliger¹⁹⁴, where it is shown that the focal length of a rectangular separator region is given by:

$$f_w = \sqrt{2}r_o / \sin(\theta_L) \quad -(4.36)$$

For example the cyclotron radius for a 1keV Ar is 97 mm. For $L=80$ mm, eq. 4.36 gives a focal length of 132 mm, and therefore introduces a significant astigmatism. As the cyclotron radius is proportional to $m_o^{1/2}$, the astigmatism is more severe for neon and worse again for helium.

When the Wein filter was removed from the prototype source, the axial variation of the magnetic field, $B(z)$ was measured, and the electrical field $E(z)$, calculated. The two distributions are shown in figure 4.33. In order to

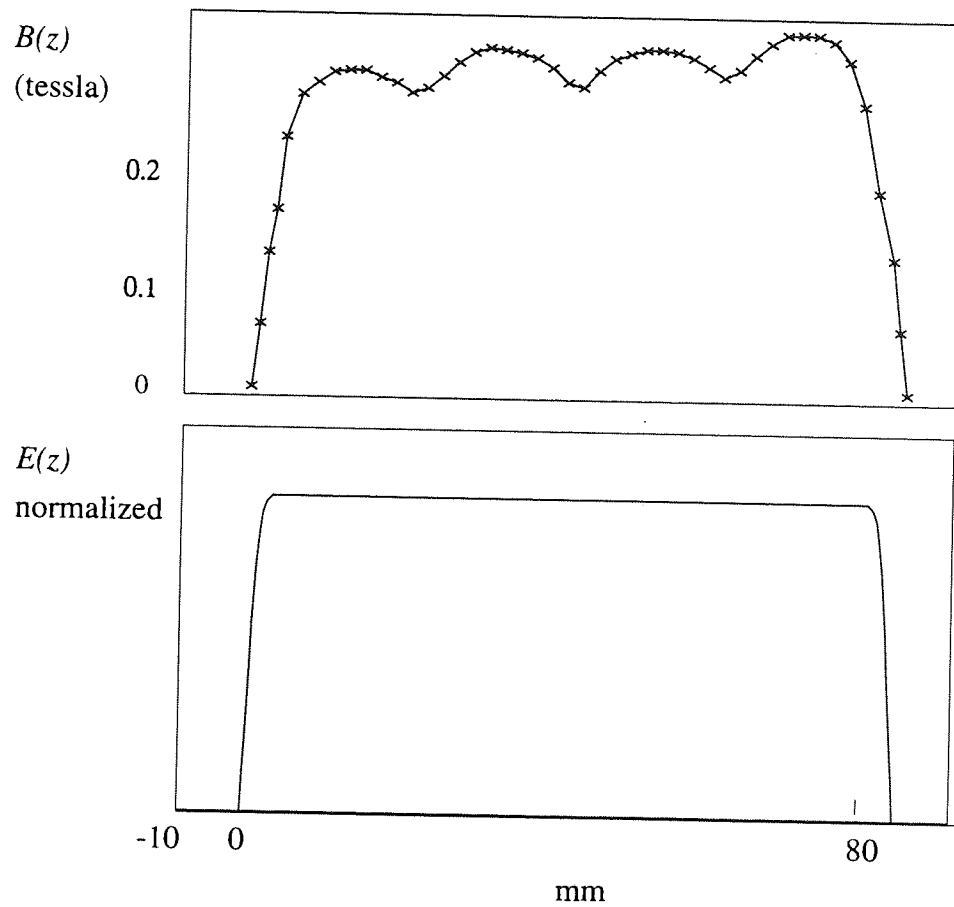


Figure 4.33 - Axial field of the prototype Wien filter.

(a) $B(z)$ - (measured by Hall Probe)

(b) $E(z)$ - (calculated)

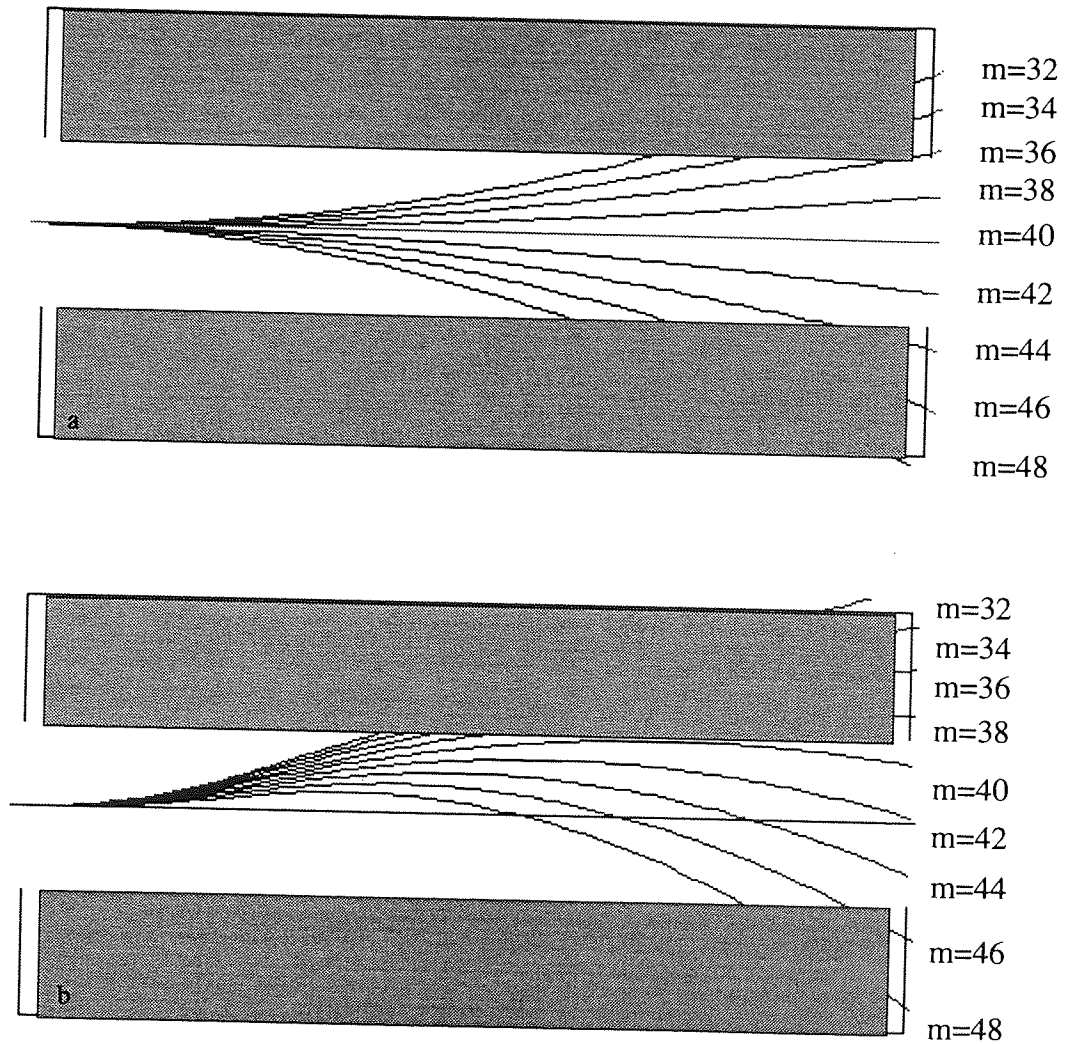


Figure 4.34 - Ion trajectories - (prototype Wien filter)
 ($B = 0.27 \text{ T}$, $d_e = 5 \text{ mm}$, $L = 80 \text{ mm}$, 1 keV argon beam)
 (a) ideal, abruptly terminated axial field distributions.
 (b) real axial field distributions.

assess the importance of the field inhomogeneities, a numerical simulation of the ion trajectories was carried out, using the above axial fields. The trajectories of axial ions, shown in figure 4.34, illustrate the result of the non-ideal field. In both figures (a) and (b), the filter is tuned to amu 40. In (a) ideal, abruptly terminated homogeneous fields were assumed. In this case, as expected, the central trajectory, amu 40, propagates without deviation. The deviation of heavier and lighter particles is shown. Whereas (b) was calculated for the axial fields of figure 4.33, and due to these field inhomogeneities, trajectories can be seen to be significantly modified. Even ions with precisely the correct energy emerge from the filter displaced from and at an angle to the axis.

These simulation results explain a number of the experimental observations.

a] Ion trajectories shown in figure 4.34 provide a possible explanation for the observed displacement in the ion and neutral beam centres.

b] Both spectral and direct measures indicate that a significant neutral current emerges from the source regardless of the value of V_w . This could be attributed to neutralisation of ions within the column prior to passing the filter. However, the data also suggests neutrals may result from ions that have been deflected by the ExB field, and returned to the beam via glancing angle collisions with the deflection plate electrodes of the filter. As the neutralisation probability of such collisions is very high, scattered particles would consist largely of neutrals. A number of experimental observations reinforce this conclusion: such a mechanism also provides a plausible explanation for the non-symmetric beam profiles and their dependence on V_w , that were shown in figure 4.18. This mechanism also provides a possible explanation for the unexpected dependency of total current on V_o for fixed V_w . In figure 4.17 the peak of $J_n(V_w)$, is displaced from that of $J_i(V_w)$ that is maximum neutral current was achieved from neutrals formed by glancing angle collisions. The spectral measurements also illustrated substantial neutral currents when the filter was significantly de-tuned. Such high neutral currents are unlikely be the result of gas phase collisions, as the source pressure was very low, $P_B < 1 \times 10^{-7}$ mbar.

c] Ions colliding with the deflection plate electrodes of the filter will also lose energy by elastic and inelastic means, as well as undergoing neutralisation. Thus the filter is a likely origin for the scattered peak observed in the primary

spectra. Additional weight is given to this conclusion, in that the shape of the scattered peak was observed to be significantly influenced by V_w .

d] The apparent mass separating power of the ExB observed experimentally is evidently not as good as that predicted by eq. 4.35. One possible source of discrepancy is that eq. 4.35 assumes the beam to consist of mono energetic axial ions. From the discussion of the source extraction optics this is clearly not a realistic assumption.

The theoretical results also reveal some further limitations of the prototype Wein filter which were not evident from the experimental data. Notably a field strength of 0.26 T introduces a strong astigmatism. This was not observed experimentally as the beam was defined by apertures, and the beam could be 'scanned' in one direction only. Further considerations concerning the stigmatic properties of the ExB separator field are discussed in later sections. A further potential problem with the geometry shown in figure 4.31 is that ceramic material is exposed to the deflected beam, giving rise to a possible charging problem.

4.5.3.4 General discussion

From the discussion of the gas pressure in the column in section 4.4.4 it can be expected that ions will undergo RCT collisions along the full length of the transport column, and not solely within the CEC as ideally would be the case. This is borne out experimentally: at least 50 % of the beam was found to be neutralized without any gas supplied to the CEC, although it is not possible to determine what proportion of this neutralisation took place from gas phase collisions. The cross-section for RCT is given by the recent expression of Sakabe and Izawa¹⁹⁰ in terms of the ion velocity, v and ionization potential, I :

$$\sigma(v) = (A - B \log_{10} v) (I/I_o)^{-1.5} \quad -(4.37)$$

where $A = 1.81 \times 10^{-14}$, and $B = 2.12 \times 10^{-15}$, and I_o is the ionisation potential of atomic hydrogen, (13.6 eV). Calculations based on eq. 4.37 show that the pressure in the column is somewhat underestimated by the calculations of section 4.4.4.

4.6 The Modified source - FAB 1

Following the analysis of the prototype source, a modified version of the source was constructed, which will be subsequently referred to as FAB-1. This section details the modifications, the resulting new characteristics, and subsequent analysis of this source version.

4.6.1 Re-Design

Of the vital areas of redesign already identified; the pulsing system, optics and Wein filter, the latter presented the most complex design problem, theoretically and also in terms of physical construction. For this reason, and to enable other changes to be observed more closely the filter was removed.

Improved brightness of the ion source was also desirable at this stage, however no changes were implemented, as greater beam current was not vital for the progress of the experimental program at this stage. Also the redesign was made with the assumption that significant gains in beam current could be achieved by improved transport optics.

4.6.1.1 Beam Chopping System

To summarize the previous discussion, a fundamental limitation of the electron impact chopping method was revealed. As applied in the prototype source, the method of beam chopping was the origin of the broad primary spectra, originating from a large dispersion of flight times. Although the simulation indicated that the time dispersion could be decreased by increasing the extraction field, the instrumental resolution, $\Delta t/t$ could not be improved sufficiently. This is because the energy dispersion increases in proportion to the strength of the extraction field. For example decreasing V_{ext} from $0.7 V_o$ to zero reduces the time spread from 4 to $\sim 0.5 \mu s$ but increases $\Delta E_o / E_o$ from 0.2 % to 5%. Confining the initial spatial co-ordinates to a more localized region was also considered as a possible solution, however it was found that this did not significantly improve instrument resolution either. Consequently despite the advantages of electron impact pulsing in terms of contamination, an alternative pulsing method was sought. There were also some experimental difficulties in implementing electron impact pulsing: the approach complicated the electronic

regulation of the emission current: In DC mode, a stable emission current can be achieved using negative feedback in the electronics. This approach was employed by the Kratos power supply. However, this scheme requires a constant emission voltage and current, and these were absent in pulsed mode operation.

A literature survey revealed that the method of ion beam chopping most widely employed in pulsed beam analytical instruments is by electrostatic deflection of the beam. An electrostatic beam chopping unit (BCU) in its most basic form is shown in figure 4.35. This comprises a pair of deflection plates, followed by an aperture. The most simple mode of operation is with one plate grounded and an appropriate pulsed waveform applied to the other. Thus effectively a voltage, V_{chop} is maintained across the plates, at all times other than during the pulse. If the pulse duration, τ_p , is longer than the time taken for individual ions to travel the length of the deflection electrodes the beam will, for a short duration, pass undeflected through the aperture. A more detailed analysis of the theory is given by Fowler¹⁹¹.

The main considerations for incorporation of the BCU into the transport column of the FAB source were:

- 1] Its position in the column with respect to the other units.
- 2] The assignment of values to the dimensions s , d , r_{ap} and l of the basic BCU, and the magnitude of the deflection voltage, V_{chop} .

The requirements that the BCU were required to fulfil were:

- a] a pulse duration giving an instrumental resolution, $\Delta t/t < 1\%$.
- b] minimum sputtered contamination of insulators arising from the deflected beam.
- c] no direct exposure of insulating components to the deflected beam.
- d] to prevent ions from returning to the beam through glancing angle scattering collisions with the deflection electrodes.
- e]) minimal neutral formation prior to passing the BCU.

However, these factors concerning the design of the BCU could not be considered in isolation, as there was considerable interdependence between

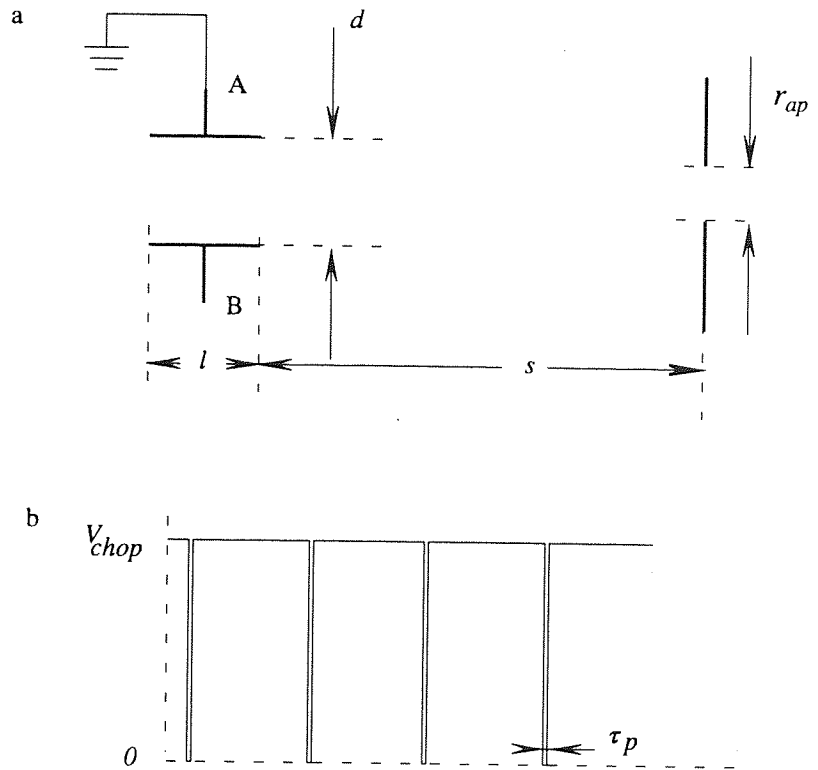


Figure - 4.35

- (a) The geometry of a basic beam chopping system.
- (b) Applied waveform

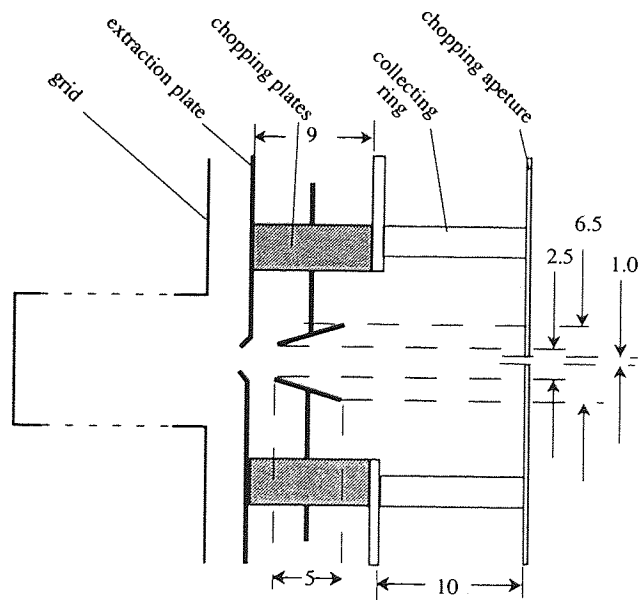


Figure 4.36 - The Beam Chopping Unit (BCU) introduced into the column of the FAB-1 source. Dimensions are shown in milli meters.

the design of all units in the transport column. The main factor influencing the position of the BCU, was the minimisation of the formation of neutrals. Any neutrals formed prior to passing through the BCU will contribute noise to the scattered particle spectrum. As the chopping 'duty cycle' is small, typically 1:1000, only 0.1 % neutralisation before the BCU would contribute a continuous current equal to the chopped current. The second influence on position concerns the minimisation of pulse duration: According to Fowler¹⁹¹ temporal dispersion is limited by the beam width relative to the diameter of the beam chopping aperture. Therefore, to minimise Δt the chopping aperture should be placed at the focal point of a proceeding lens. It can be seen that these two requirements are not compatible. In the follow section dealing with the optical design of the column, it is shown that in order to achieve acceptable optical characteristics the primary lens must be positioned away from the extraction plate. It is also shown that the divergence angle of the source must be limited in order to achieve the required beam diameter at the sample. The primary lens is also required to deliver a 'parallel' beam to the Wein filter. Thus it can be seen that placing the chopping aperture at a focal point is not compatible with the requirements of other units.

A schematic of the BCU design is given in figure 4.36. The chopping unit consists of a single pair of angled deflection plates, placed immediately proceeding the extraction plate. The dimensions were imposed by the existing column construction, that is, it was not practical to extend the overall length of the column. Although the filter was not present in FAB-1, space was reserved for its subsequent re-installation. The deflection plates are mounted within a ceramic ring coated on the inner surface with metal evaporated copper, thus preventing charging due to stray charge beam current. The second steel ring placed in the drift region collects the deflected beam and prevents exposure of the beam to the ceramic tubes. The separation between chopping plates was made as small as possible in order to minimise V_{chop} . The plates were angled to prevent them being irradiated by the deflected beam. It was the intention in the design to operate the primary lens following the BCU in acceleration mode. In this case the beam is extracted from the source with energy $V_o - V_{ext}$. After passing though the BCU it could then be accelerated by the primary lens to its full energy. This arrangement has a number of advantages in terms of the BCU and for the optics also. Firstly the chopping voltage, V_{chop} required to deflect the beam is significantly reduced, secondly

the time for ions to travel the distance, l , of the chopping plates is increased by the factor $(V_o - V_{ext} / V_o)^{1/2}$ making the pulse circuit design much less critical. A schematic of the pulsing electronics is shown in figure 4.37, which employs a single high voltage MOSFET transistor (RS BUK456-1000B), which is triggered by a 10 V positive pulse from the pulse generator. It was found that it was important to maintain the coaxial cables as short as possible in order to minimise the rise and fall times, thus the circuit is mounted on the source itself. The primary side of the circuit is operated at ground potential, and is decoupled from the deflection plates through the high voltage capacitor. An example oscilloscope trace of the resulting pulsed waveform is shown in figure 4.38.

From the previous simulation model of the ion cell it was seen that 60% of the beam was contained within a divergence angle, α_s , of $\sim 6^\circ$ which gives rise to a beam diameter of ~ 0.7 mm at the chopping aperture. However, it was important to deflect the whole beam, including the more divergent low quality part, which subtends a total angle of $\sim 16^\circ$. In the calculation the following assumptions were made:

1] The angular current distribution of the beam at $V_{chop} = 0$ was given by:

$$I(\alpha) = \sqrt{(\ln 2)/\alpha_s} \sqrt{\pi} \exp[-\alpha/\alpha_s \sqrt{(\ln 2)}]^2 \quad -(4.38)$$

2] The source was assumed to be a point source located at the extraction plate.

3] The deflection field was given by

$$E(z) = V_{chop} / (a + z (b-a)/l) \quad -(4.39)$$

within the region $0 < z < l$ and zero elsewhere.

4] The potential within the same region was given by:

$$\phi(z,x) = (V_{chop} - E(z)x)/2 \quad -(4.40)$$

5] The beam divergence, α_s , was unchanged when the beam was

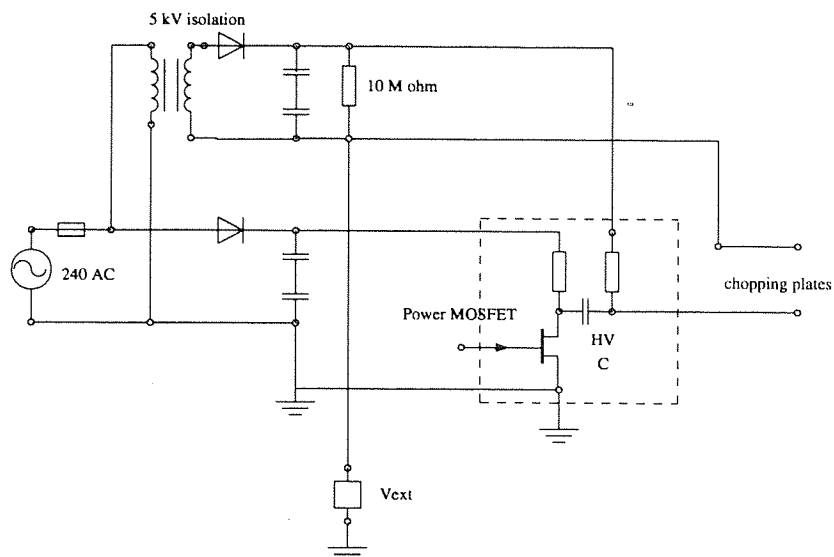


Figure 4.37 - Schematic of the chopping plate pulsing circuit. The circuit enclosed by the dashed line was positioned in a die cast box mounted on the FAB source. All connections are made with 'SHV' type BNC connectors.

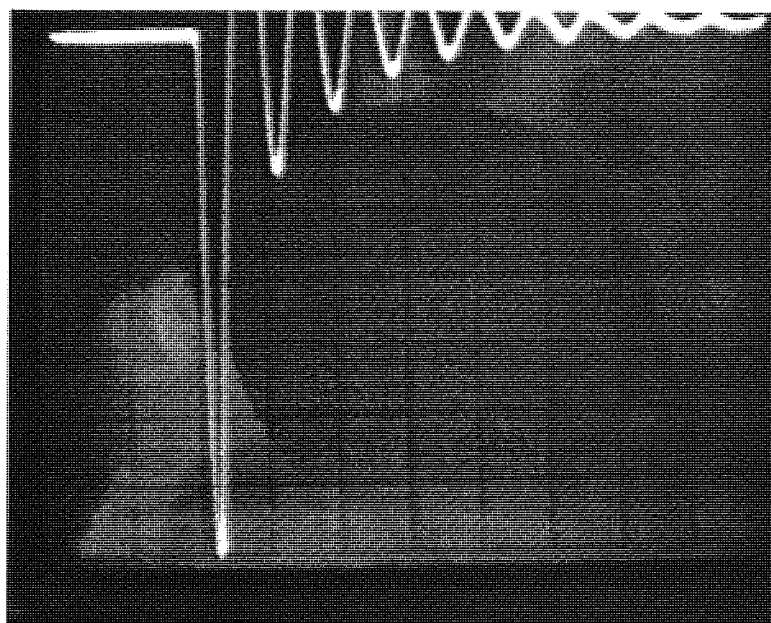


Figure 4.38 - An oscilloscope trace of the beam chopping waveform. The vertical scale is 20 V/div, and the horizontal scale is 200 ns/div.

deflected.

6] The relative intensity of the current passing through the aperture was given by the integration of $I(r)$ falling within the area of the aperture, see figure 4.39.

Figure 4.40a shows the calculated beam current, I_b passing through the aperture as a function of V_{chop} , for a beam extracted from the ion cell with energy 600 eV. The total divergence was 16° and the FWHM of the gaussian was 6° , as predicted by the ion cell simulation model. As the residual current passing through the chopping plate aperture must be very small, the required value of V_{chop} can be seen more clearly by plotting I_b on a logarithmic scale, as in figure 4.40b. Thus to reduce the current by a factor of 10^4 requires V_{chop} of 200 volts. In this case the continuous current is $\sim 10\%$ the chopped beam current. It can be seen that to deflect the beam totally, that is to deflect an axial ion through an angle of $\sim 9.5^\circ$ requires V_{chop} of 215 volts.

4.6.1.2 Ion optics

The brightness and emittance analysis of section 4.5.4 revealed that transmission losses in the prototype source were large. However, even in the case of an ideal lens system, the minimum possible beam diameter achievable at a working distance of 200 mm without transmission loss was ~ 6 mm. Thus without improved ion source design, transmission losses must be incurred in order to achieve the required beam diameter of 2 mm. It was not possible to decrease the working distance due to the CEC, which must be situated between the second lens and the sample. Also, for experimental reasons α_t must be maintained below $\sim 1^\circ$.

The aim of the re-design therefore was to achieve a beam diameter at the sample of ~ 1 to 2 mm, for $W= 200$ mm. The second requirement was to produce a 'parallel beam' at the entrance plane of the Wein filter, as a non-parallel beam degrades mass separating power. However, it is known from basic optics that a parallel beam can be achieved only in the case of an axial point source image located at the focal point of a subsequent lens. It was shown in this work that the ion source cannot be treated as a point source emitter of ions with regard to the design of the optics. This was a fundamental

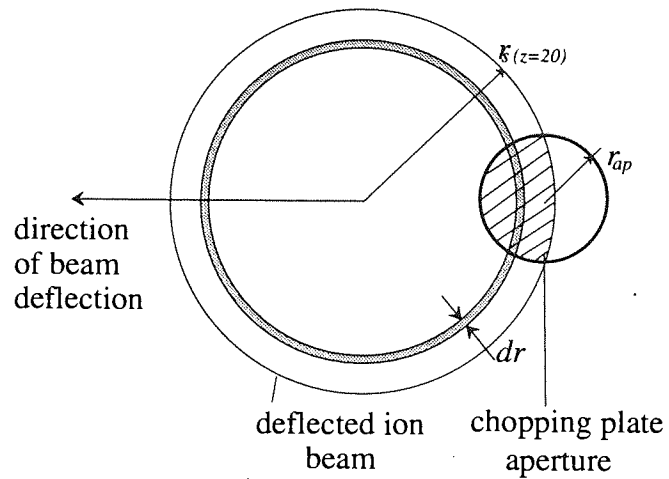


Figure 4.39 - Illustration of the model used to calculate the current passing from the beam chopping aperture as a function of V_{chop} . The dashed area represents the part of the beam that passes through the aperture.

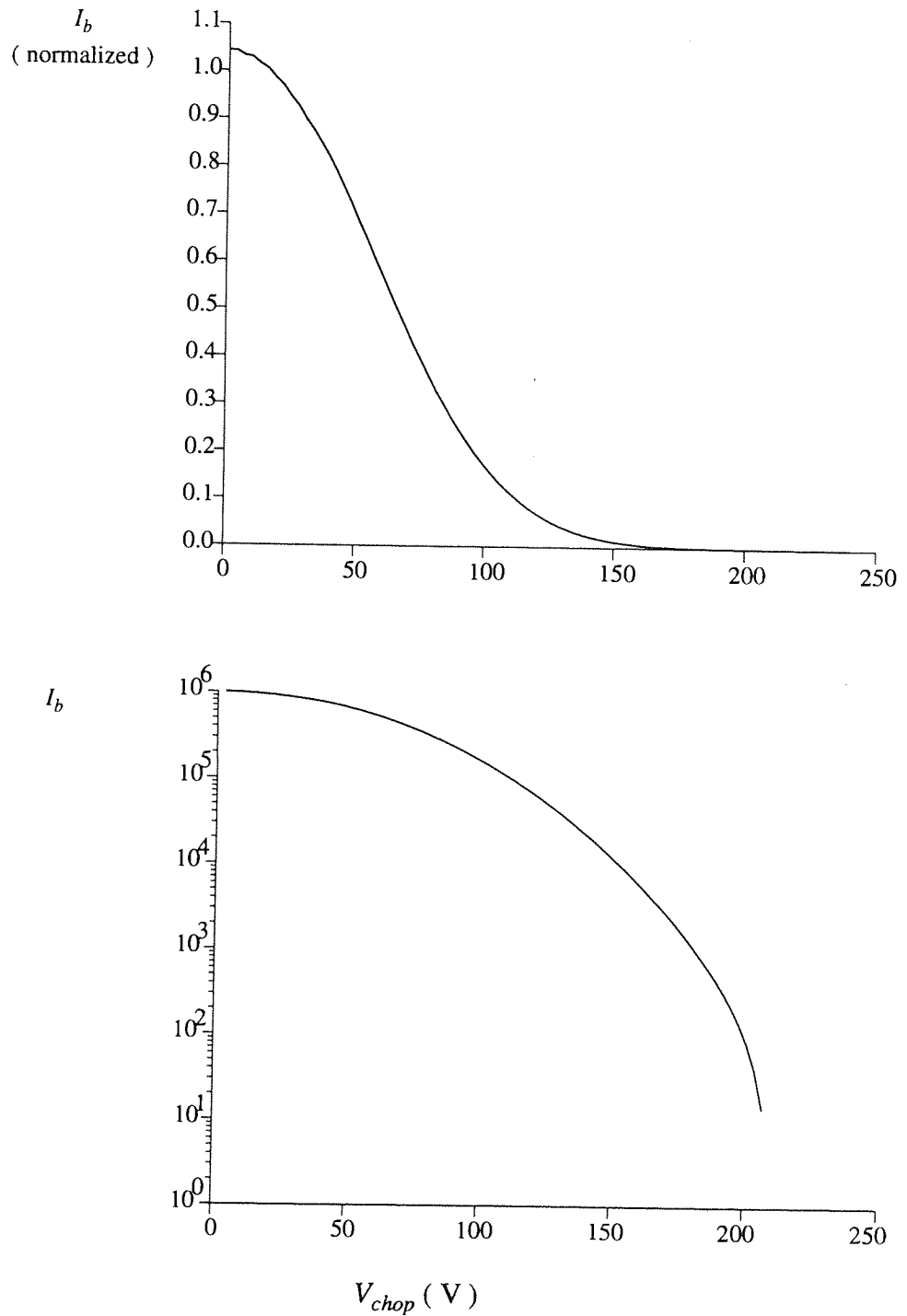


Figure 4.40 - Calculated beam current passing through the chopping plate aperture as a function of V_{chop} , beam divergence: FWHM = 6° , total width = 16° .

(a) on a linear scale.

(b) on a \log_{10} scale.

limitation of the prototype design.

The redesigned optical column was based on the principles outlined in section 4.3.4, that is:

1] to attain minimum losses the emittance of the beam should not exceed the acceptance of individual units in the transport column.

2] the beam diameter at the sample is determined by the magnification of the lens combination as given by eq. 4.12.

The main difference between the optics of a FAB source and a standard ion source is the large working distance in the former case. For example, W is typically ~ 25 mm for an ion source. For the source parameters $r_s = 0.3$ mm and $\alpha_s = 2^\circ$ the minimum achievable beam radius, r_t , is $60 \mu\text{m}$.

In order to attain r_t of 0.5 mm at $W = 200$ mm that is $\alpha_t \sim 1^\circ$ and given that $r_s = 0.3$ mm, a source divergence, α_s of:

$$\alpha_s = r_t \alpha_t / r_s \sim 1.5^\circ \quad \text{-(4.41)}$$

is required.

For the beam to pass through the Wein filter without loss, the radius of the beam, r_b must be less than ~ 2 mm, but also the divergence, α_b must be less than $\sim 1.5^\circ$. Thus the acceptance is less than the source emittance. In order to preserve the mass separating power, however, the phase space emittance diagram should be as elliptical as possible following the 1st lens, indicating a near to parallel beam. Thus it can be seen that the optical design is a compromise between the beam current, beam diameter and mass separating power of the ExB field.

The primary lens of the FAB-1 source is shown in figure 4.41. Compared to the prototype design the principle plane is a much greater distance from the extraction plane, and the lens is operated in accelerating mode. This arrangement has a number of advantages: the magnification of the lens combination is reduced, the BCU can be operated at a lower voltage, and the divergency of the beam, α_b is reduced. The geometry of the lens was designed to have maximum focal length for a given accelerating ratio, requiring large aperture diameters and electrode separation. These parameters

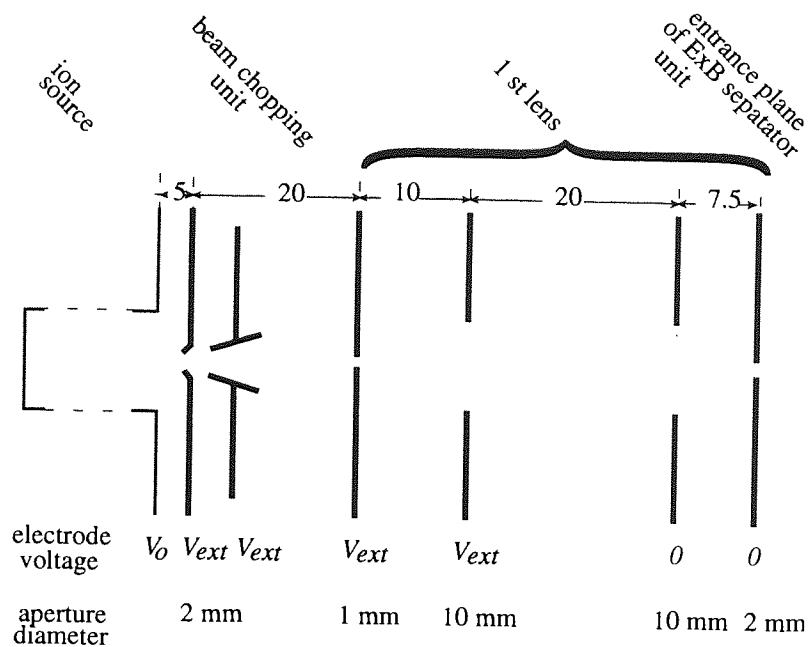


Figure 4.41 - Geometry of the 1st lens of the FAB-1 source.

were therefore maximised within the constraints of the existing column geometry. An acceleration ratio of x4 gives a focal length f_1 of 80 mm. The beam diameter in this case is given by:

$$r_b = \sqrt{(1-V_{ext}/V_o)} \cdot (\alpha_s r_s / \alpha_b) \quad -(4.42)$$

By limiting the source divergence, α_s , to 3° an acceptable beam of $\alpha_b = 0.5^\circ$, $r_b = 1$ mm is achieved for the Wein filter, and a beam diameter of 1.2 mm could be obtained at the sample. It can be seen from eq. 4.12 that the magnification of the lens combination is 2, also predicting a beam diameter at the sample of 1.2 mm. Thus the optics give the minimum possible beam diameter for $f_1 = 80$ mm and $f_2 = 94$ mm. To achieve $f_2 = 94$ mm the 2nd lens required an applied voltage of $0.36V_o$.

4.6.1.3 General

The principle of the ToF technique requires that, on average, less than one particle is received by the detector for each pulse of primary particles incident upon the sample. For a typical chopping frequency of 20 kHz, the maximum collection rate is achieved with a detector current of ~ 3 femto amps. Typically, only one in every $\sim 10^7$ primary particles will strike the detector having undergone a QS collision at the sample surface. Given a duty cycle of 1:1000 the source must produce an un-chopped DC current of $\sim 30 \mu\text{Amps}$ to attain maximum collection rates. In practice mechanisms other than QS collisions contribute to the scattered particle spectra, and so to obtain a spectra with unbiased counting statistics the current should be somewhat lower than this. For these values a spectrum with 10^5 counts composing the QS peak may be acquired in 5 seconds. The current limit imposed by this calculation is 2 to 3 orders of magnitude greater than could be produced by the prototype source. It was clear from the above analysis that such current gain could not be achieved by changes to the transport column alone. The design changes were therefore made on the basis that further current gains could be achieved in future, if necessary, by increasing the source brightness.

4.6.2 Experiment

For measurement of the DC beam current and primary spectra the instrumentation employed previously was used. For measurement of beam profiles the cross wire, allowing the beam to be scanned in both z and x directions was introduced. A port alignment stage was also introduced which allowed the angular alignment of the source axis to be accurately controlled. Initially, an extraction voltage, V_{ext} was set to $0.75V_o$. However, the beam current was found to be very small, only a few tens of nano amps in this case. Significant increases in current were gained by grounding the extraction plate. In this mode the accelerating lens has no influence on the beam. For this reason all the results presented in the following section were recorded without the accelerating lens being operated. This behaviour was in direct contrast to the predictions of the lens calculations. An explanation was found when the source was removed on completion of the characterisation. A mechanical misalignment of the column was discovered. Thus when the accelerating lens was operated the beam diameter became smaller, but only a small proportion passed through the 2 mm aperture prior to the 2nd lens. Beam profile measurements were made at two different working distances, $W=200$, $W=110$, ie with and without the port alignment stage.

4.6.3 Experimental characteristics of FAB-1

Characterisation was conducted with He, Ne and Ar, and beam energies between $V_o = 0.5$ and 3 keV. The forementioned problems of electrical breakdown of the power supply remained, restricting operation to below ~ 3.5 keV. Measurements were made with and without the column sleeve fitted. The results provided operating characteristics, for subsequent scattering experiments and also provided further data for the continued development of the source.

As before pressures quoted in this section have been corrected with appropriate gauge sensitivity factors. The IC pressures quoted have been calculated as described in section 4.4.4. Current measurements quoted have been corrected with the appropriate γ values as described in section 4.4.1.

4.6.3.1 Beam Profile

As the accelerating lens was not operated for the above reasons, the optical column was effectively reduced to a single lens with an object plane, $p = 150$ mm and image plane $q = 200$ mm, giving a magnification of $q/p = 1.33$. From the calculated lens characteristics, it can be seen that this condition requires $V_2 = 0.36V_0$ in order to bring the beam to a focus at the sample. The ion and neutral profiles were separated by application of a voltage to the x-y deflection plates, and the cross wire scanned across both beams in vertical and horizontal directions.

Typical profiles are shown in figure 4.42. For ease of comparison with previous data the profiles are plotted on the same horizontal scale of 1 mm/div. In this case the column sleeve was not fitted. The ion component has a focused beam diameter of ~ 0.6 mm, and the neutral beam is not focused and has diameter of ~ 3 mm which is aperture limited. Very similar results were also achieved by scanning in a horizontal direction. At low IC pressures ($P_{IC} = 9 \times 10^{-5}$ mbar) the proportion of neutrals formed, R , is small, figure 4.42a. At higher IC pressures ($P_{IC} = 2 \times 10^{-3}$ mbar) much larger neutral currents are observed, figure 4.42b. Emitting gas to both cells (IC and CEC), figure 4.42c, resulted in a higher neutral proportion but not a greater neutral current. Also in this latter case a third peak appeared. This was attributed to neutrals formed in the CEC, which was confirmed by the observation that the ion beam assumed the same position when the x-y deflection voltage was removed.

With the column sleeve fitted, almost complete neutralisation of the ion beam was observed, as shown in figure 4.43. Here again the working distance, W , was 200 mm, and helium gas was emitted to both cells. The figure shows the resulting neutral and ion components for a series of energies from 500 to 2500 eV. For the purpose of clarity the ion beam is shown on a $\times 10$ scale. In addition to a significant reduction in amplitude (a factor of 40) the ion beam profile is significantly broadened compared to the previous results. The neutral profile width is unchanged although comparison of the form of the profile with the previous data reveals a sharper fall off with wire position. For energies of 500 and 1000 eV a subsidiary peak is observed on the shoulder of the main neutral profile. This was again attributed to the formation of neutrals in the CEC cell.

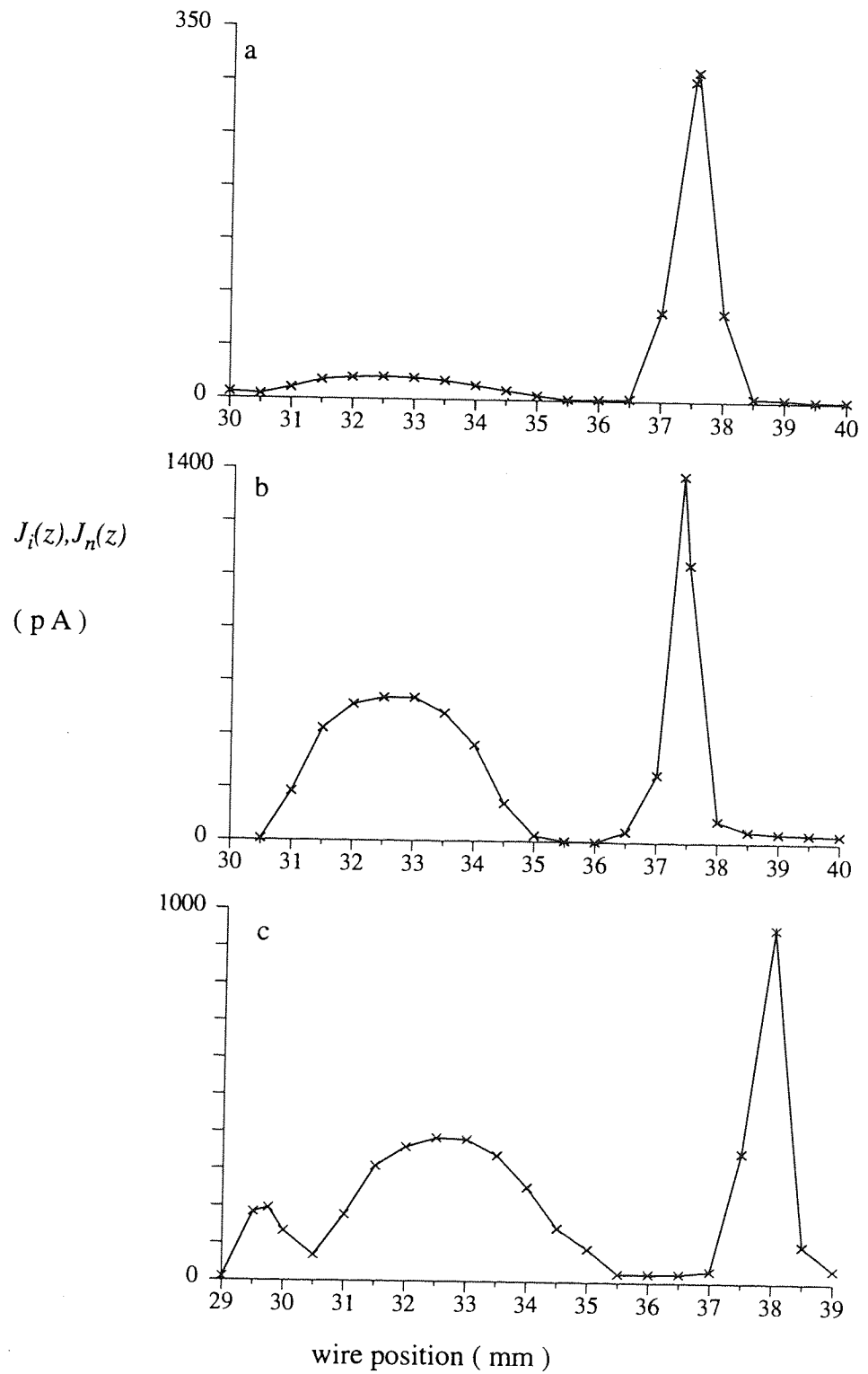


Figure 4.42 - Vertical beam scans.

Conditions: - $E_o = 2$ keV, (Sleeve not fitted)

(a) $P_{IC} = 9.2 \times 10^{-5}$ mbar, gas to IC only

(b) $P_{IC} = 2.3 \times 10^{-3}$ mbar, gas to IC only

(c) $P_{IC} = 9 \times 10^{-4}$ mbar, gas to IC and CEC

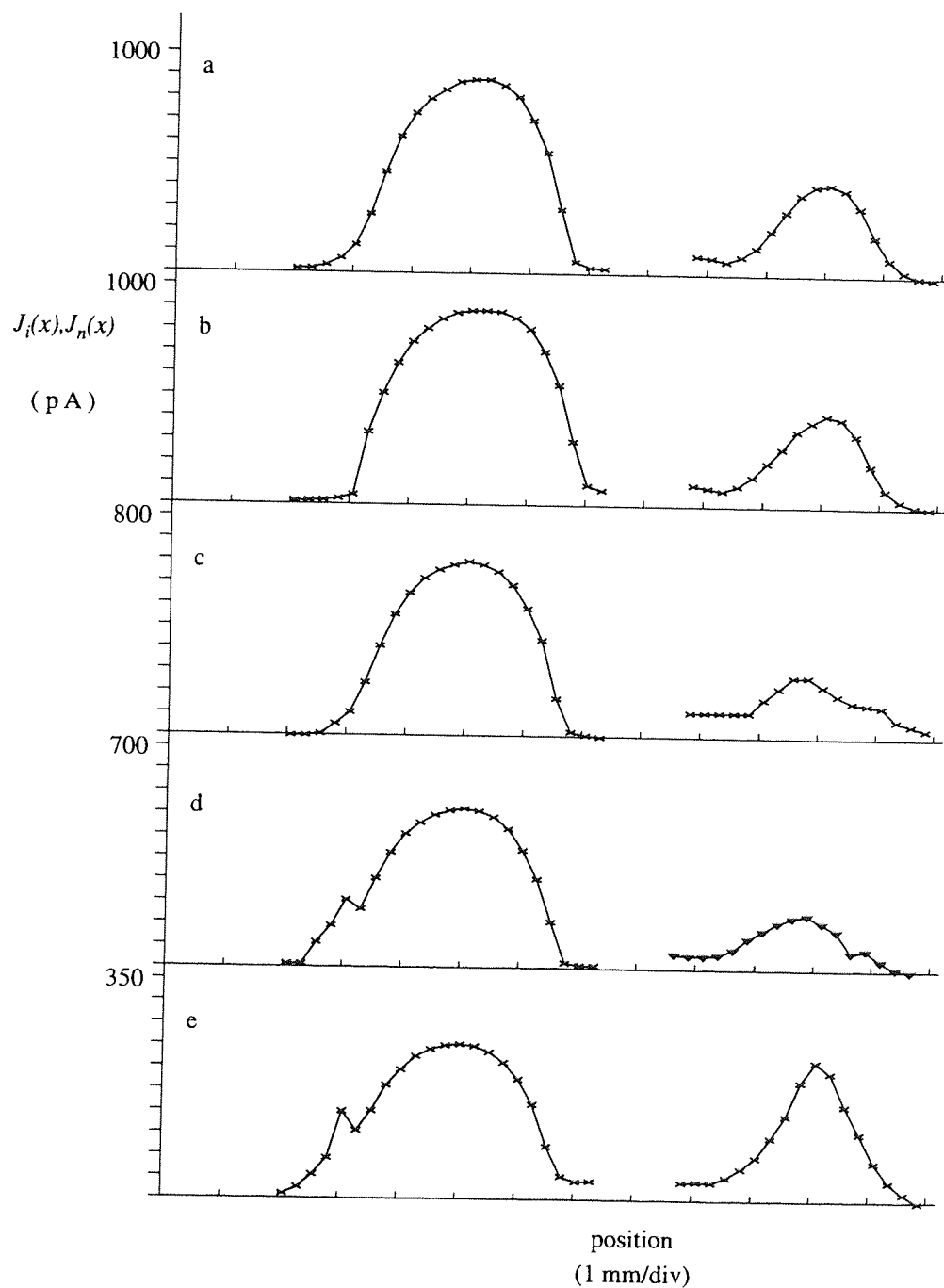


Figure 4.43 - Vertical beam scans.

Conditions: - (Sleeve fitted) $P_{IC} = 1.3 \times 10^{-3}$ mbar, gas to IC and CEC

(a) $E_o = 2500$ eV

(b) $E_o = 2000$ eV

(c) $E_o = 1500$ eV

(d) $E_o = 1000$ eV

(e) $E_o = 500$ eV

It was found that reducing W to 120 mm gave rise to an ion beam diameter of 0.4mm at a lens voltage V_2 of $0.41V_o$. Again this gives good agreement with the MUNRO calculations.

The data shown relates to a helium beam, however measurements with neon and argon gave similar results.

4.6.3.2 Beam current

The absolute current produced from the source has a complex dependence on many parameters. ($V_o, P_{IC}, P_{CEC}, I_e, V_e$). The typical dependence of total ion and neutral beam currents, I_i and I_n on P_B for fixed values of V_o are shown in figure 4.44. It can be seen that the ion current reaches a maximum for a pressure of ~ 2 to 3×10^{-4} mbar. The pressure giving maximum I_i occurs at slightly higher values as the beam energy is increased. In the region below this energy a rather more complex pressure dependence was observed. The dependence of the neutral beam I_n is shown in figure 4.45, here a generally increasing trend is observed with P_B . It is seen that the ultimate neutral current is significantly larger than the ultimate ion current. However this high current is not accessible in experiments as the chamber pressure becomes prohibitively high for $P_B > \sim 7 \times 10^{-4}$ mbar (giving a chamber pressure of $\sim 5 \times 10^{-4}$ mbar).

The ion current dependence on the beam energy V_o for a constant source pressure is shown in figure 4.46. In agreement with figure 4.43, a complex dependence is observed below ~ 1.5 keV. It can be seen that maximum I_i below 1 keV is obtained for lower pressures, (figure a), and below ~ 700 eV, I_i is very small for all pressures. The data shown here was recorded for neon gas, although qualitatively similar results can be observed for helium and argon. The maximum ion current observed was ~ 50 namps, at $P_B = 2 \times 10^{-4}$ mbar, and the maximum neutral current was 60 namps at a $P_B = 7 \times 10^{-4}$ mbar. ($V_o = 3$ keV)

With the sleeve present a greater pressure differential could be maintained between the source and chamber. The maximum atom current was slightly greater ~ 70 namps, although the neutral fraction was significantly greater, and the source could not be operated effectively in an ion only mode. The maximum I_i with the sleeve present was only 7 namps, ($V_o = 2$ keV and P_B

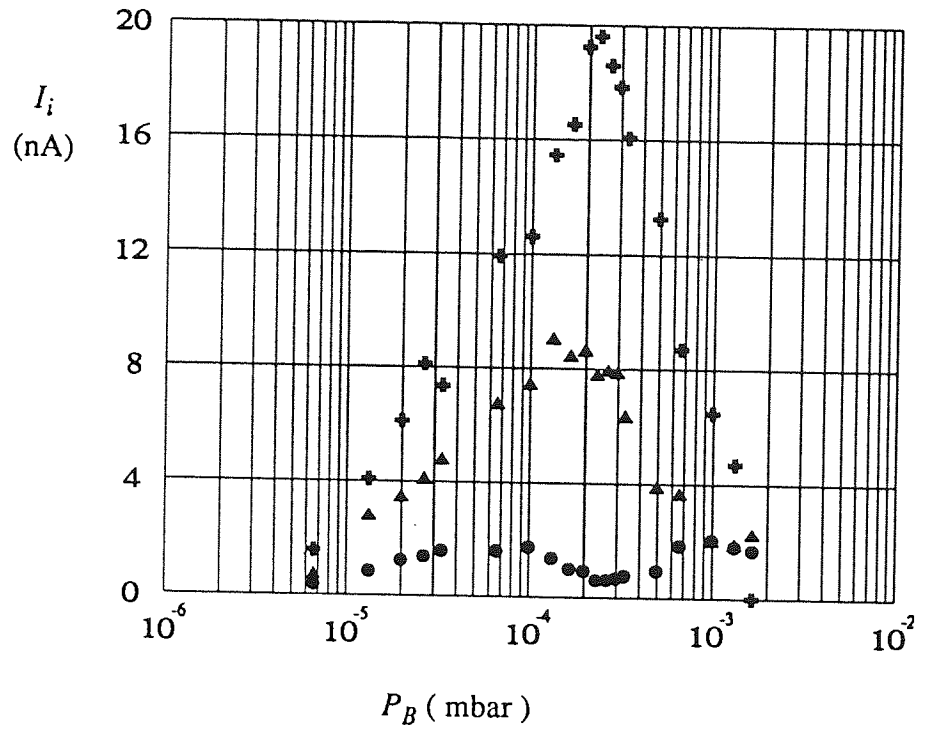


Figure 4.44 - Ion beam current measured as function of pressure. Conditions (neon), Gas to IC only, (no sleeve).

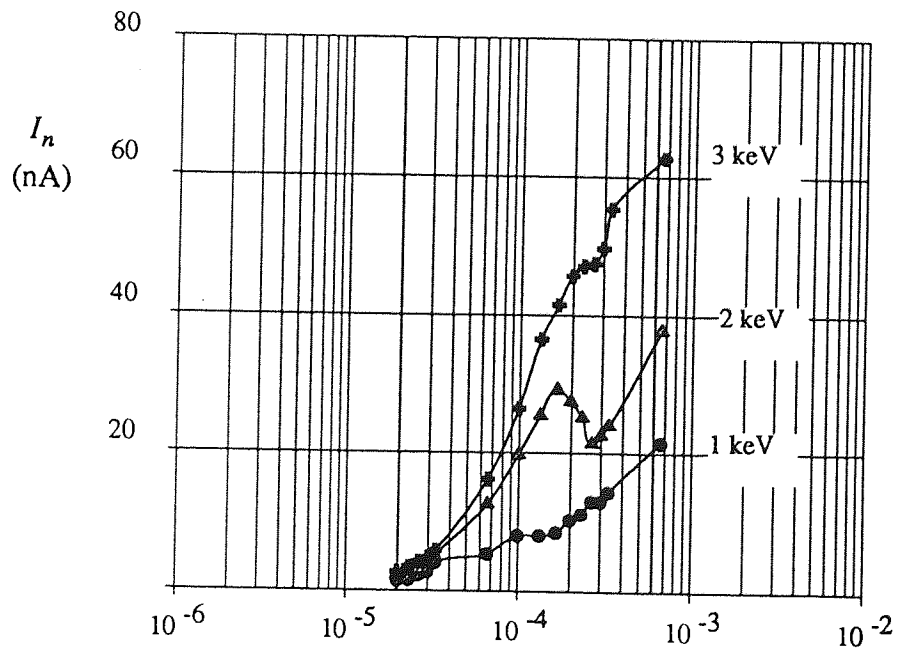


Figure 4.45 - Neutral beam current measured as function of pressure. Conditions (neon), Gas to IC and CEC, (no sleeve).

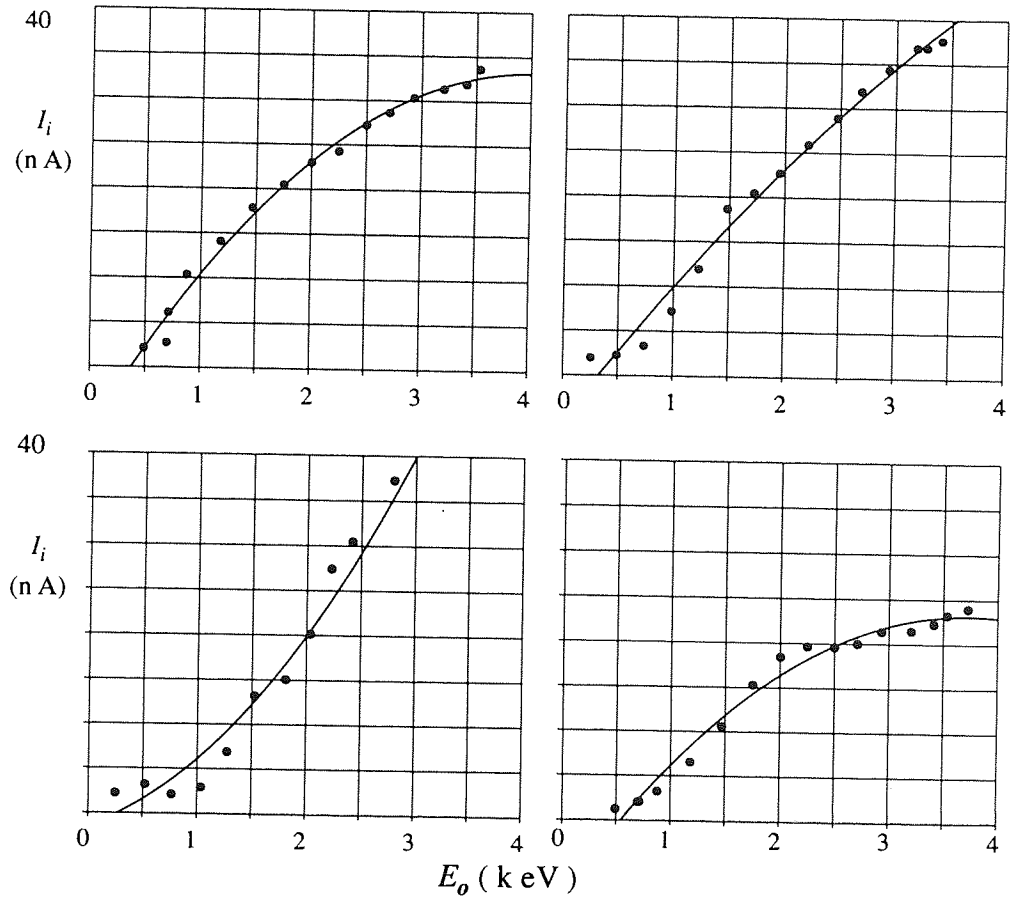


Figure 4.46 - Ion beam current measured as a function of E_o

Conditions :- Gas to IC only, (no sleeve), (neon)

- (a) $P_B = 4 \times 10^{-5}$ mbar
- (b) $P_B = 1 \times 10^{-4}$ mbar
- (c) $P_B = 2 \times 10^{-4}$ mbar
- (d) $P_B = 3 \times 10^{-4}$ mbar

= 2×10^{-4} mbar), in which case I_n was 33 namps. With gas admitted to both cells, the ion current can be almost completely neutralised, $R=99\%$, which was observed at $P_B = 2 \times 10^{-4}$ mbar.

Although some drift in the position and magnitude of the beam was observed, this was significantly smaller than was observed previously in the case of the prototype. However, like the prototype, the long term repeatability of the absolute beam current as a function of these parameters was poor. For this reason an accurate characterization of I_i and I_n in terms of P_{IC} , P_{CEC} , E_o was not attempted, as setting these parameters to given values, did not yield a predictable beam current. A system for monitoring sample current, during the course of a scattering experiment would give a more reliable approach to the sample current determination.

4.6.3.3 Primary Spectra

Primary spectra were collected employing the same experimental method described previously, with the new beam chopping electronics as described in section 4.6.1.2. All measurements were made with the extraction plate at ground potential, and so the electrical isolation of the pulse generator, described previously was not required. Figure 4.47 shows the primary spectra of a 1 keV argon beam. As the primary filter was not present the peaks of contaminant gases within the ion source are also observed in the spectrum. These peaks were significantly reduced, but not removed completely by baking the system. The pressure P_{IC} is also significantly lower than that of normal operation to ensure that the detector current is sufficiently low to ensure unbiased counting statistics, that is less than one ion/pulse. The presence of the contaminant peaks is a hindrance for scattering experiments, but provides a useful method of calibrating the spectrometer. In this case a linear least squares fit to this data yields:

$$t_{mca} = (0.1726 \pm 0.0006) m_o^{1/2} + 0.08 \quad -(4.43)$$

where the flight time t , is given by:

$$t = t_{mca} + t_{delay} \quad -(4.44)$$

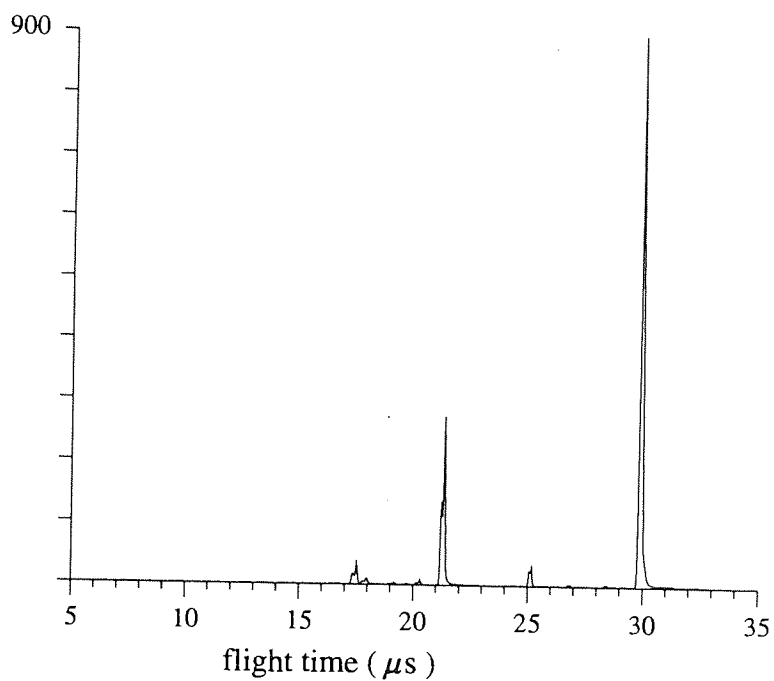


Figure 4.47 - Primary beam spectrum, FAB-1 source
Conditions : - $E_0 = 1000$ eV, argon.

A good fit indicated the mass assignments to be correct. t_{mca} is the peak position, as measured by the MCA and is given by the channel number/1024, and m_o is the corresponding primary particle mass assigned to the peak. The peak values were found from the second differential of the spectrum. The intercept gives the delay time, t_{delay} directly. In this case the delay was $0.05 \times 50 = 2.5 \mu s$. Although it was found that the delay was critically dependent on the amplitude and width settings of the pulse generator, a positive delay can be set by the delay generator so that the start pulse to the TAC is delayed by a fraction of the total time. In this case t_{delay} must be added to t_{mca} to obtain the total flight time from the deflection plates to the detector, t . The gradient of the fitted line is equal to $l/(2E_o)^{1/2}$. As the primary energy was known, the total flight length can be calculated, and is 2524 ± 9 mm. For collection of this spectra, the duration of the pulse produced by the pulse generator was 500 ns, compared to spectral peak width of ~ 150 ns, giving rise to a spectral resolution, $\Delta t/t$ of $0.15/30 = 0.5\%$.

Spectra collected with x 10 greater MCA resolution are given in figure 4.48. Figures (a) and (b) compare Ar^+ and Ar^o spectra. The Ar^o peak was obtained by the application of a voltage to the x-y plates, the Ar^+ peak by subtraction of the Ar^+ from the total ($Ar^+ + Ar^o$) which is shown in (c). Both the Ar^+ and Ar^o peaks have a width Δt of ~ 100 ns, and are displaced by ~ 100 ns. This displacement gives rise to a broader peak of the ($Ar^+ + Ar^o$) peak. The origin of the two subsidiary satellite peaks is uncertain.

Closer inspection of the Ar^+ peak revealed a broad low intensity peak on the lower energy side. It was found the intensity of this peak could be enhanced by adjustment of the x-y deflection voltage. This is illustrated in figure 4.49.

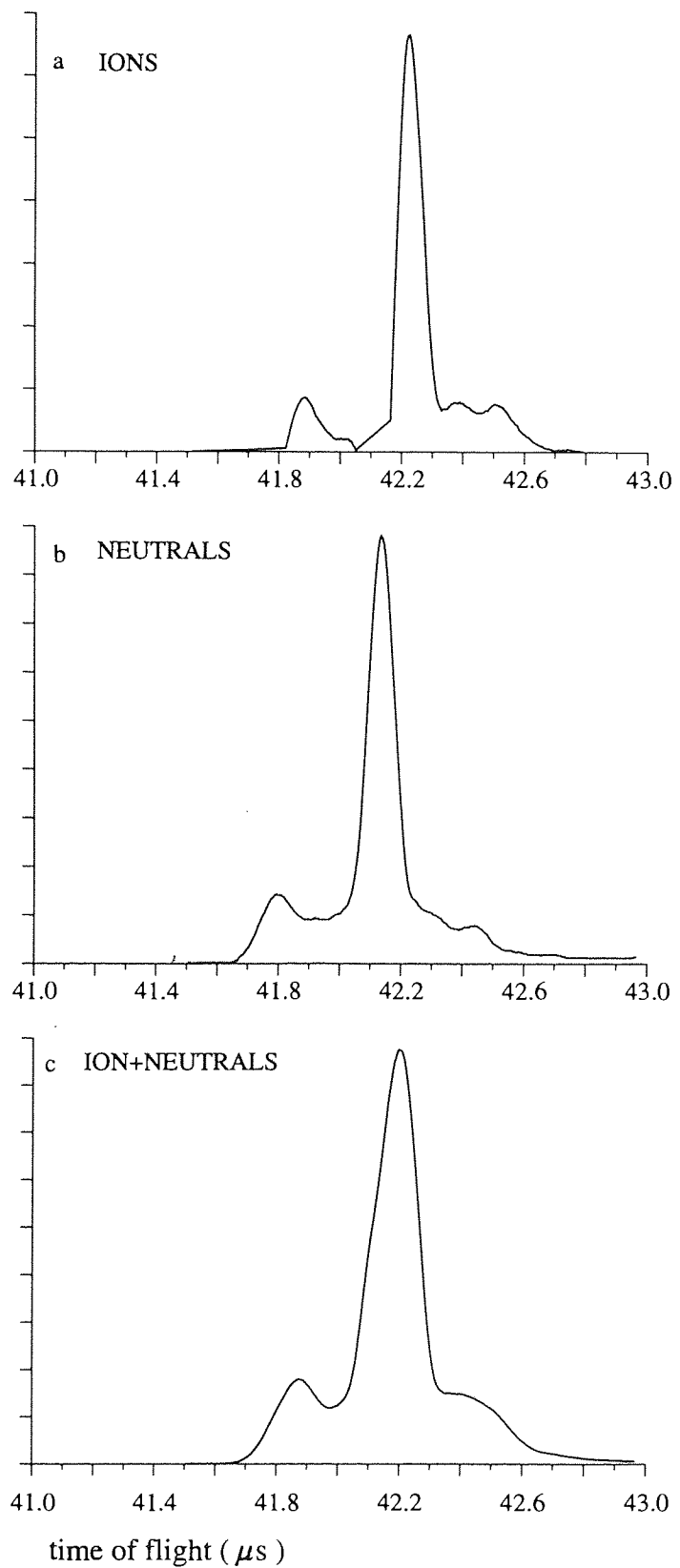


Figure 4.48 - Primary Spectra of the FAB-1 source. Conditions: $E_0 = 700$ eV
(a) ion beam, (b) Neutral beam, (c) total beam

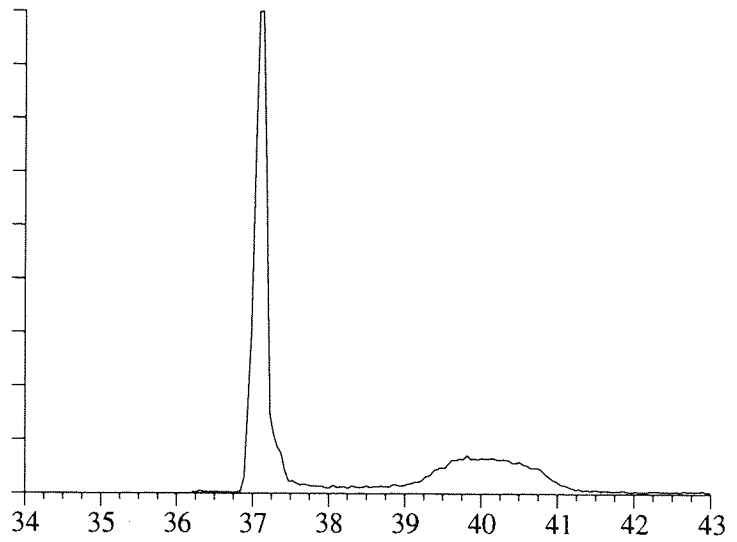


Figure 4.49 - Primary Spectra of the FAB-1 source showing a 'scattered peak' resulting from scattering from the flight tube walls, $E_0 = 900$ eV.

4.6.4 Remaining limitations

The characterization of FAB-1 showed a notable improvement in performance compared to the prototype source, such that it was possible to attempt some initial scattering experiments, the results of which are described in chapter 6. However, the performance of FAB 1 did not completely meet the specification given in section 4.2.3. The remaining shortcomings being 1] no mass filtering, 2] non-focused neutral beam 3] insufficient pressure differential between the source and chamber, 4] A substantial continuous current accompanying the pulsed neutral spectra. (This latter limitation was only revealed from the scattering data.)

4.6.5 Analysis of operation

4.6.5.1 Ion optics

The beam profile measurements of FAB-1 show the analysis of the prototype ion optics to be correct. Comparisons of the measured beam diameter with that predicted theoretically from the combined results of the ion source simulation and MUNRO showed good agreement. That is, the focused beam width and the lens voltage setting could be predicted theoretically. The measured beam diameters also agree well with the minimum value predicted for the source brightness, therefore showing that lens aberrations can be neglected. However, due to a column misalignment the operation of the accelerating lens could not be experimentally verified at this stage.

When the gas was fed to the CEC a small focused atom beam was observed, however the majority of ions were formed prior to the lens. This problem related to the source pumping rather than a limitation of the optics, and is considered further in the following sections.

4.6.5.2 Pulsing System

As the accelerating lens could not be operated, the pulsing system could not be operated in the mode for which it was designed. That is, ions with the full beam energy were deflected by the BCU, and a greater chopping

voltage, V_{chop} was required. The recalculated theoretical deflection curves are compared with experimentally derived curves in figures 4.50 and 4.51. It can be seen that the two sets of curves are in reasonable experimental agreement. The most significant difference is that the fall off is more gradual at larger values of V_{chop} in the case of the experimental data. Indicating that the angular current density of the extracted beam falls off more gradually than predicted by the gaussian given by eq. 4.38 and therefore must extend to an angle greater than 8° . The bright centre, however, appears to be represented well by a gaussian with a 2 mm FWHM. An additional implication of this operating mode was that the flight time of ions past the chopping plates was reduced by a factor of $\sqrt{5}$. Thus the performance required of the chopping circuit in terms of pulse width and pulse amplitude was greater than initially intended. A further repercussion was that the primary energy spread, ΔE_0 , according to the simulation model, is considerably greater in the case of a grounded extraction plate. Despite these limitations, reasonably sharp spectral peaks were observed, giving rise to acceptable instrument resolution, therefore demonstrating the electrostatic deflection approach to be a far more acceptable approach to beam chopping.

4.6.5.3 Pumping of the transport column and Charge Exchange Cell

The function of the CEC was to achieve neutralisation of the beam through gas phase resonant charge transfer collisions, (RCT). The gas phase collision processes for the conditions of interest to this work have already been discussed in previous sections. That is, the scattering of singularly charged ions incident on thermal neutrals of the same species. Specifically, the two processes of relevance which determine the properties of the emergent beam are those of elastic scattering and RCT. A general expression for the RCT cross-section was given by eq. 4.37. However, it was shown by the work of Jones¹⁹² and Barat¹⁹³ that the cross-section may contain oscillations within specific energy ranges. Eccles¹⁷³ also considered gas phase neutralisation as a means of neutral beam production, and concluded that RCT and elastic scattering should be considered as correlated. That is, ions which are neutralised tend not to be elastically scattered, and those which are scattered elastically tend not to contribute to the neutral beam. Similar conclusions were inferred from a computer simulation of the CEC undertaken by Wronski et

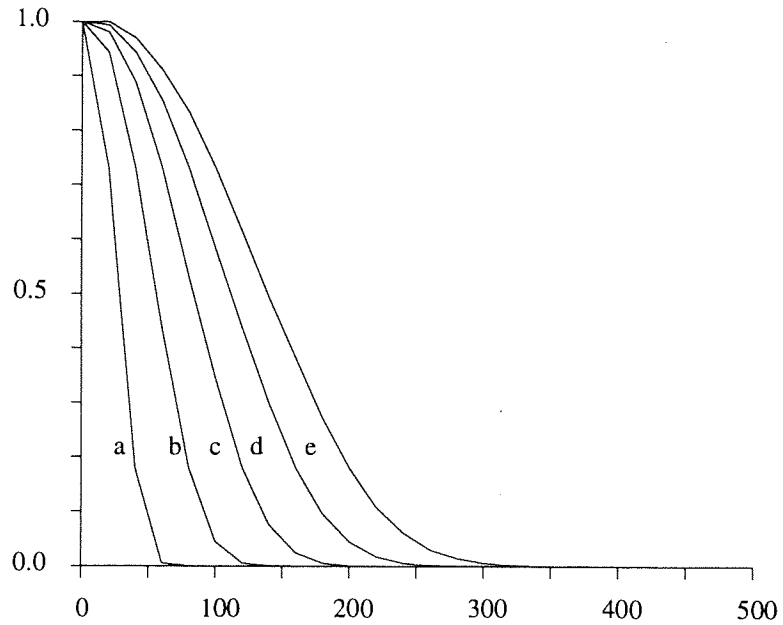


Figure - 4.50 Re-calculated deflection curves. Beam current function of V_{chop} - beam divergence: FWHM = 2° , total = 16° .
 (a) $E_0= 500$ eV, (b) $E_0= 1000$ eV, (c) $E_0= 1500$ eV, (d) $E_0= 2000$ eV, (e) $E_0=2500$ eV.

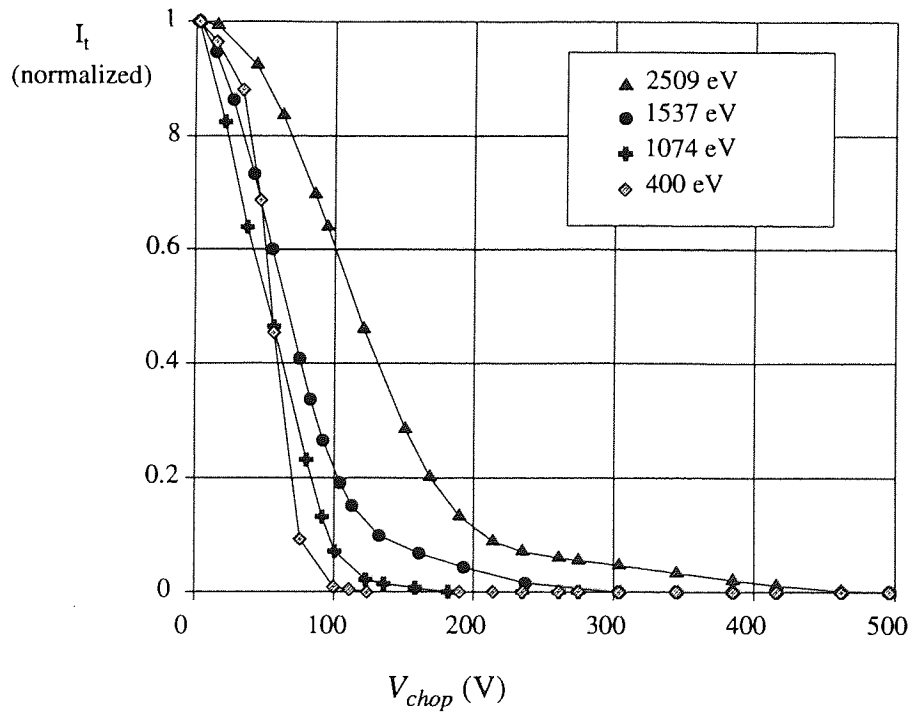


Figure 4.51 - Experimental deflection curves

al¹⁸³. It was also seen here that substantial proportions of the beam may be neutralised without the introduction of significant energy and angular dispersion: an energy dispersion of 0.01% is given. At low pressures $\sim 10^{-3}$ mbar elastic scattering produces characteristic broad low intensity tails on either side of the beam, but no broadening of the profile was seen. However, the simulation did show that to achieve a high neutral proportion, a significant proportion of the beam is lost by elastic scattering. For example, to achieve a neutral proportion of 70 %, requires that 50% of the initial beam is lost by elastic scattering.

To a first approximation, ignoring elastic scattering, the neutral proportion of the beam can be expressed as:

$$P(z) = 1 - \exp [z n \sigma_{RCT}] \quad \text{-(4.45)}$$

where n is the atomic density of the gas atoms.

For the present optical arrangement of the source, only collisions of greater than $\sim 0.3^\circ$ will remain within the beam. An ion undergoing a 0.3° collision with a stationary particle of the same species will sustain losses or 0.003% of its initial energy, according to simple kinematic considerations.

The model of Wronski assumed that the high pressure could be contained within the CEC, with the surrounding regions of the column maintained at UHV conditions. This represents ideal experimental conditions which in reality cannot be achieved. The pressure differential is limited by the conductance between the cell and the column and the pumping speed of the column, and can also be inferred from the experimental data: it was seen experimentally that the beam can be almost completely neutralised with the sleeve in placed over the transport column. The data given in figures 4.43 (a), (b) and (c) showed no evidence of a focused neutral beam. Most of the beam therefore must have been neutralised prior to the CEC. In the case of (d), the 2500 eV data, a neutral content of 99% was measured. It can be seen from eq. 4.45 that to attain $P(z) = 0.99$ within the transport column, a 300 mm length, requires a mean free path for RCT of 65 mm. The RCT cross-section for this energy is $2.9 \times 10^{-15} \text{ cm}^2$ giving rise to a pressure of 2.2×10^{-3} mbar, compared to the pressure measured by the ion gauge of $P_B = 2.3 \times 10^{-4}$ mbar. Supposing a homogeneous atomic density throughout the length of the column, a neutral

proportion of $1 - \exp(-20/6.5)$, 95 % would form prior to the CEC cell, with the remaining 4% taking place in the CEC. Thus it can be inferred that no significant pressure differential was present between the CEC and column when the column sleeve is fitted. The data recorded without the column sleeve fitted clearly exhibits a focused component to the neutral beam, see figure 4.42, indicating improved column pumping speed. Additionally, comparison of the ion beam profiles measured with and without the sleeve fitted, show the former to be considerably broadened. This is in contrast to the simulation of Wronski¹⁸³, which suggested that elastic scattering could not result in significant angular broadening.

Accurate theoretical prediction of the pumping speed within the column is complex, however, the above data indicates significant beam loss due to inefficient pumping of the column. With the sleeve fitted, this represents a severe limitation. These conclusions were also confirmed by approximate calculations based on the Knugsten formula.

Given the limited pressure differential that could be maintained between the CEC and transport column, other methods of neutralisation were briefly considered. However, a survey of the literature in this area revealed that all other obvious methods have been investigated previously and have been found to be unsatisfactory. The only viable alternative to the gas phase process is that of ion-electron re-combination. The neutralised fraction obtainable with this method was shown to be prohibitively small both from experimental and theoretical investigations, Eccles¹⁷¹

Experimental measurement showed that to obtain a significant neutral current the pressure in the analysis chamber was required to be equal to that of P_B . In order to ascertain the maximum possible chamber pressure it is necessary to assess the possible problems resulting from a high noble gas partial pressure in the chamber and flight tube during the analysis cycle. As inert gases have very low sticking co-efficient with solid surfaces, the high partial was considered to present no contamination problem of the sample surface. An important consideration, however, is that of neutralisation of ions on their voyage from sample to detector. This imposes the criteria that the mean free path for neutralising collisions must be much greater than the length of the flight path. For example, $1/\Sigma$ should be greater than 10 m, in which case a chamber and flight tube pressure of greater than 1×10^{-5} mbar must be maintained. As the energy of the ions decreases this pressure limit increases.

4.7 Second modifications - The FAB-2 Source.

Renewed interest in the work by the industrial manufacturer towards the end of the programme allowed a further version of the source to be realised, which will subsequently be referred to as FAB-2. The basic modular construction of this source was the same. The re-design was based on the analysis of the experimental data gained from FAB-1, the notable changes introduced were the re-introduction of the Wein filter, and the introduction of a 5° bend, (neutral dump). This bend was intended to remove all neutrals from the beam formed before passing the second lens element.

4.7.1 Principles of the new design

4.7.1.1 Ion optics

The changes in the design of the optical system of FAB-1 were minimal. The 2nd lens is unchanged, the philosophy of the primary accelerating lens, the design of which was discussed in detail previously, was also unchanged. However, the accelerating lens was made shorter in length due to constraints of space due to the addition of the neutral dump, and also due to concerns with regard to stray electrical fields. The optical characteristics for the new geometry are given in figure 4.52

4.7.1.2 The Wein Filter

The re-design of the Wein filter aimed to resolve the limitations described previously. The general requirements of the design can be summarised as follows:

1] Elimination of the re-entrance of dispersed ions into the beam via glancing angle collisions with the deflection plates.

2] Reduction/elimination of asymmetric focusing and distortion effects to a tolerable level, whilst maintaining satisfactory mass separating power.

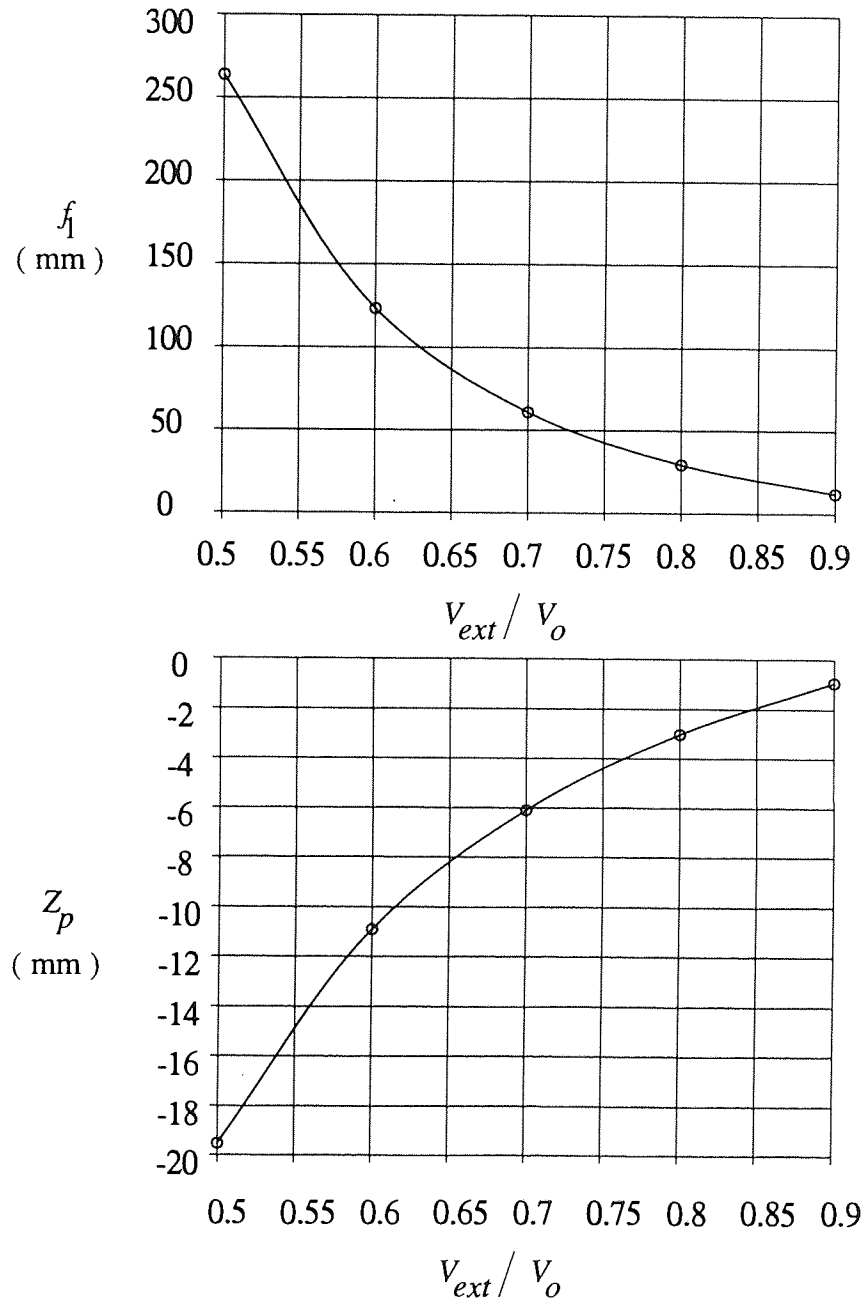


Figure 4.52 - Optical Characteristic of the 1st lens of the FAB-2 source. (a) focal length, (b) principle plane position.

The design was based on the same numerical simulation as described previously. A significant problem with the Wein filter resulted from the axial inhomogeneous magnetic field, $B(z)$. Repeating the simulation with a field distribution resulting from a single magnetic pole piece of 78 mm length demonstrated reduced distortion, but still significant distortion remained. That is, axial ions entering the ExB region at the tuned velocity emerge from the field at an angle and displaced from the axis. Close examination of the origin of this distortion revealed it to be related to a field imbalance between $E(z)$ and $B(z)$ at the entrance and exit planes. This imbalance was caused by the different relaxation distances of the two fields.

The redesigned filter is shown in figure 4.53 where the separation between the magnetic pole pieces is now equal, providing approximately equal axial termination profiles of the two fields. Further advantages of this design are, firstly, no ceramic material is exposed to the beam. Secondly, the wider magnetic poles give a more homogeneous magnetic field in the lateral direction, $B(y)$. To obtain the same improvement for the lateral electrical field the E plates were made 'C' shaped in profile, the optimum geometry being obtained by finite difference calculation. Re-simulation employing the new geometry showed significant reduction in the trajectory distortion. The remaining distortion resulted from some remaining field imbalance, the magnitude of which was dependent on the magnetic field strength.

The final magnetic field strength was determined by consideration of the trajectory distortion, asymmetric focusing, and mass discrimination power. As low distortion and low asymmetric focusing are mutually exclusive with high mass discrimination power a compromise was reached. The mass discrimination necessary was dependent on the contaminant atomic masses to be removed from the beam, relative to those of helium, neon and argon. The mass discrimination has the following dependency on the magnetic field strength:

$$\Delta M = M_o a/B(b + c/B^2)^2 \quad -(4.46)$$

where a and b are constants dependent on geometry and particle energy. Contaminant masses present in significant proportions were seen in the unfiltered primary spectra of the FAB-1 source. Heavy metal ions resulting from internal sputtering and from the filament may also contaminate the beam.

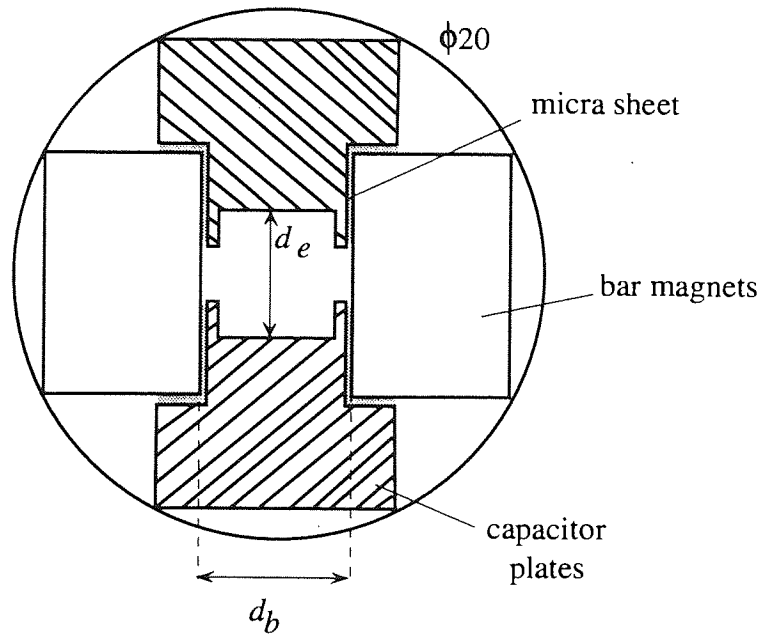


Figure 4.53 - Geometry of the Re-Design Wein Filter (FAB-2 source)

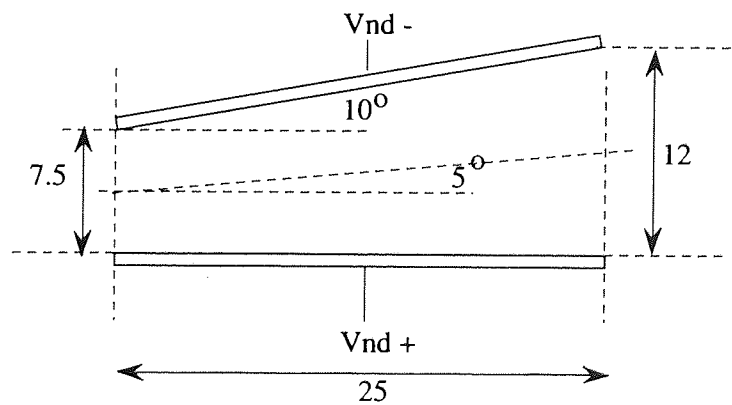


Figure 4.54 - Dimensions of the Neutral Dump Unit installed in the FAB-2 source.

Ideally it would be possible to remove all these species from helium, neon and argon beams of energies up to 5 keV. The least discrimination in terms of amu is achieved for high energies and high masses, that is a 5 keV argon beam. In this case the nearest contaminant is CO₂ at amu 44. However, greater discrimination power is required to remove H₂O at amu 18 from a Ne²⁰ beam, and this represented the most demanding separating requirement.

Consideration of the mass discrimination power achieved with an aperture of 2mm diameter located at the exit plane of the ExB field shows a 0.3 T field strength was required to discriminate H₂O from a 5 keV Ne²⁰ beam. A field of this strength, however led to unacceptable asymmetric focusing and distortion. The distortions to the trajectory described above are greatest for low atomic mass and energy. Therefore, for the purpose of design, calculations were based on a 1 keV helium beam. Acceptable distortion levels were defined by the following criteria:

- The resulting deviation of the beam at the sample should be less than one quarter of the beam width: if Δy and $\Delta\theta$ measure the lateral and angular displacements, the criteria is given by the following expression:

$$(\Delta y^2 + (W \tan\Delta\theta)^2)^{1/2} < \text{FWHM}/4 \quad \text{-(4.47)}$$

Evaluation of 4.47 on the basis of the trajectory simulation indicates a maximum field strength, B of ~ 0.1 T.

A similar criterion was adopted for the astigmatism, which limits the beam's ovality to:

$$\text{FWHM}_x / \text{FWHM}_y < 2 \quad \text{-(4.48)}$$

Evaluation of eq. 4.48 also indicated a maximum magnetic field strength of ~ 0.1 T

Distortion may be reduced whilst maintaining mass discrimination power, $m/\Delta m$, by increasing the length, L , of the ExB field region. However, in this case the angular separator strength θ_L is maintained and so the focal length, f_w , also remains unchanged. Thus, to maintain $m/\Delta m$ whilst reducing θ_L required either a reduction in the aperture diameter, or the introduction of a

drift region between the ExB field and the aperture. Such an aperture was already provided by the 3.5 mm exit aperture of the CEC, located at a distance of 150 mm from the exit plane of the ExB field. In consideration of this, $m/\Delta m$, was found to be sufficient to allow the separation of H₂O from a ²⁰Ne beam for energies less than ~ 2 keV. It was therefore not possible to fully meet all three criteria simultaneously in a single source without the introduction of smaller apertures, thus further reducing the beam current. Thus two possible alternatives were faced:

1] To operate with argon and neon only, in which case the separating field strength could be increased sufficiently to remove H₂O from a neon beam up to 5 keV

2] To operate with all three species, without the capability to fully discriminate H₂O from the neon beam above energies of ~ 2 keV.

For the purpose of the experimental programme the first option could not be considered, and so the field was set to a strength 0.1 T.

For elimination of the asymmetric focusing effects the employment of the stigmatic separator field described by Seliger¹⁹⁴ was considered. This work demonstrated that the astigmatic properties of the ExB fields may be eliminated when the magnetic pole faces are mounted at an angle. By rotating to a specific angle of inclination the focal length in the x and y planes can be made equal. However, as the angle of inclination is related to the cyclotron radius, r_o , application is limited to a particular ion mass and energy. Such operation would require the filter to be floated at high potential and the beam post accelerated by a subsequent lens to the required energy. Although this arrangement is theoretically feasible it involves extensive redesign and would incur considerable costs and therefore could not be achieved within the duration of the PhD programme.

4.7.1.3 The Neutral Dump Unit

A neutral dump unit (NDU) was introduced to remove neutrals formed in the transport column, ensuring that the final neutral beam did not contain non-focused or un-chopped components. It was therefore necessary to

place the unit immediately preceding the 2nd lens element. This arrangement presents a focused ion beam to the CEC. The geometry of the NDU is shown in figure 4.54. The unit introduces a 5° bend, and comprised two 25 mm long deflection plates to introduce the necessary deflection of the ion beam. In order that the beam remains axial it must remain on a zero volt equipotential. Thus deflection voltages of opposite polarity were applied to the deflection plates, denoted by V_{nd}^+ and V_{nd}^- . Thus, as for the Wein filter a 'dual tracking' power supply was required. In order to maintain the beam centre equidistant between the two plates, and therefore on a zero volt equipotential the plates were inclined to each other at twice the deflection angle. Strictly this condition can only be satisfied with curved deflection plates, however due to the large radius of curvature involved, straight deflection plates provide a reasonable approximation, and were considerably more simple to fabricate. To avoid interdependence between the voltage settings of the Wein filter and neutral dump the plane of deflection should be orthogonal to the dispersion plane of the Wein filter.

The electrical field of the neutral dump unit also has asymmetrical focusing properties. This can be appreciated by considering what happens to ions entering the field with a small displacement from the axis towards the positive plate. Such ions will lose velocity on entering the region of higher potential, therefore spending a longer time travelling through the NDU than axial ions, and will therefore receive a greater deflection. Ions displaced towards the negative plate will receive a smaller deflection by similar arguments. However, these focusing effects are independent of particle mass, and were found to be sufficiently weak as to be neglected.

The ideal field of the NDU can be expressed as:

$$E_x = 0 \quad \text{-(4.49)}$$

$$E_y = 2 V_{nd} \cos\theta / (s_l + z \tan \theta) \quad \text{-(4.50)}$$

$$E_z = 2 V_{nd} \sin \theta / (s_l + z \tan \theta) \quad \text{-(4.51)}$$

and the equations of motion of a particle within this field are:

$$d^2y/dt^2 = 0, \quad d^2y/dt^2 = eE_y, \quad d^2z/dt^2 = eE_z \quad \text{-(4.52)}$$

For an ion initially located at (x_o, y_o, z_o) with component velocities of:

$$(dx_o/dt=0, dy_o/dt=0, dz_o/dt=[v_o + 2 y_o V_{nd}/s_1]) \quad -(4.53)$$

The deflection voltage required can be found from consideration of axial ion trajectories and is given by:

$$V_{nd} = E_o b \tan\phi / \ln(1+bl/s_1) \quad -(4.54)$$

where b is given by:

$$b = (s_2 - s_1) / l \quad -(4.55)$$

4.7.1.4 The Chopping plates

The chopping plate assembly was basically unchanged from the design employed in the FAB-1 source. As the alignment problems were resolved at this stage and the chopping plates could be operated at the potential of the extraction plates, as was initially intended.

4.7.2 Characteristics of the FAB-2 source

As with the work on the FAB-1 source the beam accelerating voltage, V_o and other ion source voltages were supplied with the converted Kratos Mini beam power supply, and therefore operation was still confined to voltages below 3.5 kV. Beam currents, profiles, and primary spectra were measured using the methods described previously. With the exception of the persisting problem of lower than ideal beam current and insufficient pressure differentials, the FAB-2 source was capable of producing a beam with all the qualities required by the initial specification. The following section demonstrates the capabilities of FAB-2 and defines optimum operating conditions.

In order to achieve improved differential pumping the length of the differential pumping line was shortened to 700 mm, and then to 500 mm in the preceding scattering experiments. Due to construction difficulties the orientation of the filter and the neutral dump could not be freely chosen, and so

the dispersion planes of the Wein filter and the neutral dump could not be made orthogonal. During these measurements the plane of dispersion of the Wein filter was located in the horizontal plane, and that of the neutral dump was $\sim 20^\circ$ to the vertical.

4.7.2.1 Beam current

To aid initial setting up, the beam current striking the plate following the neutral dump was measured. With $V_{nd} = 0$ the full beam passing the NDU was collected on the plate. The resulting measured current recorded by the electrometer is subsequently referred to as I_{dp} . Measurement of I_{dp} enabled characterization of the Wein filter independent of the voltage settings of preceding elements. As expected, the current emerging from the tuned filter was found to be strongly influenced by V_{ext} . In agreement with the lens calculations maximum current was observed for $V_{ext}/V_o = 0.70$. This result was found to be independent of ion species and E_o . The current obtained for $V_{ext} = 0.7 V_o$ was $\sim \times 10$ that at $V_{ext} = 0$.

The MUNRO calculation of the primary lens gave an image plane located at -7 mm and a focal length of ~ 65 mm for $V_{ext}/V_o = 0.70$, see figure 4.52. Thus p_1 of ~ 70 mm, gives an image distance close to infinity. The dependence of I_{dp} on V_w for a helium beam is shown in figure 4.55. These curves are much sharper than the corresponding curves of the prototype Wein filter, despite the weaker field strength. As the mass resolving power is defined by the exit aperture to the CEC cell, a more accurate measurement of V_w could be made spectrally.

The voltage setting of the NDU can also be determined by measurement of I_{nd} . That is measurement of I_{nd} as a function of V_{nd} with V_w constant and appropriately set, produced a minimum corresponding to the ion beam passing through the neutral dump plate aperture. Values of V_{nd} found by this method as a function of energy gave good quantitative agreement with eq. 4.55, confirming V_{nd} to be a linear function of E_o . However, again V_{nd} was found to be more accurately determined by spectral measurements. The maximum total beam current ($I_i + I_n$) measured on the neutral dump plate was ~ 400 namps, corresponding to a maximum sample current of ~ 300 namps. The maximum neutral beam current achievable however was smaller than

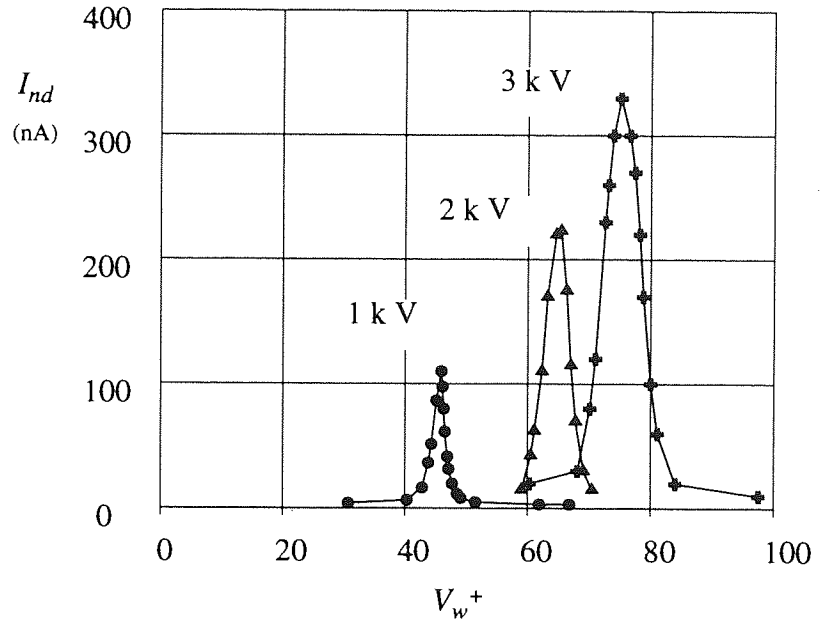


Figure 4.55 - Characteristic of the Wein filter for a helium beam of $E_o = 1, 2$ and 3 keV.(FAB-2 source).

The current was measured on the plate proceeding the neutral dump, I_{nd} .

those produced by FAB-1, with a maximum value of ~ 30 namps being recorded.

4.7.2.2 Beam profile

The minimum focused beam width of ~ 1 mm, at $W = 200$ mm was given for the conditions $V_{ext}/V_o = 0.7$, $V_2/V_o = 0.33$, in agreement with the calculation. The astigmatism introduced into the helium beam was found to be equal to that set by the Wein filter design criteria. Thus the astigmatism in effect prevents simultaneous focusing of the beam in horizontal and vertical directions: the minimum vertical profile was given for $V_2 = 0.33 V_o$, whilst the minimum horizontal profile was given by $V_2 = 0.36V_o$, and equal width profiles can be obtained for $V_2 = 0.34V_o$, as shown in figure 4.56. In the latter case the profile width was ~ 2 mm. The astigmatism was found to be less severe in the case of argon and neon, where symmetrical beam profiles of width ~ 1.5 mm were obtained at $V_2 = 0.33V_o$.

Typical neutral beam profiles are shown in figure 4.57. In (a) the source gas was admitted to the IC only with $P_B = 4 \times 10^{-4}$ mbar. Even in this case a significant focused neutral beam could be obtained. A low intensity non-focused component can also be observed, which was attributed to the formation of neutrals in the short region of the column between the NDU and the 2nd lens. In (b) gas admitted to both gas cells, first to the IC until $P_B = 5 \times 10^{-5}$ mbar and then to the CEC to give P_B was 4×10^{-4} mbar. The total neutral current was not significantly greater than (a), however the broad de-focused component of the beam was no longer visible. The significant reduction in the non-focused component shows that a much greater proportion of the neutrals are formed within the CEC. However, there is not a significant increase in the total neutral current due to the increased pressure and therefore the neutralisation in the column section before the NDU.

4.7.2.3 Primary Spectra

For the first time, the primary spectra measurements were made with apertures placed in the flight tube, and so effects arising from internal scattering from the flight tube walls were no longer present. Considerations concerning the placement of the apertures are considered in chapter 5. The

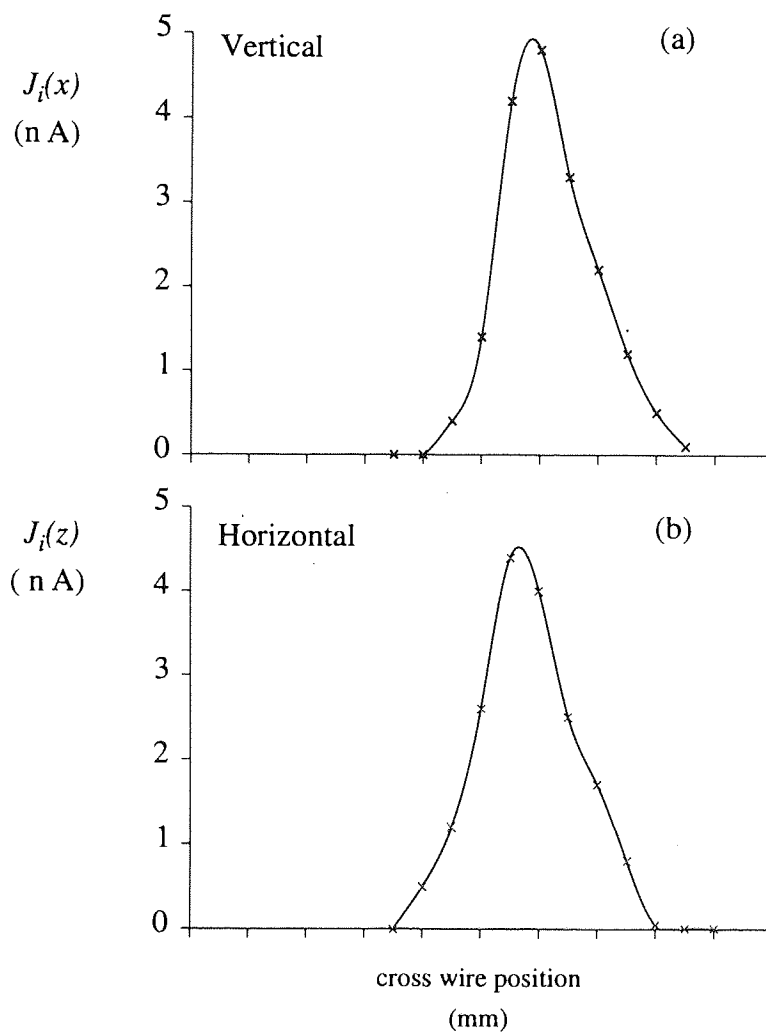


Figure 4.56 - Helium ion beam profiles - (FAB-2 source)
 $V_2/V_0 = 0.34$ (a) Vertical, (b) Horizontal

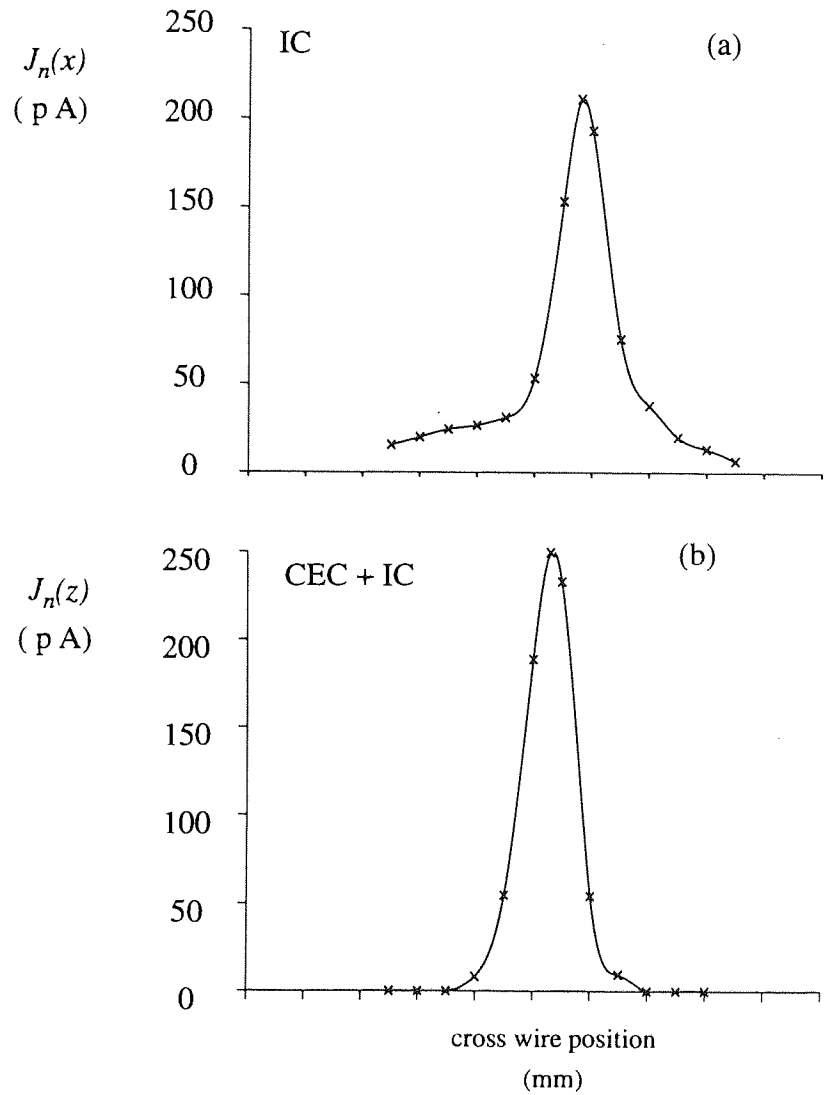


Figure - 4.57 Helium neutral beam profiles - (FAB-2 source), $P_B = 4 \times 10^{-4}$ mbar.

- (a) Gas to IC only
- (b) Gas to IC and CEC

collection times were a few seconds only, and again the count rate was maintained below 1 count per pulse.

It was found that the sharpness of the primary spectral peaks were critically dependent upon the applied electrical pulse. It was necessary to adjust to the value appropriate for the energy and species of the primary beam. For accurate setting, the chopping waveform was observed directly using an oscilloscope, although a reasonable guide is to set the primary pulse from the pulse generator to $\sim 2.5x$ the value given in figure 4.58. Below this value the pulsed current reduces sharply and the peak became broader. This low intensity broad peak was attributed to ions from the low quality fringe of the beam. This part of the beam was also present in the case of optimum chopping conditions, however, the intensity was too low to contribute significantly to the total peak width. A pulse of greater duration than the optimum led to wider spectra peaks with higher intensity. The maximum pulse width was limited in the capacitive coupling mode to ~ 300 ns. This is because the high voltage capacitor through which the pulse was coupled acted as a high pass filter, and lower frequencies could not be transmitted.

Raw data for primary spectra of 1 and 2 keV argon beams are shown in figure 4.59. Each data point corresponds to single MCA channel. No processing has been applied to the data. The FWHM of the peaks are 40 and 25 ns for 1 and 2 keV respectively giving rise to a spectra resolution of ~ 1000 . The corresponding resolution for the neon spectra, shown in figure 4.60 was ~ 400 , and ~ 700 for the helium spectra shown in figure 4.61.

The overall width of the spectral peaks have contributions from both time and energy spread within the 'ion bunch'. Thus

$$\Delta t_{spectra} = \sqrt{(\Delta t_E)^2 + \Delta t_i^2} \quad -(4.56)$$

where Δt_E represents the contribution to peak width due to the energy spread inherent in the ion bunch, and is equivalent to that of the continuous beam. Δt_i represents the temporal extent of the ion bunch and is determined by the chopping system. Eq. 4.56 may be written as:

$$\Delta t_{spectra} = \sqrt{(\Delta E_o t / 2E_o)^2 + \Delta t_i^2} \quad -(4.57)$$

where it can be seen that the contribution of Δt_E is dependent on the flight time,

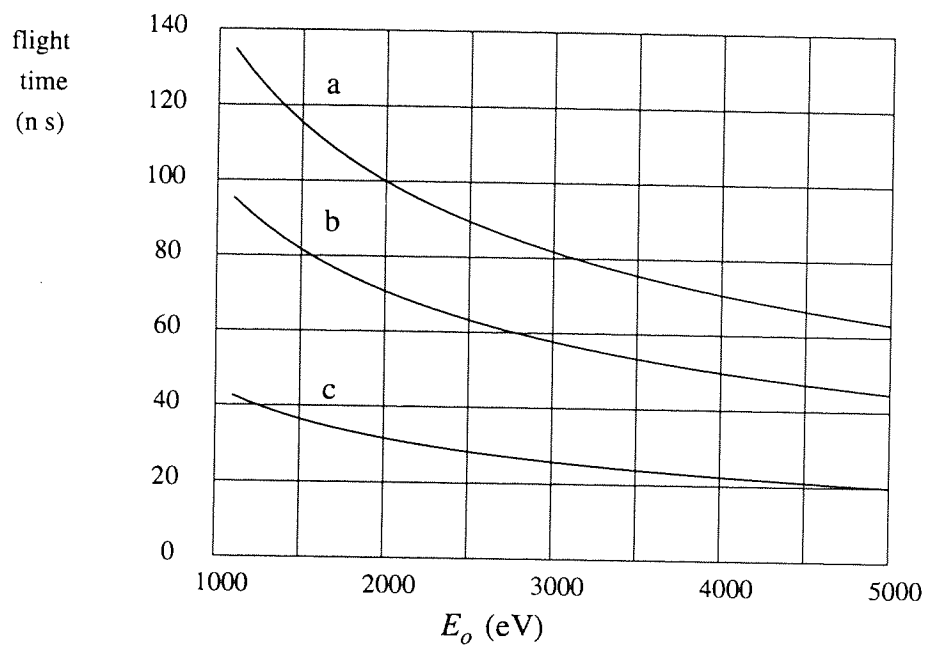
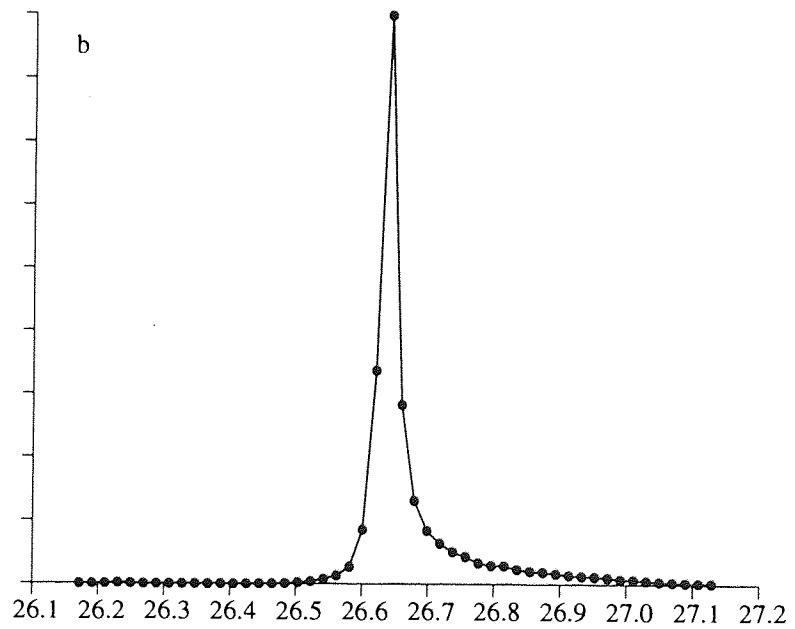
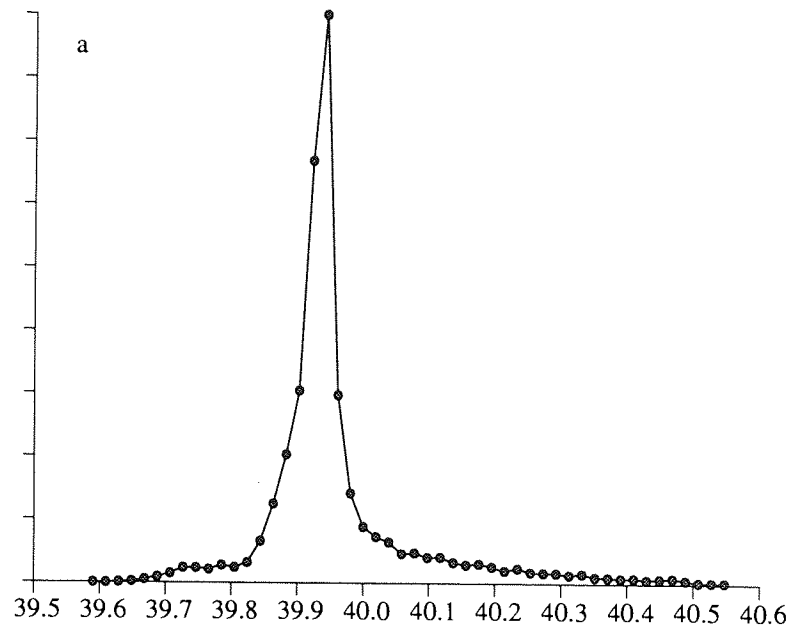


Figure 4.58 - Flight of ions through the chopping plates.
for $V_{ext}/V_0 = 0.7$
(a) argon, (b) neon, (c) helium



flight time (μs)

Figure - 4.59 Argon spectra - ion beam - (FAB-2 source)
(a) $E_o = 1$ keV, (b) $E_o = 2$ keV

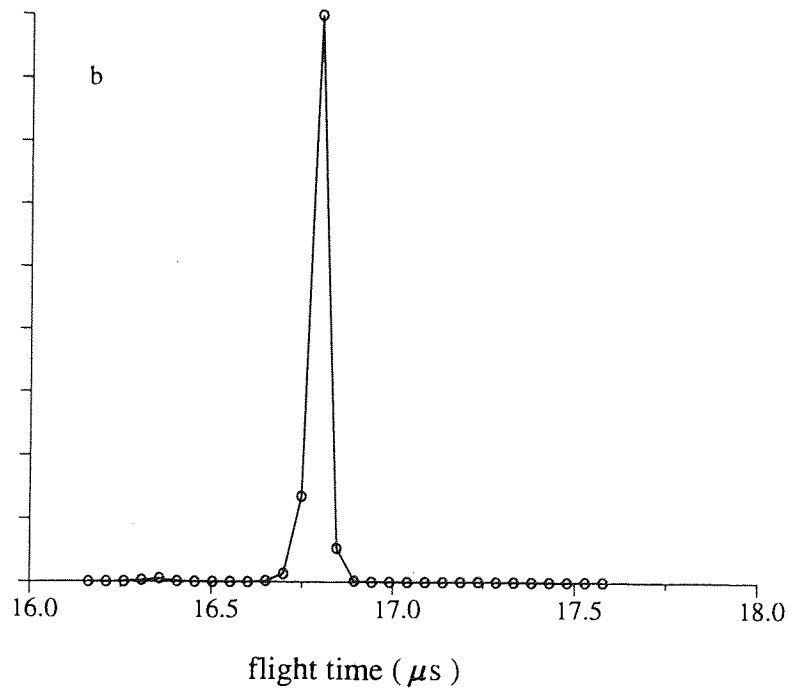
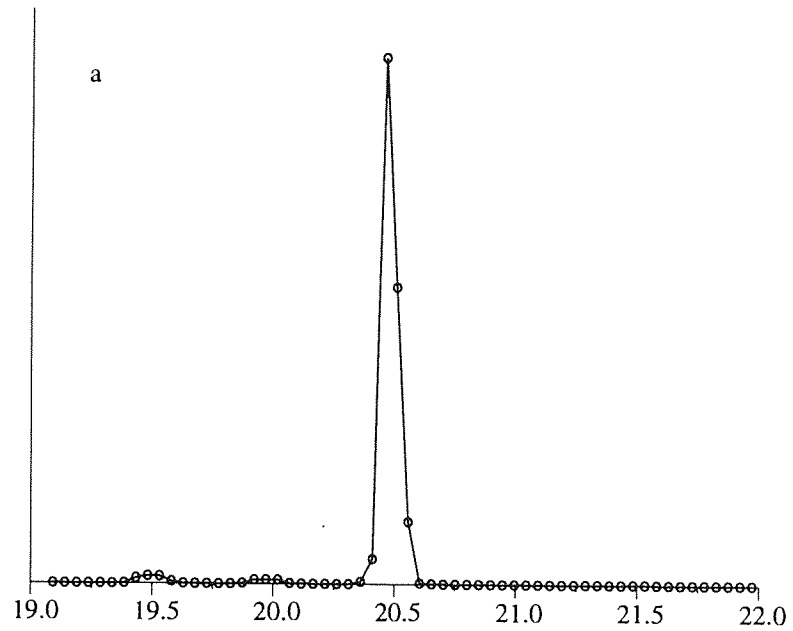


Figure 4.60 - Neon spectra - ion beam - (FAB-2 source)
(a) $E_o = 2$ keV, (b) $E_o = 3$ keV.

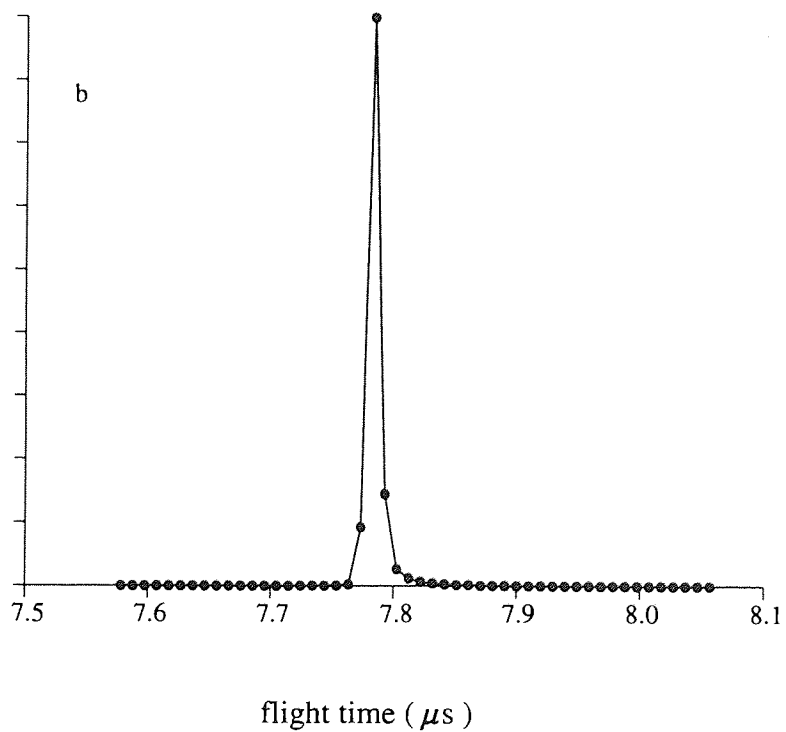
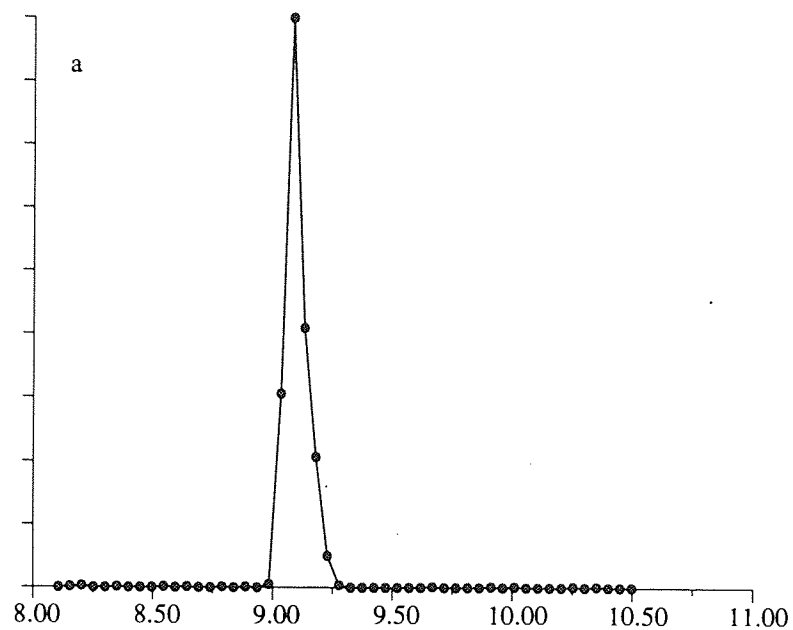


Figure 4.61 - Helium spectra - ion beam - (FAB-2 source)
(a) $E_o = 2$ keV, (b) $E_o = 3$ keV

and therefore is the most dominant contribution for long flight times. Whereas Δt_i is expected to dominate for shorter flight times.

If it is assumed that the width of the argon peak in figure 4.59a is dominated by the contribution of Δt_E , then the primary beam energy spread, ΔE_o must have been less than 2 eV, equivalent to $\Delta E_o/E_o$ of $< 0.2\%$. At the opposite extreme, ie a 3 keV He beam, the peak width is only 7ns. Thus the time spread of the ion pulse must have been less than ~ 5 ns, which is considerably shorter than the primary pulse duration. Another possibility is that the energy spread inherent in the helium beam was smaller than that of the argon beam, however there was no evidence from the ion source simulation to suggest that ΔE_o was mass dependent.

The spectrum of a neutral beam is shown in figure 4.62. It can be seen that no significant broadening of the neutral peak resulted from the neutralisation process. The displacement of the ion and neutral peaks is ~ 50 ns, and originated from the acceleration of ions on approaching the detector. (The exposed MCP plate was at a potential of -2.7 kV).

It is important to stress that the sharp peaks shown here could only be achieved if both the Wein filter and the neutral dump were precisely tuned. Indeed, observation of the primary spectra provided the most accurate method of determining the optimum settings. It was found that the neutral dump voltage was reliably predicted by eq. 4.55. In this case V_w was reasonably predicted by eq. 4.29, assuming a magnetic field strength of 0.08 T. However, the field strength was found to be subject to drift with the operating temperature of the source. The field strength was also found to be reduced by $\sim 20\%$ following baking of the system. Typically the tuned value of V_w decreased by ~ 2 volts within a period of 15 minutes after switching on the source. In the case of helium and argon the V_w setting for maximum current was co-incident with minimum peak width. For neon the situation was complicated by the presence of the two isotopes, ^{20}Ne (isotopic abundance of 91%) and ^{22}Ne (isotopic abundance of 8 %). V_w giving the best isotope separation and separation from H_2O did not give rise to maximum beam current.

The mass separating power of the Wein filter is demonstrated in figure 4.63, which shows that the two isotopes of neon could be almost completely separated: With $V_w=20$ volts, ^{20}Ne is the only selected peak, the

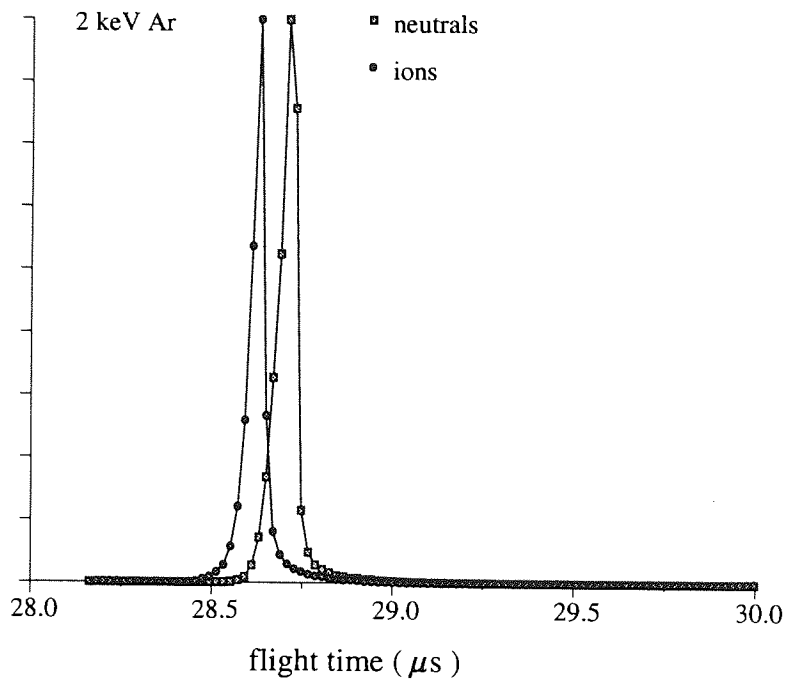


Figure 4.62 - Argon ion and neutral beam spectra. - (FAB-2 source)

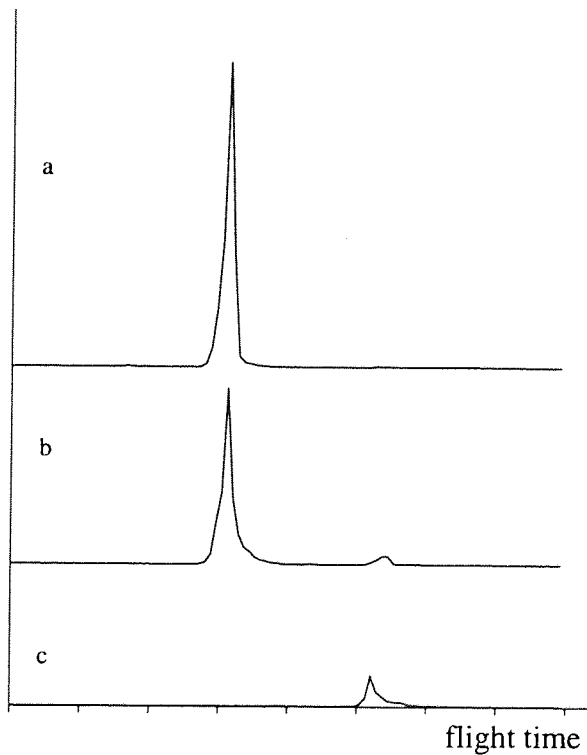


Figure 4.63 - 1 keV neon beam - (FAB-2 source).

- (a) $V_w = 20$ V - ^{20}Ne selected (small H_2O and ^{22}Ne visible either side)
- (b) $V_w = 19$ V - both isotopes selected
- (c) $V_w = 19$ V - ^{22}Ne selected

H₂O and the ²²Ne peaks lying 2 amu to either side are just visible. At $V_w=19$ volts the ²⁰Ne and ²²Ne peaks were equally selected by the filter, ie it was tuned to amu 21. At $V_w = 18$ volts the ²²Ne peak alone was selected. It can also be seen from the figure that the spectral peaks shape varied as V_w was scanned across the peak: Broader and lower intensity peaks resulted when the filter was slightly off tuned, and so it was necessary to set V_w with an accuracy of ~ 0.25 volts.

Due to reasons previously given a small interdependence between of the V_w and V_{nd} was observed.

4.8 Conclusions

4.8.1 Final characteristics

The characteristics of the final source version, FAB-2, were satisfactory to proceed with the experimental program: the final beam chopping method in particular worked very well, giving rise to very short duration pulse widths. This combined with the small energy spread of the beam offered the potential for very high instrumental resolution. The mass filter and neutral dump units also functioned well and were in agreement with calculation. The acceleration lens was also seen to be successful, giving rise to ion beam currents ~ 10 times greater than could be achieved by the FAB-1 source, which was operated without the acceleration lens. This factor may have been significantly greater in the absence of the problems of reduced emission current during the operation of FAB-2 described below. However, the greatest loss of current was thought to be due to the poisoning of the column mounting plate. This plate seals tightly with the external body of the source. From construction consideration this plate was made the first element with no applied voltage, which in the case of the FAB-2 source was the 2nd element of the primary lens. Thus the region prior to this plate was solely pumped through the central aperture of 2 mm diameter. As a result the extracted beam had to pass through a high pressure, ~ 35 mm in length, $\sim 1 \times 10^{-3}$ mbar, that is the IC pressure. This gave rise to significant beam loss due to RCT and elastic scattering. This problem could be resolved simply, by mounting the source on the extraction plate. The seal in this case would have to be constructed from insulating material and be capable of withstanding the extraction voltage. The most

significant remaining limitation of the FAB-2 source was that of low neutral beam current: the maximum neutral beam was 30 nA, which was a result of insufficient pumping of the transport column. That is most of the beam was neutralised before the neutral dump, and therefore lost. This problems could be resolved in future by the addition of a further differential pumping stage, and a greater bore tube for housing the column. Clearly it is also important to maintain the pumping lines as short and as wide as possible. The electron trajectory simulation mode described in section 4.53 indicated that simple changes to the geometry of the ion cell could also lead to greater source brightness. However, to gain more significant increases in beam current would require the replacement of the present ion source by a high brightness source, such as the magnetically confined duoplasmatron type. The beam diameter was sufficient for the purposes of this work, although improvements would be possible by reducing the working distance. One simple way to achieve this would be by removal of the alignment stage, or the introduction of a 'zero length' alignment stage.

4.8.2 Operational Problems

There were a few operational related problems with the FAB-2 source which could be overcome by some simple changes. The first operation problem related to the build up of contamination on the ceramic spacer tubes between the grid and extraction electrodes. This was despite the provision of the guard, preventing the deposition of material sputtered from the extraction electrode. The addition of this guard resolved the problem in the case of the FAB-1 source. Its return in the FAB-2 source was attributed to the reduced pumping speed of the region, leading to increased deposition of material desorbed from the filament. For the purpose of this work the problem was solved by employing a higher current rated PSU to meet the resulting leakage current. Simple geometry changes would resolve this problem in later versions. A second operation problem resulted from the availability of appropriate diameter filament wire at the time of construction. The wire used in the FAB-2 source was slightly too large, and as a consequence only ~ 9 watts of power was drawn by the filament leading to a low emission current of 12.5 milli amps compared to the 30 milli amp maximum rating of the emission current PSU.

4.8.3 Future Development

Having demonstrated the successful operation of the neutral dump it would be in future unnecessary to position the chopping plate assembly as close to the extraction plate. This opens the way in future versions of the source to re-position the chopping plates to the focal point of a preceding lens.

The experimentation with the FAB-2 source was complicated by the presence of a large number of voltages that must be set according to the operating gas and energy. Thus the setting of these voltages would be significantly simplified by the introduction of computer control. Such a system had been constructed at the time of writing, and will provide a significant advantage during the course of future operation.

The work described in this chapter has required the development of a number of simulation models of various source components, which are described and referred to in the text. These programs provide a useful tool in the event of further development of the FAB or similar sources.

CHAPTER V

Development of the Spectrometer

This chapter gives details of the developments made to the prototype Fast Atom Scattering Spectrometer (FASS) during the course of the programme.

5.1 Description and limitations of the prototype instrument

At the outset of the programme the components of a prototype FASS instrument had been assembled, from a design based on a previous instrument employed by Xu and Sullivan²⁶⁻²⁸. However, no measurements of the instrument's capabilities had been made at the start of this doctoral work. The basic elements of the prototype instrument were (1) the main vacuum chamber, (2) the flight tube and detector, (3) the primary particle source, (4) the pulse timing electronics/spectrum recording instrumentation.

The main vacuum chamber allowed the source to be mounted in five possible positions, giving rise to the five possible scattering angles of 16° , 45° , 90° , 135° and 164° , as shown in figure 5.1. Pumping of the chamber was provided by a single vapour diffusion pump, a 500 l/s Edwards, model 804, through a liquid nitrogen cold trap, which could be isolated from the main vacuum chamber. Allowing for the baffle valve and the cold trap, the effective pumping speed of the chamber was ~ 200 l/s. An xyz sample stage was provided for sample positioning, allowing ~ 10 mm of x and y travel and ~ 50 mm of z travel. A "Spectramass Dataquad" residual gas analyser was also mounted on the vacuum chamber. No other surface analysis techniques were available. The original flight tube was ~ 2000 mm in length and of 36 mm internal bore, and was terminated by a 18 mm diameter double plate micro channel plate detector (MCP), operated in positive mode, that is with a voltage of +1.8 kV applied to the anode. A more detailed description of the principles of the detector is given in section 5.6.2. No apertures were present on the flight tube and no provision had been made for the discrimination of ions and neutrals. Pumping of the tube was provided by a Varian ion pump. The only means of primary particle production was the prototype source, which had a number of severe limitations, as described in the previous chapter.

The pulse timing electronics were de-coupled from the positive

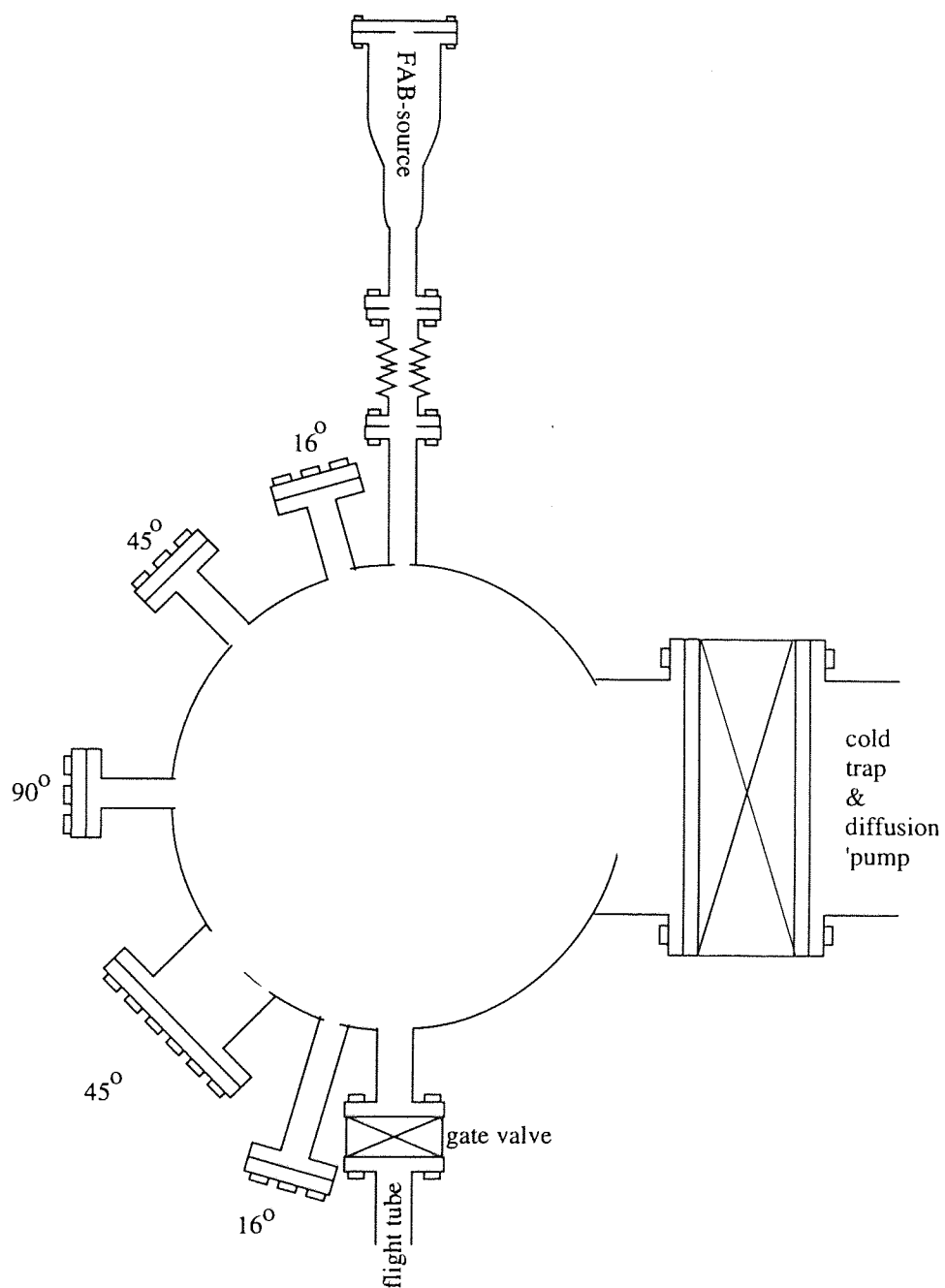


Figure 5.1 - Configuration of the vacuum chamber

anode of the detector through a 1 μF high voltage capacitor, and amplified initially by a EG&G ORTEC 9301 pre-amplifier (rms noise equivalence $< 25 \mu\text{V}$, rise time $< 1.5 \text{ ns}$, gain =10). All the remaining electronic components were mounted in a NIM bin rack, model 401B with all modules conforming to this standard. Second stage amplification was provided by a EG&G ORTEC fast filter amplifier, model 579, with a maximum gain of 500 and integral and differential filtering capabilities. Noise was removed from the pulses by a EG&G ORTEC, constant fraction discriminator (CFD), model 473A, which could be set to a discrimination level between 0 and 10 volts. The output of the CFD provided the STOP input of a EG&G ORTEC time to amplitude converter (TAC), model 566, which produced output pulses whose pulse height was proportional to the time interval between consecutive START and STOP input pulses. Time range settings between 50 ns and 2 ms could be selected with the full range corresponding to an output pulse of 10 volts. START pulses which originated from the pulse generator were passed through a EG&G ORTEC delay generator, model 416A, which enabled a time delay of between 0 and 110 μs to be introduced. Pulses from the TAC were delivered to a multiple channel analyser operated in pulse height analysis mode. The pulse height resolution of the TAC was $< 0.01 \%$ of the full time interval. The MCA could be operated in 1024, 2048 and 4096 channel modes. With this set up the MCA recorded a histogram of channel number against the number of pulses received in that channel, providing a direct representation of the time of flight spectrum. If no STOP pulse is received by the TAC within the collection period no output pulse is delivered to the MCA.

The whole vacuum system could be enclosed in a baking shroud and baked to a temperature of $\sim 200^\circ\text{C}$. Following a bake residual gas pressures of $< 10^{-10}$ mbar could be achieved.

In addition to the development and re-design required to perform surface analysis with the capabilities outlined in chapter 2 and the surface particle interaction studies in chapter 3, a number of more fundamental limitations were also identified: the ToF technique is based on timing the flight of particles over a known distance in order to deduce their energy, and so it is a fundamental instrument requirement that possible origins of instrumental time and energy dispersions are reduced to acceptable levels. The most evident source of instrumental time dispersion was that due to the

primary ion bunch. This was discussed extensively in chapter IV. Also, the scattering of detected particles from internal surfaces of the spectrometer prior to or proceeding the scattering event must be avoided, as this introduces time dispersion due to the energy loss in the collision. One obvious source of such internal scattering was from the walls of the flight tube, as discussed in the previous chapter. Apart from the consideration of the relative number of ions that may initially enter the flight tube, to the number which impinge onto the detector directly, 0.15 %, experimental evidence of such scattering was also observed. The elimination of this problem is discussed in section 5.2. A number of further instrument modifications are also discussed in section 5.6. The remaining sections of the chapter relate to the development of instrumentation essential to the experimental programme. That is the production of a primary beam consisting solely of fast atoms or low energy ions, and instrumental capabilities to detect scattered neutral and scattered ion particle spectra separately in either mode of bombardment. The development of a system for separating the ion and neutral spectra is detailed in section 5.3, and the development of a system allowing selection between neutral and ion modes of bombardment is given in section 5.4. The principles and construction of a three axis goniometer system are described in section 5.5.

5.2 Collimation of the scattered particle beam - Flight tube stop apertures

5.2.1 Evidence of internal scattering

A limitation revealed by analysis of the primary spectra was that of scattering from internal components of the spectrometer, which originated from two distinct regions of flight path, the Wein filter and the internal wall of the time of flight tube. Resolution of the former was discussed in the previous chapter, the latter is discussed below. The FAB-1 primary spectral data demonstrated that particles scattering from the walls of the flight tube could result in broadening of primary particle spectra. A 1kV Ar atom undergoing a single glancing angle with an Fe surface would lose only 2 eV of its energy elastically. This loss cannot account for the losses observed experimentally, which were the order of 160 eV. However, small angle collisions, with lighter C and O atoms, could lead to appreciable losses on the part of the primary, which can account for the observed losses. For example the kinematic factor

for a Ar-O collision in which the Ar atom is scattered through 1.4° , given by the negative solution of equation 3.7, is 0.18. For the geometry of the prototype spectrometer the solid angle subtended at the detector was 6.4×10^{-5} sr, compared to that of the tube entrance of 4.5×10^{-2} sr. On this basis only 0.15% of particles entering the tube can be expected to impinge upon the detector directly, and thus the remaining 99.85% must collide with the tube wall. From the intensity of the scattered peak shown in figure 4.49 it is clear that in practice only a small proportion of particles scattering from tube walls impinge upon the detector having lost appreciable energy. There are however, a number of differences between the case of the primary and scattered particle spectra. In the case of the primary spectra, the beam pencil angle was comparable to the angle subtended by the tube, and thus scattering was confined to localized regions of the flight tube wall. Whereas in the scattered particle spectra, particles are emitted isotropically from the sample in all directions, and must be expected to be scattered from the full length of the tube wall. This is illustrated schematically in figure 5.2. Accordingly the instrumental broadening will be greater in scattering mode than in the measurement of the primary particle spectra. Thus it can be seen that 'in tube scattering effects' could readily become convoluted with the true signal, thus obscuring spectral features and reducing resolution. For this reason it was considered necessary to take steps to eliminate in-tube scattering.

5.2.2 Reduction of internal tube scattering

To ensure that the detector received only particles coming directly from the sample, apertures were placed within the flight tube. The three main considerations in the aperture system design were:

[1] Only particles with a line of sight path to the detector face should proceed past the final aperture in the flight tube.

[2] All surface locations within the analysed sample region should 'see' the same detector face area.

[3] The number of ions entering the flight tube without a direct flight path to the detector face should be minimised, as particles colliding with the tube wall may subsequently be scattered past a preceding aperture.

In the case of 'point source' emission of scattered particles from

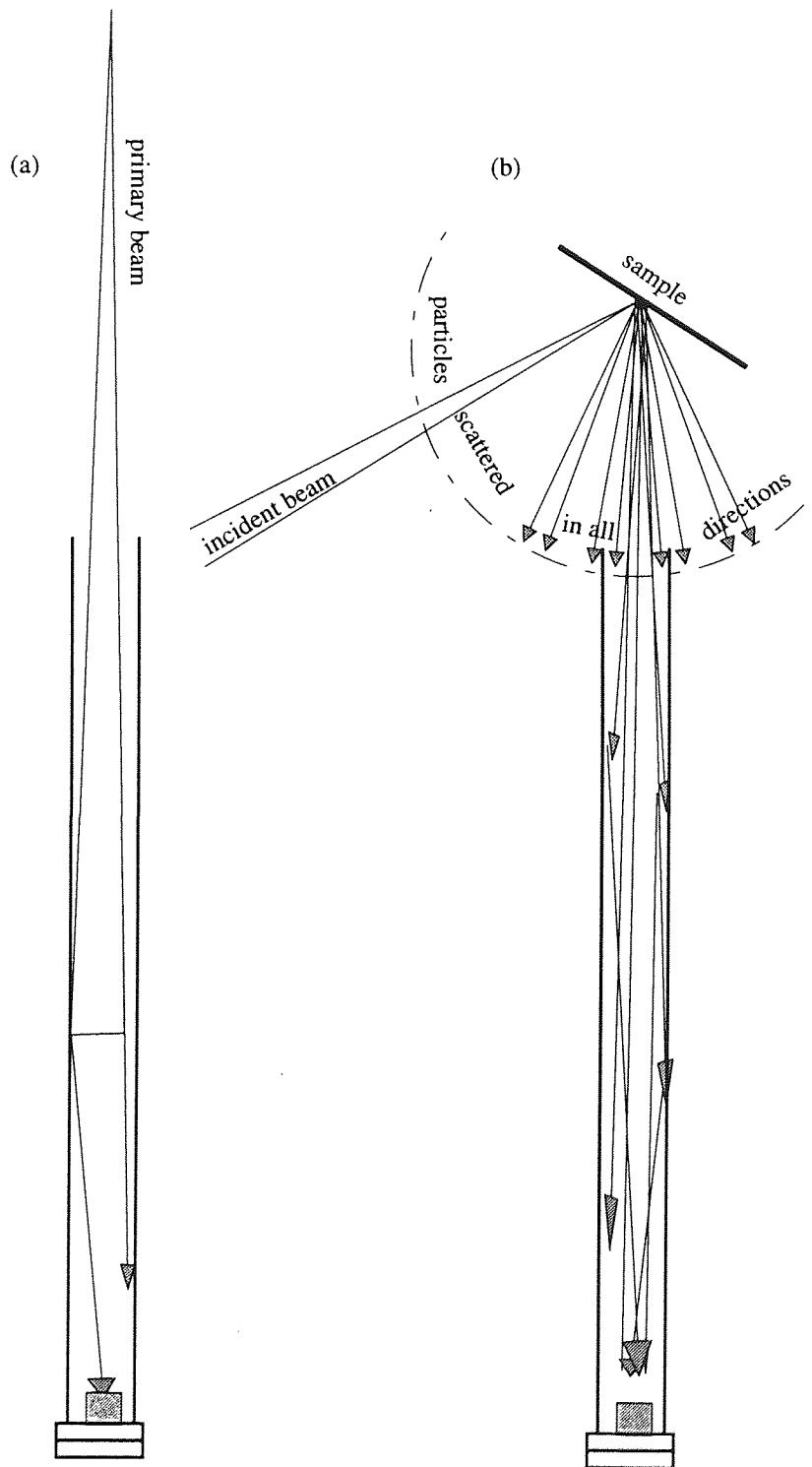


Figure 5.2 - The figure illustrates the difference between the primary and scattered particle spectral measurements with regard to 'in tube scattering'. In (a) due to the narrow pencil angle of the primary beam the scattering is localized. In (b) scattering is possible from the full length of the flight tube.

the sample, the aperture system design is clearly trivial. However, a beam diameter of ~ 2 mm, cannot be considered to be point source. In this case qualitative consideration allows the following conclusions to be drawn. To satisfy [3] an aperture must be placed at the tube entrance, close to the sample. However, the placement of an aperture of appropriate diameter to give $\Delta\Omega$ of 6.4×10^{-5} sr, violates [1] and [2], and even if the beam diameter were to be significantly reduced, precise positioning would be required, as small misalignments would also violate these two criteria. [1] and [2] can be satisfied by moving the aperture towards the detector, however, a larger number of ions can now enter the tube and [3] is violated. Thus the criteria give rise to a direct conflict with regard to the aperture position. This conflict can be resolved by the placement of a series of apertures along the length of the tube. In this case the aperture closest to the detector defines the detection angle $\Delta\theta$, and the other two apertures restrict the number of particles entering the tube, and restrict progress of particles that have collided with the walls. However, the angle subtended by these two apertures must be significantly greater than that of the final aperture. This arrangement has the advantage that 'in tube scattering' is virtually eliminated without compromising $\Delta\theta$ or r_a . A quantitative description of the problem is given below.

The geometry of a single aperture system is shown in figure 5.3, where cartesian co-ordinates are employed, the z axis is chosen in the direction of the flight tube. Vector A is used to define the boundary of the primary beam on the sample, located in the x - y plane at $z=0$, and is given by:

$$A = a_x \mathbf{i} + a_y \mathbf{j} + a_z \mathbf{k} \quad - (5.1)$$

where:

$$a_x = x_s + r_s \cos\phi \quad - (5.2)$$

$$a_y = y_s + r_s \sin\phi \quad - (5.3)$$

$$a_z = 0 \quad - (5.4)$$

$$(0 < \phi < 2\pi)$$

where r_s is the radius of the primary beam and x_s and y_s define the centre of the beam from the axis. The aperture of radius d is positioned at $z=l_d$ and is defined by the vector B .

$$B = b_x \mathbf{i} + b_y \mathbf{j} + b_z \mathbf{k} \quad - (5.5)$$

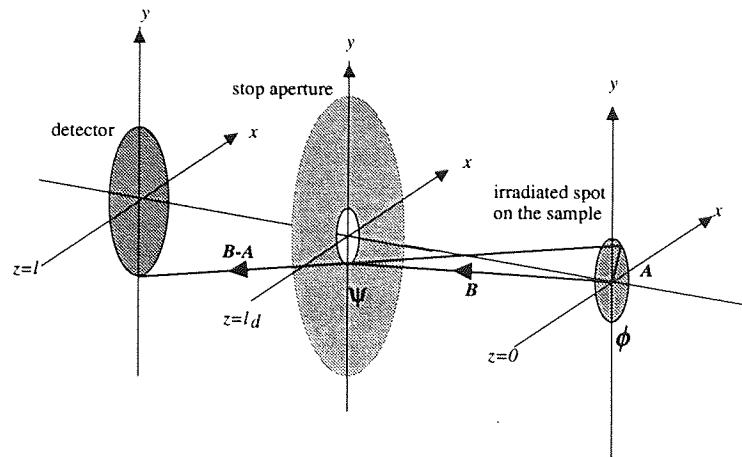


Figure 5.3 - Geometry of the aperture system for the prevention of scattering within the flight tube.

where:

$$b_x = r_d \cdot \cos \psi \quad (5.6)$$

$$b_y = r_d \cdot \sin \psi \quad (5.7)$$

$$b_z = l_d \quad (5.8)$$

$$(0 < \psi < 2\pi)$$

The detector plane is located at $z=l$. The boundary of the 'illuminated' region is defined by the vector D , which is given by:

$$D = A + l_2/l_1 [AB] = d_x i + d_y j + d_z k \quad (5.9)$$

where

$$AB = B - A = f(\phi, \psi) i + g(\phi, \psi) j + l_1 k \quad (5.10)$$

$$(0 < \psi < 2\pi \text{ and } 0 < \phi < 2\pi)$$

d_x and d_y can be found by taking the dot product of D with i and j respectively:

$$d_x = x_s(q-1) + r_s \cos \phi (q-1) - qd \cos \psi \quad (5.11)$$

$$d_y = y_s(q-1) + r_s \sin \phi (q-1) - qd \sin \psi \quad (5.12)$$

($q = l/l_d$) Where $|d_x|$ and $|d_y|$ must be less than the MCP diameter, R , to prevent over-filling of the detector. Equation 5.12 may be simplified by considering the case of maximum divergence only, which is given by $\phi=0$, and $\psi=\pi$, in which case:

$$r_d = R/q + r_s/q - r_s \quad (5.13)$$

which expresses the aperture radius in terms of the primary beam radius, aperture position, and MCP diameter. To prevent over-filling the detector, the aperture diameter must be decreased as the primary beam radius is increased. The placement of the aperture also determines the detected angle, $\Delta\theta$, figure 5.4, and defines a circular region of radius r_a , at the sample plane, figure 5.5. Within r_a emitted particles have a line of sight path to the full area of the detector. Surrounding the central 'acceptance' region is a penumbral region, (shaded area in the figure) from which emitted particles have only partial

sight to the detector. To satisfy [2] and to achieve maximum signal intensity the primary beam must be positioned fully within r_a , as in figure 5.5a. In figure 5.5b r_s is greater than r_a and [2] is violated. The radius of the acceptance region is given by:

$$r_a = (R - q \cdot r_d) / (q - 1) \quad -(5.14)$$

which shows r_a to be maximised at a given aperture position when d is made small, however, this is at the expense of $\Delta\theta$. Equation 5.14 also shows r_a to be maximised when the aperture is placed close to the detector, that is small q . However, the flight tube design was additionally complicated by the placement of an acceleration tube within the flight leg, which is discussed in the following section.

5.3 Scattered ion/atom separation

To measure neutralisation probabilities discrimination between the scattered ion and neutrals particle spectra is essential. A time domain approach was employed by post acceleration of the scattered ion beam. Alternative approaches considered include:

- 1] Subtraction of the 'atom' from the 'ion+atom' spectra collected separately.
- 2] The introduction of an angular separation of the two beams.
- 3] Generation of the particle spectra by conventional ESA analysis following electron stripping of the neutral fraction⁹⁷.

Although the first approach could have been readily implemented, the approach is unsatisfactory because the resultant ion spectra has very low intensity and was subject to large uncertainties, resulting from small drifts in the primary beam current. The second approach is experimentally complicated to achieve because the deflected ions would be dispersed according to their energy. Furthermore an investment in a second MCP and associated electronics would have been required, which was not possible. Practical difficulties concerning the electron stripping approach have also been reported. Furthermore the multichannel nature of the ToF technique would be lost and again the necessary funds for the instrumentation was not available. Thus the employment of an acceleration tube to post accelerate the

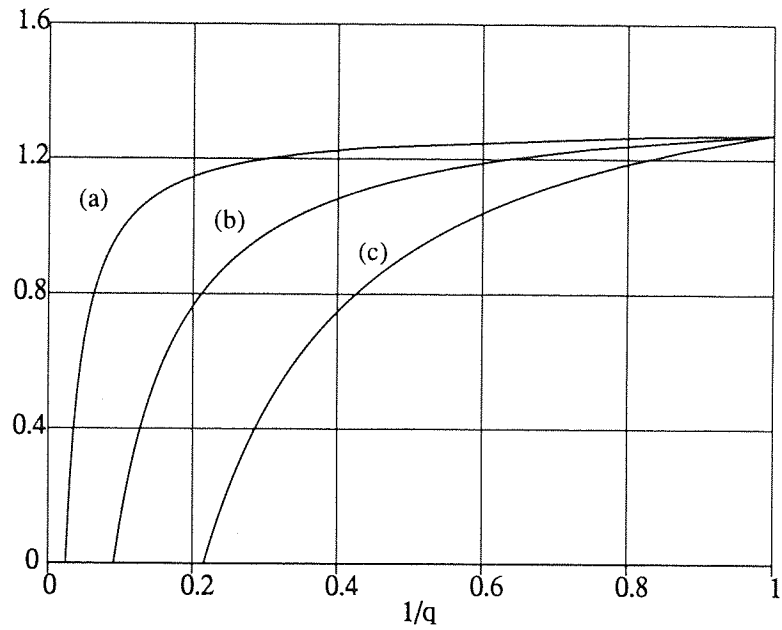


Figure 5.4 - $\Delta\theta$ plotted as a function of the position of the aperture in the flight tube. For $l=2000$ mm, $R= 40$ mm. (a) $r_s = 0.5$ mm $x_s= 0$, (b) $r_s = 0.5$ mm $x_s= 1$ mm, (c) $r_s = 0.5$ mm $x_s= 5$ mm.

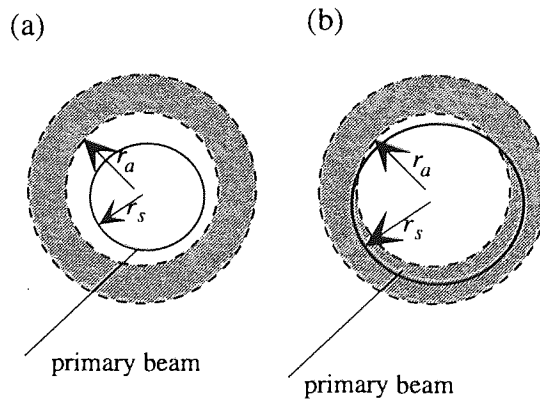


Figure 5.5 - The figure demonstrates the importance of matching r_a , the radius of the acceptance region to the primary beam radius, r_s . The shaded area represents the penumbral region.

ion fraction was considered to be the most effective approach. Furthermore it could readily be introduced into the existing flight tube, thus the prototype spectrometer could be modified without difficulty. Unlike the alternative approaches, here the separation of the ion and neutral spectra takes place in the time domain. The acceleration tube can be operated in either a positive or negative voltage mode, of which the latter was favoured; the former would introduce a larger temporal dispersion due to the energy dispersion inherent in the scattered beam. The application of a negative voltage results in an acceleration of ions, which then travel at elevated velocities with respect to neutrals through the tube and therefore arrive at the MCP at an earlier time. In this case the ion spectrum becomes compressed in the time domain rather than dispersed. A positive voltage could also be applied in order to block the ion fraction completely.

5.3.1 Acceleration tube - design

The time separation, Δt_{tube} , obtained in the negative mode can be expressed in terms of the tube length, L and the voltage, V_a by:

$$\Delta t_{tube} = L/v_o [k^{-1/2} - (k + E_a/E_o)^{-1/2}] \quad -(5.16)$$

Thus Δt_{tube} is the time separation introduced by the tube between the neutral and ion QS peaks of kinematic factor k . A more appropriate measure of the separation for design purposes is $\Delta t_{tube}/t_n$, where t_n is the total flight time from the sample to the MCP of neutrals:

$$\Delta t_{tube}/t_n = L'(1-S) \quad -(5.17)$$

where $S = (1+A)^{-1/2}$, $A = E_a/E_i$ and $L' = L/(l+L)$. Unlike the absolute time separation, $\Delta t_{tube}/t_n$ is independent of the scattered particle velocity. Clearly from eq 5.17 maximum separations are achieved for a long tube and a large applied voltage, that is maximum L' and minimum S . If the acceleration tube were to occupy the full flight path then eq 5.17 would reduce to:

$$\Delta t_{tube}/t = 1-S \quad -(5.18)$$

The parameter S has a domain between 0 and 1 corresponding to

E_d/E_1 between 0 and ∞ , and is given graphically in figure 5.6. Thus a value of $S=0.5$ is obtained for $E_a=-3E_o$. Further increases in E_a lead to diminishing decreases in S , that is the gradient dS/dA decreases rapidly with A . The required value of $\Delta t_{tube}/t_n$ to fully separate the ion and neutral spectra is dependent on the amu of the atoms composing the sample surface. In cases where atomic masses are widely dispersed, full separation is difficult to achieve. This is ultimately limited by loss of instrumental resolving power under conditions of large L' and small S . This point is illustrated by considering that the flight time tends to 0 as L' tends to 1 and S tends to 0. However, in practice separation is limited by a number of other factors which are now considered. Firstly the tube length, L and the voltage, V_a are restricted by the ion focusing properties of the tube. In this respect the diameter of the tube was restricted by the existing flight tube, which was 36mm internal bore diameter. The focusing properties of the tube arise from strong accelerating and retarding fields at the entrance and exit planes. Without the employment of a suitable lens system most ions would collide with the tube wall. The basic requirement of the lens system was to provide maximum focal length for given V_a . In order to prevent wall collisions f must be greater than $L/2$. The employment of three element lens, with $V_1 = E_1/e$ and $V_3=(V_1+V_a)$ allowed the focal length to be varied by variation of V_2/V_3 . (The convention introduced in chapter IV is applied). The extent to which f can be varied for a fixed ratio of V_3/V_1 can be obtained from the zoom lens curve¹⁷⁹ for a particular lens geometry. The zoom lens curves show that the achievable maximum focal length decreases sharply as the V_3/V_1 ratio increases. The maximum f is obtained for $V_2 \sim (V_3 - V_1)/2$, and this holds for any lens with axial symmetry around the centre plane. This was also confirmed by MUNRO¹⁷⁶ and the Gauss's Law method described previously. A number of three element lenses of varying geometry were systematically modelled using the MUNRO software. This parametric study showed the changes in geometry to have only marginal influence on the range of f , for a given lens diameter; f is linearly proportional to lens diameter. For ease of construction and mounting in the flight tube the cylinder lens, shown in figure 5.7, was chosen.

5.3.2 Acceleration tube - design criteria and constraints.

For a lens of 20 mm diameter, the maximum focal length was

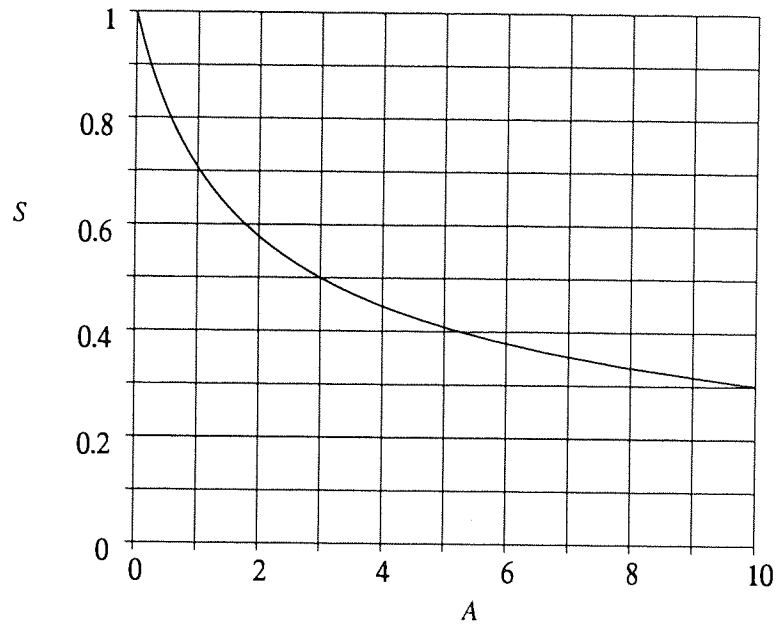


Figure 5.6 - S as function of A ; the acceleration voltage ratio, E_a/E_o . S was found to a useful parameter in the discussion of the acceleration tube.

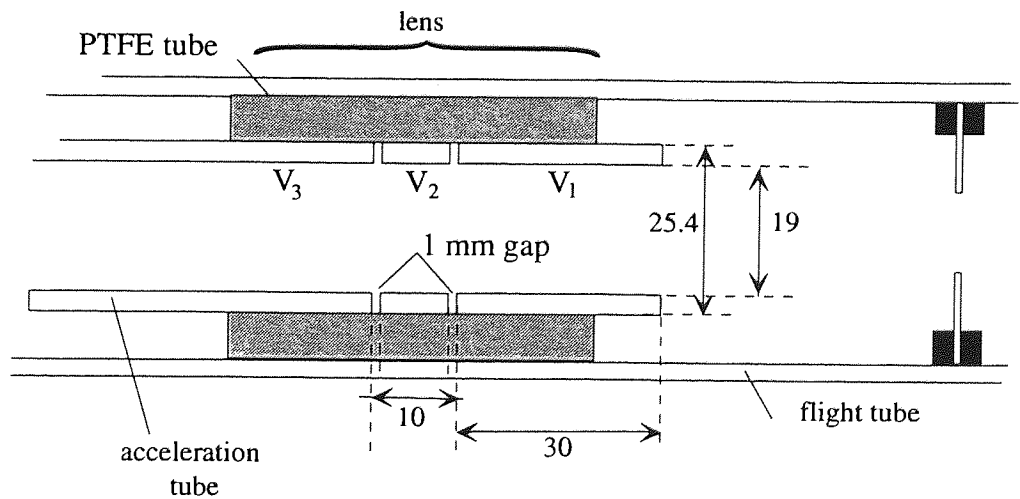


Figure 5.7 - Construction of the acceleration tube lens system.
- Dimensions given in milli meters.

found to be ~ 200 mm for $(V_3-V_1)/V_1 = 1.5$, that is $V_a = 3E_1/e$, giving a maximum acceleration tube length of 400 mm. To increase L beyond this value required either the reduction in the ratio $(V_3-V_1)/V_1$ or an increase in the lens diameter. The latter was constrained by the flight tube diameter of the prototype instrument. A second option was to employ a pair of parallel grids to generate the acceleration field, which would remove the previous restrictions on S and L . A further constraint on L , irrespective of the acceleration method was imposed by the requirement that $\Delta\Omega_{\text{ions}} = \Delta\Omega_{\text{neutrals}}$, which necessitated placing the beam limiting aperture before the acceleration tube. In the case of the electrostatic lens the parameters S and L' were restricted to 0.5 and 0.2 giving rise to an ion-neutral peak separation of $\sim 10\%$ of the neutral particle flight time. Whereas the use of grids gave separations of $\sim 47\%$. Figure 5.8 shows the corresponding separations schematically. The peak widths in these calculated spectra represent the expected FWHM due to a QS collision, and were calculated from eq. 2.12. The ion peak is given by:

$$I_i(t) = \exp[-(t-t_i)/\sigma_f]^2 \quad (5.20)$$

and the neutral peak is given by a gaussian multiplied by the function given in eq 5.21, representing the low energy tail.

$$I_n(t) = \exp[(t-t_n)/\sigma_f] + B \exp[-\lambda(t-t_n)/2] \times [\pi - 2 \tan^{-1}((t_n-t)/\sigma_f)] \quad (5.21)$$

B and λ represent the intensity and decay constant of the inelastic tail respectively, and $\sigma_f = \text{FWHM}/[2(\ln 2)^{1/2}]$. Other factors affecting the peak widths were discussed extensively in section 2.7 of chapter 2, where it was seen that the contribution of multiply scattered trajectories to the neutral spectra is very much dependent on primary and target particle mass, surface purity, crystal structure, and orientation.

Due to the presence of the acceleration tube the 'beam limiting aperture' could not be placed in close proximity to the MCP. In the first flight/acceleration tube configuration the closest position was ~ 600 mm, giving rise to a value of $q=1.42$. An aperture of 5.5 mm at this position gave an acceptance radius, r_a of 3 mm, and $\Delta\theta$ and $\Delta\Omega$ of 0.4° and of 3×10^{-5} sr respectively. This allowed for beam diameters with a full width of up to ~ 6 mm. In the case of the neutral beam produced by the FAB-1 source, precise

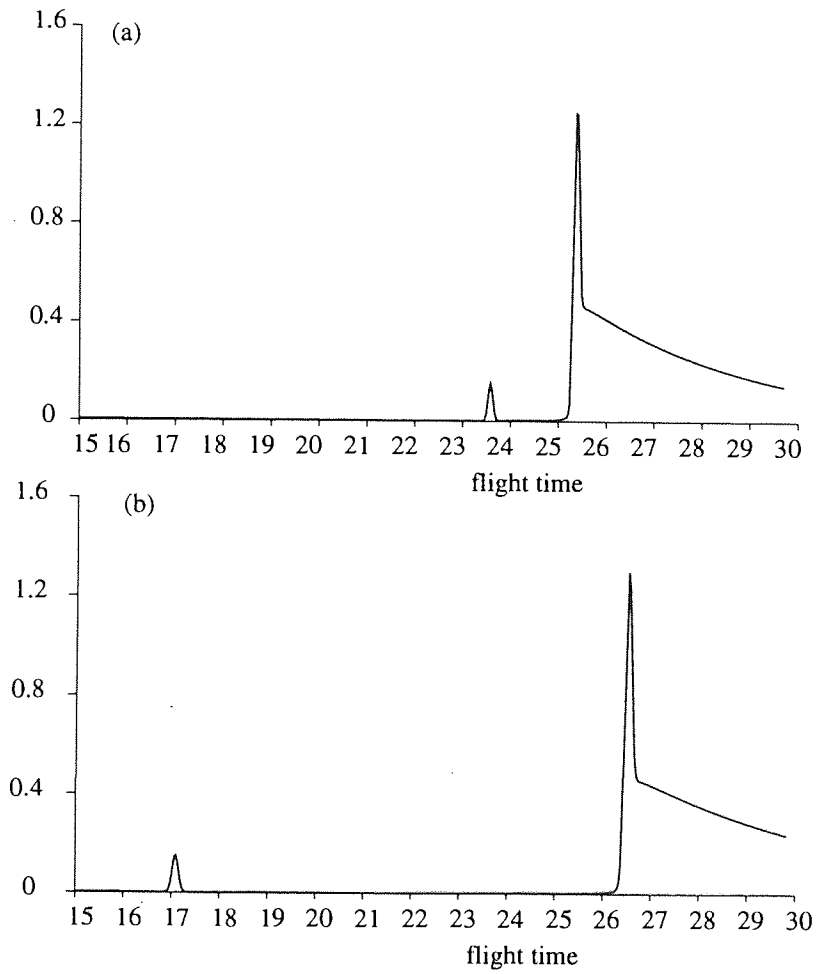


Figure 5.8 - Comparison of the peak separation achievable with the two acceleration/flight tube configurations.

(a) The 0.4 m tube.

(b) The 1.7 m tube.

The conditions in this example were: $m_1 = 20$, $m_2 = 197$, $E_o = 2$ keV

alignment as the FWHM of the beam was ~ 4 mm. As shown in figure 5.9a two further apertures were placed at $q=2.5$ and $q=10$, which limited the angular acceptance to 0.7° and 1.6° respectively. In the second flight/acceleration tube configuration an acceleration tube of 1700 mm was employed and the closest position for the aperture was ~ 1750 mm. The diameters of the two tubes were also increased to accommodate a greater diameter MCP detector, and to allow a longer acceleration tube without restricting acceptance region. The geometry which is shown in figure 5.9b gives rise to $q=3.2$, $r_a = 6.4$ mm, and $\Delta\theta = 0.85^\circ$ and $\Delta\Omega = 1.7 \times 10^{-4}$ sr. This flight tube was used in conjunction with the FAB-2 source which had a beam diameter of ~ 2 mm, and thus accurate alignment in this case was not so important.

5.3.3 Acceleration tube - construction and installation

The acceleration assembly in both cases was held in place by two PTFE collars. These collars both maintained the acceleration tube concentric and insulated it from the containing flight tube.

Correct positioning of the sample was crucial for obtaining maximum intensity spectra. This was particularly important for the first tube assembly which was employed in the 90° scattering mode, correct positioning was achieved by the following procedure. Firstly the cross wire stage, shown in figure 4.8, was designed so that the centre of the cross coincided with the sample centre. The position of the cross wire relative to the axis of the flight tube was then achieved by viewing the cross wire through an aperture located at the end of the flight tube. This procedure gave the co-ordinates z_o and y_o for which the sample centre was aligned with the flight tube axis. With the sample positioned at z_o and y_o the value of x_o was found by maximising the detector counts.

5.3.4 Acceleration tube - experimental verification

In order to demonstrate that the acceleration tube was operating as expected, that is the acceleration times were well predicted by eq. 5.16, the tube was used to separate the ion and neutral components of the primary beam. It was not possible to produce ions and neutrals simultaneously due to the very low intensity neutral beam which was obtained at low source

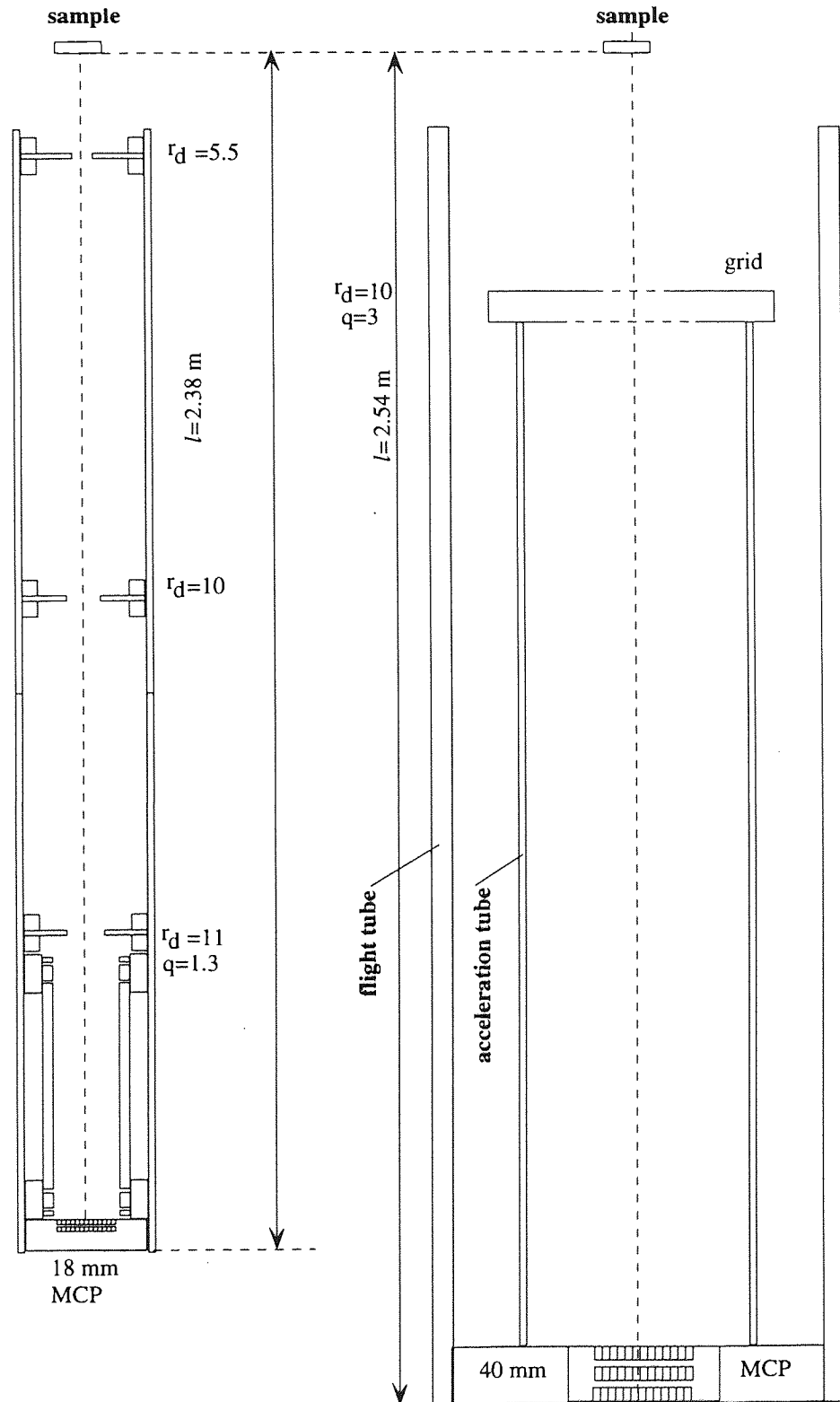


Figure 5.9 Flight/acceleration tube geometry

- (a) Flight/acceleration tube configuration 1 - $L = 0.4 \text{ m}$ /electrostatic lenses
- (b) Flight/acceleration tube configuration 2 - $L = 1.7 \text{ m}$ /electrostatic lenses

pressure. It was necessary to maintain to achieve sufficiently low ion currents, however, to obtain a sufficient neutral current it was necessary to raise the source pressure. This resulted in an ion beam current which was too high to be exposed directly to the MCP. To avoid this the ion beam was deflected by the x-y plates, when neutral beam measurements were made. The ion spectra for a range of values of V_a is shown in figure 5.10, and the experimental and calculated flight times are compared in figure 5.11.

5.4 Miscellaneous aspects of instrument development

In this section a number of practical considerations are discussed which have had important implications for the experimentation.

5.4.1 Primary beam alignment

In order to provide a means of selection between a primary ion and neutral beam, a port alignment stage was introduced. This was necessary for two reasons. Firstly, a method of positioning the primary beam accurately within the acceptance area of the detector was needed. The second requirement originated from the non-ideal properties of the source identified in chapter 4, that is a residual neutral current was present in the beam when the source was operated for maximum ion current. This problem was significantly reduced by the provision of a neutral dump in a later source. In the absence of the ND in the FAB-1 source the beam consisted of ~ 10% neutrals, in this case the port alignment stage was employed to move the residual neutral beam out of the acceptance region. The x-y plates were then used to position the ion beam. The alignment stage was constructed to allow the tilt angle to be controlled with accuracy and repeatability. This was achieved by two micrometers to control lateral and vertical motion of the stage. The system was calibrated to provide two standard orientations of the source corresponding to ion and neutral operation. The disadvantages of the stage were recorded previously, that is, as a necessity the source had to be located at a greater distance from the sample.

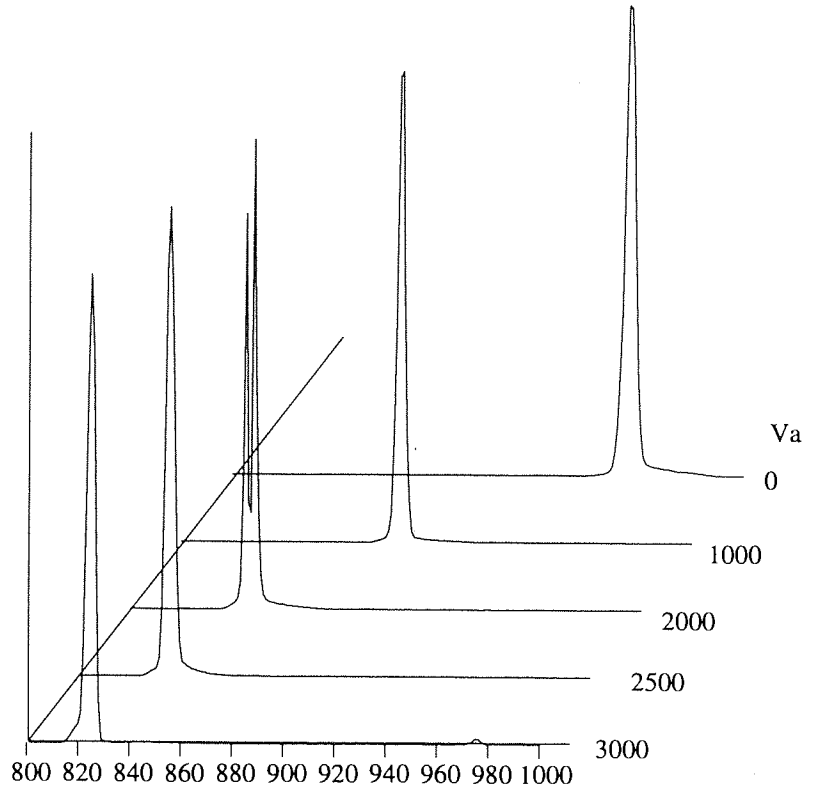


Figure 5.10 -Shift in the primary ion peak due to V_a , applied to the acceleration tube. - 1 keV Ar beam. The flight time give in terms of channel number. (48.8 ns / channel)

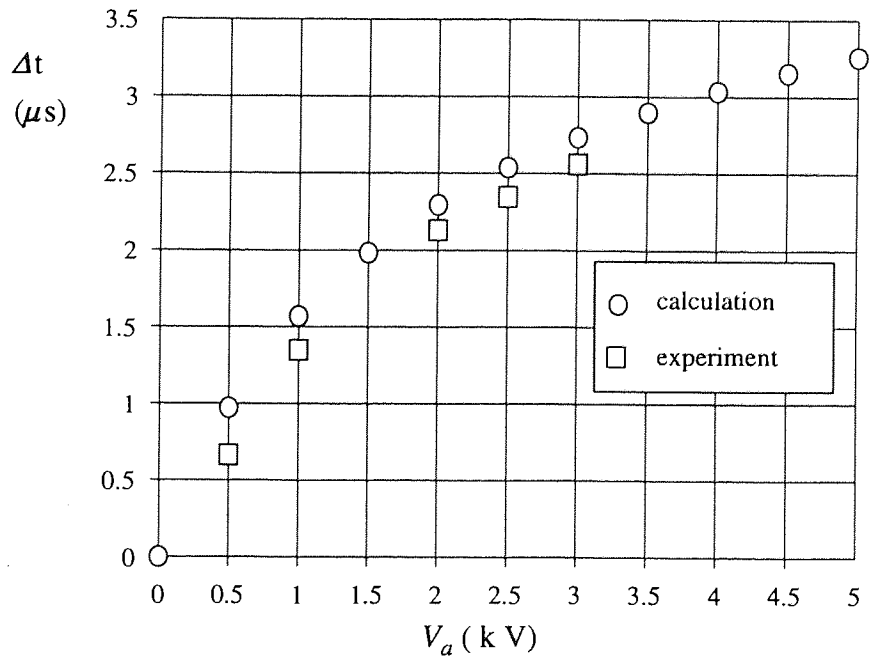


Figure 5.11 - Comparison of experimental and calculated separation times achieved with flight/acceleration tube configuration 1.

The peak shift is shown as a function of V_a .

$E_o = 1.09$ keV. (It was not possible to increase the acceleration voltage above -3 kV due to the focal properties of the tube.)

5.4.2 Source Gas Supplies

The original source gas supply configuration was found to severely limit the ultimate base pressure of the vacuum system. In this arrangement the appropriate gas cylinder was connected directly to the source, and had to be removed before baking the system. The source gas was changed by changing the gas cylinder. A schematic of the modified arrangement is shown in figure 5.12. The important considerations were.

- [1] It was necessary to bake the system with the source gas supply connected: without this it was found, even after subsequently baking the gas lines separately that the chamber pressure was previously limited to $\sim 5 \times 10^{-9}$ mbar.
- [2] It was necessary to readily interchanged the source gas. The arrangement shown in figure 5.12 allowed the source gases to be switched within minutes, without noticeable increase in the residual gas pressures. The ultimate base was found to approach 10^{-11} mbar.

5.4.3 The Sample Stage

It was recorded in chapter 4 that the primary beam was subject to significant drift over the spectrum acquisition period. To contend with this instability a method for accurately recording sample currents was sought. This was considered to be particularly important in meeting the long term objective of this research effort of achieving quantitative composition analysis, which requires accurate determination of the dose imparted to the sample by the probe beam. To achieve this accurately, for both ion and neutral beams, the SEE current must be measured as discussed previously. Thus the sample stage was required to have the capability of recording the sample current together with the resultant SEE current, simultaneous to spectrum acquisition. The following capabilities were required of the sample stage:

- [1] measurement of sample current
- [2] measurement of the emitted secondary current
- [3] the possibility of heating the substrate
- [4] access to the analysis beam by an additional high current beam for sputter cleaning.

A sample stage was constructed to meet these requirements, which is shown schematically in figure 5.13. This was a precursor to the stage with additional

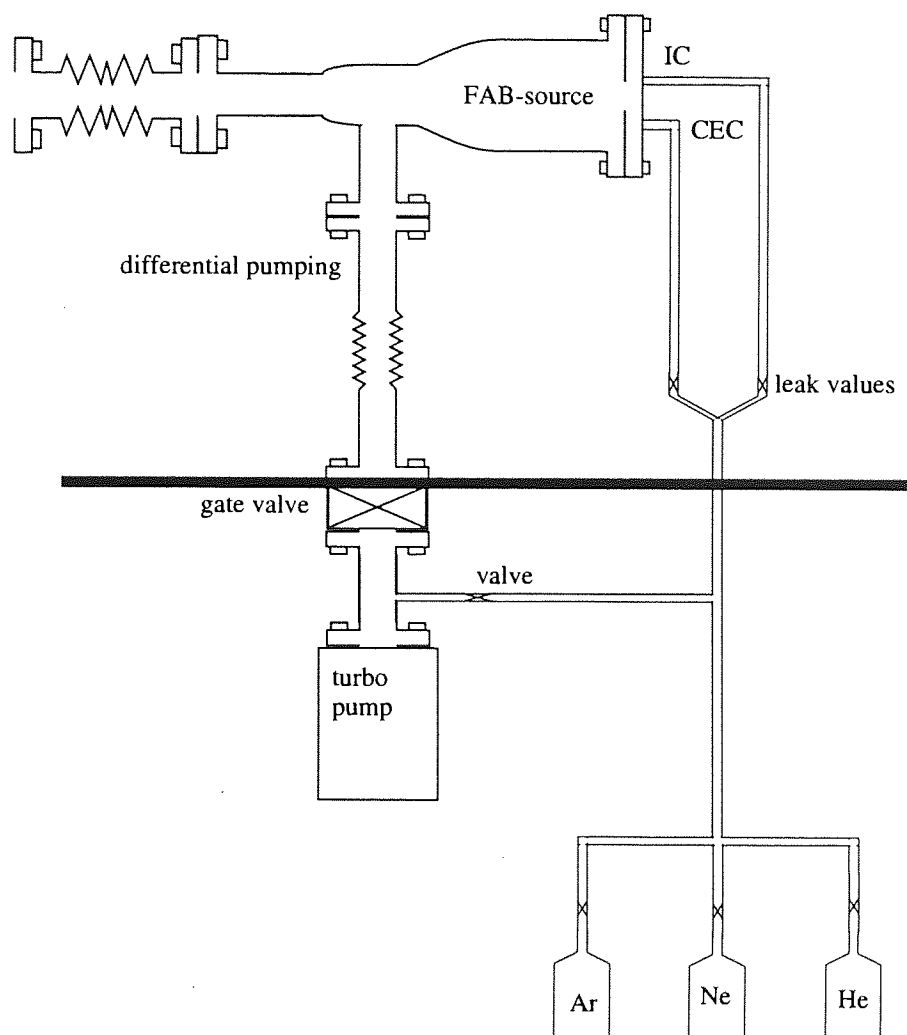


Figure 5.12 - A schematic of the modified source gas feed arrangement.

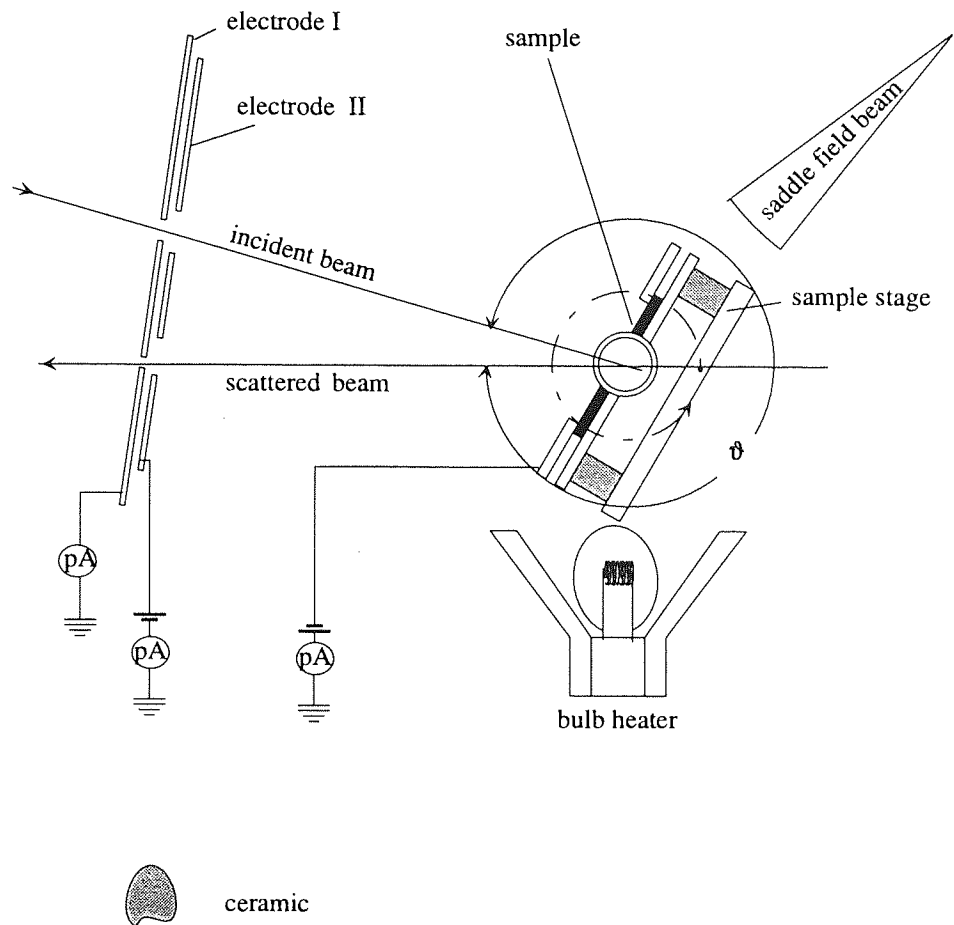


Figure 5.13 - Schematic of the sample stage.

rotational capabilities discussed in the following section. The stage was mounted on the shaft of the 4 axis sample manipulator, which provided z axis rotation. Electrical and thermal insulation of the sample were provided by a ceramic section introduced into the manipulator shaft, and also by further ceramics at the substrate platform. The sample was negatively biased by 9 volts and electrode II was positively biased. Electrode I was employed to prevent the deflected beam influencing the measurement of the secondary electron current. Thus in ion mode, the current $I_i + \gamma I_i$ was measured at the sample and $-\gamma I_i$ at electrode II. Whilst in neutral mode a current $+\gamma I_n$ was measured on the sample and $-\gamma I_n$ at plate II. A Faraday cage could also be constructed around the sample so as to fully enclose it by the electrode II, thus ensuring all secondary electrons were collected. However, the use of the Faraday cage was found to have only a marginal influence on the measured value of γ . Initially, electrical connections were made using Kapton insulated wire. However this was found to give rise to a severe contamination problem, and it was later replaced by ceramic beads. The stage was constructed from stainless steel and tantalum for the construction of the apertures and the substrate platform. Sample heating was initially provided by a tungsten filament mounted behind the sample on the substrate platform, and then latterly by a quartz bulb mounted in front of the sample, remote from the substrate platform. However, both heating arrangements were found to introduce contamination onto the sample surface. This problem is discussed further in the following chapters.

5.4.4 Scattered particle detection

Micro Channel Plate detectors (MCPs) are suited to the time-of-flight application due to their fast response (rise time ~ 150 ps), allowing single particles to be detected without introducing appreciable delay or dispersion into the measured flight time. The high spatial resolution offered by the MCP detectors is not required for the ToF application, and so the electrons are collected by a single anode plate. The individual plates of the MCP detector consist of an array of $\sim 10^6$ parallel glass capillaries fused together to form a disc¹⁹⁵. The effective dead time of the detector is very short, ~ 10 ns. An incident ion entering a channel gives rise to an avalanche consisting of $\sim 10^3$ to 10^4 output electrons. The gain is determined by the ratio of the channel length (L) to diameter (d), ($\alpha = L/d$), and can be expressed

as:

$$G \sim \exp(\gamma\alpha) \quad \text{-(5.22)}$$

where γ is the SEE coefficient of the channel wall. L is typically 0.5 mm. For $\alpha=40$ a gain of $\sim 10^4$ can be obtained for an applied voltage of 1 kV, which is the maximum achievable value using a single plate, without the onset of the ion feedback phenomena. To achieve larger gains, multi-plate devices must be used. It was observed in the course of this work that gain was strongly dependent on the energy of the exciting particles. It was not possible to utilise this feature to perform direct spectroscopy due to the broad pulse height distribution characteristics, the different form of which is dependent on the plate type and operating conditions. Normally the output pulse height distribution shows an exponential function, however when the gain becomes space charge saturated, the pulse height distribution becomes peaked. That is, electron multiplications are restricted by the high space charge density formed within the channels under conditions of high gain. The pulse height ratio (FWHM/peak amplitude) in this case is reported to be 120% and 80% for two and three plate assemblies respectively.

A crucial consideration with regard to this work is the energy dependence of the detection efficiency. A maximum detection efficiency of $\sim 80\%$ can be achieved if the capillaries are enlarged on the input side. Whereas the intrinsic response to electrons, UV and x-rays is well characterised, and special surface coatings are available to extend the response of UV¹⁹⁵. No similar data are available for low energy ions and atoms. Only the following data was available at the time of writing¹⁹⁶⁻¹⁹⁹. Detection efficiency falls off rapidly below ~ 2 keV, that is from $\sim 60\%$ at 2 keV to $\sim 5\%$ at 0.5 keV. Above 2 keV efficiency increases very gradually to a peak at 50 keV. More precise data than this was not given in the literature, or by the manufacturer, and no data was found contrasting ions and neutrals, however the two types of particle are expected to give similar responses.

The rapid fall off in MCP detection efficiency below 2 keV represents a major limitation. Surface treatments/coating materials to extend the energy response, as have been developed for UV, are not available for ions and atoms, although in principle this may be possible. The overall detection efficiency is also a feature of the pulse counting electronics, and signal losses here were improved significantly. For particle energies above ~ 1 keV high

gains were observed and the pulse height distribution was peaked for sufficiently high detector voltages, (> 0.8 kV /plate). In this case the output pulse amplitude, as measured by a 250 MHz oscilloscope was ~ 100 m volts, into a 50Ω impedance. Knowing the output pulse duration, a MCP gain of 6×10^7 can be inferred from this measurement. For such a gain, signal pulses are significantly above the noise level, and can be readily removed by the CFD. Therefore, for these conditions contributed to the spectrum. However, the gain was found to fall off rapidly as the particle energy was reduced. As a result the gain was no longer space charge limited, and the pulse height distribution took on the exponential form. Thus a large proportion of signal pulses resided below the noise level. This compounded the problems of signal loss due to low intrinsic detection efficiency in this energy region. To maximise the number of detector pulses registered, the noise level was minimised. The largest contribution to noise was found to be due to electrical interference, and this was substantially reduced by the following measures.

- [1] Improvement of earth connections between all elements of the detection system, and the introduction of low pass filters on the voltage outputs of the detector voltage PSU.
- [2] All signal cables were reduced to a minimum length to reduce signal loss.
- [3] The pre-amp was replaced with a better suited device; lower noise and high band width (1 GHz) and higher gain ($\times 100$).
- [4] The detector gain was increased by the introduction of a three stage MCP. The initial detector of the original instrument was a two stage, "V set" plate, and this was replaced by a higher gain three stage "Z set " assembly of 40 mm diameter. In both cases $\alpha=40$, $L=0.46$ mm, the open area ratios were 60% and 68.5% for the new and old detectors respectively, and the bias angles were 5° and 8° . This Chevron arrangement is designed to obtain high gain, space charge saturated output pulses. The directional change of the channels at the interface also helps to inhibit positive ion feedback, and prevents deep penetration of the exciting particles. The anode of the MCP was designed to have low output inductance and impedance matched to 50Ω .

The above modifications reduced the noise level, after the pre-amp stage to ~ 2.5 m volt, and 0.25 volts following the FFA. Low frequency noise can also be removed by the FFA. A discrimination level of ~ 0.5 volts, in this case was sufficient to remove all electrical noise, giving rise to the passage of a higher proportion of signal pulses and greater overall detection

efficiency of low energy particles than previously possible.

Dark current, that is detector pulses not resulting from an incident particle, may originate from a number of 'in channel' phenomena; thermionic or field emission, ionization of the residual gas, and localized discharges. The manufacturers quoted a dark current of less than 3 cps cm^{-1} for a three stage detector. Such levels were observed in practice following an initial settling period after installation, under good vacuum conditions. Increased vacuum pressure results in increased dark current and shorter operation lifetime due to 'ion generation' in the channels, and pressures greater than $\sim 10^{-5}$ mbar may result in possible permanent damage of the detector. In the initial format of the instrument, the flight tube was pumped by an ion pump, which is not suited to pumping large gas loads. As a result the pump became saturated after a period of source operation, which resulted in an increase of the flight tube pressure, and approached 10^{-5} mbar. This problem was particularly acute in atom beam mode operation of the source. For this reason the ion pump was replaced by a turbo molecular pump. The installation of the apertures in the flight tube also created a greater pressure differential between chamber and flight tube, of \sim one order.

5.5 Development of the three axis Sample Rotation Goniometer

It was stated in chapter 3 that information concerning surface charge exchange processes could be enhanced significantly and would be more comprehensive if incident and take off angles of the incident and scattered beams, that is θ and ϕ respectively, could be varied independently of all other angles. It is shown below that such variation can be achieved by mounting the sample on a stage capable of rotation about two independent axes, see figure 5.14. The figure shows the sample centred at the origin of a cartesian right handed set, with the primary beam incident along the y axis, and the scattered beam located in the x-y plane at an angle ϑ to the y axis. Rotation about the z axis which is standard on most 4 axis sample stages, is denoted by the angle B and is measured from the x axis. The second axis of rotation is the sample tilt angle, measured by A , which is the angle between the surface normal, N , and the z axis. Although sample tilt is provided by some commercial sample stages, the rotation is usually limited to a few degrees. Specialised 6 axis UHV goniometers are also available commercially²⁰⁰, however no system was found which provided sufficient freedom of

rotation. Furthermore, commercial devices are driven by vacuum motion feed through systems involving complex high precision mechanical coupling, and are consequently very expensive. The third rotation axis, that is azimuthal rotation is essential for studying crystal structure.

During the course of this programme a prototype goniometer was developed and constructed. A mathematical description of how a two axis sample goniometer may be employed to give independent variation of θ and ϕ is given in what follows. The angles θ and ϕ for the purpose of this treatment are measured relative to the surface normal, N . As shown in figure 5.14, the primary beam, 'detected' scattered beam, and the surface normal are defined by the unit vectors I , S and N respectively, and can be expressed as:

$$\theta = 90 - \cos^{-1}(I.N) \quad -(5.23)$$

$$\phi = 90 - \cos^{-1}(S.N) \quad -(5.24)$$

$$\vartheta = \cos^{-1}(I.S) \quad -(5.25)$$

and θ and ϕ are given in terms of the angles A and B by:

$$\theta(A,B) = \cos^{-1}(\sin A \cdot \sin B) \quad -(5.26)$$

$$\phi(A,B) = \cos^{-1}[\sin A \cdot (\cos B \cdot \sin \vartheta + \cos \vartheta \cdot \sin B)] \quad -(5.27)$$

The angles ϕ and θ are related by:

$$\cos \phi = [\cos \theta \cdot \cot B \cdot \sin \vartheta + \cos \vartheta \cdot \cos \theta] \quad -(5.28)$$

It can be seen from eq 5.28 that for a fixed scattering angle, the angle θ can be varied for fixed ϕ (mode 1), or alternatively ϕ varied for fixed θ (mode 2), which may be achieved by setting angles A and B to appropriate values. Clearly the range of angular variation possible is dependent on ϑ . As an example, the necessary values of A and B to achieve variation of θ between 45° and 90° for the fixed conditions $\vartheta=90^\circ$ and $\phi=45^\circ$ is shown in figure 5.15.

The prototype goniometer design employed two vacuum stepper motors inside the vacuum chamber to control angles A and C directly, and angle B by an externally mounted stepper motor, utilising the existing 4 axis

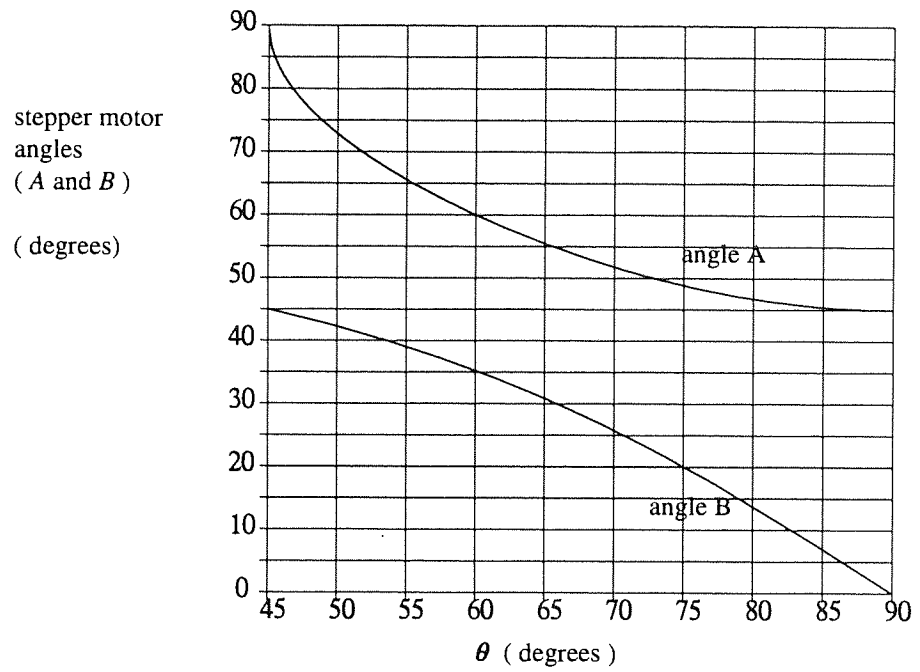


Figure 5.15 - Stepper motor angles, A and B necessary to achieve variation of the θ between 45° and 90° for $\psi=90^\circ$ and $\phi = 45^\circ$.

sample stage. The construction of the goniometer is shown in figure 5.16, and a detailed description of the architecture of the stepper motor control system is given elsewhere²⁰¹. For testing purposes the system was constructed with non-vacuum stepper motors. The stepping signals to drive and hold the three stepper motors of the goniometer were controlled by individual commercially supplied stepper motor controller boards. The control software used the equations above to calculate the angles A and B for user supplied values of θ and ϕ and moved the motors through the appropriate number of steps. The azimuthal angle could be set to any angle between 0 and 360°, or could be continuously rotated in order to simulate a polycrystalline sample using a single crystal. Datum position for each motor was provided by computer interfaced limit switches, one for each axes. The system was not tested within the vacuum as funds were not available to purchase the vacuum compatible motors. However, the unique capabilities of unlimited rotation around all three axes was provided by the system.

- angle A - (tilt , -90° to +90°)
- angle B - (z axis , 0° to 360°)
- angle C - (azimuthal Ψ 0° to 360°)

The three axes of rotation intersected at a single point at the centre of the sample surface. According to manufacturers' claims outgassing rates of vacuum comparable stepper motors²⁰² are within acceptable limits and therefore the prototype goniometer system appeared to provide a satisfactory solution.

5.6 Instrumental Resolution

As discussed in chapter 2, spectral resolution, is very much determined by the experimental conditions, of m_1 , m_2 and E_0 . As an indication of resolution for a wide range of conditions the spectral resolution is given in terms of $\Delta t/t$, as a function of θ in figure 5.17 for a number of specific experimental conditions. The instrumental parameters used in the calculation of the curves, represent those of the instrument in its final format, that is using the FAB-2 source and the second flight/acceleration tube described in section 5.3.

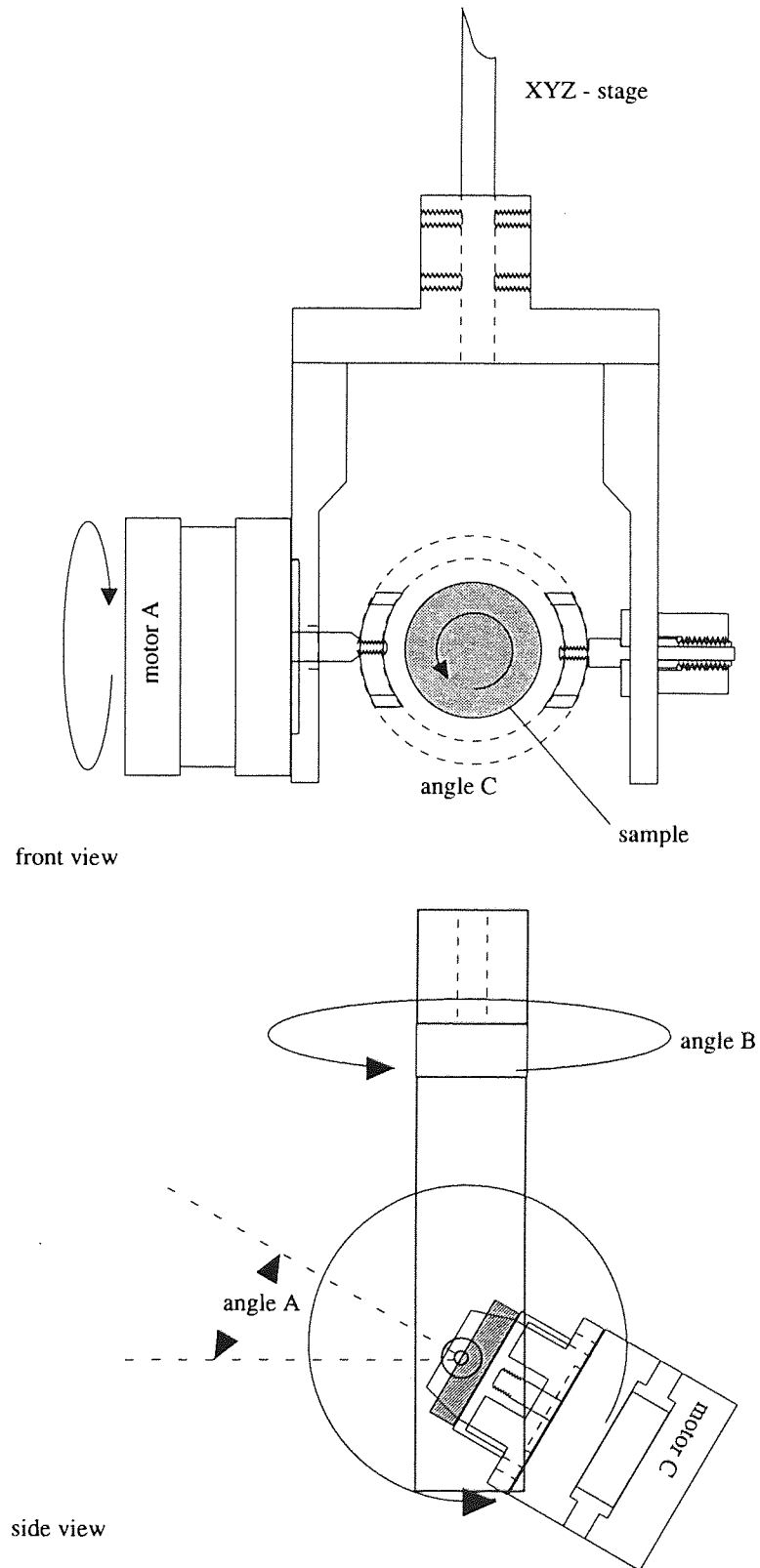


Figure 5.16 - Sketch of the 3 axis goniometer

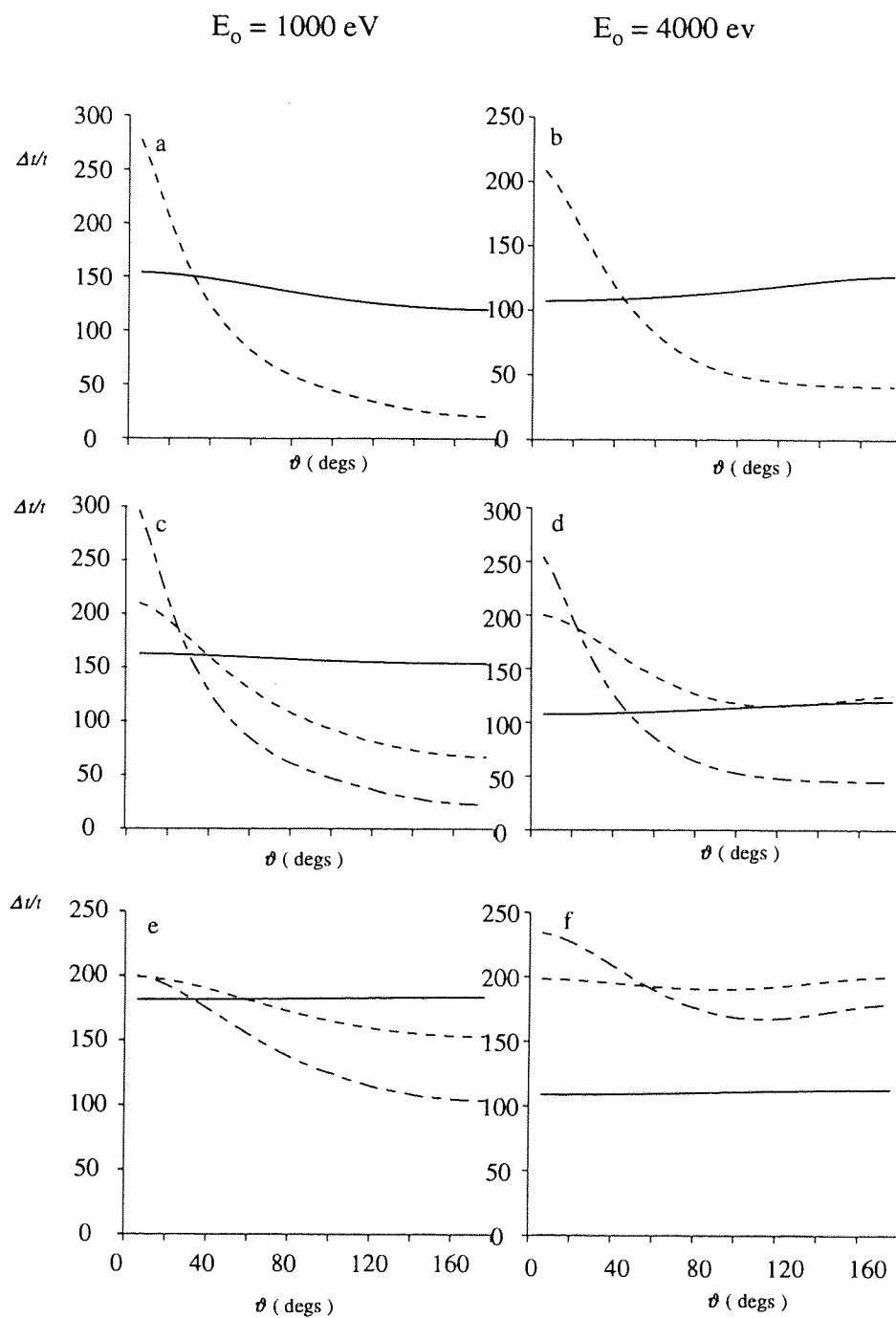


Figure 5.17 - Instrumental resolution, expressed in terms of $\Delta t/t$.

(a) and (b) $m_2 = 28$
 (c) and (d) $m_2 = 59$
 (e) and (f) $m_2 = 197$

----- Ar
 - · - · - Ne
 _____ He

CHAPTER VI

Experimental Scattering Results

The primary aim of the work described in this chapter was to investigate and assess instrument capabilities. Following this it was intended to investigate surface neutralisation and ionisation processes, however, the initial data presented here demonstrated the requirement for improvements concerning the substrate environment before meaningful results regarding these fundamental processes could be obtained. In the following sections of this chapter initial experimental results are presented and the various spectral features identified. The results are discussed in the light of similar published results together with implications regarding the substrate contamination chapter 7. Spectra were obtained with the instrument in various stages of development, and can be broadly segregated as follows;

Section 6.1 - $\theta = 90^\circ$ employing FAB-1 as the primary particle source, and flight/acceleration tube configuration 1.

Section 6.2 - $\theta = 164^\circ$ employing FAB-2 as the primary particle source, and flight/acceleration tube configuration 1.

Section 6.3 - $\theta = 164^\circ$ employing FAB-2 as the primary particle source, and flight/acceleration tube configuration 2.

During the course of this chapter the QS peak is identified, by means of the SBCE, which provides a sufficiently accurate approximation for the scattering angles employed. All experimental flight times quoted refer to the flight time from the source, that is from the chopping plates, to the detector. Flight times where necessary have been corrected to take account of electronically introduced delays: delays of up to $110 \mu\text{s}$ could be introduced by the delay generator, in which case the delay must be added to the time recorded by the MCA to obtain the true experimental flight time. In cases where a zero delay was set at the delay generator, negative delays were possible for certain pulse generator settings. Negative delays were found to arise particularly in the case of the FAB-2 pulsing system with optimum settings for a low energy argon beam.

Due to the lengthy pumping period required to reach sufficiently low base pressures following a sample change only a limited number of samples were subjected to analysis.

6.1 Experimental results - 90° scattering

The data described in this section were obtained employing the

FAB-1 source and scattering angle of 90° . The flight path geometry was as follows; $s=369$ mm, $l=1830$ mm, $\Delta\theta=0.5$, and the short, $L=400$ mm acceleration tube format was employed for ion-neutral discrimination. Initial spectra were collected from a polycrystalline copper surface, followed by a single crystal silicon wafer.

The FAB-1 source produced a primary beam energy spread, $\Delta E_o \sim 0.01 E_o$ and a pulse duration of $\Delta t \sim 150$ ns, but provided no mass filter or neutral dump. The absence of the filter therefore presented a possible source of low level substrate contamination. Substrate heating was due to a bare tungsten filament mounted behind the sample, and capable of raising the sample temperature to $\sim 400^\circ$ C. No high current source was available for sample cleaning for these initial experiments.

6.1.1 Scattering from a polycrystalline copper surface - 90° .

6.1.1.1 Helium scattering - ion bombardment

The polycrystalline copper sample was prepared following standard procedures, it was polished with diamond paste, followed by ultrasonic cleaning in 111-trichloroethane, and rinsing in propan-2-ol, followed by de-ionised water. A specular spectrum prior to any 'in vacuum' cleaning is shown in figure 6.1. The $QS_{\text{He-Cu}}$ peak energy which is given by $0.881 E_o$, is expected at a flight time of $8.26 \mu\text{s}$. However, the QS peak cannot be distinguished in the spectrum which is dominated by multiple scattering. The base of the leading edge corresponds to the flight time of a $QT_{\text{He-Cu}}$ collision, as shown in figure 6.2. This was found to be a general result for all neutral particle spectra derived from polycrystalline and amorphous surfaces, as was established in the discussion of previous data in chapter 2. This feature is subsequently referred to as the 'QT edge'. The $QS_{\text{He-Cu}}$ peak which has an expected FWHM of 160 ns does not even give rise to a shoulder on the leading edge of the peak. The scattered intensity occurring between flight times of 5.5 and $8.1 \mu\text{s}$ can be shown to be the result of hydrogen recoils. The origin of recoiling peaks which were found to be present in most spectra are discussed further in chapter 7.

A discriminating voltage of -4 kV ($= -3kE_o$) was applied to the acceleration tube in order to separate the scattered ions and neutral fractions, however this had no visible effect on the spectrum. The expected position of the accelerated ion peak is shown in figure 6.3, which should occur to the left

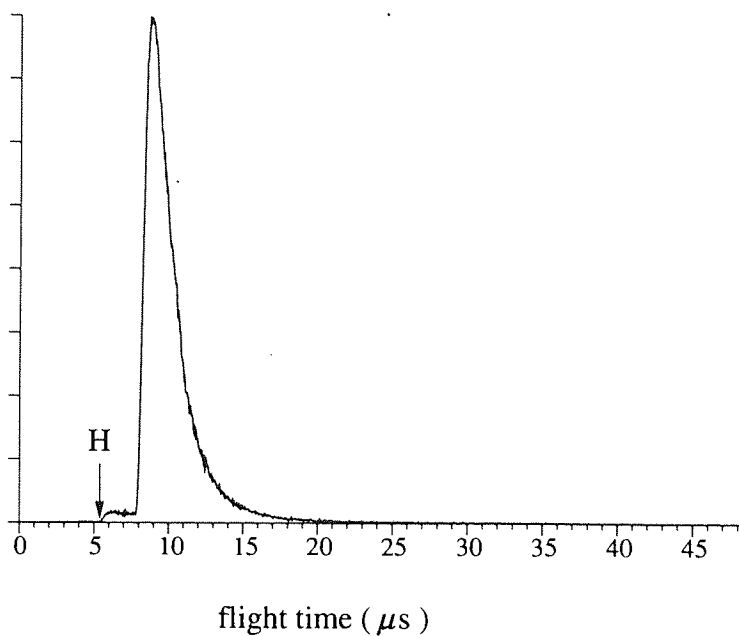


Figure 6.1 - Experimental spectra - He^+ scattered from polycrystalline Cu.

-Experimental parameters: - $E_o = 1500 \text{ eV}$ $s=369 \text{ mm}$, $l=1830 \text{ mm}$,
 $t_{\text{delay}} = 0.25 \mu\text{s}$, $\Delta t \sim 150 \text{ ns}$, $\Delta E_o = 0.01 E_o$ $\Delta\vartheta=0.5^\circ$.

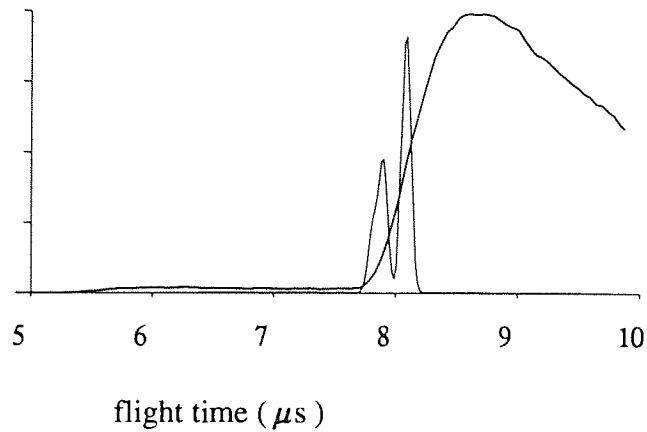


Figure 6.2 - He⁺ scattered from Cu, showing the experimental peak, and the calculated positions of the QS, QD and QT peaks.

Conditions: $E_o = 1550$ eV, delay = -0.25

Calculation parameters: $\Delta t = 150$ ns, $\Delta E_o = 0.01 E_o$, $\Delta \vartheta = 0.5^\circ$, $\Delta E_{phonon} = 30$ meV. (QS, QD, QT, have the proportions 1 : 0.5 : 0.25)

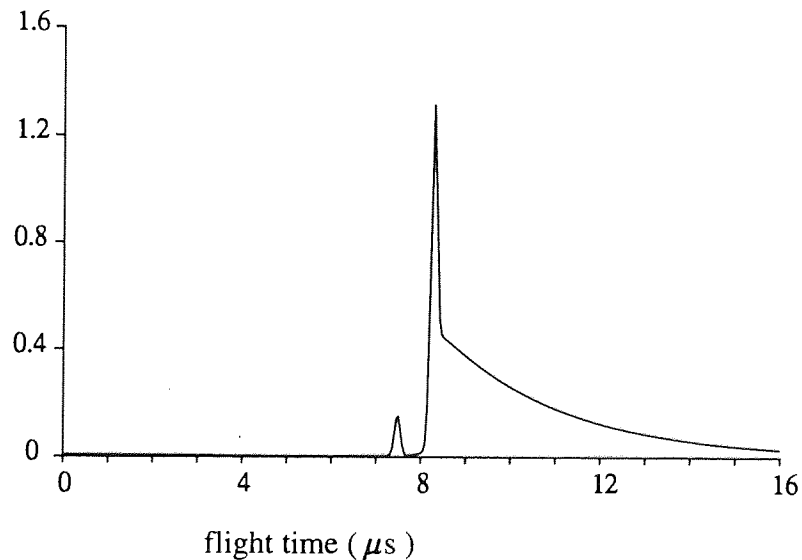


Figure 6.3 - Calculated spectrum, He scattered from Cu showing the expected position of the accelerated ion peak.

parameters $E_o = 1500$ eV $s = 369$ mm, $l = 1830$ mm.

The FWHM of the peaks were calculated assuming a SBC, and the following experimental parameters: $\Delta t \sim 150$ ns, $\Delta E_o = 0.01 E_o$, $\Delta \vartheta = 0.5^\circ$.

of the QT edge. Thus any ion peak would be completely separated from the neutral peak, but would lie within the broad hydrogen recoil peak, which in this case has an intensity of 20 counts/channel. Thus the minimum detectable ion peak intensity was ~ 20 counts/channel.

6.1.1.2 Helium scattering - Neutral bombardment

Spectra collected with a primary neutral beam yielded very similar broad spectra features. Again there was no distinct QS peak, making it impossible to measure a shift in the QS peak position due to the primary beam charge state, as described in chapter 3. The most significant differences between the two modes of bombardment were found in the angle resolved measurements, which were made with respect to the incident angle, θ . A series of such spectra are shown in figure 6.4. In both modes of bombardment the peak maxima shift towards longer flight times at low and high angles of incidence. The origin of the shift is due to increased scattering from carbonaceous contamination layers, as was observed previously by Sullivan²⁶. Possible causes of the differences resulting from the primary particle charge state are discussed later. However, it should be noted, for the reasons described in chapter 4, that the diameter of the neutral beam emergent from the FAB-1 source was significantly broader than the respective ion beam, thus the two series of spectra effectively originate from different regions of the sample. It should also be noted that the signal intensity decreased rapidly at low and high incidence angles, thus these spectra exhibit greater statistical uncertainties than the specular ones. An additional uncertainty arose from the large background count rate in the spectra of the neutral primaries which, as described in chapter IV, originated from a small continuous neutral beam due to the absence of a neutral dump in the FAB-1 source.

6.1.1.3 Neon scattering

A neon spectrum of the same copper sample is shown in figure 6.5. Here the $QS_{\text{Ne-Cu}}$ peak can just be distinguished from the MS signal, at the flight time of $19.22 \mu\text{s}$, and corresponding to $k_{\text{Ne-Cu}}$ of 0.518. The experimental peak width is $\sim 0.7 \mu\text{s}$, significantly broader than the expected value of $0.2 \mu\text{s}$. A substantial recoil signal was also observed, and for these conditions carbon and oxygen recoils as well as those of hydrogen have flight times shorter than the scattered neon spectra. The expected positions of the recoils are indicated in the figure. Also visible is a peak at a flight time of 4.5

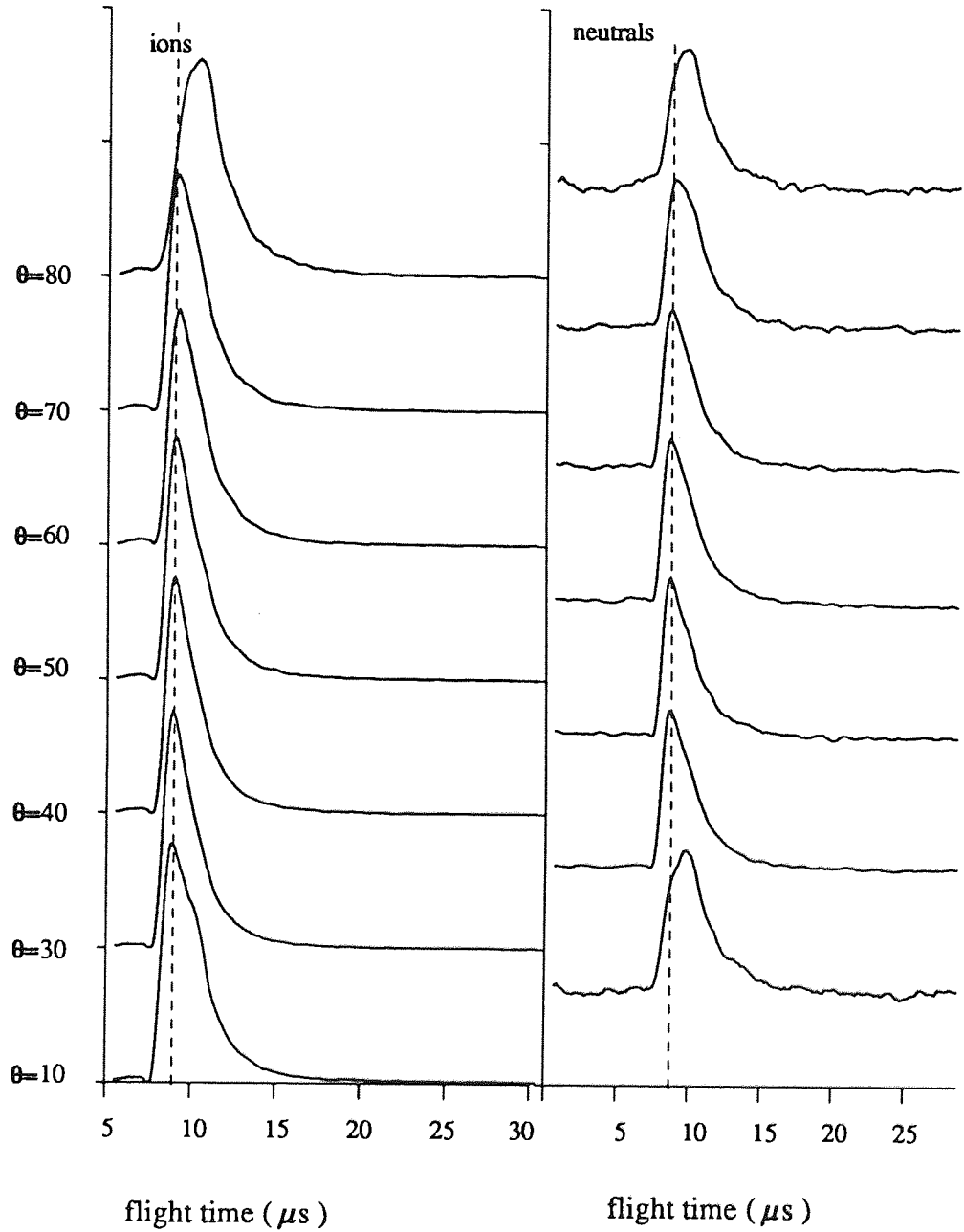


Figure 6.4 - He^+ and He^0 scattered from polycrystalline copper, showing the variation of peak shape with incident angle, $\theta=90^\circ$.

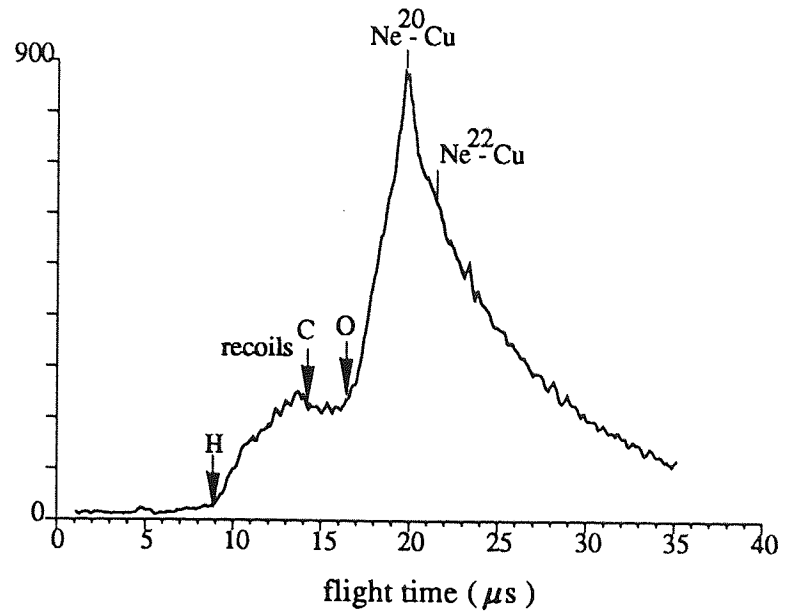


Figure 6.5 - Experimental spectra - Ne^+ scattered from polycrystalline Cu.

- Experimental parameters: $E_o = 2150 \text{ eV}$, $s=369 \text{ mm}$, $l=1830 \text{ mm}$, $t_{\text{delay}} = 0.25 \mu\text{s}$, $\Delta t \sim 150 \text{ ns}$, $\Delta E_o = 0.01 E_o$, $\Delta \theta = 0.5^\circ$

- Calculated recoil positions: H ($t=9.00$, $E_{\text{recoil}} = 375 \text{ eV}$),
 C ($t=14.3$, $E_{\text{recoil}} = 1374 \text{ eV}$), O ($t=16.7$, $E_{\text{recoil}} = 1266 \text{ eV}$)

μs which corresponds to the scattering of molecular hydrogen from copper. Again the application of the discrimination voltage to the acceleration tube had no influence on the scattered particle spectrum. The expected peak positions due to $V_a = -3kE_o$ are shown in figure 6.6, which predicts the accelerated ion peak to lie within the limits of the neutral peak, that is it appears at a longer flight time than the QT edge. Thus, in this case due to the experimental conditions, the sensitivity to the ion peak signal was poor. Following removal of the sample from the analysis chamber, LEISS analysis was performed using a separate VG-ESCA 200D instrument. Initially on transferring the sample no LEISS signal was detectable from the sample. The spectrum shown in figure 6.7 was only obtained after substantial sputter cleaning. The LEISS spectrum shows the sample to be free from any substantial surface contamination.

6.1.1.4 Argon scattering - Ion bombardment

Attempts were also made to collect scattered argon spectra, however in this case the scattered particle energy appeared to be too low ($k = 0.223$) for the detection system at the time these measurements were made. Later improvements were made to the detection system in order to extend the 'cut off' energy to ~ 200 eV.

6.1.2 Scattering from amorphous silicon

6.1.2.1 Helium Scattering

A typical silicon spectrum is shown in figure 6.8. The specular spectrum of figure 6.8b can be seen to be very similar in appearance to the copper spectra. Again there is no obvious peak relating to the $QS_{\text{He-Si}}$ scattering mechanism, although a shoulder can be observed on the leading edge which corresponds to the $QS_{\text{He-Si}}$ flight time of $7.92 \mu\text{s}$. The flight time of the leading edge base again corresponds to QT scattering. The scattered particle intensity reaches a maximum at an energy of ~ 1370 eV, which represents the most probable energy of multiply scattered particles. The low energy tail reduces to zero intensity at an energy of ~ 500 eV. The peak at shorter flight times of the main leading edge at $7.5 \mu\text{s}$ corresponds to a $QS_{\text{He-Ta}}$ peak. The tantalum was thought to have been deposited on the sample as a beam impurity species. The broader peak at smaller flight times cannot result from scattering and is due to recoils, and the hydrogen recoils position is

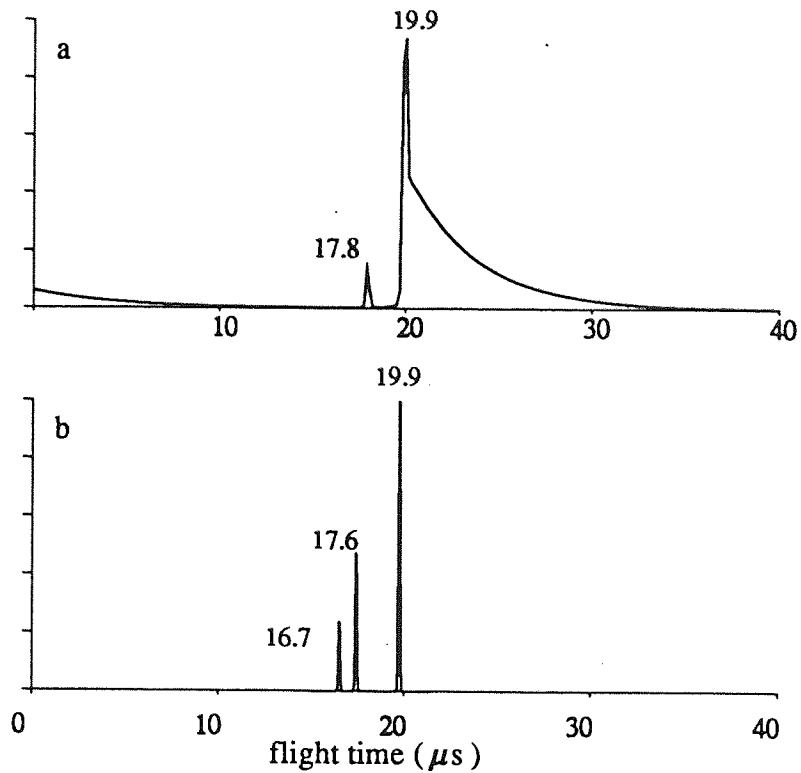


Figure 6.6 - Calculated spectra - Ne^+ scattered from polycrystalline Cu. (a) showing the positions of the ion and neutral peaks. (b) showing the positions of the QS, QD and QT peaks. -Conditions: $E_o=2150$ eV, $E_a = -3.3$ kV, $\Delta t=150$ ns, $\Delta E_o = 0.01E_o$, $\Delta\theta=0.5^\circ$, $\Delta E_{\text{phonon}} = 30$ meV.

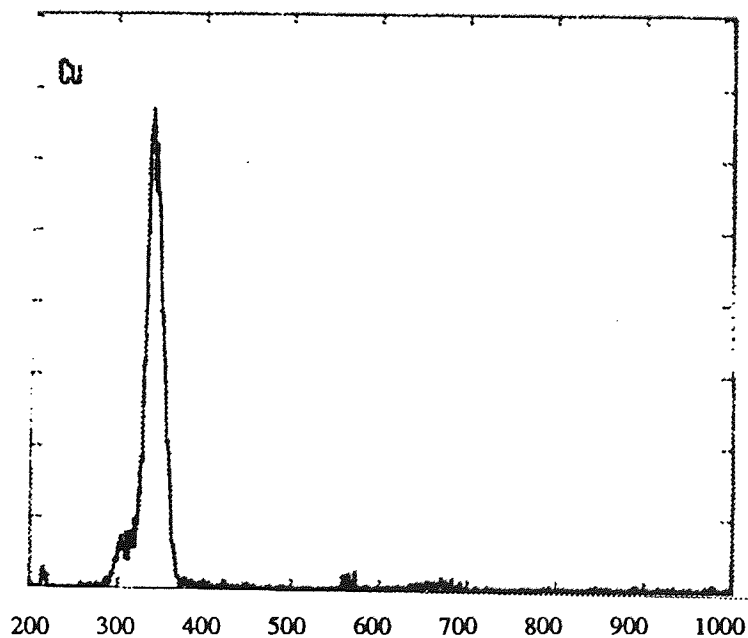


Figure 6.7 - LEISS spectrum of the copper sample after removal from the analysis chamber. This analysis was performed using a 1 k eV neon beam on the ESCALAB 200D instrument.

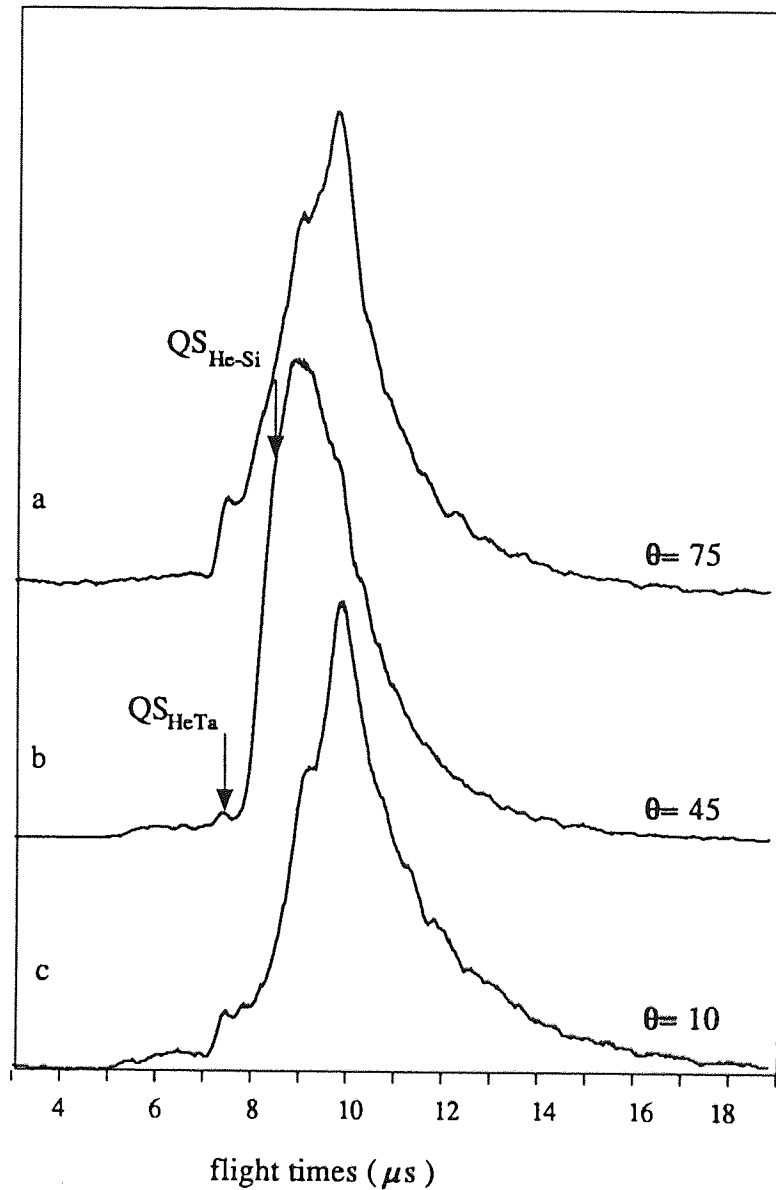


Figure 6.8 - Experimental spectra He^+ scattered from silicon surface. Showing low incidence, specular and high incidence reflection. The primary energy was 2050 eV, The spectra was collected prior to any sputter cleaning. $\vartheta=90^\circ$.

indicated in the figure. Angle resolved measurements with respect to the incidence angle, θ , were also made, and the low and high incidence spectra are shown in the figure (a) and (c). As for the copper data the peak shift is consistent with the scattering from carbon and oxygen atoms, thus demonstrating the existence of contamination layers. Following this, a 10μ amps, 8 keV argon beam, giving a removal rate of ~ 4 monolayers/minute was employed to remove the surface contamination. However, contamination was seen to persist on the surface, even after prolonged periods of bombardment: the sample was subjected to bombardment for periods varying between 5 and 30 minutes, and spectra collected with a discriminating voltage applied to the tube in order to record the ion peak intensity. As shown in figure 6.9 the ion and neutral peaks should be well separated according to calculation.

Further attempts to remove contamination were made by heating the sample to ~ 700 K, but here again the contamination persisted. According to the RGA and the penning gauge, the residual gas pressure was $< 5 \times 10^{-10}$ mbar, with CO and H₂O being predominating species. Such a pressure would give rise to an absorbed monolayer in ~ 2 hours, assuming a unity sticking coefficient. However, the operation of the heater increased the partial pressures of CO and CO₂ and H₂O by three orders of magnitude, and this was thought to be the origin of the persisting contamination layer.

Again on removal of the sample from the chamber, it was subjected to LEISS analysis, and again a LEISS signal was detectable only after substantial sputter cleaning, after which the sample was seen to be free from any substantial surface contamination. The oxygen peak could not be removed even after prolonged sputter cleaning. However, due to the uncertainties arising from the unknown neutralisation probabilities the surface concentration of oxygen cannot be quantified.

6.1.2.2 Neon Scattering

Calculation shows that neon scattered from a silicon surface gives rise to a greater shift of the ion peak in terms of the absolute time shift, due to its lower scattered velocity. The calculated ion and neutral peak positions are given in figure 6.9a. However, due to the low value of A , the QS, QD and QT peaks are widely separated in energy, and neutrals scattered at the QD and QT energies lie to shorter flight times than the accelerated ion peak. However, as the scattered energy of a 2 keV neon primary is only 332 eV it could not be detected. The peak of greatest intensity in the spectrum in this case was that due to recoils. Clearly argon scattering cannot be applied to the analysis of a

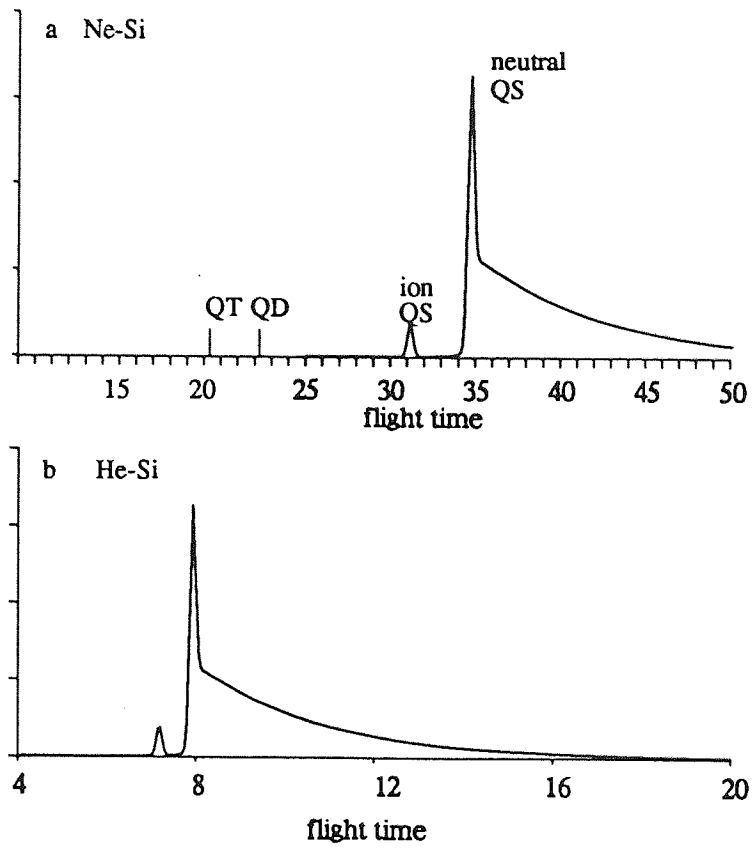


Figure 6.9 - Calculated ion neutral peak positions
a) He from Si
b) Ne from Si

native silicon surface.

6.2 Experimental results - 164° scattering - Flight/acceleration tube 1.

Before the next series of spectra were collected a number of modifications were introduced: the scattering angle was increased from 90° to 164°, and the FAB-2 source was introduced. Thus all proceeding experimental data were obtained with a mass filter and neutral dump applied to the primary beam. The new source also offered a reduced energy spread and pulse width, $\Delta E_o \sim 0.05 E_o$ and $\Delta t \sim 50$ ns. The MCP was also replaced and the modifications were made to the detection electronics. The geometry of the modified spectrometer was as follows.

$$l = 2384 \pm 13 \text{ mm}$$

$$s = 604 \pm 10 \text{ mm}$$

$$L = 400 \text{ mm}$$

$$\Delta \theta = 0.3,$$

$$\Delta \Omega \sim 2.5 \times 10^{-5} \text{ st rads.}$$

For sample cleaning the saddle field source was retained and the tungsten filament heater replaced by the bulb heater.

According to the work described in chapter 2 the high impact scattering condition should give rise to a decreased contribution from multiple scattering collision processes. Spectra were obtained from two different samples. Firstly from a Si(001) sample a proportion of which had been coated by ~ 10 nm of gold, deposited by plasma evaporation. Prior to the evaporation process the silicon wafer was subjected to hydrofluoric acid, and then prepared using the standard approach before it was inserted into the vacuum. Following a release of fluorine and magnesium contamination from the 'kapton' insulation wire within the proximity of the sample stage, polycrystalline gold and nickel foils were mounted on the sample stage, and the 'kapton' was replaced by ceramic beads.

6.2.1 Helium spectra

6.2.1.1 Scattered from single crystal Gold and Silicon surfaces

Prior to any 'in vacuum' cleaning the preliminary spectrum shown in figure 6.10 was collected from the gold covered region. As the spectrum

was preliminary the pulse width was lengthened in order to gain additional signal intensity, $\Delta t \sim 100$ ns. The sharp peak at $7.67 \pm 0.06 \mu\text{s}$, compares to the calculated value for a $\text{QS}_{\text{He-Au}}$ collision of $7.52 \pm 0.06 \mu\text{s}$, giving rise to a discrepancy in the flight time of $\sim 0.13 \mu\text{s}$. Although this difference, in the worst case, could be attributed to experimental and calculation uncertainties, the discrepancy for these conditions represents an energy loss of ~ 160 eV on the part of the scattered particle. However, if the discrepancy were to be attributed to experimental uncertainty and the peak maximum assigned to the $\text{QS}_{\text{He-Au}}$ energy, then scattered particles composing the leading edge would correspondingly have an energy of 3450 eV, equivalent to $k=0.991$. Since no scattering process is able to scatter helium through an angle of 164° with such an energy loss, the experimental flight time must be regarded as correct. Additionally, in the former case the QT edge is located at its expected flight time. In this case the peak maximum represented singular scattered particles that had lost ~ 160 eV in the collision process. Such loss processes may also be responsible for the broadening of the peak: the experimental FWHM is 300 ns, compared with the expected width of 120 ns, based on the experimental and instrumental parameters given above. The expected position of the hydrogen recoil peak is indicated in figure 6.10, however no such peak was observed.

A spectrum of the native silicon surface, was also recorded prior to any 'in vacuum' cleaning, in this case no sharp peak corresponding to that of the gold spectra was observed. Also the scattered intensity was much lower and the spectrum was dominated by MS processes. The shoulder was also observed at the base of the leading edge which corresponded to a $\text{QS}_{\text{He-Au}}$ collision.

Following these results the sample was heated to $\sim 400^\circ\text{C}$, that is considerably below the melting point of gold, 980°C . However, further experimental investigation of the above losses was not possible, as the gold surface layer evaporated as a result of the heating. The resulting spectra of the two regions after heating are shown in figure 6.11. It can be seen that the heating resulted in significant removal of the gold layer. The silicon spectra was not significantly affected by the heating, with the exception of a gold shoulder which was reduced. More importantly the heating process did not restore the crystalline surface through the annealing process, as anticipated. The sample was then subjected to further cycles of sputtering and heating, with the aim of removing surface contaminants. However, in the process of heating, the temperature of the Kapton, employed as insulation to the various electrical connections of the sample stage, was inadvertently raised above its

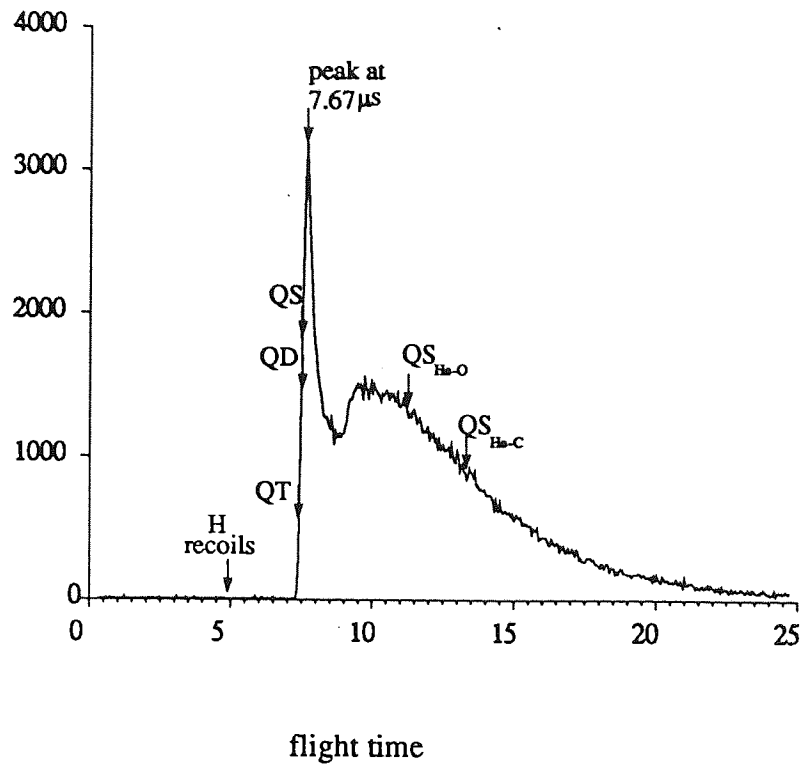


Figure 6.10 - Experimental spectra - helium scattered from gold evaporated onto Si(001) wafer.
 conditions: $E_0 = 3.5 \text{ keV}$, $\theta = 164^\circ$, specular reflection.

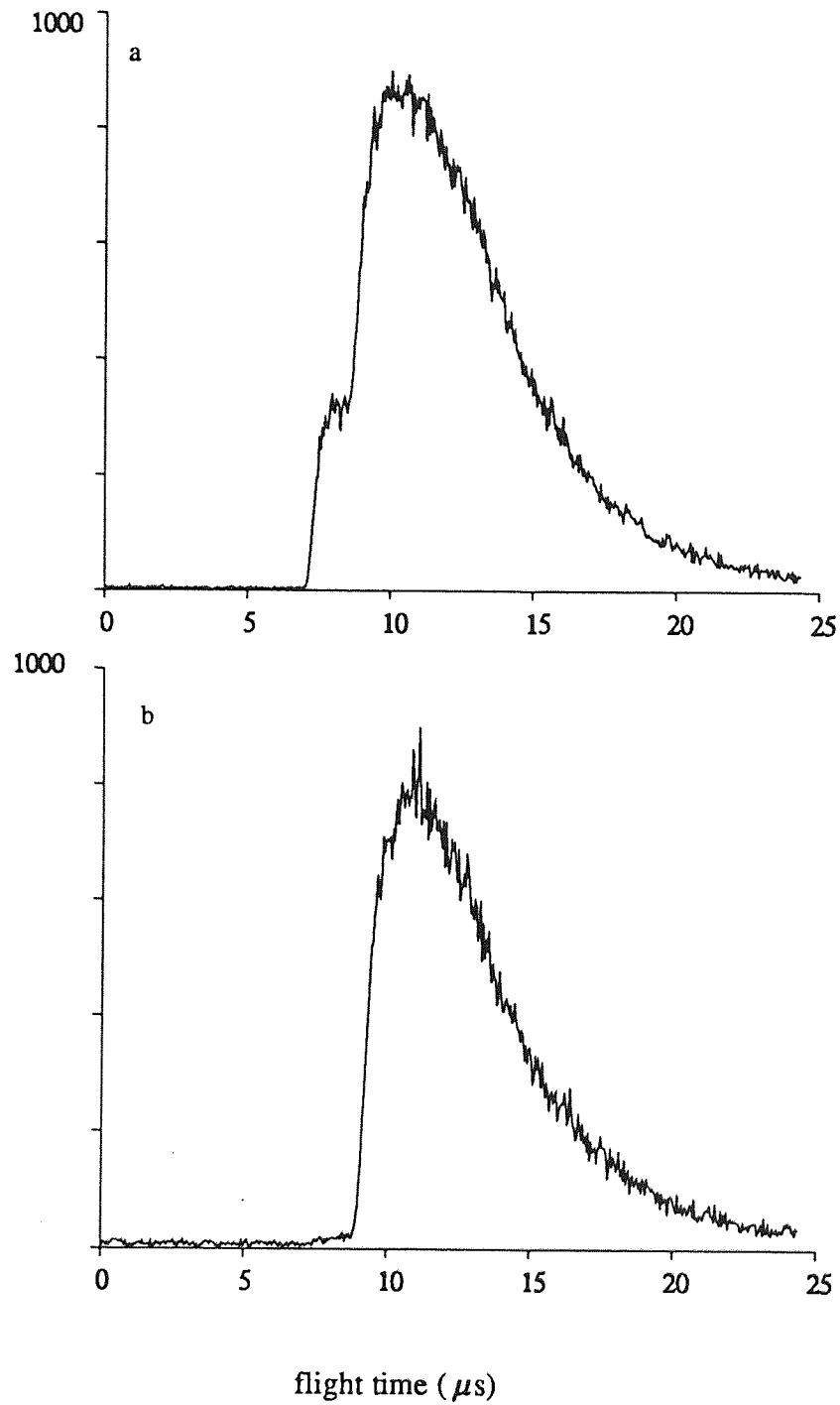


Figure 6.11 - After heating the surface to 400°C.
 (a) The gold surface evaporated region after heating.
 (b) The silicon region - Si(001)
 conditions - $E_o = 3500$ eV , $\theta = 1640$, specular reflection.

stable temperature of 210°. The contamination resulted in a high partial pressure of F1 in the vacuum chamber, which deposited a contamination layer onto the surface. This is evident from figure 6.12, which shows spectra before and after the contamination release. It can be seen in figure 6.12b that the leading edge is significantly shifted to longer flight times, indicating the silicon to be almost completely covered in contaminant species of lower amu. On transferring the sample to the ESCALAB-200D chamber, XPS analysis confirmed these conclusions, and revealed the sample to be covered in a thick layer of Mg (30%) and F1 (10 %). The silicon signal was very low indicating an atomic concentration ~ 2% only. The contamination was not significantly reduced, even after prolonged ion etching with a 5 keV, 3 μ amp argon beam. SEM and optical images showed the sample to be covered in a larger number of hillocks, ranging in sizes from 0.5 to 10 μ m.

6.2.1.2 from polycrystalline Gold and Nickel surfaces

Following the contamination of the gold-silicon sample, polycrystalline nickel and gold foils were mounted on the sample stage. He-Au spectra were collected, (a) prior to any sample cleaning, and (b) after repeated 'flash' heating to ~ 400°C. Unlike the He-Au spectra of figure 6.10 no sharp single scattering peak was observed, instead the $QS_{\text{He-Au}}$ peak resided within the leading edge of the peak, and the base of the leading edge corresponded to the QT energy. The figure 6.13 shows the spectrum after heating and sputter cleaning, however, this process had little influence on the spectrum. A typical spectrum resulting from the polycrystalline nickel region is given in figure 6.14, which was also recorded after the heating and sputter cleaning. Here again the peak is dominated by MS particles. The $QS_{\text{He-Ni}}$ peak at a flight time of 10.78 μ s, resides in the leading edge of the peak as indicated in the figure. The distinct peak at flight time 10.2 μ s, corresponds to a $QS_{\text{He-In}}$ collision, although the calibration of the time axis was not sufficient to determine the target mass to within 1 amu. However, the conclusion was confirmed by later spectra employing neon and argon as the primary species.

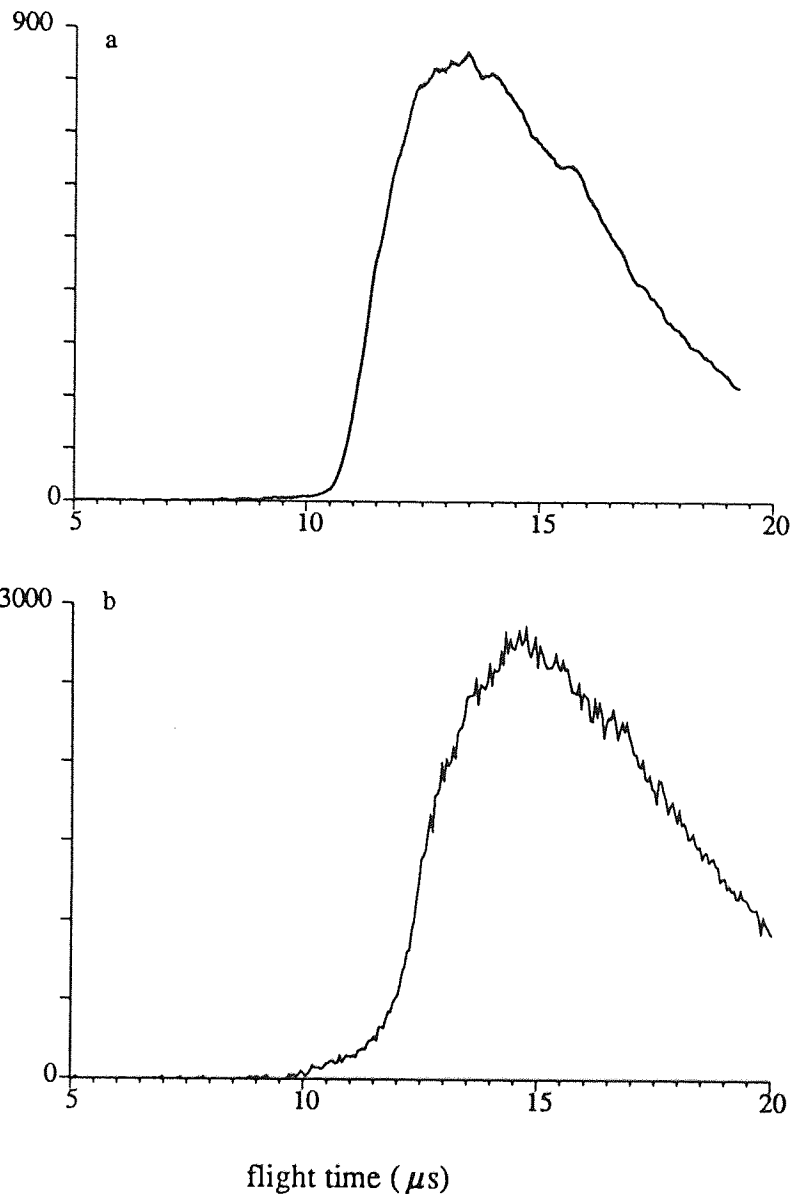


Figure 6.12 - He scattered from the Si region,
 (a) before heating
 (b) after prolonged heating, (surface covered in F1 and Mg contamination)
 conditions - $E_o = 2000$ eV, $\vartheta = 164^\circ$, specular reflection ($\theta = 90^\circ$)

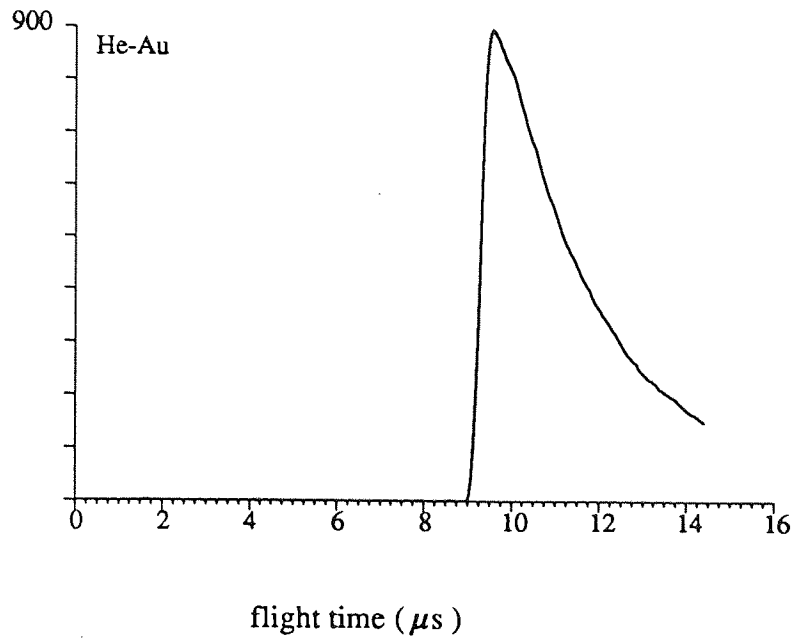


Figure 6.13 - Experimental spectrum - He⁺ scattered from polycrystalline Au.
 conditions - $E_o = 2000$ eV, $\vartheta = 164^\circ$, specular reflection.

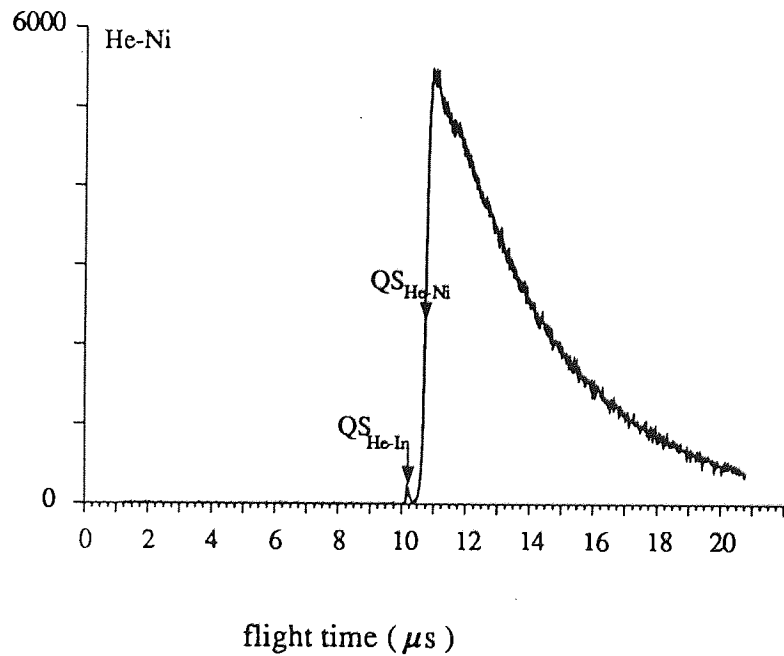


Figure 6.14 - Experimental spectrum - He scattered from polycrystalline Ni surface.
 conditions - $E_o = 2000$ eV, $\vartheta = 164^\circ$, specular reflection.

6.2.2 Neon scattering

The energy of neon scattered from the silicon surface is only $0.0284E_o$, thus for a primary energy of 2000 eV the scattered energy is only 58 eV and consequently could not be detected. However, in the case of scattered ions the effective impact energy at the detector surface is given by $kE_o + eV_{mcp}$, where V_{mcp} is the voltage applied across the detector, ~ 2.7 kV. However no ion peak was observed at the expected flight time of $109 \mu s$. The only peak visible was due to H recoils.

A typical tantalum spectrum (part of the sample holder), is shown in figure 6.15. As can be seen the Ne-Ta peak consisted largely of multiple scattered particles, however, the top of the leading edge is in good agreement with the QS_{Ne-Ta} . The bottom of the leading edge is also in good agreement with the QT_{Ne-Ta} energy.

A neon spectrum scattered from the polycrystalline gold surface is shown in figure 6.16. The spectrum was collected immediately after prolonged ion bombardment followed by heating to $400^\circ C$. The centre of the scattered peak appears at a flight time of $25.53 \mu s$, which corresponds to the QS_{Ne-Au} collision. The peak residing within the low energy tail as indicated in the figure corresponds to a ^{22}Ne . The FWHM of the QS_{Ne-Au} peak is ~ 300 ns, again broader than the theoretical value for a single binary collision, which is 118 ns. Prior to this cleaning procedure the recoil intensity was much greater. From close inspection of the recoil peak it can be seen that it contains structure which may be related to H and C recoils.

A neon spectrum scattered from the nickel surface is shown in figure 6.17. A large background was the result of a MCP fault, leading to the generation of excessive dark current counts. The MCP was subsequently replaced, however the spectrum contained some interesting information. Three distinct QS peaks are visible: the QS_{Ne-Ni} peak energy is 525 eV with a corresponding flight time of $39.6 \mu s$. The peak maximum relates to a QS collision between ^{20}Ne and the ^{58}Ni isotopic, which has an abundance of 67%. The shoulder on the left edge of the peak corresponds to the Ni^{60} isotope which has an isotopic abundance of 26%. Due to the relatively low value of A of the collision which is 2.95, the QD, and QT energies are widely spaced; 625 and 874 eV respectively giving rise to flight times of $39.6 \mu s$ and $31.5 \mu s$. The intensity of the low energy tail reduces to zero for energies of ~ 300 eV. The spectrum also contains peaks relating to Ta, In, and possibly Mo and Fe, the positions of which are indicated in the figure. XPS analysis of the sample, which was subsequently performed after some further analysis

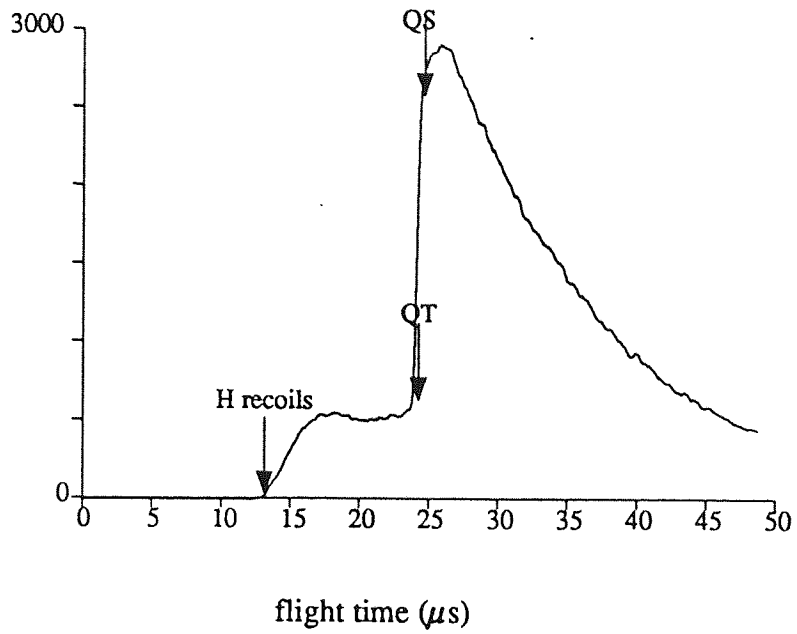


Figure 6.15 - Experimental spectrum - Ne^+ scattered from tantalum. conditions - $E_o = 2000 \text{ eV}$, $\vartheta = 164^\circ$, specular reflection.

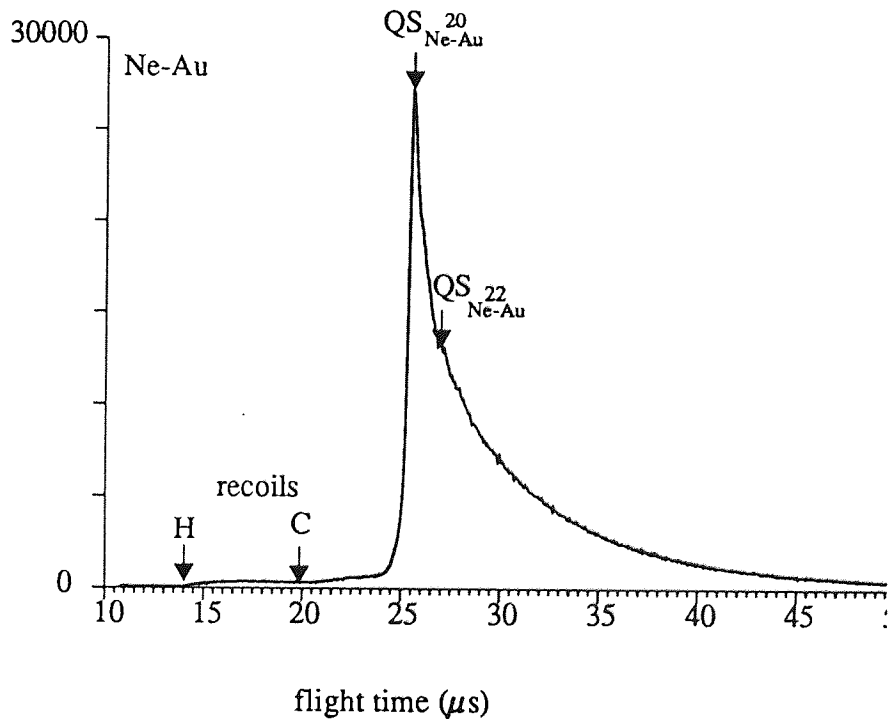


Figure 6.16 - Experimental spectrum - Ne^+ scattered from polycrystalline gold. conditions - $E_o = 2000 \text{ eV}$, $\vartheta = 164^\circ$, specular reflection.

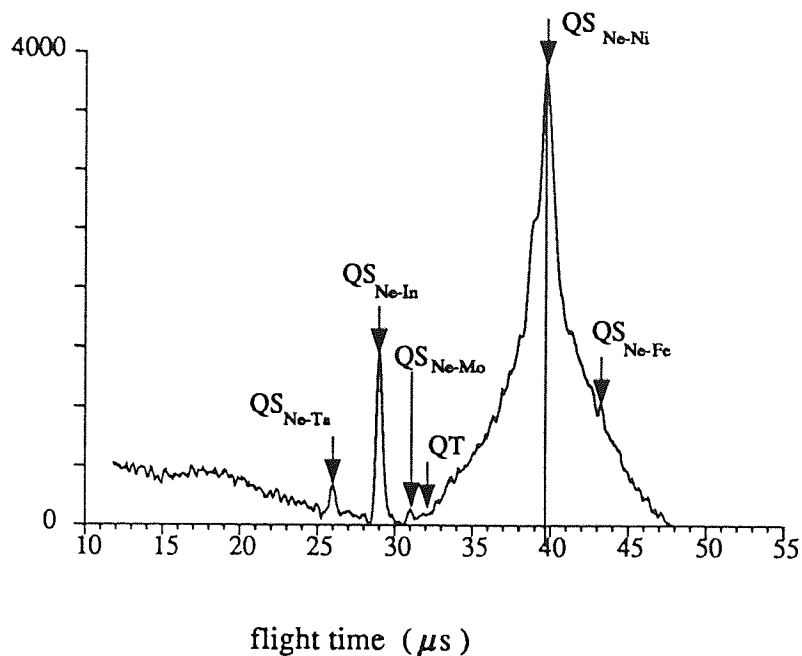


Figure 6.17 - Experimental spectrum - Ne^+ scattered from a contaminated polycrystalline Ni surface.
 conditions - $E_o = 2000 \text{ eV}$, $\vartheta = 164^\circ$, specular reflection.

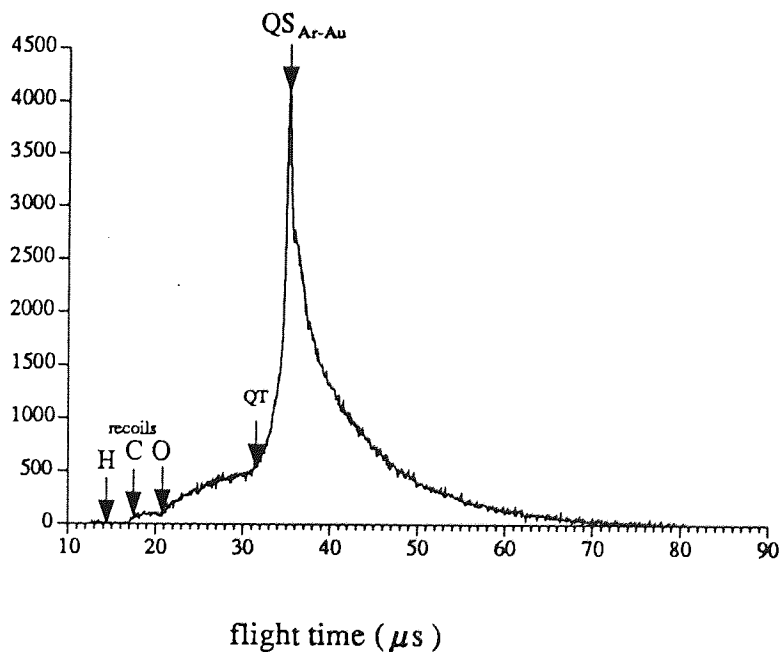


Figure 6.18 - Experimental spectrum - Ar^+ scattered from a contaminated polycrystalline Au surface.
 conditions: - $E_o = 3000 \text{ eV}$, $\vartheta = 164^\circ$, specular reflection.

described in later sections, also indicated In and Fe to be within the surface region. The source of this contamination was not known, although analysis of an untreated sample from the source did not reveal the presence of such contaminants.

6.2.3 Argon spectra. - 164°

A typical argon spectra from the polycrystalline gold surface is shown in figure 6.18. The QS_{Ar-Au} in this case is 891 eV, which corresponds to a flight time of 43.25 μs . As observed previously the FWHM of the experimental peak, ~ 500 ns, is significantly greater than the theoretical value, ~ 190 ns. Like the neon spectra from the same surface C and O recoils are clearly evident, although no H recoil peak can be observed. The recoil intensity was significantly greater relative to the scattered peak prior to heating and ion cleaning the sample. Apart from these no other surface contaminants are evident on the gold surface. These recoil peaks are present despite the absence of corresponding QS peaks in the scattered helium particle spectra, and in XPS spectra .

An argon spectrum of the nickel surface is shown in figure 6.19. As the energy of the QS_{Ar-Ni} peak was only 116 eV, it does not appear at the expected flight time of 110 μs , due to the very low detection efficiency at this energy. The broad peak results from carbon recoils and the sharp peak at a 45 μs , corresponds to a QS_{Ar-In} collision.

6.3 Experimental results - 164° scattering - Flight/Acceleration tube 2.

A final series of spectra was then obtained with the second flight/acceleration format as described in detail in chapter 5. This format offered greater ion-neutral and higher signal count rates, by a factor of ~ 5 . The revised spectrometer parameters are listed below.

$$l=2.514\pm 0.013 \text{ m}$$

$$s=0.604\pm 0.01 \text{ m}$$

$$d=1.7 \text{ m}$$

$$\Delta\theta=0.85^\circ$$

$$\Delta\Omega=1.7\times 10^{-4} \text{ st rads}$$

Initial spectra were collected from the same polycrystalline nickel/gold sample as employed in the experiments described above, and then

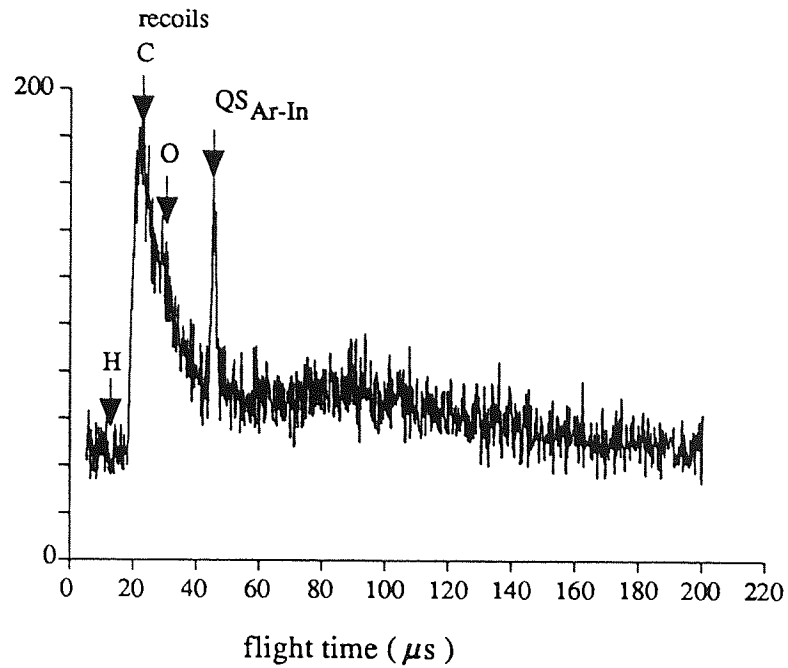


Figure 6.19 - Experimental spectrum - Ar scattered from a contaminated polycrystalline nickel surface.

conditions: - $E_o = 3000$ eV, $\vartheta = 164^\circ$, specular reflection.

Recoil flight times and energies: H (14.6, 267 eV), C (23.2, 960 eV), O (27.5, 841 eV).

from a fresh sample containing regions of gold, nickel and platinum, all of which were polycrystalline. In the latter case, the bulb heater was removed. The objectives of the experiments described below were to understand the origin of the surface contamination. As can be seen from the results above, and as discussed in chapter 7, this was the chief cause of the degraded spectral resolution and decreased sensitivity. It was therefore necessary to gain a better understanding of the contamination problems in order to meet the later objectives of the programme. As the FAB-2 source produced a greater ion beam current, at a lower chamber pressure, the investigation was conducted with ions as the primary species.

6.3.1 Helium scattering

The scattered helium spectra with the new tube configuration remained dominated by MS, but the collection rate, as expected, was significantly greater $\sim 5 \times 10^3$ cps, with a primary beam current of 50 p amps. Spectra of gold, platinum, tantalum and nickel surfaces were collected after a period of sputter cleaning, a fluence equivalent to the removal of ~ 100 monolayers. As a result of the greater signal intensity the He-Au spectra of figure 6.20a were collected in a period of only 78 seconds. A discriminating voltage of $V_a = -3.3$ kV was applied to the acceleration tube giving rise to an expected ion peak flight time of $7.96 \mu\text{s}$. Although the tube was able to provide much larger separations than the previous tube, again no ion peak was observed, above background counts. In this case the background at a flight time of $8 \mu\text{s}$ is ~ 7 counts/channel. Thus the minimum ion peak that could be detected was ~ 10 counts/channel, compared to a maximum of the neutral intensity of ~ 2500 counts/channel. The He-Pt spectra shown in figure 6.20b exhibits a very similar spectral peak shape, and the small shift in the flight time of the leading edge corresponds to the target mass difference. However, in the platinum spectra a small intensity recoil peak is visible, and the low energy tail is slightly enhanced. The spectral peak shape of the He-Ta spectrum in figure 6.20c is very different and much broader, with an increased low energy tail. This difference is significant given the small difference in the target mass species of the two spectra. (Ta^{181} , Au^{197}), and is therefore probably related to surface contamination. The He-Ni spectrum shown in figure 6.20d exhibits a similar peak shape, with the leading edge shifted to longer flight times due to the lower target mass. Although a small peak due to the scattering of the beam periphery from the gold region is visible, the QT edge is in good agreement with the $QT_{\text{He-Ni}}$ flight time.

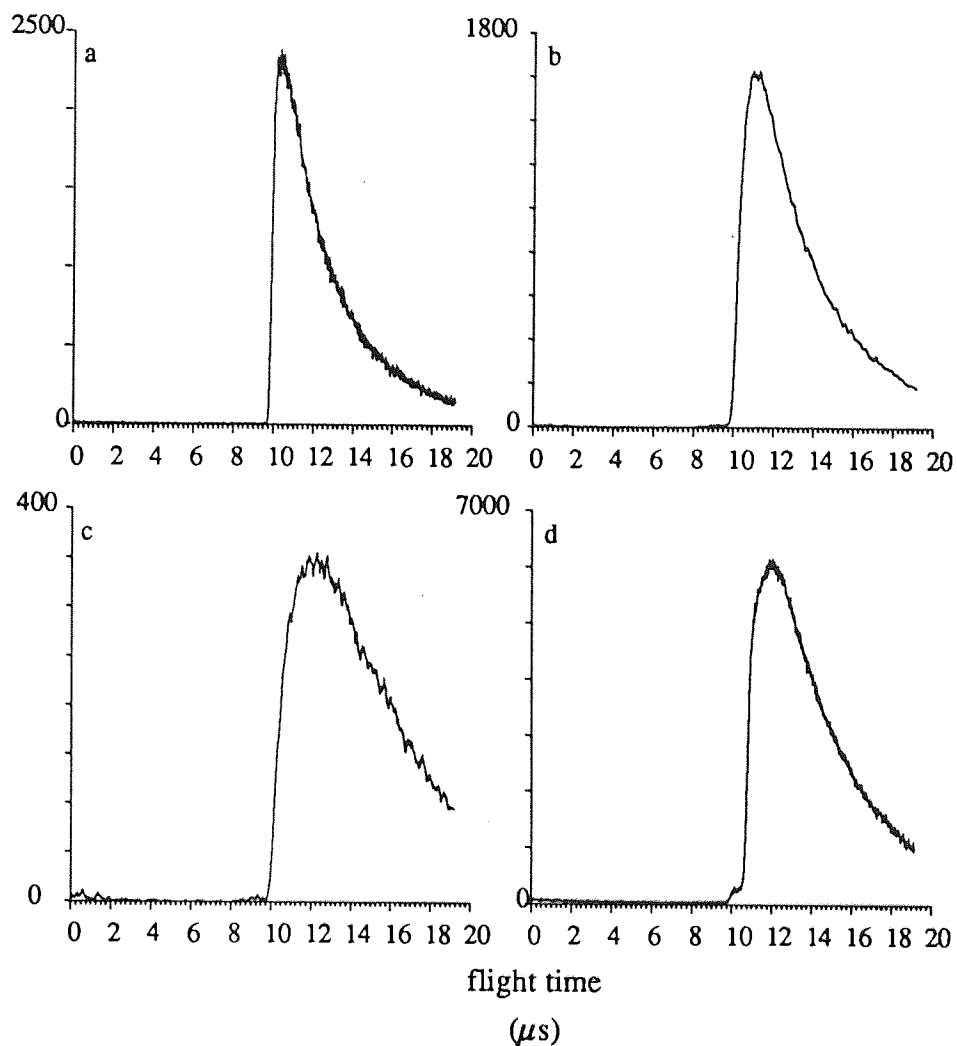


Figure 6.20 - Helium spectra scattered from (a) Au, (b) Pt, (c) Ta, (d) Ni
 -- $E_o = 2200$ eV.

6.3.2 Neon scattering

6.3.2.1 from polycrystalline gold

The spectral shape of the neon-gold spectra obtained with the new flight tube format were identical to those obtained previously. As for the helium spectra a $\sim x5$ greater increase in signal intensity was observed. A scattered beam intensity of ~ 1250 cps was obtained for a 200 pamps primary beam current. Despite modifications to the sample stage the operation of the substrate heater still gave rise to contamination of the sample surface. Although sample stage outgassing during heating was less than the previous heater; the residual gas of CO, CO₂ and H₂O was 10^{-8} and 10^{-9} mbar, sample contamination problems remained. Prior to any bombardment a number of spectra were collected from various regions of the sample, of which 6.21a is typical. The distinguishable peak at $25.08 \mu s$, corresponds to the QS_{Ne-Au} collision, although the FWHM of the peak is \sim three times the predicted value. The influence of heater operation on this spectrum is also demonstrated in the figure. Figure 6.21 (b) shows the Ne-Au spectra after heating the sample to $400^{\circ}C$, and (c) after bombardment with 3keV neon beam from the FAB-2 source, equivalent to the removal of ~ 25 monolayers. (d) was collected after further bombardment, equivalent to the removal of 500 monolayers. Heating the sample, as shown in figure 6.21(b) resulted in considerable broadening of peak, to such an extent that the QS peak can no longer be distinguished. The low energy tail also has a greater intensity, however the leading edge of the peak is un-shifted. The recoil peak intensity was also found to be enhanced by the heating, particularly the component relating to carbon recoils. However, the QS peak was found to be restored by the ion bombardment. The further bombardment led to further reductions in the MS intensity.

Having achieved the spectra shown in figure 6.21d, a further series of experiments were conducted with a discriminating voltage, V_a of -3 k, in an attempt to measure the scattered ion spectra. The expected separation obtained with this voltage is shown in figure 6.22, which shows the accelerated ion peak to lie within the recoil peak. For this reason it was important to conduct the measurements with minimum recoil intensity. The spectrum shown in figure 2.23a has a neutral peak intensity of 2.2×10^5 counts/channel, compared to the the recoil intensity of 300 counts/channel. It can be seen from 2.23b that the recoil intensity is superimposed upon a greater background intensity of ~ 600 counts/channel. This background

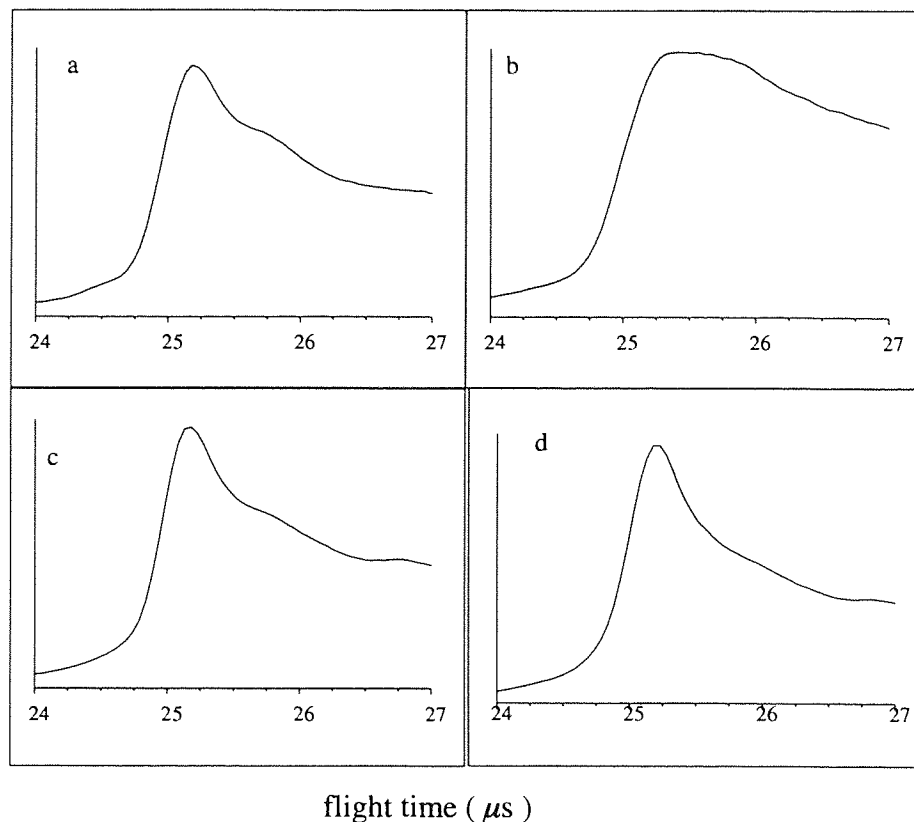


Figure 6.21 - Experimental spectra of neon scattered from polycrystalline gold.

conditions: - $E_o = 2200$ eV, $\vartheta = 164^\circ$, specular reflection ($\theta = 90^\circ$)

(a) prior to any cleaning

(b) after heating to 400°C for 3 minutes

(c) after bombardment with a DC neon beam of 3 keV and 110 namps, equivalent to the removal of 25 monolayers.

(d) after 15μ amps, 8 kV argon beam for 30 minutes.

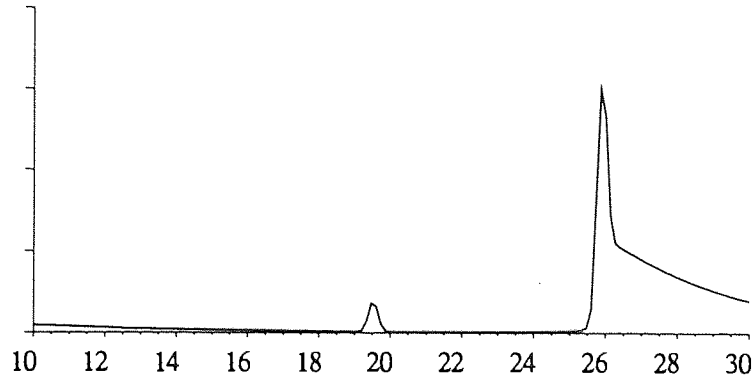


Figure 6.22 - Calculated spectra - showing ion/neutral separation of the modified acceleration/flight tube assembly.

$E_o = 2200$ eV, $l = 254$ cm, $\Delta t = 50$ ns, $\Delta E_o = 0.005 E_o$, $\Delta \theta = 0.85^\circ$

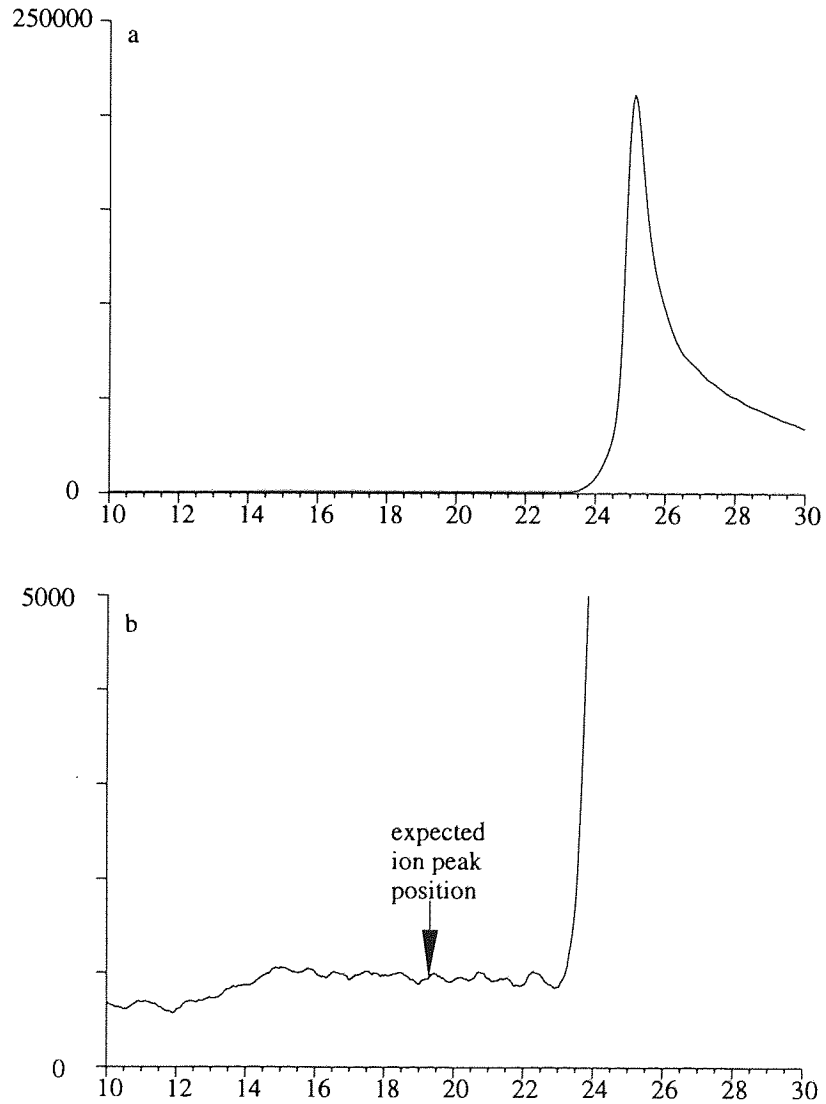


Figure 6.23 - Neon gold spectrum with - 3.0 k V applied to the acceleration tube, (a) full scale, (b) full scale/50.

- $E_o = 2200$ eV.

resulted from aliasing of scattered or recoiled particles originating from the previous pulse, and may be removed at the expense of longer collection time by decreasing the pulsing frequency. For example, particles contributing to the spectra at $10 \mu\text{s}$, have a true flight time of $60+10 = 70 \mu\text{s}$, where $60 \mu\text{s}$ is the time interval between consecutive pulses. At the expected position for the ion peak the total intensity is 1000 counts/channel, giving rise to a statistical uncertainty of ~ 30 counts/channel. Thus to be unambiguously distinguished the ion peak must be greater than ~ 90 counts/channel, giving rise to an upper limit of the ion survival probability in the case of this experiment of $\sim 0.05\%$.

Following these results, the gold sample was replaced and the bulb heater removed from the chamber, in order to eliminate it as the main source of the contamination. Similar results were obtained with the new sample, that is the MS intensity could not be further reduced. Subsequent XPS analysis of the initial gold sample revealed very little surface contamination.

The spectrum shown in figure 6.24 was collected from the new gold sample with a primary beam consisting of Ne^+ and Ar^{2+} , which was possible as the two species have the same primary velocity for equivalent primary energies, and consequently both species are passed by the Wein filter at the same value of V_w .

The shoulder observed on the long flight time side of the Ne-Au peak, is the result of ^{22}Ne isotope. Although this could be removed it could also be enhanced by careful tuning of the Wein filter, to give a distinct peak, as shown in figure 6.25b. Further adjustment was found to yield a separate ^{22}Ne -Au peak only as shown in figure 6.25c. The intensity of the ^{22}Ne is $\sim 10\%$ of that due to ^{20}Ne .

6.3.2.2 Scattering from a polycrystalline nickel surface

The same procedure of heating and ion bombardment was carried out with the nickel sample. However, in this case the process of ion bombardment, rather than removing contamination layers appeared to increase them. The spectrum corresponding to the previous neon-nickel surface, shown on figure 6.17 is given in figure 6.26. Here the recoil intensity is much increased relative to the scattered intensity, and the $\text{QS}_{\text{Ne-Au}}$ peak is significantly broader, as well as shifted to longer flight time. The Ta, Mo and In peaks that were visible in figure 6.17 can no longer be seen. A peak corresponding to the flight time of a $\text{QS}_{\text{Ne-Au}}$ collision is visible above the recoil intensity. Prolonged bombardment resulted in no increase in the nickel

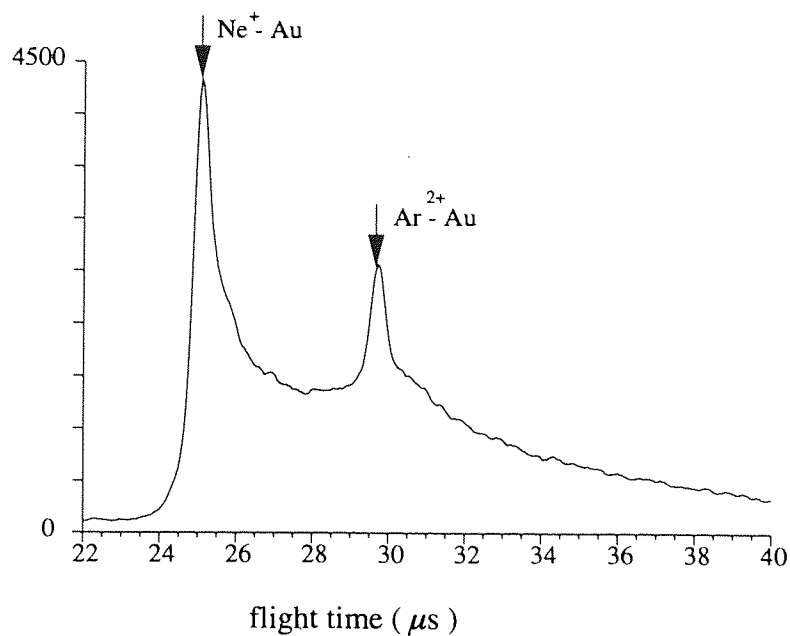


Figure 6.24 - Ne^+ and Ar^{2+} scattered from a polycrystalline gold surface. The experimental positions for the peak are 25.1 and $29.7 \mu\text{s}$, assuming a delay of $1.19 \mu\text{s}$, these correspond to the calculated values of $25.08 \mu\text{s}$ and $29.71 \mu\text{s}$.
conditions: - $E_o = 2200 \text{ eV}$, $\vartheta = 164^\circ$, specular reflection.

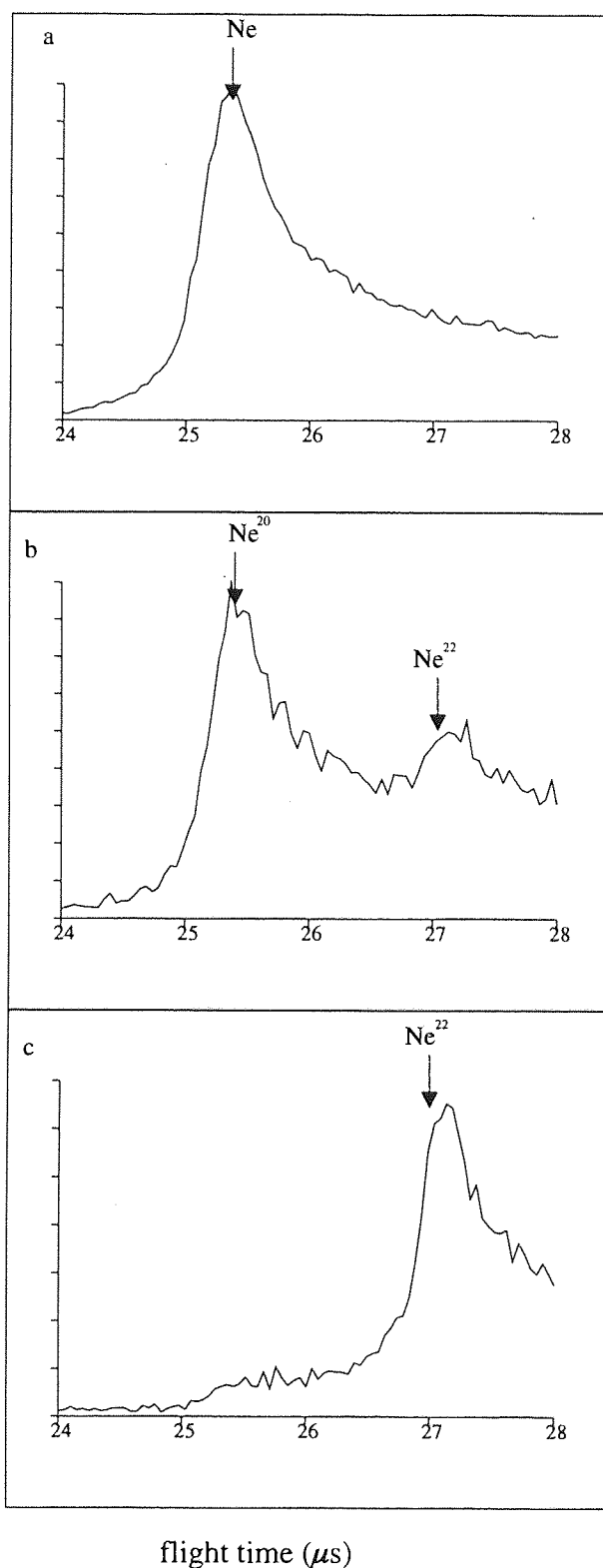


Figure 6.25 - $^{20}\text{Ne}^+$ and $^{22}\text{Ne}^+$ scattered from Au.
 (a) Wien filter tuned to ^{20}Ne , (b) between ^{20}Ne and ^{22}Ne (amu 21) and
 (c) to ^{22}Ne .
 The predicted flight times of the two peaks are $25.29\mu\text{s}$ and $26.96\mu\text{s}$.
 Conditions: - $E_o = 2200\text{ eV}$, $\vartheta = 164^\circ$, $l = 2.54$, $s = 0.604$, specular reflection.

peak signal. Subsequent XPS analysis of the sample showed the surface to be composed of 90% of carbon with traces of In and Fe. The Ni signal was observed to be very low, consistent with a high coverage surface layer of carbonaceous contamination. Following this a replacement Ni sample was analysed in the absence of the heater. The fresh replacement nickel sample, in the absence of any heating demonstrated a similar spectrum to that of figure 6.26.

6.3.3 Argon scattering

The programme of sample treatment described above for helium and neon was also followed for argon. A typical spectrum is given in figure 6.27, where a discrimination voltage of -3.3 kV was applied to the acceleration tube. The experimental QS_{Ar-Au} is very distinctive above the MS intensity, and the experimental and calculated flight times are in good agreement. However, the QS peak, ~ 600 ns remains larger than the expected value of 250 ns. A significant difference between the neon and argon was the recoil intensity which was much greater in the case of argon; a significant recoil intensity remained in cases where with neon the recoil intensity was almost completely absent. The position of the accelerated ion peak for a 3kV discriminating voltage is $29.9\mu s$, thus lying within the recoil intensity. Thus the sensitivity to the detection of the scattered ion peak, was reduced by the presence of the recoils. Even with the maximum discrimination voltage of -10kV the ion peak would still remain within the recoil intensity.

The scattering of argon from the platinum surface yielded a similar peak shape to that of the gold, with the peak centre shifted by a $\sim 0.5\mu s$ to longer flight times, as shown in figure 6.28a. The slightly increased FWHM is due to the isotopic distribution of the platinum. In addition the recoil and MS intensity is increased relative to the gold surface, (figure 6.28c). The spectrum in figure 6.28b resulted from scattering from part of the tantalum sample mounting stage. Although tantalum is composed 99.99% Ta^{181} the QS_{Ar-Ta} peak is considerably broader than that of gold or platinum.

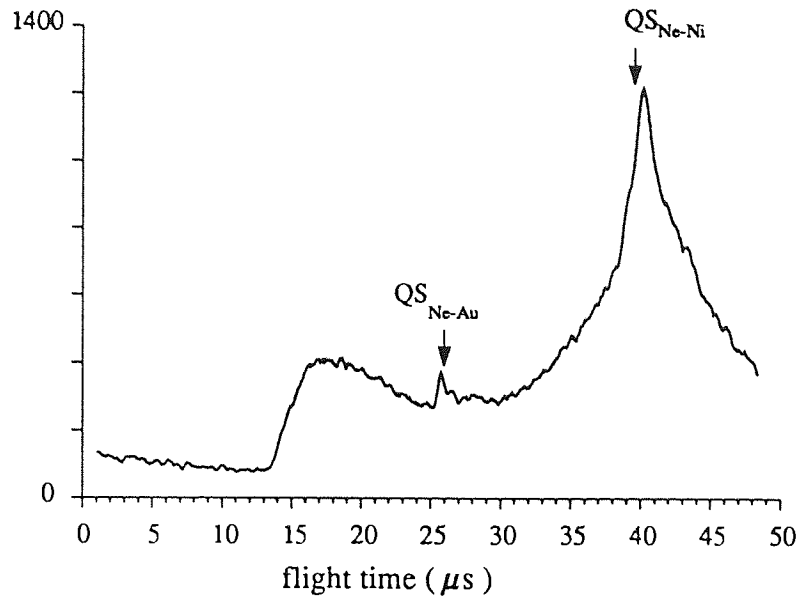


Figure 6.26 - Ne^+ scattered from a polycrystalline nickel surface. The experimental positions for the peak positions are 25.7 and 40.2 μs , assuming a delay of 0.7 μs . The corresponding calculated flight times were 29.88 and 39.22 μs .

conditions: - $\vartheta=164^\circ$, $E_o=2100$ eV, specular reflection.

H recoil peak ($t=13.3$ ms, $E_{recoil}=354$ eV).

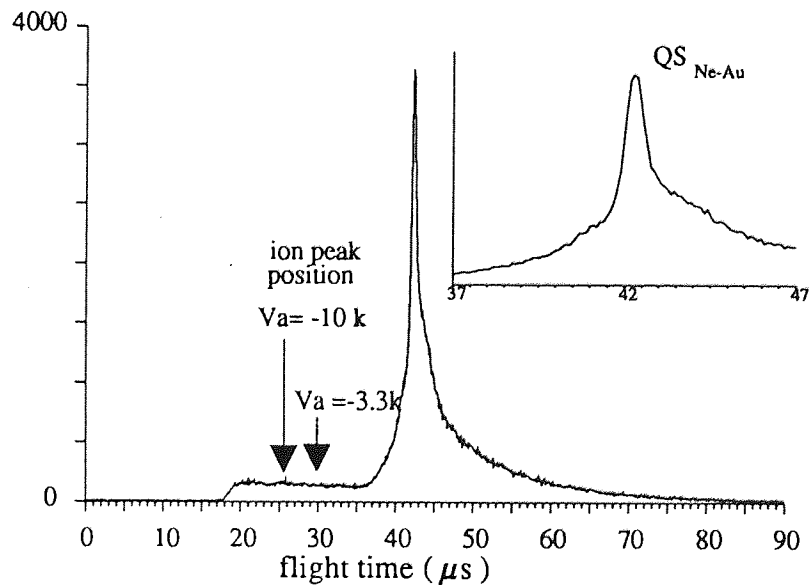


Figure 6.27 - Experimental spectrum of argon scattered from gold spectrum.

conditions: $V_a = -3.3$ k V, $E_o = 2200$ eV.

Recoils: H ($t=17.8$, $E_{recoil}=204$ eV), C ($t=22.8$, $E_{recoil}=1229$ eV),

O ($t=24.9$, $E_{recoil}=1131$ eV).

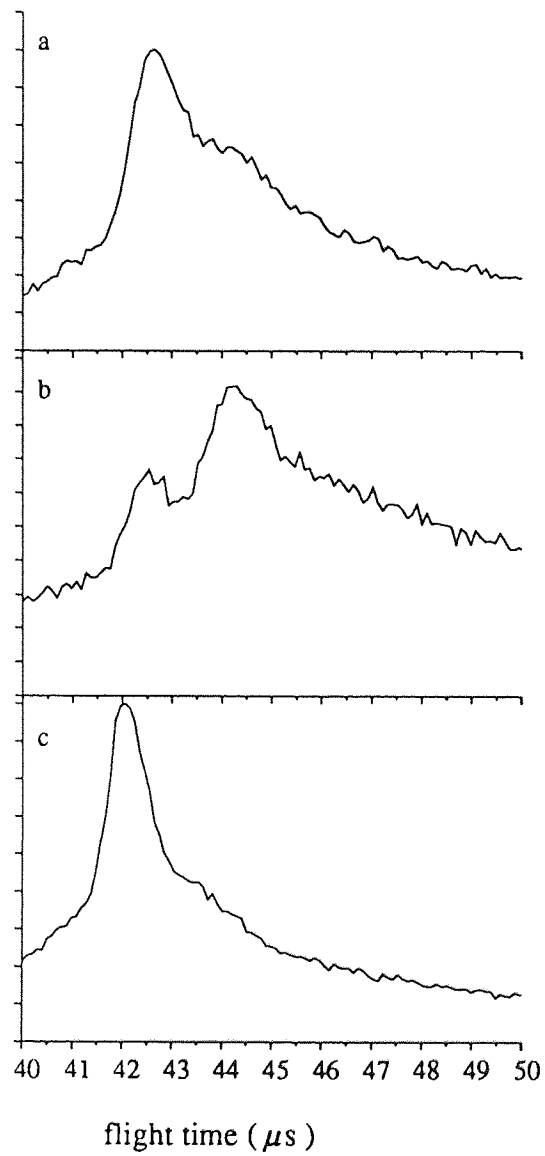


Figure 6.28 - Experimental spectra of argon scattered from
(a) Pt surface, (b) Pt and Ta surfaces, (c) Au surface
- $E_o = 2200$ eV.

CHAPTER VII

Discussion of Results

The experimental spectra presented in the previous chapter are discussed with regard to the surface-particle interaction process in section 7.1 with regard to the instrument in section 7.2.

7.1 Discussion of the experimental spectra in relation to the surface-particle interaction process and surface composition.

The data are discussed in terms of the following areas:

- spectral shape and the contribution of signals arising from processes other than single scattering, that is the multiple scattering and recoil contribution.
- the absence of a scattered ion signal
- the effect of employing a neutral beam
- surface contamination

7.1.1 Multiple Scattering and peak broadening features of the experimental spectra.

A common feature of all the spectra discussed in the previous chapter, and the ToF discussed in chapter 2, is the form of the spectral peaks relating to the native species of non-ordered surfaces. Irrespective of the value of A the base of the leading edge can be predicted by the QT energy. Where A is low, the QS and QT peaks are widely spaced leading to the scattering of particles with energies considerably above the QS energy. As the broadening is much greater than the inherent QS peak width, the QS peak can be easily distinguished from the MS signal. This is well demonstrated by the Ne-Ni and Ar-Au spectra, of figures 6.17 and 6.27. By contrast, when A is large the QS and QT separation is comparable or less than the inherent QS peak width, and QT and QD type collisions are manifested as an indistinct broadening of the QS peak.

None of the helium spectra recorded in this work, with the exception of the He-Au of figure 6.10, exhibited a distinct QS peak. In addition to QT and QD type collisions the QS peak is obscured by much larger, energetically broad MS signal, which extended from the QT energy to the lower detection limit of the detector, ~ 200 eV. This was also

characteristic of the helium spectra scattered from non ordered surfaces reported by Buck et al¹⁴, Eckstien⁹⁰ and Boers⁹¹. However, under certain conditions, for example, 1.5 keV Ne scattered from Ni at $\vartheta=135^\circ$, a small but distinct QS was visible above the MS signal. From the round robin comparison of He-Au spectra⁹¹, see figure 2.20, it was concluded that the magnitude of the QS peak related to differences in crystal grain size and substrate preparation procedure. In contrast to the results, computer simulation of the experiment condition⁹¹, using the ARGUS and TRIM codes⁹¹ which employed an amorphous surface model, did not predict a QS peak. The magnitude of the QS signal relative to the total signal can be estimated by comparing the calculated and experimental intensities as follows. The signal intensity due to binary scattering is given by:

$$I_t = I_o T(E) \Delta\Omega \frac{d\sigma}{d\Omega} N \quad -(7.1)$$

Applied to the experimental conditions relevant to the collection of the He-Au spectrum of figure 6.20a, this predicts a QS signal intensity of 42 cps, where the following parameters have been applied:

$$\begin{aligned} I_o &= 50 \text{ p amps} \approx 3.1 \times 10^8 \text{ ions/sec} \\ T(E) &= 0.8 \\ \Delta\Omega &= 1.7 \times 10^{-4} \text{ st rads} \\ \frac{d\sigma}{d\Omega} &= 50 \times 10^{-20} \text{ cm}^2 \\ N &= 2 \times 10^{15} \text{ cm}^{-2} \end{aligned}$$

This compares with the total experimental count rate of 2278 cps. Thus the comparison demonstrates the maximum theoretical QS signal to be ~2% of the total experimental signal intensity. However, a signal of this magnitude would be visible in experimental spectrum. It is not, demonstrating a lower QS signal in practice. Reasons for this are discussed below.

In contrast to the He-Au spectrum, applying the same calculation to Ar-Au spectrum of figure 6.27 predicts a QS signal intensity of 442 cps, compared to the experimental signal of 440 cps. (A detection efficiency, $T(E) = 0.31$ has been assumed due to the lower energy). This calculation confirms the conclusion that can be drawn from the spectrum, that is, a much higher proportion of the signal in this case originates from QS scattering. However, it is also apparent that the spectrum comprises MS and recoil signal showing again the experimental QS signal to be lower than predicted.

The difference between the ToF and LEISS techniques was seen

to be greatest in the case of the helium spectra. LEISS spectra corresponding to the ToF spectra of the silicon surface are shown in figure 7.1, which were again collected by the separate ESCALAB-200D instrument. Considerable sputter cleaning with an argon beam, $\cong 100$ monolayer removal, was required in order to gain a LEISS signal prior to the collection of this spectrum. The residual oxygen peak remained which could not be reduced as a result of further sputtering. It can be seen from the figure that at a primary energy of 1 keV the QS signal dominates. Increasing the primary energy to 3 keV results in a significant increase in the MS signal, to such an extent that the QS signal relating to oxygen is obscured, however, the MS signal remains significantly less than in the ToF counterpart spectrum.

The origin of the large difference in the MS signal intensity in helium and argon ToF spectra can be related to the size of the shadow cones pertaining to the respective collisions. This is illustrated in figure 7.2 where it can be seen that the shadow cone relating to a Ar-Au collision is significantly greater than the corresponding He-Au collision. As discussed in chapter 2, the shadow cone diameter relates directly to the penetration of the primary beam beyond the top atomic layer, and therefore determines the level of the energetically broad MS signal relating to sub-surface collision processes. In order to attain a helium shadow cone of similar dimensions to that of argon, the primary energy would have to be decreased to ~ 200 eV, which is outside the range accessible by the ToF spectrometer.

An important aspect of the results, relating to the objectives of quantitative analysis is that, in general, the MS spectral features accompany QS peak relating the substrate species only. This point is clearly illustrated by the neon spectrum of figure 6.17, where symmetrical QS peaks relating to the contaminant species are observed. Even in the absence of MS mechanisms the FWHM of the peaks are ~ 400 ns, and still significantly larger than expected, by a factor of ~ 2.4 .

The helium spectrum of figure 6.10 obtained from the deposited gold layer contrasted sharply with all the other helium spectra. The parameters relating to this spectrum were:

$$I_o = 100 \text{ p amps} \cong 1.6 \times 10^8 \text{ ions/sec}$$

$$T(E) = 0.8$$

$$\Delta\Omega \sim 2.5 \times 10^{-5} \text{ st rads.}$$

$$d\sigma/d\Omega = 30.5 \times 10^{-20} \text{ cm}^2$$

$$N = 2 \times 10^{15} \text{ cm}^{-2}$$

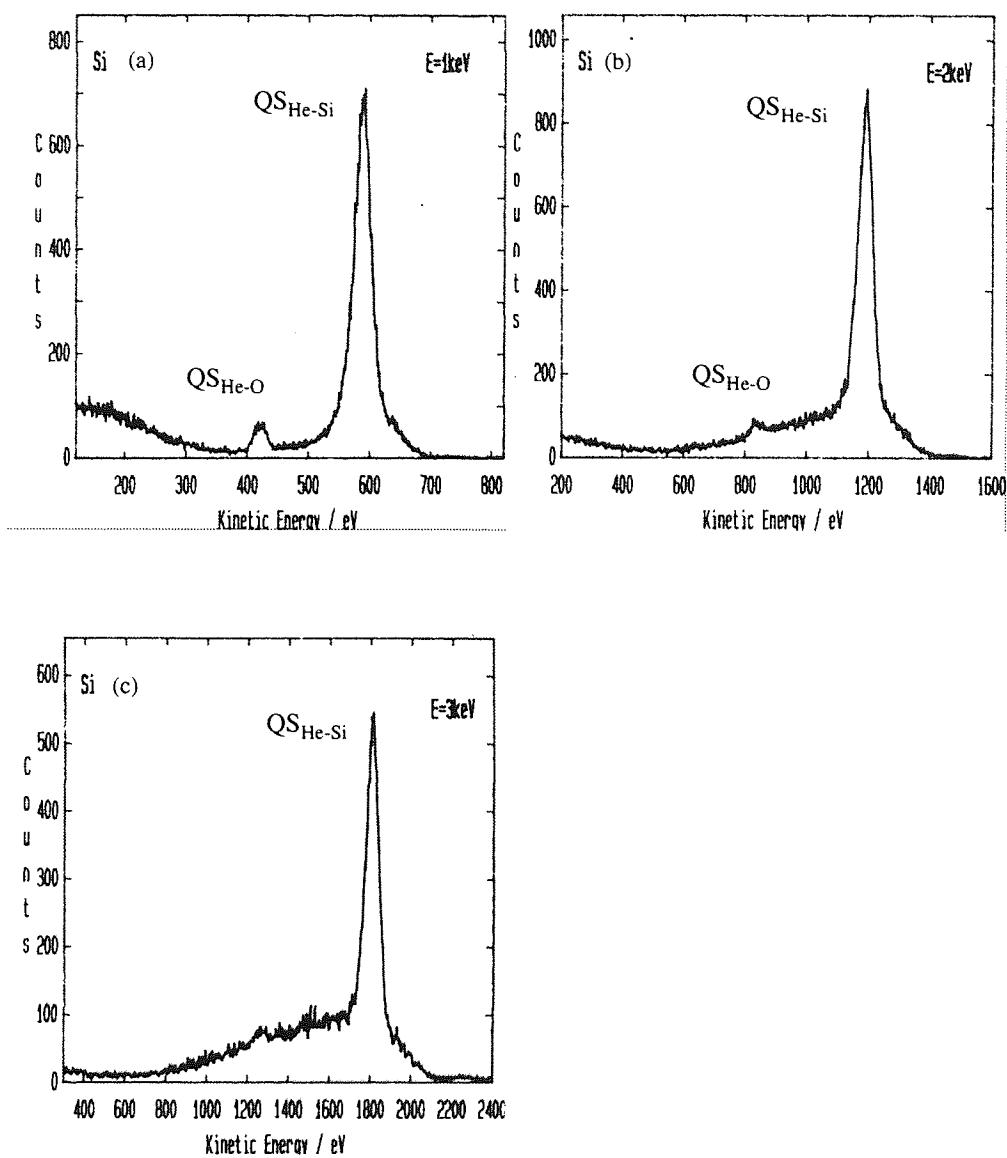


Figure 7.1 - Experimental LEISS spectra, He scattered from Si, collected on a separate ESCALAB-200D instrument.

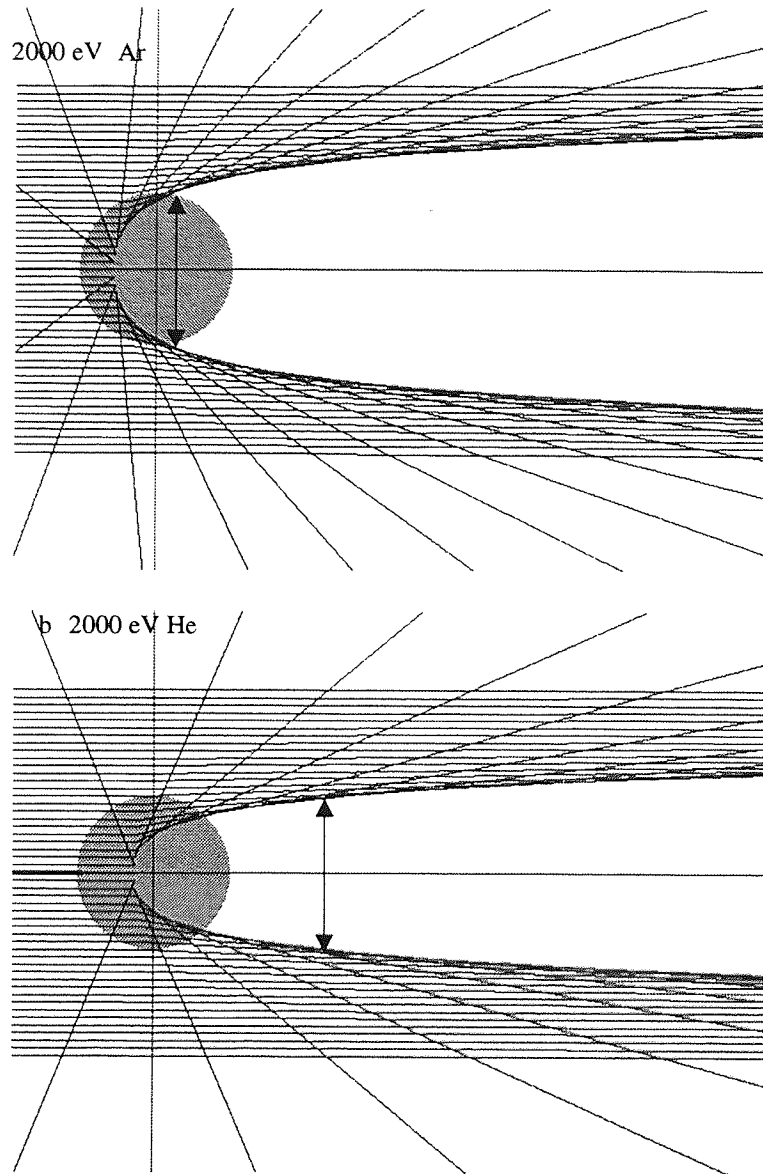


Figure 7.2 - Calculated shadow cones, (a) for a 2000 eV Ar-Au collision, and (b) for a 2000 eV He-Au collision.

These parameters give rise to an expected QS signal intensity of ~ 1 cps, compared to the total experimental signal of 84 cps. Integration of the signal intensity from the QT edge to the bottom of the saddle, as shown in figure 7.3a, gives rise to a signal of ~ 8 cps. Whereas integration over the expected peak width of 120ns, gives rise to a signal of ~ 3 cps, see figure 7.3b. Thus the signal intensity is greater than that which can be accounted for by QS scattering from an ordered surface. The additional signal intensity can only be explained by focusing effects which can only arise in the case of ordered surfaces. The results suggest therefore, that the gold coating had derived an ordered structure from the underlying Si(100) surface. This would also explain the decreased MS signal intensity. It was shown in the previous chapter that the experimental peak position appeared at a longer flight time than the expected position, consistent with an additional loss of ~ 160 eV. The origin of this loss was not certain, but is probably due to the presence of contaminant overlayers. A 'loosely bonded' salvage layer containing H, C, O atoms would present a region through which the incident and exit beam would have to pass in order to reach the true surface. Thus a layer of this nature would induce electron and nuclear stopping losses.

7.1.2 The absence of a scattered ion peak

Within the detection limits of the technique no scattered ion peak was observed in any of the experimental systems described above. This result contrasts sharply with previous results reported in the literature. As an example the reader is referred to work of Aono⁹⁵ where a 2 keV He beam was scattered from a Si-Ag surface. The discriminated ToF spectrum of figure 2.31 demonstrates an ion survival probability of $\sim 40\%$ from Ag and $\sim 5\%$ from Si. Whereas Grizzi et al¹²² reported ion survival probabilities of 70%, for the scattering of Ne⁺ from Si. Ion survival probabilities reported by Buck et al⁹⁰, relating to 5 keV He, Ne and Ar from a non-ordered Au surface are summarised in table 7.1.

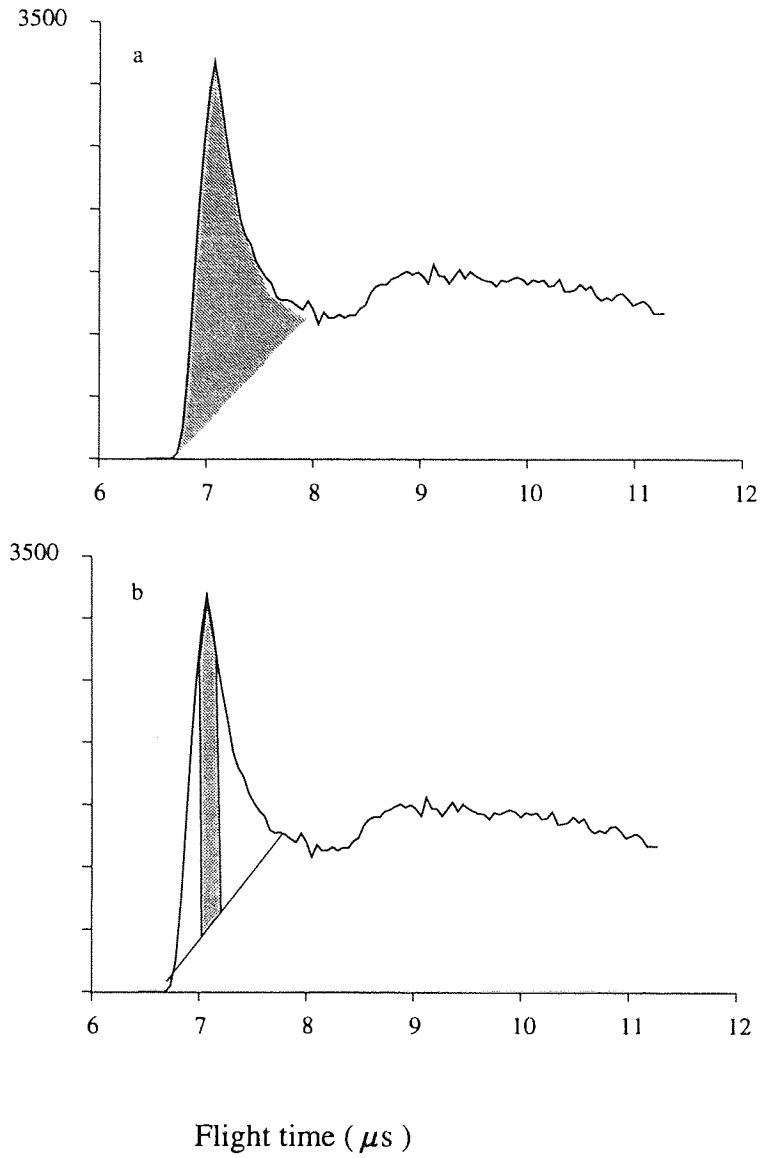


Figure 7.3 - Schemes of integrating the spectrum to extract an estimation of the QS signal intensity

Table 7.1 : Ion survival probabilities

	S-ESA	ToF
He	8%	3% to 4%
Ne	22%	5% to 12%
Ar	-	4% to 8%

It should be noted that these figures relate to the QS scattering only. In contrast to these results the minimum experimental sensitivity to the ion peak in this work are listed below. (In the case of helium the calculated peak intensity is used, due to the absence of an experimental QS peak.)

Table 7.2 - Ion peak detection limits (this work) 2.2 keV primaries scattered from a Au surface.

primary species	detection limit
He	3%
Ne	0.05%
Ar	0.1 %

The percentages given in table 7.2 represent the maximum possible ion signal relating to these measurements. The apparent inconsistency of these results is attributed to the presence of the contamination salvage layer. The presence of the low density selvage region as well as causing energy loss would provide neutralising centres. According to the model of Woodruff and Godfrey^{146,147} a neutralising region of radius a_{at} surrounds each individual surface atom. They also found a_{at} in the case of oxygen to be significantly greater than the atomic radius. Thus as illustrated in figure 7.4 there may be a high probability that the scattering particle will pass within a distance a_{at} of an atom centre in the selvage layer on either its' inward or outward path. A similar model was used by Niehus⁷⁶ to explain results relating to scattering from oxygen absorbed onto a tungsten surface. The results demonstrated the scattered ion signal to be strongly influenced by the oxygen coverage in a non linear manner, and very low ion survival probabilities were obtained at high coverages.

Supporting evidence for these conclusions was also obtained by

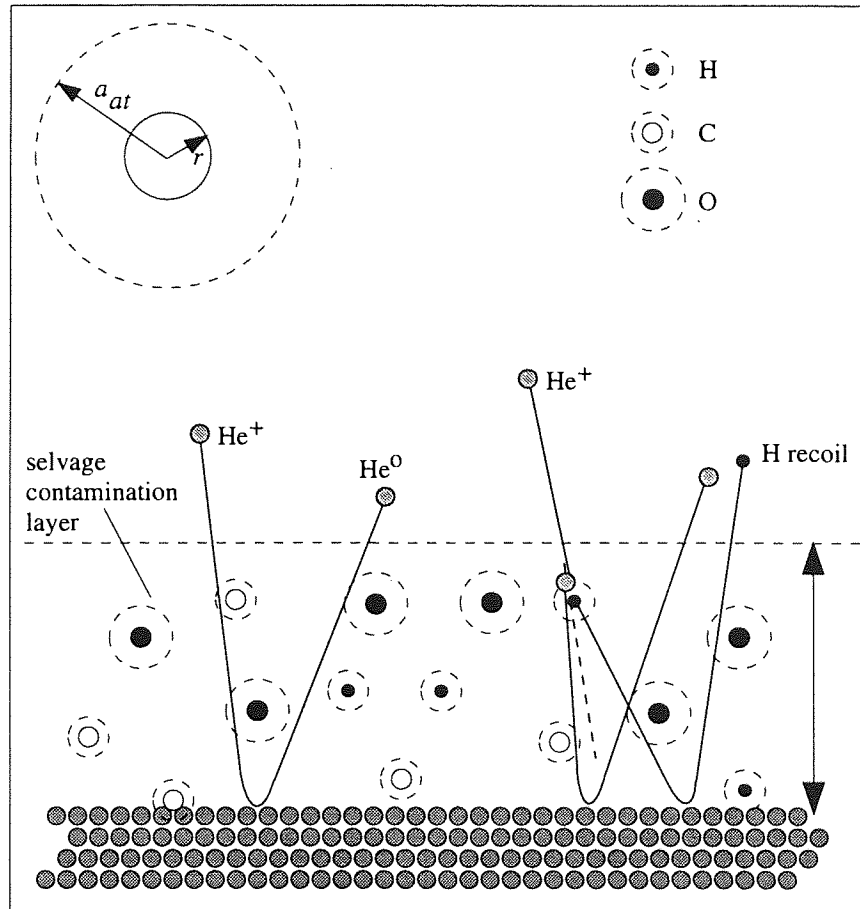


Figure 7.4 - Schematic of the contamination layer, depicting some of the possible scattering, neutralisation and recoil process.

comparing the LEISS signal intensity to that calculated by equation 7.1. As an example the peak intensity of the 1 keV Ne-Cu spectrum of figure 6.7 was $\sim 9 \times 10^3$ c/s, compared to the calculated intensity of $\sim 7 \times 10^6$ c/s, from which an ion survival probability of ~ 0.1 % can be inferred. However, signals of this intensity were obtained only after exposing the surface to an ion beam fluence, equivalent to the removal of ~ 100 monlayers, and the absence of any spectra prior to any surface cleaning must have originated from the presence of surface contamination.

7.1.3 Recoiling features of the experimental spectra.

Most of the spectra in addition to the scattered intensity exhibited a signal relating to ejection of recoil atoms, which were also predominantly in the neutral state. As the experimental scattering angle was greater or equal to 90° the signal cannot be attributed to 'direct' recoils. A mechanism in which the target atom may gain appreciable energy travelling in the direction of the detector is shown schematically in figure 7.5, which will subsequently be referred to as 'scattered recoils' as opposed to 'direct' recoils. In this case, the scattered recoil process involves a collision sequence leading to the ejection of a hydrogen recoil at 90° to the primary beam. In this example the helium atom is shown to impinge on the hydrogen atom with zero impact parameter, corresponding to maximum energy transfer. The recoiling hydrogen atom may then scatter from a surface atom in the usual manner. The value of A in this case is 64, leading to a k value close to unity. For a zero impact collision, the recoil atom receives an energy, E_{recoil} given by :

$$E_{recoil} = 4kA/(1+A)^2 E_o \quad (7.2)$$

Non-zero impact collisions will lead to the ejection of scattered recoils of energy less than E_{recoil} . A scattered recoil signal corresponding to the above collision is indicated in figure 6.1. The recoil energy, E_{recoil} for hydrogen in this case is 948 eV, corresponding to a $5.42 \mu s$ flight time, in good agreement with the experiment. A scattered recoil ToF spectrum can be seen more clearly in figure 6.19, which was the dominant feature in that case. The sharp edge at $24 \mu s$ corresponds to the maximum possible energy of a carbon recoil, 960 eV, and the peak intensity falls to zero at a flight time of $\sim 60 \mu s$, corresponding to a recoil energy of ~ 240 eV. It should be noted that the spectral shape of the recoil peak was strongly influenced by the detector

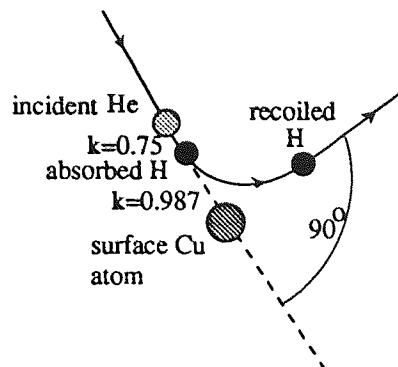


Figure 7.5 - A collision sequence leading to a target atom from the selvage layer gaining appreciable energy travelling away from the surface. In this case, the process leads to the ejection of a hydrogen recoil at 90° to the primary beam. The helium atom is shown to impinge on the hydrogen atom with zero impact parameter, corresponding to maximum energy transfer.

efficiency, and in this respect figure 6.19 does not give an accurate representation of scattered recoil spectrum. It is probable also that the peak has a contribution from oxygen recoils which are emitted with a maximum energy of 841 eV, corresponding to a flight time of 28 μ s. The absence of an edge relating to hydrogen recoils, which would be expected at 15.5 μ s, can be explained by the low recoil energy of only 261 eV.

Scattering data relating to collisions within the selvage layer, that is cross-sections, maximum θ of the primary, and energy transfer factors are presented in tables 7.3 to 7.5.

Table 7.3 Total collision cross-sections for collisions $> 1^\circ$ deflection by the primary / 10^{-16} cm²

	H	C	O
He	0.39	1.64	1.95
Ne	1.17	3.81	4.32
Ar	1.14	4.66	5.22

Table 7.4 Maximum deflection angles (degrees)

	H	C	O
He	14.5	180	180
Ne	2.9	36.9	53.1
Ar	1.4	17.5	23.6

Table 7.5 Energy transferred factors to recoil atoms

	H	C	O
He	0.64	0.75	0.64
Ne	0.18	0.94	0.99
Ar	0.095	0.71	0.82

The helium spectra exhibited a significant H recoil intensity at $\theta=90^\circ$, but not at 164° . Its absence in the latter case must be attributed to either the decreased cross-section of H-Au collision, or a reduction in the hydrogen concentration in the overlayer. Carbon and oxygen recoils cannot be observed as the associated flight times lie within the scattered particle peak. Additionally, the

collision cross-sections giving rise to appreciable energy transfer from helium is small. The neon spectra generally exhibit hydrogen, carbon and oxygen recoils, as exemplified by figure 6.16, here the recoil energies, E_{recoil} , were 352, 1480 and 1439 eV for the H, C and O respectively and the respective flight times are indicated in the figure. All three recoil species were also observed in the argon spectra, and with significantly greater intensity than the neon spectra counterpart: even when the Au surface appeared free from the C and O overlayer, according to a very low recoil signal in the neon spectrum, as shown in figure 6.23, a relatively large signal remained in the argon spectra, as shown by figure 6.27, which was collected immediately proceeding the neon spectrum. It is significant that hydrogen recoils were observable as their recoil energy is close to the detection limit, indicating a very high recoil signal. The greatly increased H recoil signal in the argon spectrum cannot be related to the total cross-section, as according to table 7.2, these are of similar magnitude. A number of factors combine to give a greater scattered recoil to scattered primary signal ratio: firstly it is more appropriate to compare the cross-section relating to energy transfer to the hydrogen recoil. Such a cross-section can be obtained from figure 7.6 which shows the energy received by the hydrogen recoil as a function of impact parameter. This comparison shows a factor of ~ 3 greater cross-section in favour of argon. Secondly the scattered signal in the argon spectrum was found to be a factor of ~ 4 smaller than neon for equivalent primary beam currents, which coincides with an increase in the differential cross-section of a factor of 1.3. These factors combine to predict an increased recoil signal in the case of Ar of a factor of ~ 16 , therefore providing a qualitative explanation of the increased recoil signal in the argon spectra.

Finally, it is noted that no recoil signal due to hydrogen was apparent in the argon spectra of figures 6.18 and 6.19. This was attributed to the fault, described previously, with the MCP, which gave rise to a significant increase in the low energy detection limit. As E_{recoil} for hydrogen in the case of argon bombardment is ~ 200 eV no signal was detectable due to the fault.

7.1.4 Surface Contamination

The absorbed selvage of hydrocarbons and water persisted throughout the experiments as indicated by the recoil signal: in the case of the gold, the selvage could be reduced but not removed completely by exposing the sample to the high fluence beam. No reduction in the selvage was

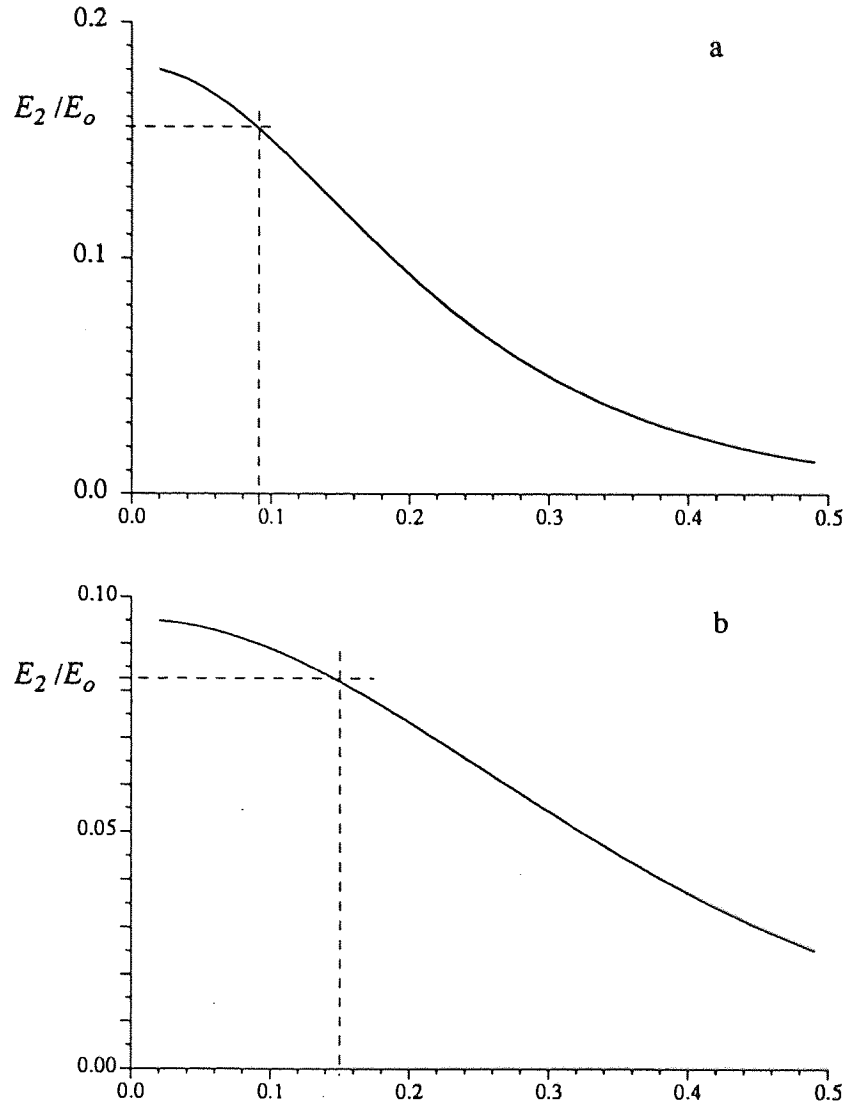


Figure 7.6 - Energy received by a hydrogen recoil as a function of the impact parameter, b . (a) Ne primary, (b) Ar primary.

obtained in the case of nickel. This contamination was attributed to either inadequate vacuum, or contaminant species in the saddle field beam. Although, the former is in conflict with the pressure indicated by the RGA and penning gauge which showed a base pressure of less than 10^{-10} mbar. It was also found that the selvage layer could be increased as a result of prolonged sample heating.

In addition to giving rise to the increased recoil intensity, the selvage was found to influence the ToF spectra in a number of other respects, which were discussed above. As well as causing low ion survival probability, and introducing energy loss, the selvage also reduces the scattering signal from the 'true' surface. Although this latter effect was observable in all the experimental spectra, it was most evident in the case of neon scattering from the nickel surface, where continued sample heating completely obscured the $QS_{\text{Ne-Ni}}$ peak.

As discussed in chapter 6, other contaminant species were also found on the surface. The presence of F1 and Mg on the silicon sample was clearly traced to the decomposition of the Kapton insulation. This was also identified by XPS analysis after the sample was removed from the vacuum chamber. These materials could not be identified by the helium scattering due to the domination of the MS signal, whereas the neon spectrum was outside the detector's energy range. The indium contamination on the nickel surface was identified by helium, neon and argon scattering, although the origin of the indium was not known.

7.1.5 Neutral bombardment

ToF spectra resulting from helium ion and neutral bombardment were shown in section 6.1.1.2. Although it was not possible to study a resulting shift in the QS peak due to the domination of the MS signal, some differences were observed, which are discussed here. The greatest differences appeared in the angle resolved measurements shown in figure 6.4. Both sets of spectra show a shift of the MS peak maximum towards longer flight times at low and high angles of incidence. The origin of the shift can be attributed to increased scattering from the selvage layer, and shielding of the underlying copper surface. At low incidence, $\theta=10^\circ$, the overlayer shields the incident beam, whilst for high incidence, $\theta=80^\circ$, the exit path of scattered particles is blocked by the overlayers. Comparison of the two sets of spectra suggested that the shielding was greater in the case of incident neutrals. This effect was

consistently observed, although it is necessary to exercise caution in attributing the differences solely to the charge state of the primary beam, for the reasons discussed in section 6.1.1.2.

7.2 Limitations of the ToFFASS technique.

Although the use of ToFFASS as a technique for surface analysis has a number of advantages compared with conventional LEISS, the results also demonstrate a limitation inherent in ToF analysis compared to ESA. In particular the helium spectra from non-ordered surfaces have demonstrated a dominant MS signal, which obscured that of the QS signal. This makes analysis of non-ordered surfaces containing species with atomic mass less than ~ 30 difficult. For example, although all surfaces analysed contained C and O within the surface layer, corresponding peaks were not clearly evident in the scattered particle spectra. In this work, the problem was compounded by the presence of a selvage layer, with a high hydrogen content, leading to further reductions in the QS signal. It would be possible in principle, as shown above, to reduce the MS signal by reducing the primary energy to ~ 200 eV. However, in practice this is prevented by difficulties relating to production and detection of neutrals of this energy. Furthermore, the validity of the binary collision approximation (BCA), upon which the principles of the technique are based, is called into question at this energy, see section 2.3.2.

7.3 Discussion of instrument capabilities and limitations.

7.3.1 Detection efficiency

The significant variation of detector efficiency over the experimental range was seen to have a pronounced influence on the spectra. As a result, the inherent spectra of both scattered and recoil particles were distorted, in particular the fall off in the low energy tail was significantly enhanced as a result of the reducing detector efficiency. The low energy cut off of the detector was initially ~ 500 eV and was later decreased to ~ 200 eV by the measures described in chapter 5. For the purpose of spectral interpretation of these results, in the absence of more accurate data, a linear calibration curve was employed. However, the results also suggested that the detector efficiency was species dependent as well as energy dependent, with

higher efficiencies for lighter species. This finding is exemplified by the presence of a significant hydrogen recoil peak in figure 6.27, where the recoil energy is only ~ 200 eV.

An obvious inconvenience arising as a consequence of the energy dependent detector efficiency was the necessity, in the case of quantitative analysis, to apply an appropriate correction. If this were done, spectra such as that of figure 6.17 would give rise to quantitative compositional information. The major limitation relating to the detector efficiency is the signal loss as the low energy limit is approached. This is particularly significant when it is considered, as shown in section 2.3.5, that the greatest mass resolving power is obtained when A is close to unity. However, this condition also gives rise to a large loss of energy, and consequently a low scattered energy. It is therefore apparent that a detector exhibiting a greater detection efficiency at lower energies would give rise to a significant instrumental advantage. It should be noted that these arguments apply to the scattering of neutrals only, as ions of low scattered energy can be accelerated onto the detector face in order to achieve optimum detection efficiency.

7.3.2 Collection rates and sample dose

One factor that would possibly limit the application of the ToFFASS instrument in its present form is the relatively long time required to collect the data. Collection times are dependent on many factors, and in particular the information required from the spectrum. Typically, a LEISS spectrum contains $\sim 10^5$ counts relating to the QS peaks. The collection times required to gain equivalent counts in the case of the present ToFFASS are given in table 7.6 for the case of He, Ne and Ar spectrum from a gold surface.

Table 7.6 - Sample dose and collection times to gain a QS peak composing 10^5 counts, assuming a 2 keV beam scattered from gold, of surface density of 2×10^{15} atoms/cm² ($\Delta\theta = 0.85^\circ$)

	T(E)	Collection	total dose
	(%)	time (s)	
He	0.76	544	6.8×10^{11}
Ne	0.617	172	2.1×10^{11}
Ar	0.422	196	2.5×10^{11}

It can be seen that even at this small angle of collection the sample dose is much smaller than encountered in the collection of LEISS spectra, which is 5×10^{13} for the equivalent conditions, however in this case the detection angle was much larger, at 8° . The collection rate can be increased either by increasing the primary beam current, or by increasing the detection angle. The second solution also has the advantage of decreasing the sample dose required. The figures of table 7.6 are recalculated for an 8° detection angle in table 7.7.

Table 7.7 - Sample dose and collection times to gain a QS peak composing 10^5 counts, assuming a 2 keV beam scattered from a gold surface of surface density = 2×10^{15} atoms/cm² ($\Delta\theta = 8^\circ$)

	T(E) (%)	Collection time (s)	total dose
He	0.76	6.2	7.7×10^9
Ne	0.617	1.9	2.4×10^9
Ar	0.422	2.2	2.7×10^9

These collection rates however would not be achieved in practice as they required the collection of more than one ion/pulse. In the case of neon and argon, collection times of a factor of 5 greater could be achieved. Whereas in the case of helium scattered from a non-ordered surface, the count rate would exceed the 1 ion/pulse threshold, by approximately two orders of magnitude, due to the presence of the large additional MS signal. However, a detection angle of this magnitude would clearly be an advantage in the detection of surface species with very low concentrations, although increasing $\Delta\theta$ would also lead to large reductions in spectra resolution. Table 7.8 gives the resolution in terms of $\Delta t/t$, for three different values of $\Delta\theta$. The resolution is calculated on the basis of reducing the flight path rather than increasing the detector diameter, thus compounding the reduction of resolution. To achieve $\Delta\theta=8^\circ$ whilst retaining the present tube length would require a detector of 35 cm, which is clearly not practical.

Table 7.8 Spectral resolution, $\Delta t/t$ - calculated for various $\Delta\theta$.

($\Delta t = 50$ ns, $E_0 = 2$ keV, $m_2 = 197$)

	$\Delta\theta=0.85^\circ$ ($l = 2.5$ m)	$\Delta\theta=4^\circ$ ($l = 0.57$ m)	$\Delta\theta=8^\circ$ ($l=0.28$ m)
He	151	37	19
Ne	188	88	48
Ar	140	99	62

The second option of simply increasing the primary current, is clearly an advantage where collection times are critical, and very low sample dose is not crucial. The increased sample current would not give rise to an increase in the sample dose unless the 1 ion/pulse threshold was exceeded.

7.3.3 Ion-neutral peak separation

Due to the absence of the scattered ion peak it was not possible to demonstrate the capabilities of the acceleration tube directly. However, the operation of the tube was confirmed experimentally in primary mode, showing good agreement between the experimental and calculated separation times. The second tube format was capable of introducing large temporal separations, as shown by the calculated spectra. For all the experimental cases investigated it was possible to separate the neutral and ion peaks completely. Using the second tube format calculations showed that the ion peak would appear to shorter flight times than the QT edge. This was also found to be the case in Ne scattered from Si, for which A is only 1.4, leading to a large separation between the QS and QT peaks. It was shown however, that it was not generally possible to accelerate the ion peak to lower flight times than the recoil peak edge. This reduced the sensitivity to the detection of the ion peak, however, in the case of a contamination free surface no recoil peak would be present, therefore significantly enhancing sensitivity.

CHAPTER VIII

Conclusions

8.1 Performance of the pulsed FAB source.

Initial operation of the prototype FAB source showed that a number of factors made it inadequate for the purpose of the ToFFASS. This led to the development of the two subsequent versions of the FAB source, FAB-1 and FAB-2. The operation of the FAB-2 source was generally found to be reliable, and in agreement with the theoretical predictions. The only operation problem related to the build up of contamination on the ceramic spacer tubes between the grid and extraction electrodes. This was despite the provision of a guard, preventing the deposition of material sputtered from the extraction electrode. The addition of this guard resolved the problem in the case of the FAB-1 source. Its return in the FAB-2 source was attributed to the reduced pumping speed of the region, leading to increased deposition of material desorbed from the filament, however, simple geometry changes could resolve this problem in later versions. The low beam current, ~ 300 namps, although sufficient for the preliminary work, would ideally be improved prior to further work. Modest increases in beam current could be made by changing the diameter of the filament wire: the diameter used in the FAB-2 source was slightly too large, leading to an emission current $\sim 1/3$ of the maximum possible with the present PSU. Further increases could be gained by increasing the power rating of the PSU composing the ion source supply. A more significant gain, particular in the case of the neutral current, could be gained by addressing the inadequate differential pumping. These changes have been adopted for a source presently under construction. Greater increases in beam current would require the replacement of the present ion source by a higher brightness source, such as the magnetically confined duoplasmatron type, which could be introduced to the proven optical column. When installed in the 164° position the source was further from the sample than in the 0° characterising position. As a consequence, the pumping of the CEC by the chamber was reduced leading to a lower neutral current for equivalent chamber pressure. In this position the maximum neutral fraction was $\sim 7\%$ of the maximum ion beam current. This problem would be readily resolved by the introduction of a second differential pumping stage to the column in the region of the CEC.

The development of the pulsed FAB of the required specification represented the greatest challenge of this work, and was a pivotal step in combining the ToF technique with fast atom bombardment. Despite these recommended modifications, the characteristics of the FAB-2 were seen to be impressive in terms of energy spread, pulse width and beam purity, exceeding the requirements laid down in the initial stages. With decreased working distance the beam diameter would become acceptable for many applications. The FAB-2 source therefore forms the basis of a unique analytical tool providing a useful addition to standard surface analysis instruments. It is presently been marketed for commercial applications.

8.2 Performance of the ToFFASS instrument.

Due to the problems of sample contamination the capabilities of the instrument could not be fully tested. These problems appeared to originate either from the vacuum chamber, in which case the associated pressure measurement system must be suspected, or the sample cleaning source. Specifically the high resolution capabilities of the instrument could not be demonstrated, as the experimental widths of the QS peaks were broadened by the presence of the contamination layer, and were at best 2 to 3 times broader than those predicted by calculation, taking worst case instrumental parameters. In addition to this the scattered ion intensity was found to be below the detection limits, and also significantly lower than that expected according to previous data. Consequently, the capabilities of the ion-neutral discriminator could not be demonstrated, and neutralisation probabilities could not be measured. However, the acceleration tube was shown to operate as expected by measurements made in the primary beam. The low ion intensity was also attributed to the presence of the contamination layer. Scattered particle intensities of neon and argon were in reasonable agreement with prediction, demonstrating the sample dose and collection times quoted in chapter 8 to be valid. Additionally, spectra were obtained whilst operating the source in neutral mode, where no additional instrumental problems were found relating specifically to neutral bombardment, other than the lower than ideal primary current. The most significant instrumentation limitation identified was due to poor detection efficiency of low energy neutrals.

8.3 Quantitative composition analysis.

The composition analysis of non-ordered surfaces using a helium beam is severely complicated by the large MS signal. This is particularly true of low mass species absorbed onto a heavier substrate. In view of these difficulties it is apparent that the real strength of the techniques lies in the analysis of ordered surfaces, where these problems are eliminated due to focusing and channelling effects. The inability to detect neutrals below ~ 200 eV excludes experimental conditions involving A less than ~ 2 . This is particularly inconvenient from the point of view of composition analysis, as these conditions give rise to maximum mass resolution. The result also indicates the detector efficiency to be dependent on the particle mass, and clearly some further work is necessary to calibrate MCP detector efficiency, before accurate quantitative interpretation of the ToF spectra is possible. The instrumental advantage brought about by the ToF technique in relation to the structural analysis of ordered surfaces is not challenged by this work. However, due to the difficulties regarding the surface contamination it was not possible to reproduce previous results. In conclusion, the remaining problems to be solved, in general, relate to the preparation of the surface. In this sense the capabilities of the instrument are not challenged. Thus given that the contamination problems can be eliminated the ToFFASS instrument opens the way towards the analysis of a whole range of insulating samples not accessible to LEISS. This combined with reduction of sample consumption to almost insignificant levels represents a significant step forward.

8.4 Charge transfer studies

The lengthened format of the flight and acceleration tubes were chosen to satisfy the requirements of the charge transfer studies. The format offers higher spectra resolution and larger ion-neutral separations than any similar facility. Although, due to the aforementioned contamination problems, it has not yet been possible to carry out these studies, the necessary instrumental components have been constructed and have been demonstrated experimentally, albeit on an individual basis. However, the results to date raise some questions with respect to the derivation of sensitivity factors for the quantification of LEISS data: that is, such data must be very well qualified with respect to hydrocarbon and water vapour contamination, which is

presented on any surface exposed to atmospheric conditions. It also appears that the method, in the case of helium, could only be applied to ordered surfaces. In view of the already significant contamination problems, the three axis goniometer containing the in vacuum stepper motors was not introduced into the chamber, and clearly must be investigated further in order to verify manufacturer's claims concerning outgassing rates. In view of the possible advantages this line of investigation is recommended, as the goniometer would allow unique investigation of charger transfer mechanisms.

8.5 Future Research

The construction of the ToFFASS has opened a range of possibilities for future research, which could be taken in a number of directions. The most immediate and greatest challenge concerning the instrument is the elimination of the contamination problem and the extension of detector operation to lower particle energies. On resolution of these problems the instrument could be used simply as an analysis facility for samples that cannot be analysed by LEISS, or a quantitative form of LEISS. However, to fully explore the potential of the instrument it is recommended that it is applied to the investigation of the surface particle interaction process, following an approach set out in chapter 3. Such a line of investigation promises to elucidate charge exchange and energy loss processes, providing data for comparison with the large body of theoretical model descriptions for these processes. As this line of research would require the implementation of the goniometer, this would also open the way to the important area of surface structure investigation. The experimentation in this work was greatly complicated by the absence of any other surface analytical technique available on the chamber. Whichever line of investigation is pursued the experimental investigation could be made considerably more straightforward by the addition of one or more established analysis technique.

The Design and Development of a Time of Flight Fast Atom/Ion Scattering Spectrometer

R. Giles,* J. L. Sullivan and C. G. Pearce

Electronic Engineering and Applied Physics, Aston University, Birmingham, England



Aston University

Content has been removed for copyright reasons

Appendix

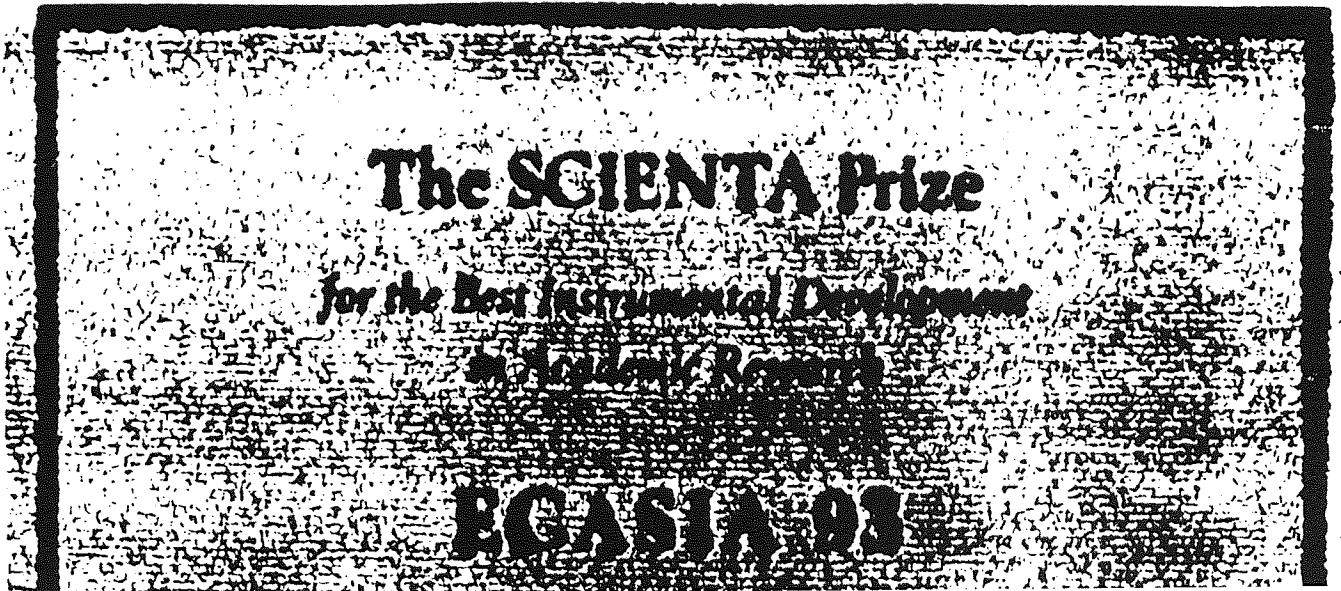
Citation - The scienta prize for the best Instrument Development in Accademic Research (ECASIA -93)

Orator: Professor H.Oechsner.



Aston University

Content has been removed for copyright reasons



Aston University

Content has been removed for copyright reasons

Reference

- [1] D. P. Smith, Surf. Sci., 25, 171, 1979.
- [2] D. G. Armour, Int.J.Mass Spec. and Ion Pro. 60,265, 1984.
- [3] T. M. Buck, in Methods of Surface Analysis, McGraw-Hill, NY, 1975.
- [4] V.Y.Young,G.B.Hofland,Surf. Sci,235,60,1990
- [5] M.H.Mintz,U.Atzmony,N.Shamir,Phys.Rev.Lett,59,90,1987.
- [6] P.Bertrand,E.Pierson,Nucl. Instr. and Meth. B67,340,1992
- [7] M.Aono,R.Souda, Jpn.J.Appl.Phys,24,1249,1985.
- [8] Th.Fauster, Vacuum, 38, 129,1988.
- [9] M.J.Ashwin,D.P.Woodruff,,Surf. Sci,237, 108,1990.
- [10] D.Briggs,M.P.Seah, Eds,Ion and neutral Mass Spectroscopy, Vol 2 of Practical Surface Analysis (Wiley Chichester, 1992)
- [11] E.Tagleuer,W.Heiland Nucl. Instr. and Meth.132, 535, 1976.
- [12] J.O'conner, Surf. Sci.173,593,1986.
- [13] H.Niehus.G.Comas, Surf.Sci.93,L147,1980.
- [14] T.M.Buck,Y.S.Chen,G.H.Wheatley,W.F. van der Weg, Surf.Sci.47,244, 1975.
- [15] S.B.Luitjens,A.J.Algra,E.P.Th.M.Suurmeijer,A.L.Boers,Surf.Sci.99,65-2,1980.
- [16] S.B.Luitjens,A.J.Algra,E.P.Th.M.Suurmeijer,A.L.Boers,Surf.Sci.99,63-1,1980.
- [17] S.B.Luitjens,A.J.Algra,A.L.Boers,Surf.Sci,80,566,1979.
- [18] H.Niehus,G.Comsa,Nucl.Inst.Meth,B15,122,1986.
- [19] T.M.Buck,G.L.Wheatley,G.L.Miller,D.A.H.Robinson,Y.S.Chen,Nucl Instrm and Meth. 149, 594,1978.
- [20] T.M.Buck,G.H.Wheatley,D.P.Jackson,Nucl.Instrum and Meth, 218,257,1983.
- [21] W.Rabalais,J.A.Schiltz,R.kumar,Nucl.Instrm and Meth 218,719,1983.
- [22] K.W.Sulston,A.T.Amos,Surf.Sci,224,543,1989.
- [23] M.Aono,M.Katayama,E.Nomura, Nucl. Instr. and Meth. B64,29,1992.
- [24] O.Grizzi,M.Shi,H.Bu,J.W.Rabalais, Rev.Sci.Instrm.61(2),740,1990.
- [25] J.W.Rabalais,H.Bu,C.Roux, Nucl. Instr. and Meth. B64,559,1992.

Reference

- [26] N.S. Xu, S.O. Saied, J.L. Sullivan, *Vacuum*, 42, 13, 849, 1991
- [27] N.S. Xu and J. L. Sullivan, *Surf. Int. Anal.*, 16, 18, 1990.
- [28] N.S. Xu, C.G. Pearce, J.L. Sullivan, *Surf. Int. Anal.*, 16, 154, 1990.
- [29] W. Eckstein, H. Verbeek, J.P. Biersack, *J. App. Phys.*, 51, 1194, 1980.
- [30] H.F. Helbig, M.W. Linder, G.A. Morris, S.A. Steward, *Surf. Sci* 114, 251, 1982.
- [31] P. Sigmund, *Phys Rev*, 184, 383, 1969.
- [32] P. Sigmund, *Sputtering by ion Bombardment*, Vol 1, *Topics in Appl. Phys.*, Springer Verlag, Heidelberg, 1981
- [33] B.H. Bransden, M.R.C. McDowell in *Charge Exchange and the theory of ion-atom collisions*, *International Series of Monographs on Physics*, Clarendon press, 1992 ISBN 0 19 852020 4
- [34] D.P. Smith, *J. Appl. Phys.*, 38, 340, 1967
- [35] R.G. Hart, C.B. Cooper, *Surf. Sci* 82, L233, 1979
- [36] M.T. Robinson, I.M. Torrens, *Phys. Rev B* 9, 5008, 1974.
- [37] V. Rosato, G. Maino, A. Ventura, *J. Phys. Condens. Matter*
- [38] B.J. Garrison, *Surf. Sci.* 87 683 1979
- [39] J.A. Yarmoff, R.S. Williams, *Surf. Sci.*, 127, 461, 1983.
- [40] R. Walker, Thesis, University of Salford, 1985.
- [41] C.C. Hsu, J.W. Rabalais, *Surf Sci.*, 256, 77, 1991.
- [42] R.H. Bergmans, A.C. Kruseman, C.A. Severijns, H.H. Brongersma, *Applied Surface Science* 70/71, 283-286, 1993.
- [43] E. Hulpke, *Surf Sci* 52, 1975, 615.
- [44] D.J. O'connor, R.J. Macdonald, *Nucl Inst and Meth* 170, 495, 1980
- [45] H. Niehus, *Surf Sci.* 166, L07, 1986
- [46] M. Aono, C. Oshima, S. Zaima, Otani, Y. Ishizawa, *Jpn. J. Appl. Phys.*, 20, L829, 1981
- [47] M. Aono, Y. Hou, C. Oshima, Y. Ishizawa, *Physical Review Letters*, 49, 567, 1982.
- [48] M. Aono, R. Souda, C. Oshima, Y. Ishizawa, *Physical Review Letters*, 51, 801, 1983.
- [49] T. Fauster *Vacuum* 3/2, 129, 1988.
- [50] W. Heiland, E. Taglauer, *Surf Sci*, 68, 96, 1977
- [51] E. Taglauer, W. Heiland, *Proc 7th Intern Congr & rd Intern Conf. Solid Surfaces*, Vienna 1977
- [52] E. Taglauer et al, *J Nucl Mat* 63, 193, 1976.
- [53] H.H. Brongersma, J.B. Theeten, *Surf Sci*, 54, 519, 1976.

Reference

- [54] H.H.Brongersma et al, Surf Sci. 71,657,1978.
- [55] O.S.Oen, Surf Sci 131.1407,1983.
- [56] D.P.Jackson, Nucl.Inst.Meth,132.603,1976.
- [57] R.Spitzl,H.Niehus,G.Comsa, Rev.Sci.Instrum 61(2),760,1990
- [58] E.Taglauer,W.Heiland,Surf. Sci.33,27,1972
- [59] B.J.Garrison,Surf. Sci. ,87,683,1979
- [60] H.B.Nielsen,T.A.Delchar,Surf.Sci., 141,487,1984
- [61] E.Hulpke,K.Mann,Surf.Sci.,133,171,1983
- [62] T.VonDemHagen,Surf.Sci.,117,1982.
- [63] D.P.Jackson,W.Heiland,E.Taglauer,Phys.Rev.,B24,4198,1981
- [64] E.Taglauer,W.Heiland,D.P.Jackson,Phys.Rev.,Lett.45, 740,1980
- [65] H.Overbury,Nucl.Instr.and Meth.B27,65,1987
- [66] H.Niehus,E.Preuss,Surf. Sci,119,349,1982
- [67] B.Poelsema,L.K.Verhey, Surf. Sci. 60,485,1976
- [68] B.Poelsema,L.K.Verhey, Surf. Sci. 133,344,1983
- [69] V.E.Yurasova,V.I.Shulga,D.S.Karpuzov,Can.J.phys.,46,759,1968
- [70] G.Engelmann,E.Taglauer,D.P.Jackson,Surf.Sci., 162,921,1985
- [71] E van de Riet,J.M.Fluit,A.Niehus, Surf.Sci. 231,386,1990
- [72] I.Stengaard, R.Fiedenhans, J.E.Sorensen, Surf. Sci.128,281,1983.
- [73] M.Copel, T.Gustafon, W.R.Graham,S.M.Yalisove, Phys. Rev.,B33,8110,1983.
- [74] E.Taglauer, W. Hieland, Proc 7th Intern Congr & 3rd Conf. Solid Surf. , [Vienna 1977.
- [75] E.Taglauer et al, Nucl Inst and Meth B35,404,1988.
- [76] H.Niehus,E.Bauer, Surf. Sci 47,222,1975
- [77] L.C.A.van den Oetelaar,S.N.Mikailov,H.H.Brongersma,Nucl. Instr. and Meth. B85,420,1994
- [78] A.Barcz,M.Croset,L.M.Mercandalli, 2nd Int Conf on Low-energy Ion Beams, 1980,p124.
- [79] M.A.Wheeler,Anal Chem 47,146,1975
- [80] D.G.Swartzager,Anal Chem,56,55,1984
- [81] T.A.Flaim: Research Publication GMR-1942,1975,Research Laboratories, General Motors, Michigan
- [82] Y.Wei,Sullivan.J.L,S.O.Saied, Surf Sci
- [83] H.Niehus, W.Heiland, E.Taglauer, Surface Science Reports, Volume 17 Nos 4/5, 1993, "Low-energy ion scattering at surfaces",

Reference

p259-279.

- [84] A.Brown et al J.Chem.Soc Commun,1684,1984
- [85] J.L.Sullivan,S.O.Saied, Vacuum 43/1,89,1992.
- [86] Brongersma, H.H. and J.-P. Jacobs, App. Surf.Sci.,75/1-4, 1994.
- [87] H.F.Helbig,P.J.Adelmann,A.C.Miller,A.W.Czanderna, Nucl. Instr. and Meth,149,1978,581
- [88] S.N.Luitjens, A.J.Algra,E.P.Th.M.Suurmeijer,A.L.Boers,J.Phys. E13, 655, 1980
- [89] H.Niehus,G.Comsa,Nucl. Instr. and Meth. B13,213,1986.
- [90] W.Eckstein in Spinger Series in Chemical Physics 17. Inelastic Particle-Surface Collisions.
- [91] T.M.Buck et al, Nucl. Instr. and Meth 194,649.1982.
- [92] Rabalais et al J.Chem.Phys 78(8),5250,1983
- [93] F.Masson,J.W.Rabalias, Surf. Sci. 253, 245, 1991
- [94] M.Katayama, M.Aono, H.Oigawa, Y.Nannichi, H.Sugahura, M.Oshima, Jpn,J.Appl.Phys 30,L786,1991.
- [95] I.Kamiya, M.Katayama,E.Nomura,M.Aono, Surf. Sci 242,404,1991.
- [96] Y.S.Chen, G.L.Miller et al, Surf Sci 62,133,1977
- [97] S.B. Luitjens et al Appl. Phys 21,205,1980.
- [98] O.Grizzi,M.Shi,H.Bu,J.W.Rabalias,Rev.Sci.Instrum. 61(2), 740,1990.
- [99] M.Aono,M.Katayama,E.Nomura,T.Chasse,D.Choi.M.Kato,Nucl. Instr. Meth. B37/38,264,1989.
- [100] T.M.Buck,G.H.Wheatley,L.K.Verheij,Surf.Sci,90,635,1979
- [101] R.Souda,M.Aono,Nucl Instra and Meth B15,114,1986
- [102] S.Tsuneyuki,M.Tsukada, Phy. Rev. B34, 5758,1986
- [103] R.Souda,M.Aono,C.Oshima,S.Otani,Y.Ishizawa, Surf. Sci, 179, 199, 1987.
- [104] L.K.Verhey,B.Poelsema,A.L.Boers,Rad.Effects, 31,23,1976
- [105] S.Schippers et al,Surf. Sci 257,289,1991.
- [106] R.J.Macdonald, D.J.O'conner, Surface Sci, 124,433,1983
- [107] R.J.MacDonald,C.M.Loxtton,P.J.Martin in Inelastic Particle Surface Collisions, Eds E.Taglauer,W.Hieland, Vol. 17 of Springer series in Chemical Physics (Springer, Berlin, 1981) p 224
- [108] I.S.T.Tong, in Inelastic Particle Surface Collisions, Eds E.Taglauer,W.Hieland, Vol. 17 of Springer series in Chemical Physics (Springer, Berlin, 1981) p 258

Reference

- [109] A.J.Algra,E.van,Loenen,E.P.Th.M.Suumeijer,A.LK.Boers,Rad eff. 60,173,1982.
- [110] E.G.Overbosch,J.Los,Surf. Sci.,108,99,1981.
- [111] G.A.Kimmel,D.M.Goodstein,Z.H.Levine,B.H.Cooper,Phys.Rev, B43, 9403, 1991.
- [112] J.K.Nfrskov,B.I.Lundqvist,Phys Rev., B19,5661,1979.
- [113] T.W.Rusch, R.L.Erickson in Inelastic ion Surface Collisions, Eds N.H.Tolk et al,1977,p73.
- [114] A.Zartner,E.Taglauer,W.Hieland, Phys. Rev.Lett. 40,1259,1978
- [115] J.C.Tully & Tolk,N.H. (1977) in Inelastic Ion-Surface Collisions, eds N.H.Tolks,J.C.Tully,W.Hieland & C.W.White (academic Press, London), p 105.
- [116] H.D.Hagstrum, Phys. Rev, 123, 758, 1961.
- [117]
- J.Möller,K.J.Snowdon,W.Hieland,H.Niehus,Surf.Sci.165,327,1986.
- [118] T.W.Rusch,R.L. Erickson in: Inelastic ion-surface collisions Academic Press 1977 page 79.
- [119] M.Barat,W.Lichten, Phys Rev, A6,211,1972.
- [120] L.K.Verhey,B.Poelsema.A.L.Beers, Nucl. Instr. and Meth., 132, 565, 1976.
- [121] T.M.Thomas et al Surf. Sci., 175,L737,1986.
- [122] O.Grizzi,M.Shi,H.Bu,J.W.Rabalais,R.A.Baragoila,Phy. Rev.,B41(7),4789,1990
- [123] S.Lacombe,L.Guillemot,M.Huels,T.Vu Ngoc, V.A. Esaulov, Surf. Sci. Lett., 295, L1011,1993.
- [124] P.A.Zeijlmans Van Emmichoven, P.A.A.F.Wouters, A.Niehaus, Surf. Sci 195, 115],1988,
- [125] T.Vu.Ngoc - private communication
- [126] W.Heiland, E.Taglauer, in Inelastic ion Surface Collisions, Eds N.H.Tolk et al,1977,p27.
- [127] W.Eckstien et al, Nucl. Instr. Meth, 149, 599, 1978.
- [128] P.Bertrand,Nucl. Instr. and Meth. B170,489,1980
- [129] E.Tagleuer,W.Heiland, Nucl. Instr. and Meth., 132,535,1976.
- [130] F.Shoji,T.Hanawa, Nucl. Instr. and Meth., B2,401,1984.
- [131] O.B.Firsov, Sov. Phys. JETP 36,1076,1959.
- [132] O.S.Oen and M.T.Robinson,Nucl. Instr. and Meth. 132,647,1976.
- [133] J.Lindhard,M.Scharff,Phys. Rev 124,128,1961
- [134] P.M.Echenique,F.Flores,R.Ritchie, Solid State Phys. 43,229,1990.

Reference

- [135] L.K.Verhey,B.Poelsema,A.L.Boers,Rad Effects 27,47,1975
- [136] M.T.Robinson,I.M.Torrens,Phys Rev B9,5008,1994.
- [137] W.Brandt,J.Rienheimer,Phys Rev 2B,3104,1970.
- [138] H.Winter, Nucl. Instr. and Meth. B78,38,1993.
- [139] A.Närmann,W.Hieland,R.Monreal,F.Flores,P.M.Echenique, Phys Rev B44,2003,1991.
- [140] A.Närmann,R.Monreal,P.M.Echenique,F.Flores,W.Hieland,S.Schubert,- Phys. Rev. Lett. 64,1601,1990.
- [141] A.Närmann,H.Franke,K.Schmidt,A.Arnau,W.Hieland,Nucl. Instr. and Meth. B69,158,1991.
- [142] A.Narmann, Phys Rev B44,2003,1991.
- [143] H.D.Hagstrum , Phys. Rev, 96, 336, 1954.
- [144] H.D.Hagstrum, in Inelastic Ion-Surface Collisions, Eds N.H. Tolk, J.C.Tully, W.Hielnad, C.W.White (Academic Press, New york, 1977) pp1-25
- [145] J.R.McDonald,C.M.Loxton, P.J.Martin, Instr. and Meth. B132,224,1976.
- [146] D.J.Godfrey,D.P.Woodruff,Surf.Sci.105,1981,459.
- [147] D.J.Godfrey,D.P.Woodruff,Surf.Sci.105,1981,438.
- [148] G.Verbist,J.T.Derrees Surf. Sci. 223, 323, 1990
- [149] J.A.Applebaum,D.R.Hamann,Phy. Rev., 12,12,5590,1975.
- [150] E.Pierson,I.M.Beuken,P.Bertrand,Surf. Sci 223,201,1989.
- [151] M.Beckschulte , E.Taglauer ucl. Instr. and Meth. B78,29,1993.
- [152] Pierson,I.M.Beuken,P.Bertrand,Surf. Sci 214,560,1989.
- [153] A.L.Boers, Nucl. Instr. and Meth. B4,98,1984
- [154] J.N.Beuken,E.Pierson,P.Bertrand,Surf. Sci.223,201,1989.
- [155] ch3-41 G.Verbist,C.A.Severijns, H.H.Brongersma, J.T.Derreese, Nucl. Instr. and Meth., B73,517,1993.
- [156] D.M.Newns,K.Makoshi,R.Brako,J.N.M.van Wunnik, Phys. Scr.,T6,5,1983.
- [157] D.M.Newns,Phys.Rev., 178,1123,1969.
- [158] W.Bloss,D.Hone Surf. Sci.,72,277,1978.
- [159] R.Brako,D.M.Newns, Surf. Sci.,108,253,1981
- [160] G.C.van Leerdam, H.H.Brongersma,Surf. Sci., 254, 153,1991.
- [161] Y.Muda,D.M.Newns, Nucl. Inst. and Meth., B33,388,1988.
- [162] K.W.Sulston.A.T.Amos,S.G.Davison,Phy.Rev., B37,16 ,9121,1988.

Reference

- [163] K.J.Snowdon, R.Hentschke,A.Narmann,W.Heiland, Surf. Sci,173,581,1986.
- [164] E.E.Nikitin,S. Ya.Umanskii,Theory of slow atomic collisions (Springer-Verlag,Berlin,1984)
- [165] E.Pierson,J.M.Beuken,P.Bertrand,Nucl. Instr. and Meth. B45,374,1990.
- [166] R.Souda,M.Aono ,Nucl. Instr. and Meth. B27,54,1987.
- [167] R.J.Macdonald,D.J.O'Conner, Nucl. Instr. and Meth. B33,446,1988
- [168] R.Souda,M.Aono,C.Oshima,S.Otani,YIshizawa, Surf. Sci 150,L59,1985
- [169] P.Steffens, E.Niehuis,T.Friese,D.Greifendorf,A.Benninghoven, J.Vac.Sci.Tecnol. A3(3), 1322,1985.
- [170] B.T.Chait,K.G.Standing,Int J Mass Spec and Ion Phys, 40, 185, 1981
- [171] J.Schwieters, J.F.Zehnpennig, E.Niehuis, A.Benninghoven, J.Vac.S ci.Tecnol, A8(5), 3752, 1990.
- [172] M.van de Grift, Eindhoven University of Technology, Dept of Physics, "Time of flight ion scattering and recoiling spectrometer. Optimisation and first results".
- [173] A.J.Eccles,Thesis, Umist,1986.
- [174] B.Chapman in "Glow discharge processes", Wiley 1980 p91
- [175] K.Wittmaack, Nucl. Instrum.Meth 143,1,1977
- [176] E.Munro, A set of programs for calculating the properties of electron lenses, User Manual, 1975.
- [177] SIMION
- [178] T.Mulvey, M.J Wallington, Rep Prog Phys, 36, 347, 1973
- [179] E.Harting,F.H Read, Electrostatic Lenses, Elsevier, Amsterdam, 1976.
- [180] F.H.Read, Int Phys Comp Ser, No 38, chapter 6,1978
- [181] H.D.Hagstrum Phys. Rev. 104, 672,1956
- [182] K.Oda,T.Kaine,A.Ichimiya,S.Ohtani,K.Ohya,H.Tawara, Surf.Sci.,262,6,1992
- [183] Z.Wronski, C.G.Pearce, Vacuum 43/10, 931,1992.
- [184] N.S.Xu,S.O.Saied,J.L.Sullivan, C.G.Pearce,Vacuum, 39/5, 475,1989.
- [185] N.Xu,J.Sullivan. Aston University Report, "The Aston Fast Atom Scattering Spectrometer and Fast Atom/Ion Beam

Reference

- Source", 1989, Unpublished work.
- [186] P.J.Szwemin, M.Kaczanowski, M.Niewinski, *Vacuum*, 44/(5-7), 451, 1993.
- [187] R.Giles, Z.Bochnick, Monte Carlo simulation of the Ion Cell, Unpublished work.
- [188] L.Lany, C.G.Pearce unpublished work.
- [189] C.E.Carlston, G.D.Maguson, *Rev.Sci.Instrum*, 33, 90, 1962
- [190] S.Sakabe, Izawa, *Phys Rev*, V45, 3, 2086.
- [191] T.K.Fowler, W.M.Good, *Nucl. Instrum.Meth* 7, 245, 1960.
- [192] P.R.Jones, N.W.Eddy, H.P.Gilman, A.k.Jhaveri, G.VanDyk, *Phys. Rev*, 147, 76, 1966.
- [193] M.J.Barat, M.Abignoli, J.C.Houwer, *J.Phys.B: Atom.Molec.Phys*, 3, 230, 1970.
- [194] R.L.Seliger, *J.Appl.Phys* 43, 1972, 2352
- [195] Hamamatsu, technical information, MCP Assembly, 1991.
- [196] H.Verbeek, *J.Phys. E* 10 1977 944
- [197] E.W.Kuipers, A.W.Boers, *Nucl. Instr. Meth B* 29, 567, 1987.
- [198] M.A.Gruntmann, V.A.Morozov, *J.Phys E* 15, 1356, 1982.
- [199] P.Schagen in *Advances in image pick-up and display*, vol . Academic Press, New York, p1, 1974.
- [200] Panure Instruments Limited
- [201] L.Stallard-Mullin, final years project report, 1992.
- [202] Private communication with STEBBON